

**Multi-Satellite Orbit Determination Using Interferometric
Observables with RF Localization Applications**

by

Jeroen L. Geeraert

B.S., Embry-Riddle Aeronautical University, 2011

M.S., Georgia Institute of Technology, 2012

A thesis submitted to the
Faculty of the Graduate School of the
University of Colorado in partial fulfillment
of the requirements for the degree of
Doctor of Philosophy
Department of Aerospace Engineering Sciences

2017

This thesis entitled:
Multi-Satellite Orbit Determination Using Interferometric Observables with RF Localization
Applications
written by Jeroen L. Geeraert
has been approved for the Department of Aerospace Engineering Sciences

Dr. Jay McMahon

Dr. Penina Axelrad

Dr. Brandon Jones

Dr. Daniel Scheeres

Dr. Behrouz Touri

Date _____

The final copy of this thesis has been examined by the signatories, and we find that both the content and the form meet acceptable presentation standards of scholarly work in the above mentioned discipline.

Geeraert, Jeroen L. (Ph.D., Aerospace Engineering Sciences)

Multi-Satellite Orbit Determination Using Interferometric Observables with RF Localization Applications

Thesis directed by Dr. Jay McMahon

Very long baseline interferometry (VLBI) specifically same-beam interferometry (SBI), and dual-satellite geolocation are two fields of research not previously connected. This is due to the different application of each field, SBI is used for relative interplanetary navigation of two satellites while dual-satellite geolocation is used to locate the source of a radio frequency (RF) signal. In this dissertation however, we leverage both fields to create a novel method for multi-satellite orbit determination (OD) using time difference of arrival (TDOA) and frequency difference of arrival (FDOA) measurements. The measurements are double differenced between the satellites and the stations, in so doing, many of the common errors are canceled which can significantly improve measurement precision.

Provided with this novel OD technique, the observability is first analyzed to determine the benefits and limitations of this method. In all but a few scenarios the measurements successfully reduce the covariance when examining the Cramér-Rao Lower Bound (CRLB). Reduced observability is encountered with geostationary satellites as their motion with respect to the stations is limited, especially when only one baseline is used. However, when using satellite pairs with greater relative motion with respect to the stations, even satellites that are close to, but not exactly in a geostationary orbit can be estimated accurately. We find that in a strong majority of cases the OD technique provides lower uncertainties and solutions far more accurate than using conventional OD observables such as range and range-rate while also not being affected by common errors and biases. We specifically examine GEO-GEO, GEO-MEO, and GEO-LEO dual-satellite estimation cases. The work is further extended by developing a relative navigation scenario where the chief satellite is assumed to have perfect knowledge, or some small amount of uncertainty considered but

not estimated, while estimating the deputy satellite state with respect to the chief. Once again the results demonstrate that the TDOA and FDOA OD results are favorable with faster dynamics over classical measurements.

This dissertation not only explores the OD side, but also gaps in geolocation research. First the mapping of ephemeris uncertainty to the geolocation covariance to provide a more realistic covariance was implemented. Furthermore, the geolocation solution was improved by appending a probabilistic altitude constraint to the posterior covariance, significantly reducing the projected geolocation uncertainty ellipse. The feasibility of using the geolocation setup to passively locate a LEO satellite was also considered. Finally the simulated results were verified using a long-arc of real data. The use of FDOA for small-body navigation and gravity recovery was also examined as an extended application.

Dedication

To Ben, Rémi, Matt, Nicola, & Samm.

Acknowledgements

A special thanks goes to my advisor, Dr. Jay McMahon, without his guidance and insight I would have never made it this far. I also appreciate you taking me on when you did and setting me on a clear trajectory, you are a fantastic advisor! I would also like to thank the other members of my committee, Dr. Penina Axelrad, Dr. Brandon Jones, Dr. Daniel Scheeres and Dr. Behrouz Touri for their willingness to meet and discuss my research. The Aerospace Engineering Sciences faculty and staff in general are incredibly knowledgeable and helpful.

I am also deeply indebted to the friends I have made at CU, especially Matt, Nicola, and Samm. Matt, I looked forward to just about all the runs we did together, allowing me to think clearly. Nicola, your brilliance amazes me, thanks for all the advice and pasta over the years. Of course, Samm, thanks for being my rock during shaky times, I can always count on you. A big thanks also to everyone in my lab and CSML for the wonderful years and for all the help and iteration of ideas.

To my parents, Filip and Johanna, who instilled in me the passion for learning, to aim high, and taught me the value of doing your best. To my sister and brother, Hannelore and Ruben, who probably brewed up some healthy competitiveness in me, and will likely always call me a 'fake' doctor as MDs. Thank you so much!

Contents

Chapter		
1	Introduction	1
1.1	Background	1
1.2	Fundamentals of Orbit Determination	3
1.3	Interferometry Overview	7
1.4	Radio Frequency Localization Overview	10
1.5	Original Dissertation Contributions	12
1.6	Dissertation Organization	16
2	Preliminaries	19
2.1	Dynamical Models	19
2.1.1	Two-Body Problem	19
2.1.2	N-Body Problem	21
2.1.3	Geopotential Model	23
2.1.4	Solar Radiation Pressure Model	24
2.2	Measurement Models	28
2.2.1	Time and Frequency Difference of Arrival	28
2.2.2	Light-Time Correction	38
2.2.3	Range and Range-Rate	39
2.2.4	Angles: Azimuth and Elevation	41
2.3	Coordinate Frames	44

3	Orbit Determination Filters	46
3.1	Batch Processor	46
3.1.1	Cholesky Decomposition	48
3.1.2	Singular Value Decomposition (SVD)	49
3.1.3	Consider Batch Processor	50
3.2	Kalman Filter	52
3.2.1	Process Noise	53
3.2.2	Smoothing	56
3.2.3	Extended Kalman Filter (EKF)	57
3.3	Square-Root Information Filter (SRIF)	57
3.3.1	Process Noise	58
3.4	Unscented Kalman Filter (UKF)	58
3.4.1	Square-Root Unscented Kalman Filter (SR-UKF)	59
3.4.2	Square-Root Unscented Schmidt-Kalman Filter (SR-USKF)	61
4	Absolute Dual-Satellite Orbit Determination	69
4.1	Observability	69
4.1.1	Definition of Observability	69
4.1.2	Observability Matrix Formulation	71
4.1.3	Numerical Evaluation of the Observability Matrix	78
4.1.4	Condition Number	81
4.1.5	Degree of Observability	82
4.1.6	Correlations	87
4.1.7	Cramér-Rao Lower Bound (CRLB)	88
4.2	Dual-Satellite Orbit Determination	96
4.2.1	TDOA/FDOA and Range/Range-Rate CRLB Comparison with Varying Measurement Uncertainties	97

4.2.2	GEO-LEO Orbit Determination	106
4.2.3	GEO-MEO Orbit Determination	110
4.2.4	GEO-GEO Orbit Determination	113
5	Relative Orbit Determination	116
5.1	Satellite State Dynamics	116
5.2	GEO Chief + LEO-to-GEO Deputy Satellite Pairing	120
5.2.1	Estimating the Deputy with Perfect Chief Knowledge	120
5.2.2	Estimating the Deputy with Considered Chief Uncertainty	126
5.3	LEO-to-GEO Chief and Deputy in Leader-Follower Formation Flight	131
5.3.1	Estimating the Deputy with Perfect Chief Knowledge	131
5.3.2	Estimating the Deputy with Considered Chief Uncertainty	136
5.4	Bounded Relative Motion	140
5.4.1	Deputy Equations of Motion for Bounded Relative Motion	140
5.4.2	Estimating the Deputy with Perfect Chief Knowledge	141
5.4.3	Estimating the Deputy with Considered Chief Uncertainty	146
6	Radio Frequency Localization	155
6.1	Geolocation	155
6.1.1	Ephemeris Uncertainty Mapped into Geolocation Covariance	158
6.1.2	Simultaneous Ephemeris Correction and Geolocation	169
6.2	Satellite Localization	172
6.2.1	Ephemeris Uncertainty Mapped into Satellite Localization Covariance	173
7	GEO-GEO Orbit Determination and Geolocation with Real Data	180
7.1	GEO-GEO Orbit Determination	180
7.1.1	Prediction Analysis	182
7.1.2	Long-Arc Overlap Analysis	183

7.1.3	Short-Arc Overlap Analysis	184
7.2	Geolocation	186
7.2.1	Geolocate Miami Transmitter	187
7.2.2	Geolocate Chantilly Transmitter	189
8	Small Body Navigation and Gravity Estimation	192
8.1	Navigation Truth Models	193
8.2	Filter Dynamical Model	197
8.3	Filter Measurement Model	199
8.4	Simulation Results	200
8.4.1	Cramér-Rao Lower Bound (CRLB) Analyses	200
8.4.2	Navigation Results	202
9	Conclusion and Future Work	211
	Bibliography	215
	Appendix	
A	Observability Matrix Time Derivatives	221
A.1	Gravity Gradient Time Derivatives	221
A.2	SRP Gradient Time Derivatives	222
A.3	SRP Partial with Respect to Coefficient of Reflectivity Time Derivatives	224

Tables

Table

4.1 Monte Carlo simulation inputs	80
4.2 CRLB 1σ a-priori uncertainty for dual-estimated states and measurements	88
4.3 Orbit parameters of satellites in CRLB analysis	89
4.4 Latitude, longitude and altitude of transmitters and receivers	89
4.5 Time available to take measurements with a GEO-LEO setup in a 9 hour period [min] 91	91
4.6 Satellite orbital elements for dual-satellite CRLB analysis	94
4.7 Measurement Uncertainty Ranges	97
4.8 Orbit parameters of GEO-LEO satellites	107
4.9 GEO-LEO: $\pm 3\sigma$ covariance and state errors at the end of 9 hour observation span .	109
4.10 Orbit parameters of GEO-MEO satellites	110
4.11 GEO-MEO: $\pm 3\sigma$ covariance and state errors at the end of 24 hour observation span	112
4.12 Orbit parameters of GEO-GEO satellites	113
4.13 GEO-GEO: $\pm 3\sigma$ covariance and state errors at the end of 24 hour observation span	115
5.1 Latitude, longitude and altitude of transmitters and receivers used in relative OD cases	119
5.2 CRLB 1σ a-priori uncertainty for relative estimated states and measurements	120
5.3 Orbital elements for GEO chief + LEO-to-GEO deputy	120
5.4 Orbital elements for LEO-to-GEO chief and deputy	131

5.5	Relative orbit parameters for face-on and edge-on relative orbits	141
6.1	Latitude, longitude and altitude of transmitters and receivers used in geolocation examples	158
6.2	Summary of covariance ellipses (major axis \times minor axis) and errors [m]	170
6.3	Orbit parameters of satellites used in satellite localization	173
7.1	15 hr overlap analysis: errors and covariance [m & mm/s]	184
7.2	4.5 hr overlap analysis: errors and covariance [m & mm/s]	185
7.3	Evolving AGOM over 45 hour long-arc data span	186
7.4	Real-data geolocation error [km]	186
8.1	Truth model parameters	197
8.2	CRLB 1σ a-priori uncertainty for estimated states and measurements	201

Figures

Figure

1.1 OD problem (adapted from [83])	4
1.2 Example VLBI configurations	8
1.3 Geolocation geometry	11
1.4 Fundamental literature to the fields of VLBI and geolocation	13
1.5 Merging of two fields that forms a new innovative technique for multi-satellite OD .	14
2.1 Two-body problem (adapted from[83])	20
2.2 N-body problem	21
2.3 SRP shadow model geometry	27
2.4 TDOA/FDOA geometry, antennas in box are at same location	28
2.5 Range/range-rate geometry, antennas in box are at same location	39
2.6 Geometry for angles observables: E is the central body, m is the main satellite and i are the observed satellites	42
3.1 Batch processor flow chart (adapted from [83])	48
3.2 Sequential processor computational algorithm (adapted from [83])	54
4.1 TDOA RMS for sat ₁ /sat ₂ X_0 perturbation from truth in km	84
4.2 FDOA RMS for sat ₁ /sat ₂ X_0 perturbation from truth in km	84
4.3 TDOA RMS for sat ₁ /sat ₂ Y_0 perturbation from truth in km	84
4.4 FDOA RMS for sat ₁ /sat ₂ Y_0 perturbation from truth in km	84

4.5	TDOA RMS for $\text{sat}_1/\text{sat}_2$ Z_0 perturbation from truth in km	84
4.6	FDOA RMS for $\text{sat}_1/\text{sat}_2$ Z_0 perturbation from truth in km	84
4.7	TDOA RMS for $\text{sat}_1/\text{sat}_2$ \dot{X}_0 perturbation from truth in km/s	85
4.8	FDOA RMS for $\text{sat}_1/\text{sat}_2$ \dot{X}_0 perturbation from truth in km/s	85
4.9	TDOA RMS for $\text{sat}_1/\text{sat}_2$ \dot{Y}_0 perturbation from truth in km/s	85
4.10	FDOA RMS for $\text{sat}_1/\text{sat}_2$ \dot{Y}_0 perturbation from truth in km/s	85
4.11	TDOA RMS for $\text{sat}_1/\text{sat}_2$ \dot{Z}_0 perturbation from truth in km/s	85
4.12	FDOA RMS for $\text{sat}_1/\text{sat}_2$ \dot{Z}_0 perturbation from truth in km/s	85
4.13	TDOA RMS for $\text{sat}_1/\text{sat}_2$ AGOM perturbation from truth of 0.0625/0.0425	86
4.14	FDOA RMS for $\text{sat}_1/\text{sat}_2$ AGOM perturbation from truth of 0.0625/0.0425	86
4.15	Correlations	87
4.16	GEO-LEO CRLB: trace of covariance for TDOA/FDOA with varying number of baselines	92
4.17	GEO-MEO CRLB: trace of covariance for TDOA/FDOA with varying number of baselines	92
4.18	GEO-GEO CRLB: Trace of Covariance for TDOA/FDOA with varying number of baselines	93
4.19	Dual-satellite CRLB of a GEO satellite (left column) paired with LEO-to-GEO sec- ondary satellite (right column). Secondary satellite semi-major axis shown on or- dinate. Showing CRLB covariance bounds using TDOA/FDOA measurements over various observation time spans shown on abscissa. Five baselines used.	95
4.20	Dual-satellite estimation of a GEO satellite (left column) paired with LEO-to-GEO secondary satellite (right column). Secondary satellite semi-major axis shown on ordinate. Showing % difference of CRLB covariance bounds between TDOA/FDOA and range/range-rate measurements over various observation time spans shown on abscissa. Color values above 0 indicate a region where TDOA/FDOA has lower covariance bounds compared to range/range-rate and vice versa. Five baselines used.	100

4.21	Case 1: Dual-satellite estimation of a GEO satellite (left column) paired with LEO-to-GEO secondary satellite (right column). Secondary satellite semi-major axis shown on ordinate. Showing % difference of CRLB covariance bounds between TDOA/FDOA and range/range-rate measurements over various observation time spans shown on abscissa. Color values above 0 indicate a region where TDOA/FDOA has lower covariance bounds compared to range/range-rate and vice versa. Five base-lines used.	103
4.22	Case 2: Dual-satellite estimation of a GEO satellite (left column) paired with LEO-to-GEO secondary satellite (right column). Secondary satellite semi-major axis shown on ordinate. Showing % difference of CRLB covariance bounds between TDOA/FDOA and range/range-rate measurements over various observation time spans shown on abscissa. Color values above 0 indicate a region where TDOA/FDOA has lower covariance bounds compared to range/range-rate and vice versa. Five base-lines used.	106
4.23	GEO-LEO: RSS position state errors and 3σ covariance for TDOA/FDOA, range/range-rate with and without bias	108
4.24	GEO-LEO: RSS velocity state errors and 3σ covariance for TDOA/FDOA, range/range-rate with and without bias	108
4.25	GEO-LEO: AGOM state errors and 3σ covariance for TDOA/FDOA, range/range-rate with and without bias	109
4.26	GEO-MEO: RSS position state errors and 3σ covariance for TDOA/FDOA, range/range-rate with and without bias	111
4.27	GEO-MEO: RSS velocity state errors and 3σ covariance for TDOA/FDOA, range/range-rate with and without bias	111
4.28	GEO-MEO: AGOM state errors and 3σ covariance for TDOA/FDOA, range/range-rate with and without bias	112

4.29	GEO-GEO: RSS position state errors and 3σ covariance for TDOA/FDOA, range/range-rate with and without bias	113
4.30	GEO-GEO: RSS velocity state errors and 3σ covariance for TDOA/FDOA, range/range-rate with and without bias	114
4.31	GEO-GEO: AGOM state errors and 3σ covariance for TDOA/FDOA, range/range-rate with and without bias	114
5.1	Spacecraft formation flying: chief with deputy (adapted from [71])	116
5.2	Circular GEO chief + circular deputy at various semi-major axes, shown on ordinate. Showing CRLB covariance over various observation time spans shown on abscissa. Coordinates are in the LVLH frame of the deputy. Three baselines used.	123
5.3	State error and 3σ covariances for circular GEO chief + circular MEO deputy ($0.5 \times a_{GEO}$) in the deputy LVLH frame. Comparison between TDOA/FDOA (TF) and range/range-rate (RR) observables. Three baselines used.	124
5.4	Circular GEO chief + circular deputy at various semi-major axes, shown on ordinate. Showing % difference of CRLB covariance bounds between TDOA/FDOA and range/range-rate measurements over various observation time spans shown on abscissa. Color values above 0 indicate a region where TDOA/FDOA has lower covariance bounds compared to range/range-rate and vice versa. Coordinates are in the LVLH frame of the deputy. Three baselines used.	125
5.5	Circular GEO chief with considered 1σ position uncertainty of 10 m and 1σ velocity uncertainty of 1 mm/s in each direction + circular deputy at various semi-major axes, shown on ordinate. Showing CRLB covariance over various observation time spans shown on abscissa. Coordinates are in the LVLH frame of the deputy. Three baselines used.	128

5.6	State error and 3σ covariances for circular GEO chief with considered 1σ uncertainty of 10 m and 1 mm/s in each direction + circular MEO deputy ($0.5 \times a_{GEO}$) in the deputy LVLH frame. Comparison between TDOA/FDOA (TF) and range/range-rate (RR) observables. Three baselines used.	129
5.7	Circular GEO chief with considered 1σ position uncertainty of 10 m and 1σ velocity uncertainty of 1 mm/s in each direction + circular deputy at various semi-major axes, shown on ordinate. Showing % difference of CRLB covariance bounds between TDOA/FDOA and range/range-rate measurements over various observation time spans shown on abscissa. Color values above 0 indicate a region where TDOA/FDOA has lower covariance bounds compared to range/range-rate and vice versa. Coordinates are in the LVLH frame of the deputy. Three baselines used.	130
5.8	Circular chief and deputy at various semi-major axes, shown on ordinate. Showing CRLB covariance over various observation time spans shown on abscissa. Coordinates are in the LVLH frame of the deputy. Three baselines used.	133
5.9	State error and 3σ covariances for circular MEO chief and deputy ($0.5 \times a_{GEO}$) in the deputy LVLH frame. Comparison between TDOA/FDOA (TF) and range/range-rate (RR) observables. Three baselines used.	134
5.10	Circular chief and deputy at various semi-major axes, shown on ordinate. Showing % difference of CRLB covariance bounds between TDOA/FDOA and range/range-rate measurements over various observation time spans shown on abscissa. Color values above 0 indicate a region where TDOA/FDOA has lower covariance bounds compared to range/range-rate and vice versa. Coordinates are in the LVLH frame of the deputy. Three baselines used.	135
5.11	Circular chief with considered 1σ position uncertainty of 10 m and 1σ velocity uncertainty of 1 mm/s in each direction and deputy at various semi-major axes, shown on ordinate. Showing CRLB covariance over various observation time spans shown on abscissa. Coordinates are in the LVLH frame of the deputy. Three baselines used.	137

5.12	State error and 3σ covariances for circular MEO chief with considered 1σ position uncertainty of 10 m and 1σ velocity uncertainty of 1 mm/s in each direction and deputy ($0.5 \times a_{GEO}$) in the deputy LVLH frame. Comparison between TDOA/FDOA (TF) and range/range-rate (RR) observables. Three baselines used.	138
5.13	Circular chief with considered 1σ position uncertainty of 10 m and 1σ velocity uncertainty of 1 mm/s in each direction and deputy at various semi-major axes, shown on ordinate. Showing % difference of CRLB covariance bounds between TDOA/FDOA and range/range-rate measurements over various observation time spans shown on abscissa. Color values above 0 indicate a region where TDOA/FDOA has lower covariance bounds compared to range/range-rate and vice versa. Coordinates are in the LVLH frame of the deputy. Three baselines used.	139
5.14	Relative orbits of cases in Table 5.5. Green central circle is the chief, red line is relative deputy orbit. Plotted in the chief Hill frame.	141
5.15	Close proximity bounded relative motion at various semi-major axes, shown on ordinate. Showing CRLB covariance over various observation time spans shown on abscissa. Coordinates are in the LVLH frame of the deputy. Three baselines used.	143
5.16	State error and 3σ covariances for close proximity bounded relative motion with chief at MEO ($0.5 \times a_{GEO}$) in the deputy LVLH frame. Comparison between TDOA/FDOA (TF) and range/range-rate (RR) observables. Three baselines used.	144
5.17	Close proximity bounded relative motion at various semi-major axes, shown on ordinate. Showing % difference of CRLB covariance bounds between TDOA/FDOA and range/range-rate measurements over various observation time spans shown on abscissa. Color values above 0 indicate a region where TDOA/FDOA has lower covariance bounds compared to range/range-rate and vice versa. Coordinates are in the LVLH frame of the deputy. Three baselines used.	145

5.18	Close proximity bounded relative motion with considered 1σ position uncertainty of 10 m and 1σ velocity uncertainty of 1 mm/s in each direction of the chief at various semi-major axes, shown on ordinate. Showing CRLB covariance over various observation time spans shown on abscissa. Coordinates are in the LVLH frame of the deputy. Three baselines used.	148
5.19	Close proximity bounded relative motion with considered 1σ position uncertainty of 10 m and 1σ velocity uncertainty of 1 mm/s in each direction of the chief. Satellite formation pair in GEO orbit resulting in low observability in the in-track y position direction of deputy. Comparing 1 st to 92 nd iteration.	149
5.20	Close proximity bounded relative motion with considered 1σ position uncertainty of 10 m and 1σ velocity uncertainty of 1 mm/s in each direction of the chief. Chief in $0.95 \times a_{GEO}$ orbit demonstrating the low observability in the in-track y position direction is limited to GEO only and not its neighboring orbits.	150
5.21	State error and 3σ covariances for close proximity bounded relative motion with considered 1σ position uncertainty of 10 m and 1σ velocity uncertainty of 1 mm/s in each direction of chief with chief at MEO ($0.5 \times a_{GEO}$) in the deputy LVLH frame. Comparison between TDOA/FDOA (TF) and range/range-rate (RR) observables. Three baselines used.	151
5.22	Close proximity bounded relative motion with considered 1σ position uncertainty of 10 m and 1σ velocity uncertainty of 1 mm/s in each direction of the chief at various semi-major axes, shown on ordinate. Showing % difference of CRLB covariance bounds between TDOA/FDOA and range/range-rate measurements over various observation time spans shown on abscissa. Color values above 0 indicate a region where TDOA/FDOA has lower covariance bounds compared to range/range-rate and vice versa. Coordinates are in the LVLH frame of the deputy. Three baselines used.	152

5.23	Close proximity bounded relative motion with considered 1σ position uncertainty of 10 m and 1σ velocity uncertainty of 1 mm/s in each direction of the chief at various semi-major axes, shown on ordinate. Showing % difference of CRLB covariance bounds between TDOA/FDOA and range/range-rate measurements over various observation time spans shown on abscissa. Color values above 0 indicate a region where TDOA/FDOA has lower covariance bounds compared to range/range-rate and vice versa. Coordinates are in the LVLH frame of the deputy. One baseline used.	154
6.1	1000 point Monte Carlo of Chicago transmitter (TX) geolocation with TLE-level ephemeris uncertainty	157
6.2	1000 point Monte Carlo of geolocation with ephemeris uncertainty of Chicago TX .	159
6.3	Geometry for projected covariance	163
6.4	Sensitivity matrix, S_{xc}	164
6.5	2D side view of iterative computation of $\hat{\mathbf{X}}_{alt}$	166
6.6	Geolocation of a Chicago, IL based TX	168
6.7	Geolocation of a Prescott, AZ based TX	169
6.8	Geolocation of a Atlanta, GA based TX	170
6.9	Satellite localization geometry	172
6.10	Position state error and 3σ covariance bounds. Step 1 uses SRIF, while step 2 uses CBF, no noise	174
6.11	Velocity state error and 3σ covariance bounds. Step 1 uses SRIF, while step 2 uses CBF, no noise	175
6.12	AGOM state error and 3σ covariance bounds. Step 1 uses SRIF, while step 2 uses CBF, no noise	175
6.13	Dual-satellite TDOA/FDOA prefit residuals of first iteration and postfit residuals of last iteration, no noise	176

6.14	Localized satellite TDOA/FDOA prefit residuals of first iteration and postfit residuals of last iteration, no noise	176
6.15	Position state error and 3σ covariance bounds. Step 1 uses SRIF, while step 2 uses CBF	177
6.16	Velocity state error and 3σ covariance bounds. Step 1 uses SRIF, while step 2 uses CBF	178
6.17	AGOM state error and 3σ covariance bounds. Step 1 uses SRIF, while step 2 uses CBF	178
6.18	Dual-satellite TDOA/FDOA prefit residuals of first iteration and postfit residuals of last iteration	179
6.19	Localized satellite TDOA/FDOA prefit residuals of first iteration and postfit residuals of last iteration	179
7.1	Complete arc: prefit and postfit residuals	181
7.2	First half of data processed in filter	182
7.3	Passthrough of second half of data	183
7.4	Long arc overlap: 15 hrs	184
7.5	Short arc overlap: 4.5 hrs	185
7.6	Dual-satellite ephemeris estimation without Miami baseline: first iteration prefit and last iteration postfit residuals (step 1)	187
7.7	Geolocation of Miami transmitter: first iteration prefit and last iteration postfit residuals (step 2)	188
7.8	Geolocation of a Miami, FL based TX	189
7.9	Dual-satellite ephemeris estimation without Chantilly baseline: first iteration prefit and last iteration postfit residuals (step 1)	190
7.10	Geolocation of Chantilly transmitter: first iteration prefit and last iteration postfit residuals (step 2)	190

7.11	Geolocation of a Chantilly, VA based TX	191
8.1	Truth beacon orbits over 8 day span with EROS reference sphere: beacon 1 in blue, beacon 2 in red	195
8.2	Differential Doppler and FDOA geometries: two differenced differential Doppler mea- surements generates the FDOA measurement	200
8.3	Cramér-Rao Lower Bounds for angles ($\sigma = 2e-5$ rad) with either range-rate or FDOA for various σ_s	203
8.4	Angles and FDOA: position state errors with 3σ bounds	204
8.5	Angles and FDOA: velocity state errors with 3σ bounds	204
8.6	Angles and range-rate: position state errors with 3σ bounds	205
8.7	Angles and range-rate: velocity state errors with 3σ bounds	206
8.8	Angles and range-rate with bias: position state errors with 3σ bounds	207
8.9	Angles and range-rate with bias: velocity state errors with 3σ bounds	207
8.10	Angles and FDOA: gravity coefficient errors and 3σ bounds shown for coefficients where coefficient value RMS is less than its coefficient RMS uncertainty	208
8.11	Angles and range-rate: gravity coefficient errors and 3σ bounds shown for coefficients where coefficient value RMS is less than its coefficient RMS uncertainty	209
8.12	Angles and range-rate with bias: gravity coefficient errors and 3σ bounds shown for coefficients where coefficient value RMS is less than its coefficient RMS uncertainty .	210

Chapter 1

Introduction

[T]he problem of orbit
determination was of a sort
which Newton said belonged to
the most difficult in
mathematical astronomy.

Eric Temple Bell

1.1 Background

In 1769 a Finnish-Swedish mathematician named Anders Johan Lexell, an assistant and collaborator of Leonhard Euler, was starting to make a name for himself with the processing of astronomical observations in a manner that would lay the groundwork for modern statistical orbit determination (OD) [79]. Lexell used the transit of Venus of 1769 to compute the solar parallax, formulating a system of equations that utilized the whole set of observation data obtained from all over the world each with varying levels of accuracy [79]. In the same year he determined the orbit of a 1769 comet followed by another in 1770, the latter discovered by Messier, would come to be known as Lexell's comet [17, 54]. Only a few years later Lexell investigated observations of a new body discovered by William Herschel, first thought to be another comet, but actually turned out to be the 7th planet, Uranus. After analyzing Uranus' orbit he concluded there must be an 8th planet as its motion could not be explained using only the gravitational influence of the other

known planets. In 1846, his inference was proven to be correct with the discovery of Neptune.

Lexell's early OD works used at its basis the publishings of Johannes Kepler with his three laws of planetary motion [48, 49] and Isaac Newton's law of gravitation [64]. Newton had previously devised a method for computing an orbit but his efforts used a deterministic approach, meaning the same number of observations were used as there were unknowns. Edmond Halley was the first to use Newton's OD method in his famous computation of Halley's comet's orbit. Other giants of the time such as Lambert, Lagrange, Legendre and Laplace made significant contributions to the early field of OD. Perhaps the most famous, however, is the German mathematician Carl Friedrich Gauss who, at the turn of the 19th century, is credited with inventing the 'method of least squares' (with some help from Legendre), taking Lexell's work another step further, and fitting the best orbit given a large set of observations [6]. Gauss' genius still prevails to this day with many of the future discoveries deeply rooted in his early estimation work. Around the time of Gauss, Thomas Bayes had published a formulation that allows a hypothesis to be updated contingent on the introduction of new information. However, Bayes had never applied his theorem to OD problems, it was not until Laplace generalized his formulation, that it was used in mathematical astronomy. Modern estimation research is firmly grounded in Bayes' theorem, with Bayesian inference providing the core approach.

A century later, at the turn of the 20th, Ronald Fisher developed the method of Maximum Likelihood Estimation (MLE). Fisher proposed that given a random variable defined by a probability density function (PDF) the MLE of the random variable (generally the state) is the value of the state that maximizes the PDF of the state conditioned on the observations. When a Gaussian density function is used for the random variable, the MLE and Bayes estimate are identical [83].

Then, during the late 1950s, with the advent of the digital computer, Rudolph Kalman extended the classical filtering and prediction problem with his recursive Kalman filter [47] (technically Peter Swerling published a practically identical algorithm only a few years before, yet the technique has retained Kalman's name) allowing for rigorous and far more complex force models to describe the motion of satellites. Around the same time, the start of the space race between the USA and

the USSR caused an explosion of artificial satellites to be launched around the Earth and into deep space. The space race sparked a large increase in OD research interest along with the other astrodynamics sub-disciplines. The next section describes in basic terms the orbit determination problem itself.

1.2 Fundamentals of Orbit Determination

Gauss' stochastic rather than deterministic approach submits to the fact that all models, dynamical or measurement are subject to contain errors. Dynamical models for example cannot perfectly predict the forces that include stochastic processes such as the atmosphere or solar radiation pressure. Furthermore, even the conservative forces may not be known exactly either, even if they are not stochastic. An example is the central body's gravity field as that is highly dependent on the mass distribution which may not be entirely known, if at all. Measurement models often contain errors due to clock biases or drift in the tracking station or satellite. Delays caused by an imperfectly modeled tropo- and ionosphere can further add to the errors. As a result of these potential error sources the OD problem is formulated in a statistical sense where the law of large numbers applies. As the number of observations increase the estimate of the satellite state is expected to approach the truth state. This is effectively an optimization problem where the optimal estimated state is the state that minimizes the distance between it and all the observations.

Provided that we have a tracking station as shown in Figure 1.1 which has some arbitrary measurement, such as range (ρ) and range-rate ($\dot{\rho}$), or angle (θ) and angle-rate ($\dot{\theta}$), or something else entirely, we need to process these measurements (shown with red '+' marks) over a time span to obtain an estimated trajectory. The method that allows this is called filtering, which can be either formulated as a batch process (all measurements at once) or a sequential process which updates the estimated state after each new measurement is added. In all but the simplest of cases the observations do not directly measure the state, rather, a mapping is required between the measurement types and the state. In OD, this relationship is usually non-linear, and because the dynamics are non-linear too, the equations are linearized about a reference trajectory.

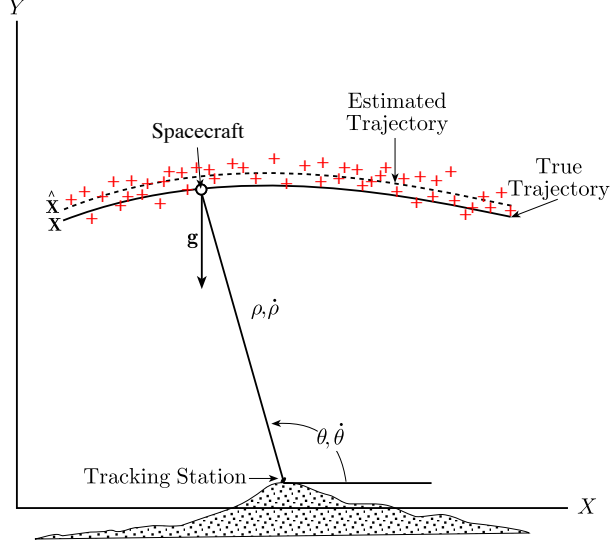


Figure 1.1: OD problem (adapted from [83])

The non-linear dynamics can be written as,

$$\dot{\mathbf{X}}(t) = F(\mathbf{X}(t), t). \quad (1.1)$$

When written as a Taylor series we obtain,

$$\dot{\mathbf{X}}(t) = F(\mathbf{X}, t) = F(\mathbf{X}^*, t) + \left[\frac{\partial F(t)}{\partial \mathbf{X}(t)} \right]^* [\mathbf{X}(t) - \mathbf{X}^*(t)] + \text{H.O.T}, \quad (1.2)$$

where, evaluation using the reference trajectory is denoted by $[\]^*$ and,

$$\mathbf{A}(t) = \left[\frac{\partial F(t)}{\partial \mathbf{X}(t)} \right]^*. \quad (1.3)$$

The deviation, $\mathbf{x}(t)$ from the reference trajectory is,

$$\mathbf{x}(t) = \mathbf{X}(t) - \mathbf{X}^*(t). \quad (1.4)$$

With some rearranging of Eq. 1.2 and ignoring higher order terms, the time evolution of the deviation can be expressed as,

$$\dot{\mathbf{x}}(t) = \mathbf{A}(t)\mathbf{x}(t). \quad (1.5)$$

The solution of which commonly utilizes the state transition matrix (STM),

$$\mathbf{x}(t) = \Phi(t, t_k)\mathbf{x}_k, \quad (1.6)$$

where \mathbf{x}_k is the value of \mathbf{x} at t_k and is mapped to time t using the STM, $\Phi(t, t_k)$. The STM is obtained by integrating,

$$\dot{\Phi}(t, t_k) = \mathbf{A}(t)\Phi(t, t_k), \quad (1.7)$$

with initial conditions $\Phi(t_k, t_k) = \mathcal{I}$.

The nonlinear measurement expression can be written as,

$$\mathbf{Y}_k = G(\mathbf{X}_k, t_k) + \boldsymbol{\epsilon}_k \quad k = 1, \dots, l \quad (1.8)$$

where \mathbf{Y}_k for $k = 1, \dots, l$ is a set of observations. Therefore, the nonlinear measurement mapping function, $G(\mathbf{X}_k, t_k)$ maps a state at time t_k to the measurement space. Errors in the observations are represented by $\boldsymbol{\epsilon}$.

Similar to the linearized dynamics model, the measurement model can also be linearized about the reference trajectory. Setting up the Taylor series expansion,

$$\mathbf{Y}_k = G(\mathbf{X}_k, t_k) + \boldsymbol{\epsilon}_k = G(\mathbf{X}_k^*, t_k) + \left[\frac{\partial G(\mathbf{X}_k, t_k)}{\partial \mathbf{X}_k} \right]^* [\mathbf{X}_k - \mathbf{X}_k^*] + \text{H.O.T} + \boldsymbol{\epsilon}_k. \quad (1.9)$$

The first order partial, or mapping matrix, required by the filter is defined as,

$$\tilde{\mathbf{H}}_k = \left[\frac{\partial G(\mathbf{X}_k, t_k)}{\partial \mathbf{X}_k} \right]^*. \quad (1.10)$$

The measurement deviation or prefit residual is,

$$\mathbf{y}_k = \mathbf{Y}_k - G(\mathbf{X}_k^*, t_k), \quad (1.11)$$

where \mathbf{Y}_k is the actual set of observations and $G(\mathbf{X}_k^*, t_k)$ are the computed set of observations on the reference trajectory. Rearranging Eq. 1.9 and ignoring higher order terms we obtain,

$$\mathbf{y}_k = \tilde{\mathbf{H}}_k \mathbf{x}_k + \boldsymbol{\epsilon}_k \quad k = 1, \dots, l \quad (1.12)$$

Using the STM we can express all observations of the state at a single epoch,

$$\mathbf{H}_k = \tilde{\mathbf{H}}_k \Phi(t_k, t_0) \quad k = 1, \dots, l \quad (1.13)$$

Now that the two main functions of a filter are defined, namely the linearized dynamics and measurement equations, we can define Gauss' least-squares as the minimization of the observation errors using the following performance index,

$$J(\mathbf{x}) = \frac{1}{2} \boldsymbol{\epsilon}^\top \boldsymbol{\epsilon}. \quad (1.14)$$

Substituting Eq. 1.12 into 1.14 we obtain,

$$J(\mathbf{x}) = \frac{1}{2} (\mathbf{y} - \mathbf{H}\mathbf{x})^\top (\mathbf{y} - \mathbf{H}\mathbf{x}). \quad (1.15)$$

Because we are attempting to minimize the performance index, we take the first and second derivatives. The second derivative must be positive to ensure that it is indeed a minimization rather than maximization of the measurement errors. Taking the first derivative and setting the expression equal to zero, the most basic and fundamental expression for obtaining the best estimate of the spacecraft state is found,

$$\hat{\mathbf{x}} = (\mathbf{H}^\top \mathbf{H})^{-1} \mathbf{H}^\top \mathbf{y}. \quad (1.16)$$

Where, $\hat{\mathbf{x}}$ is the best estimate of the deviation state. Furthermore, we find that $\mathbf{H}^\top \mathbf{H}$ must be positive definite to ensure minimality, which is synonymous with being full rank. Since the filter developed here is fundamentally based in statistical inference, the state is actually described as a PDF with the final estimate of the state having values that maximizes the PDF.

Armed with the basic knowledge of estimation theory, we delve into an overview of interferometry which forms one of the two basis for the research in this dissertation. Following the interferometry subsection, an overview of radio frequency (RF) localization is provided as the second basis for this research. These two bases are merged to obtain an innovative method for OD of multiple satellites.

1.3 Interferometry Overview

In OD, range and conventional Doppler are commonly used and were solely relied upon until the 1980s for deep space radio tracking [85]. However, some limitations exist that are alleviated with another technique known as Very Long Baseline Interferometry (VLBI), already known to radio astronomers, it was developed for OD in the late 1970s [85]. One of these range and Doppler limitations is the lack of angular or plane of sky positioning information that is available with the VLBI system. The VLBI technique is particularly powerful when multiple, angularly close, spacecraft are tracked simultaneously as it provides much stronger information than is obtained by tracking a single spacecraft [8]. Same Beam Interferometry (SBI) is an example of a VLBI implementation for tracking two spacecraft at once within the same beamwidth of a radio antenna. As a result of this simultaneous tracking, common errors along the four ray paths from the two spacecraft and two ground stations can be double differenced, first between the receivers and then the spacecraft, resulting in a very precise measurement, see Figure 1.2 [8, 20]. Furthermore, differenced carrier phase and Doppler are less sensitive to station location errors and poorly modeled dynamics [19, 30].

SBI has a long history, not only for OD but also for scientific purposes. In 1972 during Apollo 16, the Lunar Rover was tracked relative to the Lunar Module in this manner, and lunar librations were measured using signals from the Apollo Lunar Surface Experiments Package (ALSEP) transmitters [15]. Then in 1985 the winds of Venus were measured by differentially tracking atmospheric balloons with respect to the Vega Spacecraft [69]. In 1990, SBI was successfully applied for deep-space navigation of Pioneer 12 and the Magellan spacecraft around Venus [8, 20]. It was

shown that Doppler plus SBI has better accuracy compared to Doppler plus differenced Doppler by a factor of four and better than Doppler only by a factor of 18 [20]. VLBI was also used for the Galileo and Mars Observer missions where, in some situations, it provided at least 5 times more accuracy than that determined from several days of range and conventional Doppler [85].

The geometry for SBI is shown in Figure 1.2(a), with two widely separated transceivers. The distance between the receivers is the baseline and often spans intercontinental distances. The beamwidth of the transmitted signal encompasses both the primary and secondary satellite since they are assumed to have a small angular separation, this is especially true in the case of deep space navigation where the distances can be far larger than the separation of two spacecraft orbiting or navigating to the same celestial body. The signal is then returned from both spacecraft and acquired by both receivers. This geometry is ideal for double differencing of observables and eliminating or reducing common errors.

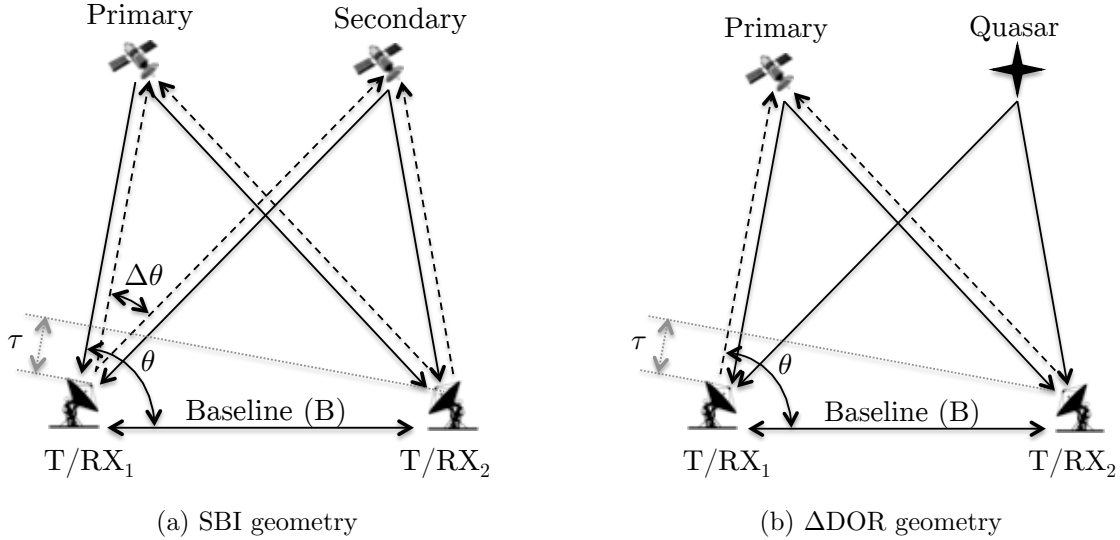


Figure 1.2: Example VLBI configurations

With SBI the antennas accumulate the spacecraft signal phase at each of the stations where the double difference phase $\Delta^2\phi$, is computed as follows [8, 44],

$$\Delta^2\phi = (\phi_{12}(t) - \phi_{11}(t)) - (\phi_{22}(t) - \phi_{21}(t)) + b. \quad (1.17)$$

Where, ϕ_{ij} is the phase of the signal transmitted at spacecraft i and received at station j , and b is the unknown integer bias. To resolve the integer bias, sufficient a-priori knowledge on the spacecraft states must be provided which is usually not the case. As result, only the relative states can be estimated rather than the absolute spacecraft states, unless the phase bias is also estimated and some additional tricks are used. The delay τ , between the two stations is computed by,

$$\tau(t) = \frac{\Delta^2\phi}{f}. \quad (1.18)$$

Where f is the signal frequency. To relate the time delay to plane of sky information we can approximate the measurement equation as,

$$\tau(t) = \frac{(B \cos \theta)\Delta\theta}{c}. \quad (1.19)$$

The angle θ is between the baseline (B) and the direction of the spacecraft, whereas $\Delta\theta$ is the difference in θ between the two spacecraft [8]. The SBI measurement equation in Eq. 1.18 is similar to the time difference of arrival (TDOA) measurement used throughout this dissertation. Differenced Doppler (sometimes referred to as narrow-band VLBI) is commonly used in conjunction with SBI and is collected by the two receivers for a single spacecraft [20]. By using the SBI geometry and also differencing the differenced Doppler between the two spacecraft we obtain double differenced Doppler which is effectively frequency difference of arrival (FDOA) which, like TDOA, has not yet been previously investigated for OD. The full details of the TDOA and FDOA measurements are left for chapter 2.

A similarly strong interferometric observable is Δ -Differential One-way Ranging (Δ DOR) which also provides plane-of sky information and is shown in Figure 1.2(b). Rather than having two spacecraft on which to perform OD simultaneously, only one is targeted at a time where the second spacecraft is replaced with a known radio source such as a quasar. Due to the well-known

position of the extra-galactic object, the spacecraft plane-of-sky position can be computed relative to this source very precisely. The delay τ , can be computed in a similar fashion as with SBI, using Figure 1.2(b) we obtain,

$$\tau(t) = \frac{B \cos \theta}{c}. \quad (1.20)$$

Generally with Δ DOR the stations slew between the quasar and the spacecraft because it is unlikely for both to be within the same beamwidth of the antenna up to a maximum angular separation of 15 degrees. Once again the measurements are double differenced to remove many common errors [1].

In summary, the geometrical setup used in VLBI, specifically SBI, is used to generate the double differenced range, and double differenced Doppler measurements. In this thesis however, rather than correlating with the phase of the signal, the modulation on the signal is used instead in order to obtain absolute state information, similar to the field of RF localization described next.

1.4 Radio Frequency Localization Overview

Since the dawn of the space age satellites have been employed to uncover the locations of transmitters for intelligence purposes. Two of the first such satellites were Grab and Poppy, launched in June 1960 and December 1962 respectively, these were early electronic intelligence (ELINT) satellites under the development of the Naval Research Laboratory (NRL). Grab was an acronym for Galactic Radiation and Background Satellite which was a cover mission for Tattletale – the actual code name of Grab. Grab and Poppy’s purpose was to intercept Soviet radar signals in an effort to provide a tactical advantage during the height of the cold war [57]. During the early days of satellite geolocation, there was a heavy focus on its military application.

Geolocating signals, however, is not limited to the intelligence community and can be used to locate an airplane’s, ship’s or personal emergency beacon for rescue purposes as well [70]. By the 1990s a need was shown to exist for an international Search and Rescue (SAR) system since

thousands of lives were lost each year in accidents that could otherwise be mitigated. As a result the United States, Canada, France, Norway, United Kingdom and the former USSR developed the Cospas-Sarsat system [70]. This system is still in use today and continues to evolve and improve. In 2013, a Medium Earth Orbit SAR (MEOSAR) system was proposed that would independently provide distress beacon location information. The previously implemented Geosynchronous Earth Orbit SAR (GEOSAR) system only provided location information if it was available from an external source which was then modulated into the beacon message [2]. MEOSAR instead uses a dual-satellite geolocation method with TDOA and FDOA which provide lines of position (LOP) in the North-South and East-West directions respectively shown by the blue lines in Figure 1.3. The intersection of the two LOPs is the location of the unknown transmitter or in this case the distress signal. The transmitters and receivers in the box of Figure 1.3 is referred to as the reference side, while the unknown transmitter is referred to as the secondary transmitter.

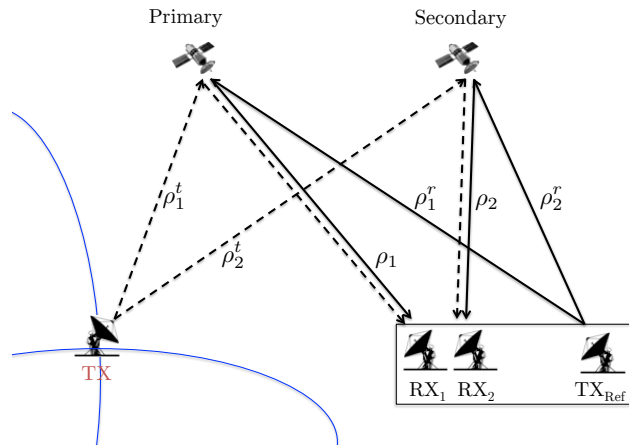


Figure 1.3: Geolocation geometry

Another geolocation application, perhaps not immediately obvious, is for the positioning of transmitters with deliberate or undeliberate access to satellite communication channels [34, 75]. A famous example of deliberate interference was in 1986, when “Captain Midnight” hijacked the Home Box Office’s Galaxy II transponder to protest their price [55]. Naturally, accidental interference is more common with hundreds of events recorded per year (as of 1995) and likely to grow with an

increase in traffic [5].

These listed examples of satellite geolocation are the most common and many applications fall within one of these categories. The methods available for satellite geolocation, however, are widely varied. Reference [32] lists a number of typical geolocation techniques some of which are:

- Single-satellite geolocation based on direction finding,
- Multi-satellite geolocation using TDOA,
- Dual-satellite geolocation using TDOA and FDOA.

The geolocation research within this dissertation implements the dual-satellite form as illustrated by Figure 1.3. The geolocation research focuses on the mitigation of interference signals, but irrespective of the application a more accurate geolocation solution is always desired and the key drivers are addressed using both real and simulated data.

1.5 Original Dissertation Contributions

In this dissertation the field of relative deep-space satellite navigation with VLBI is merged with the field of satellite geolocation to employ an innovative approach to multi-satellite OD. Both Δ DOR and SBI are a form of measurement types that in most circumstances only allows for relative angular navigation due to the unresolved nature of the integer ambiguity in the phase correlation. On the other hand, the geolocation process has a similar setup with a baseline formed between two stations, but where one of the stations' location is unknown, and where two satellites are also within the same beamwidth of the transmitters. The difference is that the geolocation setup is based around the Earth rather than in deep space, and knowledge on the satellites is often times assumed perfect or the uncertainty is simply ignored. The TDOA and FDOA measurement types used in geolocation are also double differenced just like with VLBI, but the correlation occurs on the modulation of the wave rather than the phase itself thereby eliminating the integer ambiguity. Figure 1.4 cites some of the most fundamental works for both of these fields.

In Figure 1.5 we show the merging of the two fields to create this new technique for multi-

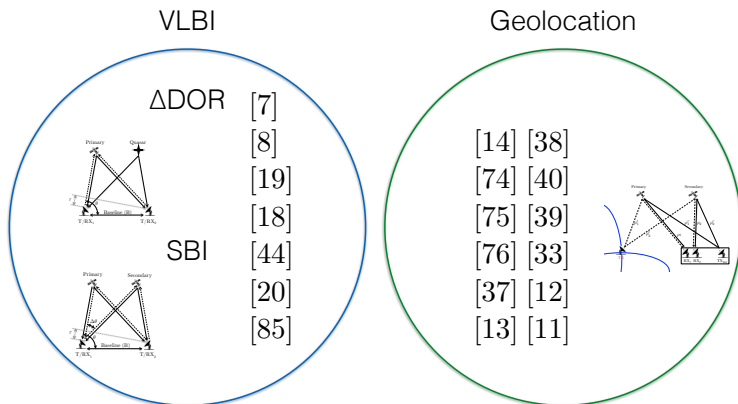


Figure 1.4: Fundamental literature to the fields of VLBI and geolocation

satellite OD, the references listed in the overlap is work produced by the author. The geometry and measurements used are those from the geolocation field but rather than locating an unknown transmitter we define a baseline just like with VLBI and instead estimate the states of the two satellites. Due to the lack of the integer ambiguity with the TDOA and FDOA measurements, the absolute states can be estimated of the two satellites rather than just their relative states. Another way to explain this new OD setup is that the TDOA and FDOA observables generate LOPs on the surface of the Earth, but unless the estimated satellite states are in their true position the intersection of the LOPs will not coincide with the location of the secondary transmitter. Therefore the satellite states are perturbed until the LOPs do indeed line up with the known location of the secondary transmitter.

Provided that we have a novel OD technique with applications to geolocation we naturally arrive at the following thesis statement:

Thesis Statement

Precise orbit determination of neighboring spacecraft is achievable with time (TDOA) and frequency (FDOA) double differenced measurements derived from the geolocation community and implemented with an SBI geometry. Incorporating the impact of ephemeris uncertainty on geolocation accuracy is an important step toward covariance realism, and the associated improvement in orbit determination solutions of the relay satellites increases geolocation accuracy significantly.

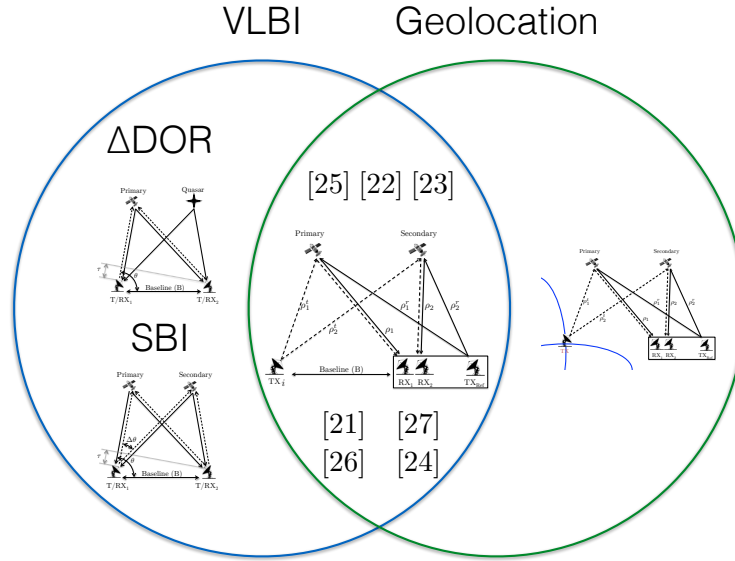


Figure 1.5: Merging of two fields that forms a new innovative technique for multi-satellite OD

In support of this thesis statement we investigate the feasibility of using TDOA and FDOA for OD in both an absolute and relative sense. We also explore the effect of the OD solution uncertainty on the geolocation accuracy. The main contributions of this dissertation are listed below by topic:

- Dual-satellite OD:
 - * Observability analysis to determine dual-satellite OD tractability with TDOA and FDOA;
 - * High-fidelity architecture for neighboring dual-satellite OD capable of handling real data;
- Relative OD:
 - * Implementation of non-linear relative navigation of two satellites with TDOA and FDOA;
- Geolocation of unknown RF sources:
 - * Development of a consider batch filter to ensure covariance realism;

- * Implementation of a probabilistic altitude constraint to significantly reduce projected covariance;
- * Understanding of the three-dimensional shape of the geolocation covariance;
- * Development of simultaneous ephemeris and source localization estimation;
- Satellite localization:
 - * OD of a sub GEO satellite using dual-satellite GEO configuration for GPS denied environments;
- Filter extension:
 - * Derivation of the Square-Root Unscented Schmidt-Kalman Filter, a consider SR-UKF.

The following is a list of journal publications and conferences that constitute the backbone of this dissertation:

Journal Papers

- [25] **J. Geeraert** and J. McMahon. Square-Root Unscented Schmidt-Kalman Filter. *Journal of Guidance Control and Dynamics*, 2017. [Accepted]
- [22] **J. Geeraert** and J. McMahon. Dual-Satellite Geolocation with Ephemeris Correction and Uncertainty Mapping. *IEEE Transactions on Aerospace and Electronic Systems*, 2017. [Paper In Review]
- [23] **J. Geeraert** and J. McMahon. Dual-Satellite Orbit Determination with Time and Frequency Difference of Arrival. *Journal of Guidance Control and Dynamics*, 2017. [Submitted]
- **J. Geeraert** and J. McMahon. Relative Orbit Determination with Time and Frequency Difference of Arrival Measurements. *Journal of Guidance Control and Dynamics*, 2017. [Work in Progress]

Conferences

- **J. Geeraert** and S. Nandi. Quicklook: A Testbed for an Automated Orbit Determination System using the Cassini Spacecraft. 21st Improving Space Operations Workshop, 2015.
- [21] **J. Geeraert**, B. Jones and J. McMahon. Improving Geolocation Accuracy through Refined Satellite Ephemeris Estimation in an Ill-Conditioned System. AIAA/AAS Astrodynamics Specialist Conference, 2015.
- [27] **J. Geeraert**, J. McMahon, and B. Jones. Orbit Determination Observability of the Dual-Satellite Geolocation System with TDOA and FDOA. AIAA/AAS Astrodynamics Specialist Conference, 2016.
- [26] **J. Geeraert**, J. McMahon. and S. Hesar. Small Body Navigation and Gravity Estimation using Angle and FDOA Observables. AIAA/AAS Astrodynamics Specialist Conference, 2017.
- [24] **J. Geeraert** and J. McMahon. Relative Orbit Determination of Multiple Satellites Using Double Differenced Measurements. AMOS, 2017.

1.6 Dissertation Organization

This first chapter provides historical context and background of the general orbit determination problem. We specifically introduce the interferometric data type, upon which TDOA and FDOA are heavily based. We also introduce the RF localization problem because the OD research in this dissertation is directly applicable. The original contributions are summarized along with journal and conference publications. Finally the thesis is outlined in the dissertation organization.

Chapter 2 introduces the dynamical models used in the filters which starts with the simple 2-body problem and goes up to the full JPL ephemeris model. All of the measurement models used throughout this dissertation are also derived and explained here including their partials. Finally, a brief mention is given to the use of coordinate systems, as they play a significant role in real-world

navigation applications. The OD tools developed are capable of processing real-world data and therefore include all the necessary coordinate transformation details and fidelity.

Chapter 3 discusses the preliminaries on OD filters. It includes the batch, various Kalman Filter (KF) variations including the conventional, extended and unscented versions, square-root information filters in addition to smoothing and considered parameters.

Chapter 4 first provides an extensive observability analysis, and second an investigation into the use of TDOA and FDOA for dual-satellite OD in the following configurations: GEO-LEO, GEO-MEO, and GEO-GEO. Each of these cases are run along side more conventional range and range-rate observables to establish a baseline of comparison.

Chapter 5 focuses on solving the relative OD problem with two-body dynamics only, again using TDOA and FDOA. Three configurations are used: a GEO chief + a LEO-to-GEO deputy, a leader-follower setup with a LEO-to-GEO chief and deputy, and finally a close orbiting deputy in a relative bounded case with orbits ranging from LEO to GEO. In all three cases, two variants are examined, one where the chief has perfect knowledge, and another where the chief has some uncertainty considered.

Chapter 6 introduces RF localization, first geolocation and then satellite localization. Geolocation has a number of different methods, a two-step process which first does OD on the dual satellites and second performs the actual geolocation with a consider batch filter. Another method is a one-step process which simultaneously solves for the dual satellite ephemeris as well as the unknown RF source. The former is more flexible as the OD can be performed at any time before the geolocation step and then propagated to the time of geolocation. To further improve the accuracy of the geolocation solution a probabilistic altitude constraint is implemented. The satellite localization also utilizes the two-step process where the dual-satellite ephemeris is first estimated, and then the state of the unknown satellite is determined passively by routing the signals through the dual satellite configuration. This has close ties to the Tracking and Data Relay Satellite System (TDRSS) and is useful if there is no direct link with the satellite to be localized and no GPS information available.

Chapter 7 illustrates the OD and geolocation methods applied to a long-arc of real data. A pass-through analysis is conducted to determine how well an estimated orbit can predict a future satellite state as well as a long and short arc overlap analysis to determine the magnitude of the errors.

Chapter 8 demonstrates the use of FDOA for other OD applications, such as small body navigation and gravity field estimation. In this chapter we show its use along side optical observations for navigation around Eros and also compare the results to those obtained with range and range-rate.

Finally chapter 9 provides a quick summary of this dissertation in addition to concluding remarks and potential areas of future research.

Chapter 2

Preliminaries

2.1 Dynamical Models

This section on the dynamical models details the forces acting upon the spacecraft which include both gravitational and non-conservative forces such as Solar Radiation Pressure (SRP). We first start out by introducing the most fundamental gravitational law which is the interaction between two celestial bodies or a celestial body and a spacecraft. Then the gravitational laws are generalized to include up to N bodies, which is known as the N-body problem. From there, we include perturbative gravitational forces such as those from a non-spherical body, and finally outline the SRP models implemented.

2.1.1 Two-Body Problem

Understanding the two-body problem is fundamental to the field of celestial mechanics and astrodynamics. We define an inertial coordinate system \mathcal{N} defined by the (X,Y,Z) axes in Figure 2.1, meaning the frame is not accelerating. We assume that the two bodies m_1 and m_2 are perfectly symmetrical so that they act like point masses from their centers. Furthermore, we assume that the only force present is the gravitational force acting between the two bodies along the vector \mathbf{r} .

Starting from Newton's second law,

$$F = m \frac{d\mathbf{v}}{dt} = m\ddot{\mathbf{r}} \quad (2.1)$$

and Newton's law of Gravitation,

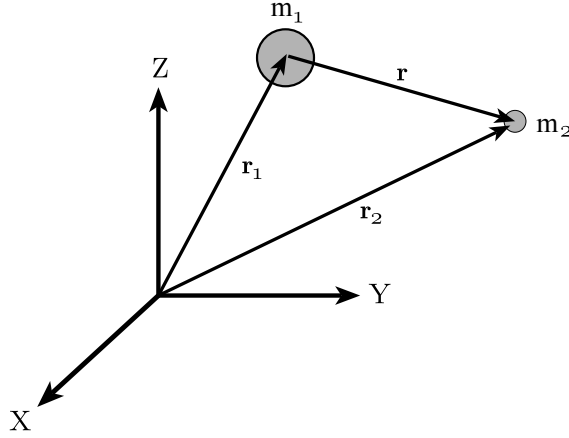


Figure 2.1: Two-body problem (adapted from[83])

$$\mathbf{F} = G \frac{m_1 m_2}{r^3} \mathbf{r} \quad (2.2)$$

we can write the equations of motion of both bodies in the inertial frame as,

$$m_1 \ddot{\mathbf{r}}_1 = G \frac{m_1 m_2}{r^3} \mathbf{r} \quad (2.3)$$

and,

$$m_2 \ddot{\mathbf{r}}_2 = G \frac{m_1 m_2}{r^3} \mathbf{r}. \quad (2.4)$$

Then, the relative motion of body 2 with respect to body 1 can be described as,

$$\ddot{\mathbf{r}} = \ddot{\mathbf{r}}_2 - \ddot{\mathbf{r}}_1. \quad (2.5)$$

Substituting in Eqs. 2.3 and 2.4 into Eq. 2.5 while also defining $\mu = G(m_1 + m_2)$ we obtain,

$$\ddot{\mathbf{r}}_{2B} = -\frac{\mu}{r^3} \mathbf{r}. \quad (2.6)$$

The subscript $2B$ is used to denote the two-body acceleration for the remainder of this dissertation. In most applications involving a satellite or spacecraft $m_1 \gg m_2$, and therefore μ can be

approximated as simply $\mu = Gm_1$. Equation 2.6 illustrates the inverse square relationship of the acceleration with distance from the center of the central body.

2.1.2 N-Body Problem

The two-body problem can be used to model the gravitational effect of a spacecraft around a primary body as a first order method of analysis. However, in reality there are many additional gravitational forces acting upon a spacecraft, the degree to which these forces have an impact varies, but in order to improve a model's fidelity, more of these gravitational forces should be included. For example, a GEO spacecraft will have as the primary force, the gravitational attraction of the Earth but will also experience gravitational forces from the Moon, Sun, Venus and Jupiter. In this section we generalize the problem to a system of N-bodies, where we can compute the gravitational forces acting on the i^{th} body from body 1 to N, see Figure 2.2 for a visual representation.

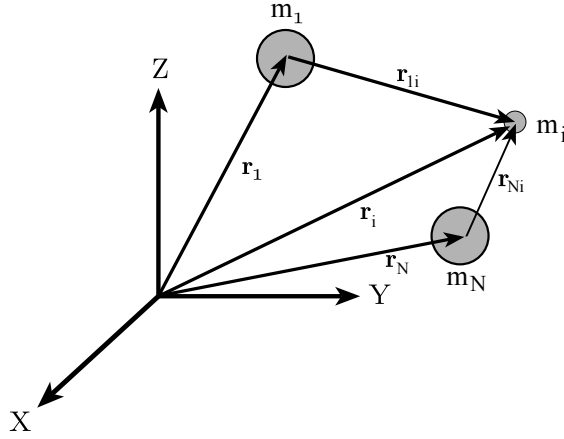


Figure 2.2: N-body problem

The vector sum of all the gravitational forcing acting on i can be represented as

$$\mathbf{F} = -G \frac{m_i m_1}{r_{1i}^3} \mathbf{r}_{1i} - \dots - G \frac{m_i m_N}{r_{Ni}^3} \mathbf{r}_{Ni}. \quad (2.7)$$

Which can be written using a summation as follows,

$$\mathbf{F} = -Gm_i \sum_{\substack{j=1 \\ j \neq i}}^N \frac{m_j}{r_{ji}^3} \mathbf{r}_{ji}. \quad (2.8)$$

Consequently we can write the inertial equation of motion for the i^{th} body as,

$$\ddot{\mathbf{r}}_i = -G \sum_{\substack{j=1 \\ j \neq i}}^N \frac{m_j}{r_{ji}^3} \mathbf{r}_{ji}. \quad (2.9)$$

If we assume that body 1 is the Earth and body 2 is the spacecraft and bodies 3 to N represent all other relevant gravitational bodies affecting the spacecraft, then the relative acceleration of the spacecraft about Earth becomes,

$$\ddot{\mathbf{r}}_{12} = -G \frac{m_1 + m_2}{r_{12}^3} \mathbf{r}_{12} + G \sum_{j=3}^N m_j \left(\frac{\mathbf{r}_{2j}}{r_{2j}^3} - \frac{\mathbf{r}_{1j}}{r_{1j}^3} \right). \quad (2.10)$$

The first part of Eq. 2.10 is the gravitational effect due to the Earth alone and is identical to that of the 2-body equation of motion. The second part consists of the gravitational effects of all other bodies. The first term in the parenthesis is called the direct effect, because it describes the acceleration of the j^{th} body on the spacecraft. The second term in the parenthesis is called the indirect effect because it is the effect that the other bodies have on body 1, in this case the Earth. When the position of the Earth changes as a result of the N bodies' effect, it also carries through to the equation of motion for the spacecraft. Often times when orbiting the Earth, the only other gravitational attractors taken into account are the Moon and the Sun, we can also utilize their specific symbols to improve readability of the equation. If that is the case, we can write the spacecraft equation of motion due to point mass bodies of gravity as,

$$\ddot{\mathbf{r}}_{sat} = \ddot{\mathbf{r}}_{2B} + \ddot{\mathbf{r}}_{NB} \quad (2.11)$$

Where, $\ddot{\mathbf{r}}_{2B}$ is defined by Eq. 2.6 using a gravitational parameter of the Earth μ_{\oplus} , and the Sun and Moon gravitational accelerations are defined by,

$$\ddot{\mathbf{r}}_{NB} = -\mu_{\odot} \left(\frac{\mathbf{r}_{\odot,sat}}{r_{\odot,sat}^3} - \frac{\mathbf{r}_{\odot,\oplus}}{r_{\odot,\oplus}^3} \right) - \mu_{\mathbb{D}} \left(\frac{\mathbf{r}_{\mathbb{D},sat}}{r_{\mathbb{D},sat}^3} - \frac{\mathbf{r}_{\mathbb{D},\oplus}}{r_{\mathbb{D},\oplus}^3} \right). \quad (2.12)$$

Rather than integrate the N-body problem for all the major celestial bodies in the solar system, the Jet Propulsion Laboratory (JPL) has already done this to a very high fidelity. Using numerous of observations from a variety of sources, JPL fits the data to generate high accuracy ephemeris products that can be used for operations and research. JPL releases these ephemeris files as Development Ephemerides (DE) and in this dissertation the DE405 ephemeris is implemented. The DE405 ephemeris provides position and velocity data between 1600 AD and 2170 AD in the form of Chebyshev coefficients which can be interpolated for any time within the valid range of years. The DE405 uses the International Celestial Reference Frame (ICRF) unlike previous versions which uses the dynamical equator and equinox of J2000. The difference between the dynamical J2000 reference frame and the ICRF is at a level of 0.01 arcsec, and determined with an accuracy of 0.003 arcsec [1, 61].

2.1.3 Geopotential Model

In both the two-body and N-body problem, the masses are assumed to be perfectly spherical and therefore acting as point masses. To further improve the fidelity of the dynamics the non-sphericity of the central body is modeled. The acceleration can be written as the gradient of the geopotential function U . A subscript NS is used to denote the acceleration due to the non-sphericity.

$$\ddot{\mathbf{r}}_{NS} = \nabla U \quad (2.13)$$

Where U is expanded in a series of Legendre polynomials,

$$U = \frac{\mu}{r} \sum_{l=2}^{\infty} \sum_{m=0}^l \left(\frac{R}{r} \right)^l P_{l,m}(\sin \phi_{ac}) [C_{l,m} \cos(m\lambda) + S_{l,m} \sin(m\lambda)]. \quad (2.14)$$

R is the reference radius of the central body, $P_{l,m}$ are the associated Legendre functions, ϕ_{gc} is the geocentric latitude of the satellite, λ is the longitude of the satellite, and $C_{l,m}$ and $S_{l,m}$ are the spherical harmonics coefficients for the l^{th} degree and m^{th} order [31]. For Earth's spherical harmonics coefficients we use the GRACE Gravity Model 2 (GGM02) and while it is complete up to degree and order 200, we use up to degree and order 10 for the OD and geolocation applications about the Earth and up to degree and order 15 for navigation about the asteroid Eros. The geopotential coefficients with $m = 0$ are the zonal coefficients and do not depend on longitude, when $m < n$ they are known as the tesseral coefficients and when $m = n$ they are known as the sectorial coefficients [61]. It should be noted that the use of the geopotential function from Eq. 2.14 is only valid for points outside of the circumscribing sphere of the body. Hence care needs to be taken when navigating about an asteroid such as Eros which has an elongated shape and is much longer than it is wide, or other irregularly shaped celestial bodies.

2.1.4 Solar Radiation Pressure Model

SRP is the largest non-gravitational force acting on a spacecraft, other than Earth's (or potentially other celestial body's) atmospheric drag encountered by low flying satellites. The force imparted, due to the reflection or absorption of photons, is dependent on a number of factors, including the shape, orientation and optical properties [58]. In this section we discuss three different SRP models starting with the cannonball model, a low fidelity zeroth order model, going up to the Fourier coefficient model which can be very high fidelity depending on the number of coefficients and accuracy of the satellite model used.

2.1.4.1 Cannonball Model

The cannonball model assumes the satellite is perfectly spherical with constant optical properties over the whole surface. The SRP force points directly away from the Sun as the incident light rays in the tangential direction cancel perfectly due to symmetry. Naturally due to these assumptions the cannonball model is only a zeroth order approximation of a complex many faceted

satellite. The acceleration due to SRP is provided in 2.15,

$$\ddot{\mathbf{r}}_{SRP} = -p_{SR} C_r \frac{A_{\odot} \mathbf{r}_{\odot,sat}}{m r_{\odot,sat}}. \quad (2.15)$$

The solar radiation pressure, p_{SR} , is assumed to be a constant and the value used is 4.52×10^{-6} Pa at 1 AU. The value of p_{SR} is found by dividing the solar constant flux by the speed of light, essentially rearranging Einstein's mass and energy relation.

$$p_{SR} = \frac{1357 \text{ W/m}^2}{3 \times 10^8 \text{ m/s}} = 4.52 \times 10^{-6} \text{ Pa} \quad (2.16)$$

Equation 2.16 is valid at 1 AU only, because the solar radiation pressure varies inversely with the distance we can relate the value of p_{SR} at other distances from the Sun by the following relation,

$$p_{SR} = p_{SR_{1AU}} \frac{1AU}{r_{\odot,sat}^2}. \quad (2.17)$$

Note that the distance $r_{\odot,sat}$, carries units of AU for consistency. Next, looking at the other variables in Eq. 2.15, the satellite area exposed to the Sun is A_{\odot} and the satellite mass is m . The reflectivity and optical properties of the spacecraft are bundled together in the C_r variable which varies between 0 and 2 and was initially designated as γ [51, 86]. Notice that $C_r \frac{A_{\odot}}{m}$ is a grouping of terms known as the Area [times] Gamma Over Mass (AGOM) parameter. Due to the linearity between the three variables that make up AGOM, it is impossible to estimate all three of the parameters together. Often times both A_{\odot} and m are difficult to determine if one is not the operator of the satellite, consequently in this research the area-to-mass ratio is set to 1. Therefore when estimating the coefficient of reflectivity C_r the effects of both the area as well as the mass will impact the estimate. In essence we are actually estimating the AGOM parameter instead.

2.1.4.2 Fourier Coefficient Model

The Fourier coefficient model derived by Ref. [72] and expanded upon by Ref. [58] is briefly described, for more detail see the aforementioned references. The Fourier coefficient model

characterizes the acceleration due to the Sun's irradiation on N number of surface elements used to model the spacecraft (or even small bodies) by taking into account the orientation of the surface element as well as its optical properties. This can be represented as a Fourier expansion shown as follows,

$$\ddot{\mathbf{r}}_{SRP} = \frac{P(R)}{m} \sum_{n=0}^{\infty} [\mathbf{A}_n(\delta_s) \cos(n\lambda_s) + \mathbf{B}_n(\delta_s) \sin(n\lambda_s)]. \quad (2.18)$$

In Eq. 2.18, we divide by the mass m , to obtain the acceleration rather than the force of the cumulative radiation pressure on the spacecraft. The function $P(R)$ is the solar pressure as a function of the distance R from the Sun such that,

$$P(R) = \frac{G_1}{R^2} \quad (2.19)$$

where G_1 is the solar radiation constant of approximately 1×10^{14} kg-km/s². The SRP acceleration is also a function of the solar latitude δ_s and the solar longitude λ_s . The Fourier coefficients \mathbf{A}_n and \mathbf{B}_n have units of area and capture the information associated with the spacecraft's shape, optical properties, and the Sun's location in the spacecraft body frame and can be estimated in a filter. The Fourier coefficient model is higher fidelity than the cannonball model because a spacecraft, in the majority of cases, does not behave like a uniform sphere with constant optical properties, rather, a spacecraft has many angled faces made of various materials which can be better approximated using the Fourier SRP model.

2.1.4.3 SRP Shadow Model

The cannonball and Fourier coefficient SRP models both employ a shadow model to ensure the SRP force is adjusted depending on the shadow condition. With an Earth-orbiting spacecraft, the Earth regularly occults the Sun from the spacecraft point of view while the Moon does so on a much more sporadic and rare basis. Both of these celestial bodies have shadows through which the spacecraft may pass. Consequently we adjust the SRP equation to include a fractional term,

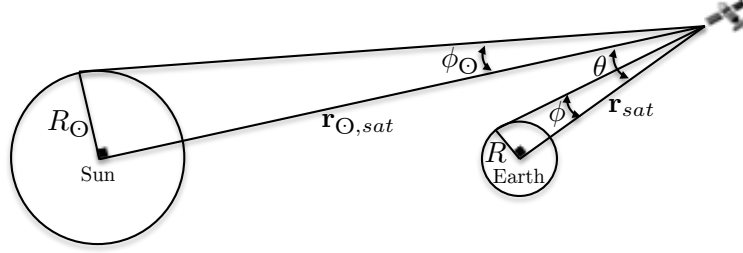


Figure 2.3: SRP shadow model geometry

ν , where 1 is fully lit, 0 is fully eclipsed and between 0 and 1 is a partial eclipse. Equation 2.20 defines ν with the assumption that $\phi \gg \phi_{\odot}$ [36].

$$\nu = \begin{cases} 1, & \theta \geq \phi + \phi_{\odot} \\ \frac{\theta - \phi}{2\phi_{\odot}} + \frac{1}{2}, & \phi - \phi_{\odot} \leq \theta < \phi + \phi_{\odot} \\ 0, & \theta < \phi - \phi_{\odot} \end{cases} \quad (2.20)$$

The angles are illustrated in Figure 2.3, where R_{\odot} and R are the radius of the Sun and the radius of the occulting body respectively. The vector from the center of the Sun to the spacecraft is $\mathbf{r}_{\odot,sat}$, and the vector from the center of the occulting body to the spacecraft is \mathbf{r}_{sat} . The angles are computed as follows,

$$\theta = \cos^{-1} \left(\frac{\mathbf{r}_{\odot,sat} \cdot \mathbf{r}_{sat}}{r_{\odot,sat} r_{sat}} \right) \quad (2.21)$$

and,

$$\phi_{\odot} = \sin^{-1} \left(\frac{R_{\odot}}{r_{\odot,sat}} \right) \quad (2.22)$$

and finally,

$$\phi = \sin^{-1} \left(\frac{R}{r_{sat}} \right). \quad (2.23)$$

2.2 Measurement Models

In this section we define all of the measurement models used throughout this dissertation along with their partials for direct use in the filter. We start off by introducing the two primary measurements: TDOA and FDOA, then we briefly discuss some of the associated media corrections. In subsequent sections, the range, range-rate and optical measurements are presented as well.

2.2.1 Time and Frequency Difference of Arrival

Figure 2.4 illustrates the setup to generate the TDOA and FDOA measurements. The receiver (RX) dishes marked by RX_1 and RX_2 each represent a single receiver channel rather than the actual physical number of RXs required. Therefore in the current setup, while two RXs could be used, a single RX with two channels would likely be preferred. The two RXs and the reference transmitter (TX_{Ref}) are generally located in the same complex with i number of arbitrary TXs located across the continent to generate large baselines.

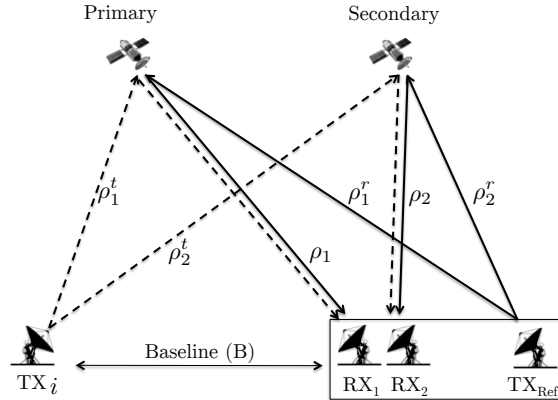


Figure 2.4: TDOA/FDOA geometry, antennas in box are at same location

A waveform is generated by both the i^{th} TX and the reference TX (not necessarily the same waveform) which is intercepted by both the primary and secondary satellites. A bent pipe architecture on the satellites immediately returns the signals back to Earth which are then acquired by the RXs. Temporarily ignoring the reference TX we see that the waveform generated by the i^{th} TX is received by both RX_1 and RX_2 , despite being the same waveform when emitted, the difference

in path lengths to each of the satellites and the difference in relative motion causes a time delay and Doppler shift between the two received signals. Generally the time delay and Doppler shift are estimated jointly in order to determine either one adequately, which is done through a generalized form of the correlation process known as the complex ambiguity function (CAF) [78],

$$A(\tau, f) = \int_0^T [s_1(t)s_2^*(t + \tau)] e^{-j2\pi ft} dt. \quad (2.24)$$

Where, $s_1(t)$ and $s_2(t)$ are the two waveforms to be correlated, where * represents the complex conjugate. The correlation time for all simulated data is 3 minutes, this means a TDOA and FDOA measurement is generated with the same frequency. The time delay and frequency offsets are τ and f respectively. The values of τ and f that maximize $|A(\tau, f)|$ are known as the differential time offset (DTO) and the differential frequency offset (DFO) respectively. Since the reference TX was previously ignored these DTO and DFO values correspond to the i^{th} TX denoted by the superscript t such that we have a DTO^t and DFO^t . Similarly we can correlate the waveforms from the reference TX to obtain DTO^r and DFO^r where the superscript r indicates the values associated with the reference TX. Finally the difference of the DTOs between the i^{th} and reference TX is TDOA,

$$TDOA = DTO^t - DTO^r. \quad (2.25)$$

While the difference of the DFOs between the i^{th} and reference TX is FDOA,

$$FDOA = DFO^t - DFO^r. \quad (2.26)$$

A key driver for the TDOA/FDOA system to work is that both satellites are required to be within the beamwidth or an accompanying side lobe of the transmitting antenna, inevitably restricting the angular separation of the two satellites [37]. Smaller antennas are consequentially preferred as they have wider beamwidths and provide a stronger signal to the secondary satellite which in turn improves the correlation of the DTO and DFO estimation [12].

The previous equations for TDOA and FDOA show how those measurements are acquired using hardware. In the following part we describe the actual models used for these measurements that allow the acquired TDOA and FDOA measurements to be related to the states of the satellites.

The satellite positions and velocities relative to the stations can be modeled as ranges and range-rates. By deriving the measurement models we show that one of the major strengths of these observables is the cancellation of many common errors. We start by defining the pseudo-range as $\tilde{\rho}$ shown in Eq. 2.27,

$$\tilde{\rho} = \rho + c\delta_{RX} + c\delta_{TX} + \delta_{\rho_{atm}} + \epsilon. \quad (2.27)$$

Where ρ is the true range, c is the speed of light, δ_{RX} is the receiver delay due to clock bias, δ_{TX} is the transmitter delay also due to clock bias, $\delta_{\rho_{atm}}$ are the path delays caused by the tropo and ionosphere, and finally ϵ are any other unaccounted for measurement errors. In a similar fashion the pseudo-range-rate $\dot{\tilde{\rho}}$ is defined as the time derivative of pseudo-range,

$$\dot{\tilde{\rho}} = \dot{\rho} + c\dot{\delta}_{RX} + c\dot{\delta}_{TX} + \dot{\delta}_{\rho_{atm}} + \zeta. \quad (2.28)$$

Where, $\dot{\rho}$ is the true range-rate, $\dot{\delta}_{RX}$ is the receiver clock drift rate, $\dot{\delta}_{TX}$ is the transmitter clock drift rate, $\dot{\delta}_{\rho_{atm}}$ is the tropo and ionospheric delay rate, and finally ζ are the additional unaccounted for measurement errors. Note that in Eqs. 2.27 and 2.28 these are one-way range and range-rates, therefore a TX can mean the actual ground-based TX but also the satellite. Similarly a RX can mean the ground-based receiver but also the satellite depending on whether the range or range-rate is an uplink or a downlink signal.

A DTO is the time difference between the signals acquired by the ground receivers with the signal relayed through the primary and secondary satellite transmitted from the same TX. The signal path in a DTO includes both the uplink and the downlink portion, from the transmitter to the satellite and from the satellite to its respective receiver. Using Eq. 2.27 a DTO measurement can be written as follows:

$$\begin{aligned}
DTO^* = \frac{1}{c} & \left[(\rho_2^* + c\delta_{sat_2}^* + \cancel{c\delta_{TX}^*} + \delta_{\rho_{atm_2}}^* + \epsilon_2^*) + (\rho_2 + c\delta_{RX_2} + c\delta_{sat_2} + \delta_{\rho_{atm_2}} + \epsilon_2) - \right. \\
& \left. (\rho_1^* + c\delta_{sat_1}^* + \cancel{c\delta_{TX}^*} + \delta_{\rho_{atm_1}}^* + \epsilon_1^*) - (\rho_1 + c\delta_{RX_1} + c\delta_{sat_1} + \delta_{\rho_{atm_1}} + \epsilon_1) \right]
\end{aligned} \tag{2.29}$$

where,

$$\rho_i^* = \sqrt{(x_i - x_{TX}^*)^2 + (y_i - y_{TX}^*)^2 + (z_i - z_{TX}^*)^2}, \tag{2.30}$$

and

$$\rho_i = \sqrt{(x_i - x_{RX_i})^2 + (y_i - y_{RX_i})^2 + (z_i - z_{RX_i})^2}. \tag{2.31}$$

Where, c is the speed of light, and $*$ is either t or r correspondingly for the secondary or reference transmitter, and ρ is the signal path length defined by either Eq. 2.30 or Eq. 2.31. From Eq. 2.29 we see that the TX delays cancel so that we end up with Eq. 2.32.

$$\begin{aligned}
DTO^* = \frac{1}{c} & \left[(\rho_2^* + c\delta_{sat_2}^* + \delta_{\rho_{atm_2}}^* + \epsilon_2^*) + (\rho_2 + c\delta_{RX_2} + c\delta_{sat_2} + \delta_{\rho_{atm_2}} + \epsilon_2) - \right. \\
& \left. (\rho_1^* + c\delta_{sat_1}^* + \delta_{\rho_{atm_1}}^* + \epsilon_1^*) - (\rho_1 + c\delta_{RX_1} + c\delta_{sat_1} + \delta_{\rho_{atm_1}} + \epsilon_1) \right]
\end{aligned} \tag{2.32}$$

Recall from Eq. 2.25 that TDOA is comprised of the secondary DTO minus the reference DTO, therefore using Eq. 2.32 we obtain,

$$\begin{aligned}
TDOA = \frac{1}{c} & \left[(\rho_2^t + \cancel{c\delta_{sat_2}^t} + \delta_{\rho_{atm_2}}^t + \epsilon_2^t) + (\rho_2 + c\delta_{RX_2} + \cancel{c\delta_{sat_2}} + \delta_{\rho_{atm_2}} + \epsilon_2) - \right. \\
& \left. (\rho_1^t + \cancel{c\delta_{sat_1}^t} + \delta_{\rho_{atm_1}}^t + \epsilon_1^t) - (\rho_1 + c\delta_{RX_1} + \cancel{c\delta_{sat_1}} + \delta_{\rho_{atm_1}} + \epsilon_1) \right] - \\
& \frac{1}{c} \left[(\rho_2^r + \cancel{c\delta_{sat_2}^r} + \delta_{\rho_{atm_2}}^r + \epsilon_2^r) + (\rho_2 + c\delta_{RX_2} + \cancel{c\delta_{sat_2}} + \delta_{\rho_{atm_2}} + \epsilon_2) - \right. \\
& \left. (\rho_1^r + \cancel{c\delta_{sat_1}^r} + \delta_{\rho_{atm_1}}^r + \epsilon_1^r) - (\rho_1 + c\delta_{RX_1} + \cancel{c\delta_{sat_1}} + \delta_{\rho_{atm_1}} + \epsilon_1) \right].
\end{aligned} \tag{2.33}$$

Using TDOA, the downlink legs cancel as do the clock biases of the satellite. Cleaning up and re-arranging Eq. 2.33 we get,

$$\begin{aligned}
TDOA = \frac{1}{c} & \left[\rho_2^t - \rho_2^r + \rho_1^r - \rho_1^t \right] + \left(\delta_{\rho_{atm_1}}^r - \delta_{\rho_{atm_2}}^r - \delta_{\rho_{atm_1}}^t + \delta_{\rho_{atm_2}}^t \right) + \\
& (\epsilon_1^r - \epsilon_2^r - \epsilon_1^t + \epsilon_2^t).
\end{aligned} \tag{2.34}$$

Equation 2.34 shows that we are left with the uplinks, atmospheric delays, as well as unaccounted for range errors. Examining the atmospheric errors we see that they effectively cancel to zero because the signal path to satellite 1 and 2 is nearly identical over the first 10's of kilometers. In effect we can say that $\delta_{\rho_{atm_1}}^r \approx \delta_{\rho_{atm_2}}^r$ and $\delta_{\rho_{atm_1}}^t \approx \delta_{\rho_{atm_2}}^t$ as the localized atmospheric effects over each of the TXs are the same. Finally the unaccounted for range errors are generally in the noise and are due differences in, for example, the time varying thermal noise of the receivers. While the unaccounted for range errors are not completely canceled, they are significantly reduced in magnitude due to the differencing between the secondary TX and reference TX. As a result the final TDOA equation is reduced to,

$$\boxed{TDOA = \frac{1}{c} [\rho_2^t - \rho_2^r + \rho_1^r - \rho_1^t]} \quad (2.35)$$

Just like DTO, the differential frequency offset (DFO) which includes both the uplink and downlink components of the signal path can be written using the pseudo range-rate shown in Eq. 2.28 as follows:

$$\begin{aligned} DFO^* = \frac{1}{c} & \left[\left(f_{TX}^* \cdot \left(\dot{\rho}_2^* + c\dot{\delta}_{sat_2}^* + c\dot{\delta}_{TX}^* + \dot{\delta}_{\rho_{atm_2}}^* + \zeta_2^* \right) + \right. \right. \\ & \left. \left(f_{TX}^* - f_{tr1} \right) \cdot \left(\dot{\rho}_2 + c\dot{\delta}_{sat_2} + c\dot{\delta}_{TX_2} + \dot{\delta}_{\rho_{atm_2}} + \zeta_2 \right) \right) - \\ & \left(f_{TX}^* \cdot \left(\dot{\rho}_1^* + c\dot{\delta}_{sat_1}^* + c\dot{\delta}_{TX}^* + \dot{\delta}_{\rho_{atm_1}}^* + \zeta_1^* \right) + \right. \\ & \left. \left. \left(f_{TX}^* - f_{tr2} \right) \cdot \left(\dot{\rho}_1 + c\dot{\delta}_{RX_1} + c\dot{\delta}_{sat_1} + \dot{\delta}_{\rho_{atm_1}} + \zeta_1 \right) \right) \right]. \end{aligned} \quad (2.36)$$

where,

$$\begin{aligned} \dot{\rho}_i^* &= (\mathbf{v}_i - \mathbf{v}_{TX}^*) \cdot \frac{\mathbf{r}_i - \mathbf{r}_{TX}^*}{\rho_i^*} \\ &= \begin{bmatrix} \dot{x}_i - \dot{x}_{TX}^* \\ \dot{y}_i - \dot{y}_{TX}^* \\ \dot{z}_i - \dot{z}_{TX}^* \end{bmatrix} \cdot \frac{1}{\rho_i^*} \begin{bmatrix} x_i - x_{TX}^* \\ y_i - y_{TX}^* \\ z_i - z_{TX}^* \end{bmatrix}, \end{aligned} \quad (2.37)$$

and

$$\begin{aligned}\dot{\rho}_i &= (\mathbf{v}_i - \mathbf{v}_{RX_i}) \cdot \frac{\mathbf{r}_i - \mathbf{r}_{RX_i}}{\rho_i} \\ &= \begin{bmatrix} \dot{x}_i - \dot{x}_{RX_i} \\ \dot{y}_i - \dot{y}_{RX_i} \\ \dot{z}_i - \dot{z}_{RX_i} \end{bmatrix} \cdot \frac{1}{\rho_i} \begin{bmatrix} x_i - x_{RX_i} \\ y_i - y_{RX_i} \\ z_i - z_{RX_i} \end{bmatrix}.\end{aligned}\quad (2.38)$$

First the transmit frequencies of the reference and secondary transmitter are defined as f_{TX}^r and f_{TX}^t respectively. Next the translation frequency or the deliberate shift in frequency by the satellite's translation oscillators is defined as f_{trl_1} and f_{trl_2} for the primary and secondary satellite respectively. The time derivatives of the paths, also known as the line-of-sight velocities, are defined as $\dot{\rho}$.

Recall from Eq. 2.26 that FDOA is comprised of the secondary DFO minus the reference DFO, therefore using Eq. 2.39 we obtain,

$$\begin{aligned}FDOA &= \frac{1}{c} \left[\left(f_{TX}^t \cdot \left(\dot{\rho}_2^t + c\dot{\delta}_{sat_2}^t + c\dot{\delta}_{TX}^t + \dot{\delta}_{\rho_{atm_2}}^t + \zeta_2^t \right) + \right. \right. \\ &\quad \left. \left(f_{TX}^t - f_{trl_1} \right) \cdot \left(\dot{\rho}_2 + c\dot{\delta}_{sat_2} + c\dot{\delta}_{TX_2} + \dot{\delta}_{\rho_{atm_2}} + \zeta_2 \right) \right) - \\ &\quad \left(f_{TX}^t \cdot \left(\dot{\rho}_1^t + c\dot{\delta}_{sat_1}^t + c\dot{\delta}_{TX}^t + \dot{\delta}_{\rho_{atm_1}}^t + \zeta_1^t \right) + \right. \\ &\quad \left. \left. \left(f_{TX}^t - f_{trl_2} \right) \cdot \left(\dot{\rho}_1 + c\dot{\delta}_{RX_1} + c\dot{\delta}_{sat_1} + \dot{\delta}_{\rho_{atm_1}} + \zeta_1 \right) \right) \right] - \\ &\quad \frac{1}{c} \left[\left(f_{TX}^r \cdot \left(\dot{\rho}_2^r + c\dot{\delta}_{sat_2}^r + c\dot{\delta}_{TX}^r + \dot{\delta}_{\rho_{atm_2}}^r + \zeta_2^r \right) + \right. \right. \\ &\quad \left. \left(f_{TX}^r - f_{trl_1} \right) \cdot \left(\dot{\rho}_2 + c\dot{\delta}_{sat_2} + c\dot{\delta}_{TX_2} + \dot{\delta}_{\rho_{atm_2}} + \zeta_2 \right) \right) - \\ &\quad \left(f_{TX}^r \cdot \left(\dot{\rho}_1^r + c\dot{\delta}_{sat_1}^r + c\dot{\delta}_{TX}^r + \dot{\delta}_{\rho_{atm_1}}^r + \zeta_1^r \right) + \right. \\ &\quad \left. \left. \left(f_{TX}^r - f_{trl_2} \right) \cdot \left(\dot{\rho}_1 + c\dot{\delta}_{RX_1} + c\dot{\delta}_{sat_1} + \dot{\delta}_{\rho_{atm_1}} + \zeta_1 \right) \right) \right].\end{aligned}\quad (2.39)$$

The FDOA terms do not cancel as cleanly as with TDOA due to the TX frequency pre-multiplier for all the terms. If the TX frequencies are identical however then all the clock drift terms do completely cancel and the atmospheric drift delays are nearly identical while the unaccounted for range-rate errors are significantly reduced as well so that the following FDOA measurement equation is realized,

$$FDOA = \frac{f_{TX}}{c} [\dot{\rho}_1^t - \dot{\rho}_2^t - \dot{\rho}_1^r + \dot{\rho}_2^r]. \quad (2.40)$$

If on the other hand the TX frequencies are nearly equal then the clock drift terms do not cancel exactly but are significantly reduced so that we can still approximate FDOA as,

$$FDOA = \frac{1}{c} [f_{tr}^t (\dot{\rho}_1^t + \dot{\rho}_1 - \dot{\rho}_2^t - \dot{\rho}_2) - f_{tr}^r (\dot{\rho}_1^r + \dot{\rho}_1 - \dot{\rho}_2^r - \dot{\rho}_2)]. \quad (2.41)$$

In this dissertation we use the approximate form so that two different TX frequencies can be inputted if desired. If the two TX frequencies inputted are the same however, the approximate form effectively turns into Eq. 2.40. The following section goes through the partials of the TDOA and FDOA measurements for use in the filter.

2.2.1.1 Time and Frequency Difference of Arrival Partial

In filtering, the measurement equation is linearized which means the first term of the Taylor series is needed. The first term, of course refers to the first order partial of the measurement equation with respect to the states which is also known as the measurement mapping matrix. For the following partials we assume that the state is,

$$\mathbf{X} = \left[\mathbf{r}_1^\top \quad \mathbf{v}_1^\top \quad C_{r_1} \quad \mathbf{r}_2^\top \quad \mathbf{v}_2^\top \quad C_{r_2} \right]^\top. \quad (2.42)$$

This estimated state vector is used in the dual-satellite state estimation problem discussed in chapter 4. In the relative estimation case discussed in chapter 5 a different state vector is estimated, but throughout that research a UKF is implemented so no partials are required for that filter. The measurement mapping matrix using Eq. 2.42 is shown below,

$$\begin{aligned} \tilde{\mathbf{H}}_k &= \left[\frac{\partial G(\mathbf{X}_k, t_k)}{\partial \mathbf{X}_k} \right] \Bigg|_{\mathbf{X}_{ref}} \\ &= \begin{bmatrix} \mathbf{T}_1 & \mathbf{0}_{1 \times 3} & 0 & \mathbf{T}_2 & \mathbf{0}_{1 \times 3} & 0 \\ \mathbf{F}_1 & \mathbf{J}_1 & 0 & \mathbf{F}_2 & \mathbf{J}_2 & 0 \end{bmatrix} \in \mathcal{R}^{2 \times 14}. \end{aligned} \quad (2.43)$$

The coefficient of reflectivity is not a parameter within the measurement model, consequently columns 3 and 6 are both zero. In addition, TDOA is not a function of the velocity, therefore those partials are also zero. The resulting submatrices of the analytical partials are shown next. First we look at \mathbf{T}_i , which is the partial of TDOA defined by Eq. 2.35 with respect to the position vector of the satellite, \mathbf{r}_i . The subscript i refers to either satellite 1 or 2. The component form of this partial is given by Eq. 2.44,

$$\begin{aligned} \mathbf{T}_i^\top &= \frac{(-1)^{i-1}}{c} \begin{bmatrix} \frac{x_i - x_{TX}^r}{\rho_i^r} + \frac{x_{TX}^t - x_i}{\rho_i^t} \\ \frac{y_i - y_{TX}^r}{\rho_i^r} + \frac{y_{TX}^t - y_i}{\rho_i^t} \\ \frac{z_i - z_{TX}^r}{\rho_i^r} + \frac{z_{TX}^t - z_i}{\rho_i^t} \end{bmatrix} \\ &= \frac{(-1)^{i-1}}{c} \left[\frac{\mathbf{r}_i - \mathbf{r}_{TX}^r}{\rho_i^r} + \frac{\mathbf{r}_{TX}^t - \mathbf{r}_i}{\rho_i^t} \right] \in \mathcal{R}^{3 \times 1}. \end{aligned} \quad (2.44)$$

After \mathbf{T}_i , there is \mathbf{F}_i , which is the partial of FDOA defined by Eq. 2.41 with respect to the position vector of the satellite, \mathbf{r}_i . Rewriting \mathbf{F}_i in terms of DFOs for conciseness we obtain,

$$\mathbf{F}_i^\top = \mathbf{F}_{DFO_i^t}^\top - \mathbf{F}_{DFO_i^r}^\top \in \mathcal{R}^{3 \times 1} \quad (2.45)$$

Where $\mathbf{F}_{DFO_i^t}^\top$ and $\mathbf{F}_{DFO_i^r}^\top$ are calculated by Eq. 2.46.

$$\begin{aligned} \mathbf{F}_{DFO_i^*}^\top &= (-1)^{i-1} \frac{f_{TX}^*}{c\rho_i^*} \begin{bmatrix} 1 - (u_{x_i, TX}^*)^2 & -u_{x_i, TX}^* u_{y_i, TX}^* & -u_{x_i, TX}^* u_{z_i, TX}^* \\ -u_{y_i, TX}^* u_{x_i, TX}^* & 1 - (u_{y_i, TX}^*)^2 & -u_{y_i, TX}^* u_{z_i, TX}^* \\ -u_{z_i, TX}^* u_{x_i, TX}^* & -u_{z_i, TX}^* u_{y_i, TX}^* & 1 - (u_{z_i, TX}^*)^2 \end{bmatrix} \begin{bmatrix} v_{x_i, TX}^* \\ v_{y_i, TX}^* \\ v_{z_i, TX}^* \end{bmatrix} \\ &+ (-1)^{i-1} \frac{(f_{TX}^* - f_{tr_i})}{c\rho_i} \begin{bmatrix} 1 - (u_{x_i, RX})^2 & -u_{x_i, RX} u_{y_i, RX} & -u_{x_i, RX} u_{z_i, RX} \\ -u_{y_i, RX} u_{x_i, RX} & 1 - (u_{y_i, RX})^2 & -u_{y_i, RX} u_{z_i, RX} \\ -u_{z_i, RX} u_{x_i, RX} & -u_{z_i, RX} u_{y_i, RX} & 1 - (u_{z_i, RX})^2 \end{bmatrix} \begin{bmatrix} v_{x_i, RX} \\ v_{y_i, RX} \\ v_{z_i, RX} \end{bmatrix}. \end{aligned} \quad (2.46)$$

All terms are previously defined except for u and v . There are two variations of both u and v associated with either the transmitter or receiver shown in Eqs. 2.47-2.50. Note that for conciseness

ζ is a stand-in variable for the components x, y and z .

$$u_{\zeta_i, TX}^* = \frac{\zeta_i - \zeta_{TX}^*}{\rho_i^*} \quad (2.47)$$

$$v_{\zeta_i, TX}^* = \dot{\zeta}_i - \dot{\zeta}_{TX}^* \quad (2.48)$$

$$u_{\zeta_i, RX} = \frac{\zeta_i - \zeta_{RX_i}}{\rho_i} \quad (2.49)$$

$$v_{\zeta_i, RX} = \dot{\zeta}_i - \dot{\zeta}_{RX_i} \quad (2.50)$$

The last submatrix in $\tilde{\mathbf{H}}_k$ is \mathbf{J}_i , which is the partial of FDOA defined by Eq. 2.41 with respect to the velocity vector of the satellite, \mathbf{v}_i . Once more for conciseness we can write \mathbf{J}_i in terms of DFOs,

$$\mathbf{J}_i^\top = \mathbf{J}_{DFO_i^t}^\top - \mathbf{J}_{DFO_i^r}^\top \in \mathcal{R}^{3 \times 1}. \quad (2.51)$$

Where $\mathbf{J}_{DFO_i^t}^\top$ and $\mathbf{J}_{DFO_i^r}^\top$ are computed by Eq. 2.52,

$$\mathbf{J}_{DFO_i^*}^\top = (-1)^{i-1} \frac{f_{TX}^*}{c} \begin{bmatrix} u_{x_i, TX}^* \\ u_{y_i, TX}^* \\ u_{z_i, TX}^* \end{bmatrix} + (-1)^{i-1} \frac{(f_{TX}^* - f_{tr_i})}{c} \begin{bmatrix} u_{x_i, RX} \\ u_{y_i, RX} \\ u_{z_i, RX} \end{bmatrix} \quad (2.52)$$

where u is defined by Eqs. 2.47 and 2.49. Similar to Eq. 2.46 the translation frequencies in Eq. 2.52 also cancel when substituted back into Eq. 2.51.

2.2.1.2 Time and Frequency Difference of Arrival Troposphere and Ionosphere Corrections

Using TDOA the atmospheric path delays are canceled almost perfectly, with FDOA it depends on the whether the frequencies of the transmitters are the same or not. If they are not, then larger atmospheric path delays may be encountered. In order to address these errors a correction is added to the TDOA and FDOA measurement that accounts for the delays from the tropo- and ionosphere, the following setup is obtained from Ref. [41] and chapter 9 of Ref. [66]. The TDOA correction is,

$$\delta TDOA = \frac{1}{c} [\delta \rho_2^t - \delta \rho_2^r + \delta \rho_1^r - \delta \rho_1^t]. \quad (2.53)$$

Where,

$$\delta\rho_i^* = dTrop_i^* + dIono_i^* \quad (2.54)$$

Where, $dTrop$ and $dIono$ are the tropo- and ionosphere corrections for the path associated with satellite i and transmitter $*$. The FDOA correction is,

$$\delta FDOA = \frac{1}{c} [f_{tr}^t (\delta\dot{\rho}_1^t + \delta\dot{\rho}_1 - \delta\dot{\rho}_2^t - \delta\dot{\rho}_2) - f_{tr}^r (\delta\dot{\rho}_1^r + \delta\dot{\rho}_1 - \delta\dot{\rho}_2^r - \delta\dot{\rho}_2)]. \quad (2.55)$$

Where,

$$\delta\dot{\rho}_i^* = \frac{(dTrop_i^*(t) - dTrop_i^*(t - dt)) - (dIono_i^*(t) - dIono_i^*(t - dt))}{dt} \quad (2.56)$$

and,

$$\delta\dot{\rho}_i = \frac{(dTrop_i(t) - dTrop_i(t - dt)) - (dIono_i(t) - dIono_i^*(t - dt))}{dt}. \quad (2.57)$$

The troposphere model used is,

$$dTrop = z_h m_h + z_w m_w \quad (2.58)$$

Where, z_h and z_w are zenith delays, while m_h and m_w are mapping functions. The zenith delays are defined as follows,

$$z_h = \frac{0.0022768P}{\psi} \quad (2.59)$$

where, P is the pressure in millibars and,

$$\psi = 1 - 2.66 \times 10^{-3} \cos(2\phi_{gd}) - 2.8 \times 10^{-7} h \quad (2.60)$$

where, ϕ_{gd} is the geodetic latitude of the ground stations in radians and h is the height above the WGS84 ellipsoid in meters. The z_w zenith delay is defined as,

$$z_w = 2.2768 \times 10^{-3} \frac{1255/T + 0.05}{\psi} \quad (2.61)$$

where T is the temperature in Kelvin and ψ is previously defined in Eq. 2.60. The m_h and m_w Vienna mapping functions are provided in Ref. [66] as well as Ref [41].

The ionosphere model used is,

$$dIono = 40.309 \frac{TEC(t, \mathbf{r}_i)}{f^2} F \quad (2.62)$$

where,

$$F = \left[1 - \frac{r_i \cos \alpha}{R} \right]^{-1/2} \quad (2.63)$$

where α is the elevation of the spacecraft with respect to the ground station and R is a value from the TEC map file.

2.2.2 Light-Time Correction

The TDOA and FDOA measurements are recorded by the receivers and time-tagged at a time t . This means the signal was transmitted by the satellite at time t minus the downlink time, τ_{dwn} or at time td . In many cases there is a small delay between the satellite receiving and re-transmitting the signal, therefore the signal was received by the satellite at time td minus the delay, τ_{del} or at time tdd . Finally the signal was transmitted at time tdd minus the uplink time, τ_{up} or at time $tddu$. As a consequence both the uplink and the downlink require a fixed-point iteration in order to solve for the path length, ρ [61]. The downlink segment is computed first and then the uplink since we must go in reverse from the time the signal was received. For simplicity, the equations below are generalized and the specific satellite and transmitter/receiver subscripts are not included,

$$\rho_{dwn} = c\tau_{dwn} = \|\mathbf{r}_{sat}(t - \tau_{dwn}) - \mathbf{r}_{rec}(t)\|_2. \quad (2.64)$$

The downlink path is thus the difference of the position of the satellite from whence the signal departed and the position of the receiver at which the signal was received. Continuing backwards, the uplink path is,

$$\rho_{up} = c\tau_{up} = \|\mathbf{r}_{sat}(t - \tau_{dwn} - \tau_{del}) - \mathbf{r}_{tr}(t - \tau_{dwn} - \tau_{del} - \tau_{up})\|_2. \quad (2.65)$$

The uplink path is therefore the difference of the position of the satellite at which the signal was received and the position of the transmitter from whence the signal departed. Due to this light-time correction, care should be taken to ensure that the positions of the satellite, transmitters and receivers are computed at the appropriate times when calculating the TDOA and FDOA measurements.

2.2.3 Range and Range-Rate

A number of times within this dissertation, other measurement observables such as range and range-rate are utilized as well, primarily for comparison purposes with TDOA and FDOA. While TDOA and FDOA have a high fidelity level with media and light time corrections, the range and range-rate measurement equations are assumed to be instantaneous. If the range and range-rate measurements are used for comparison to TDOA and FDOA the geometry from Figure 2.5 is used.

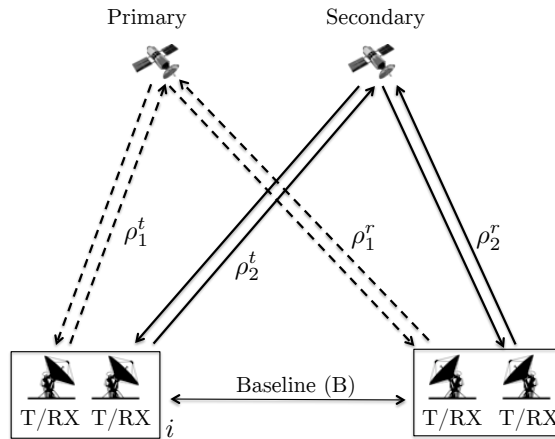


Figure 2.5: Range/range-rate geometry, antennas in box are at same location

The antennas inside each box are at the same location and actually represent channels rather than physical antennas. The two stations would be in the same locations as those found with TDOA and FDOA so as to reproduce the same baseline.

The range is computed by differencing the satellite position vector from the station position vector and taking the L2-norm,

$$\rho = \|\mathbf{r}_{sat} - \mathbf{r}\|_2 \quad (2.66)$$

The measured range is not the true range but rather the pseudo-range as defined by Eq. 2.27 reproduced below,

$$\tilde{\rho} = \rho + c\delta_{RX} + c\delta_{TX} + \delta_{\rho_{atm}} + \epsilon. \quad (2.67)$$

The extra terms corrupting the true range can be estimated using a range bias.

The range-rate observable is computed by taking the velocity vector in the direction of ρ such that we have,

$$\dot{\rho} = \dot{\boldsymbol{\rho}}^\top \hat{\boldsymbol{\rho}} \quad (2.68)$$

Once again, the measured range-rate is not the true range-rate which is corrupted by clock bias drifts and other errors. The measured range-rate is the pseudorange-rate previously shown in Eq. 2.28 reproduced below,

$$\dot{\tilde{\rho}} = \dot{\rho} + c\dot{\delta}_{RX} + c\dot{\delta}_{TX} + \dot{\delta}_{\rho_{atm}} + \zeta. \quad (2.69)$$

The extra terms bias terms can also be estimated similar to range.

2.2.3.1 Range and Range-Rate Partial

For the following partials we assume that the state is,

$$\mathbf{X} = \left[\mathbf{r}_1^\top \quad \mathbf{v}_1^\top \quad C_{r_1} \quad \mathbf{r}_2^\top \quad \mathbf{v}_2^\top \quad C_{r_2} \right]^\top. \quad (2.70)$$

This estimated state vector is used in the dual-satellite state estimation problem discussed in chapter 4. In the relative estimation case discussed in chapter 5 a different state vector is estimated, but throughout that research a UKF is implemented so no partials are required for that filter. The measurement mapping matrix using Eq. 2.70 is shown below,

$$\begin{aligned}\tilde{\mathbf{H}}_k &= \left[\frac{\partial G(\mathbf{X}_k, t_k)}{\partial \mathbf{X}_k} \right] \bigg|_{\mathbf{x}_{ref}} \\ &= \begin{bmatrix} \mathbf{R}_1 & \mathbf{0}_{1 \times 3} & 0 & \mathbf{R}_2 & \mathbf{0}_{1 \times 3} & 0 \\ \mathbf{R}\mathbf{R}_1 & \mathbf{R}\mathbf{V}_1 & 0 & \mathbf{R}\mathbf{R}_2 & \mathbf{R}\mathbf{V}_2 & 0 \end{bmatrix} \in \mathcal{R}^{2 \times 14}.\end{aligned}\quad (2.71)$$

The partials with respect to the satellite position and velocity are shown below:

$$\mathbf{R}_i = \frac{\partial \rho}{\partial \mathbf{r}_i} = \hat{\boldsymbol{\rho}}^\top \in \mathcal{R}^{1 \times 3} \quad (2.72)$$

and,

$$\mathbf{R}\mathbf{R}_i = \frac{\partial \dot{\rho}}{\partial \mathbf{r}_i} = \frac{\dot{\boldsymbol{\rho}}^\top}{\rho} \left[\mathcal{I}_{3 \times 3} - \hat{\boldsymbol{\rho}}\hat{\boldsymbol{\rho}}^\top \right] \in \mathcal{R}^{1 \times 3} \quad (2.73)$$

and,

$$\mathbf{R}\mathbf{V}_i = \frac{\partial \dot{\rho}}{\partial \mathbf{v}_i} = \hat{\boldsymbol{\rho}}^\top \in \mathcal{R}^{1 \times 3}. \quad (2.74)$$

The partials with respect to the station rather than the satellite would have the same magnitude but would be in the opposite direction.

2.2.4 Angles: Azimuth and Elevation

Another set of observables used in this dissertation is optical, referring to the azimuth and elevation angles. The angles shown in this section however, are not taken from a central body such as Earth, but rather from a spacecraft around the central body measuring the angles to another spacecraft also orbiting the central body where the central body is the origin or zero angle of both azimuth and elevation, see Figure 2.6.

The azimuth and elevation angles made between the observed satellites, main satellite (from which the angles are taken) and central body must be measured on a plane which must now be defined, and is shown in Figure 2.6(a) for clarity. The normal to this plane is a vector pointing from

the main satellite towards the central body CoM illustrated by the blue arrow in Figure 2.6(b). This normal vector is coincident with the camera LOS and is defined as the spacecraft body $\hat{\mathbf{b}}_1$ axis. The unit vector from the central body to the main satellite is defined as follows,

$$\mathcal{N}\hat{\mathbf{r}}_m = \frac{\mathcal{N}\mathbf{r}_m}{r_m} = \begin{bmatrix} \mathcal{N}\hat{x}_m \\ \mathcal{N}\hat{y}_m \\ \mathcal{N}\hat{z}_m \end{bmatrix}. \quad (2.75)$$

The $\hat{}$ indicates the vector is of unit length, a $\hat{}$ is also used on the vector's components to denote that they are normalized. The superscript \mathcal{N} specifies that the vector is expressed in the inertial frame. With the LOS vector $\hat{\mathbf{b}}_1$ defined as the negative of Eq. 2.75, the plane is still free to rotate about $\hat{\mathbf{b}}_1$, so another constraint is required to fix the plane. The $\hat{\mathbf{b}}_2$ vector is constrained to the plane of \hat{n}_1 and \hat{n}_2 and finally $\hat{\mathbf{b}}_3$ completes the right-hand rule.

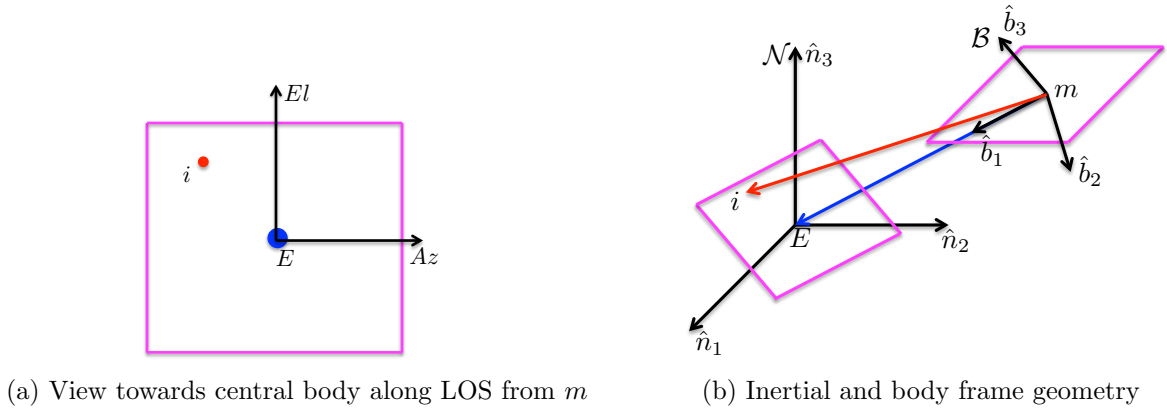


Figure 2.6: Geometry for angles observables: E is the central body, m is the main satellite and i are the observed satellites

As a result the spacecraft attitude is defined and constrained to the $\hat{\mathbf{b}}$ basis vectors. To compute the azimuth and elevation angles of the satellites, their position vectors with respect to the main satellite must be known in the body frame rather than the inertial frame. We start by defining the body frame basis vectors in terms of the inertial components as shown in Eq. 2.76.

$$\begin{bmatrix} \hat{\mathbf{b}}_1 \\ \hat{\mathbf{b}}_2 \\ \hat{\mathbf{b}}_3 \end{bmatrix} = \begin{bmatrix} -\mathcal{N}\hat{x}_m & -\mathcal{N}\hat{y}_m & -\mathcal{N}\hat{z}_m \\ \frac{-\mathcal{N}\hat{y}_m}{\sqrt{(\mathcal{N}\hat{x}_m)^2+(\mathcal{N}\hat{y}_m)^2}} & -\sqrt{1-\frac{(\mathcal{N}\hat{y}_m)^2}{(\mathcal{N}\hat{x}_m)^2+(\mathcal{N}\hat{y}_m)^2}} & 0 \\ -\mathcal{N}\hat{z}_m\sqrt{1-\frac{(\mathcal{N}\hat{y}_m)^2}{(\mathcal{N}\hat{x}_m)^2+(\mathcal{N}\hat{y}_m)^2}} & \frac{\mathcal{N}\hat{y}_m\hat{z}_m}{\sqrt{(\mathcal{N}\hat{x}_m)^2+(\mathcal{N}\hat{y}_m)^2}} & \mathcal{N}\hat{x}_m\sqrt{1-\frac{(\mathcal{N}\hat{y}_m)^2}{(\mathcal{N}\hat{x}_m)^2+(\mathcal{N}\hat{y}_m)^2}} - \frac{(\mathcal{N}\hat{y}_m)^2}{\sqrt{(\mathcal{N}\hat{x}_m)^2+(\mathcal{N}\hat{y}_m)^2}} \end{bmatrix} \quad (2.76)$$

Next, the inertial basis vectors in the inertial frame is trivial and shown in Eq. 2.77.

$$\begin{bmatrix} \hat{\mathbf{n}}_1 \\ \hat{\mathbf{n}}_2 \\ \hat{\mathbf{n}}_3 \end{bmatrix} = \begin{bmatrix} 1 & 0 & 0 \\ 0 & 1 & 0 \\ 0 & 0 & 1 \end{bmatrix} \quad (2.77)$$

Using Eqs. 2.76 and 2.77 a rotation matrix can be constructed from the inertial frame \mathcal{N} to the main satellite body frame \mathcal{B} denoted by $[BN]$ and illustrated in Eq. 2.78 [71].

$$[BN] = \begin{bmatrix} \hat{\mathbf{b}}_1 \cdot \hat{\mathbf{n}}_1 & \hat{\mathbf{b}}_1 \cdot \hat{\mathbf{n}}_2 & \hat{\mathbf{b}}_1 \cdot \hat{\mathbf{n}}_3 \\ \hat{\mathbf{b}}_2 \cdot \hat{\mathbf{n}}_1 & \hat{\mathbf{b}}_2 \cdot \hat{\mathbf{n}}_2 & \hat{\mathbf{b}}_2 \cdot \hat{\mathbf{n}}_3 \\ \hat{\mathbf{b}}_3 \cdot \hat{\mathbf{n}}_1 & \hat{\mathbf{b}}_3 \cdot \hat{\mathbf{n}}_2 & \hat{\mathbf{b}}_3 \cdot \hat{\mathbf{n}}_3 \end{bmatrix} \quad (2.78)$$

Then the position vector from the main satellite the i^{th} satellite is computed,

$${}^{\mathcal{N}}\mathbf{r}_{mi} = {}^{\mathcal{N}}\mathbf{r}_i - {}^{\mathcal{N}}\mathbf{r}_m. \quad (2.79)$$

Using the previously found rotation matrix, the main satellite to satellite vector is rotated into the body frame. The resulting components are used in the azimuth and elevation equations.

$${}^{\mathcal{B}}\mathbf{r}_{mi} = [BN]{}^{\mathcal{N}}\mathbf{r}_{mi} = \begin{bmatrix} {}^{\mathcal{B}}x_{mi} \\ {}^{\mathcal{B}}y_{mi} \\ {}^{\mathcal{B}}z_{mi} \end{bmatrix} \quad (2.80)$$

Finally the azimuth (Az) and elevation (El) angles are then computed as follows

$$Az_i = \tan^{-1} \left(\frac{{}^{\mathcal{B}}y_{mi}}{{}^{\mathcal{B}}x_{mi}} \right), \quad (2.81)$$

and

$$El_i = \tan^{-1} \left(\frac{{}^{\mathcal{B}}z_{mi}}{\sqrt{({}^{\mathcal{B}}x_{mi})^2 + ({}^{\mathcal{B}}y_{mi})^2}} \right). \quad (2.82)$$

For implementation in the code the `atan2` function is used to ensure that the angle has the correct sign. The azimuth and elevation observables are used in chapter 8 in conjunction with FDOA for small-body navigation around the asteroid Eros.

2.3 Coordinate Frames

The developed OD framework using TDOA and FDOA must have the capability to process real data, consequently the coordinate frames that are used must be consistent and have a high fidelity. Often times, in the dual-satellite estimation case, the a-priori state vector of the satellites is in the form of a Two-Line Element (TLE) which is propagated using the SGP4 orbit propagator to the time of the first measurement. This propagation occurs in the True Equator, Mean Equinox (TEME) of Date where the x-axis points along the mean vernal equinox and the z-axis points along the true rotation axis of the Earth at the specified date or coordinate epoch [1]. Then the TEME state vector is rotated into the inertial dynamical mean equator, mean equinox (MEME) J2000 reference frame using the IAU 1976 precession theory, full 106-term IAU 1980 nutation theory, and the 1982 equation of the equinoxes with the kinematic correction terms. Then the J2000 state is converted to the Geocentric Celestial Reference Frame (GCRF) a realization of the International Celestial Reference System (ICRS) which is the most current fundamental inertial coordinate system. The GCRF frame is closely aligned with the J2000 frame with an angular difference of only 0.01 arcsec, and determined with an accuracy of 0.003 arcsec [60]. Finally if desired, the GCRF state can also be outputted in the International Terrestrial Reference Frame (ITRF) an Earth centered Earth fixed reference frame, the rotation uses the following equations:

$$\mathbf{r}_{ITRF} = \mathbf{\Pi}(t)\mathbf{\Theta}(t)\mathbf{N}(t)\mathbf{P}(t)\mathbf{r}_{GCRF} \quad (2.83)$$

and,

$$\mathbf{v}_{ITRF} = \mathbf{\Pi}(t)\mathbf{\Theta}(t)\mathbf{N}(t)\mathbf{P}(t)\mathbf{v}_{GCRF} + \mathbf{\Pi}(t)\frac{d\mathbf{\Theta}(t)}{dt}\mathbf{N}(t)\mathbf{P}(t)\mathbf{r}_{GCRF} \quad (2.84)$$

where, $\mathbf{\Pi}$ is the polar motion, $\mathbf{\Theta}$ is the Earth transformation matrix, \mathbf{N} is the nutation transformation matrix, and \mathbf{P} is the precession transformation matrix. On occasion the GCRF state is outputted as an Earth-Fixed Greenwich (EFG) reference frame which is a pseudo-Earth fixed geocentric reference frame because the polar motion is ignored.

Chapter 3

Orbit Determination Filters

In this chapter a relatively brief overview of the filters used throughout this dissertation work are described. Because this is an OD dissertation filtering lies at the heart of the methodology. We start out with the most basic filter, the batch processor with regular inversion but then also explore other numerical methods such as Cholesky decomposition and singular value decomposition (SVD) as well as a the correlation or scaled form. The consider batch filter is also derived for use with the geolocation estimation side. Then we explore sequential filters such as the Kalman filter (KF), extended Kalman filter (EKF) and square-root information filter (SRIF) with and without smoothing and state noise compensation (SNC) process noise. Finally we look at the unscented Kalman filter (UKF) in square-root form and we extend the field of filtering ever so slightly by deriving the square-root unscented Schmidt-Kalman filter (SR-USKF) a consider SR-UKF.

3.1 Batch Processor

The Batch processor as the name suggests processes all observations over a given time span in a single batch, this is unlike the sequential processors such as the KF which is discussed later. The most basic derivation of the Batch filter was in fact already shown in chapter 1.2, we duplicate the least-squares solution below for convenience,

$$\hat{\mathbf{x}} = \left(\mathbf{H}^\top \mathbf{H} \right)^{-1} \mathbf{H}^\top \mathbf{y}. \quad (3.1)$$

Generally, a weighted estimate based on the uncertainty of the measurements is more accurate and is preferred. There may also be some previous a-priori information available. We can re-derive the best estimate equation which include these additional parameters, and in so doing we obtain the following equation,

$$\hat{\mathbf{x}}_0 = \left(\mathbf{H}^\top \mathbf{R}^{-1} \mathbf{H} + \bar{\mathbf{P}}_0^{-1} \right)^{-1} \left(\mathbf{H}^\top \mathbf{R}^{-1} \mathbf{y} + \bar{\mathbf{P}}_0^{-1} \bar{\mathbf{x}}_0 \right). \quad (3.2)$$

Where \mathbf{R} is the measurement covariance matrix, $\bar{\mathbf{P}}$ is the a-priori state covariance matrix and $\bar{\mathbf{x}}$ is the a-priori state deviation. With the Batch processor all the information is mapped back to a single time, often times the epoch, denoted by the subscript 0. Equation 3.2 can also be written in terms of the information and normal matrices as follows,

$$\hat{\mathbf{x}} = \mathbf{\Lambda}^{-1} \mathbf{N}. \quad (3.3)$$

Where $\mathbf{\Lambda}$ is the information matrix and \mathbf{N} is the normal vector. From Eq. 3.3 it is clear that the inverse of the information matrix must be taken to find the best estimate of the state deviation. In some cases this inversion can cause numerical issues which is why there are other methods in place such as the Cholesky decomposition and the singular value decomposition which are discussed in the two subsequent sections. Furthermore, the batch processor in this research uses the scaled form of the measurement equation to reduce the condition number which is discussed in chapter 4.1.4.

Recall that the estimate is a deviation rather than the actual state of the spacecraft as a result of the linearization process. In order to obtain the actual state estimate the estimated state deviation is added to the reference state or the state about which the filter was originally linearized, usually the best estimate of the state at the time. This is illustrated below in Eq. 3.4,

$$\hat{\mathbf{X}}_0^* = \mathbf{X}_0^* + \hat{\mathbf{x}}_0. \quad (3.4)$$

The Batch processor can be iterated as many times as necessary where with each iteration the previous iteration's solution is used as the next iteration's reference trajectory. The iterations can

be stopped when the estimated state deviation is below some specified tolerance, often times only three to five iterations are required to obtain a very accurate estimate of the spacecraft state, where the measurement residuals are all the way down into the noise. Figure 3.1 outlines the complete Batch processor in a step-by-step procedure.

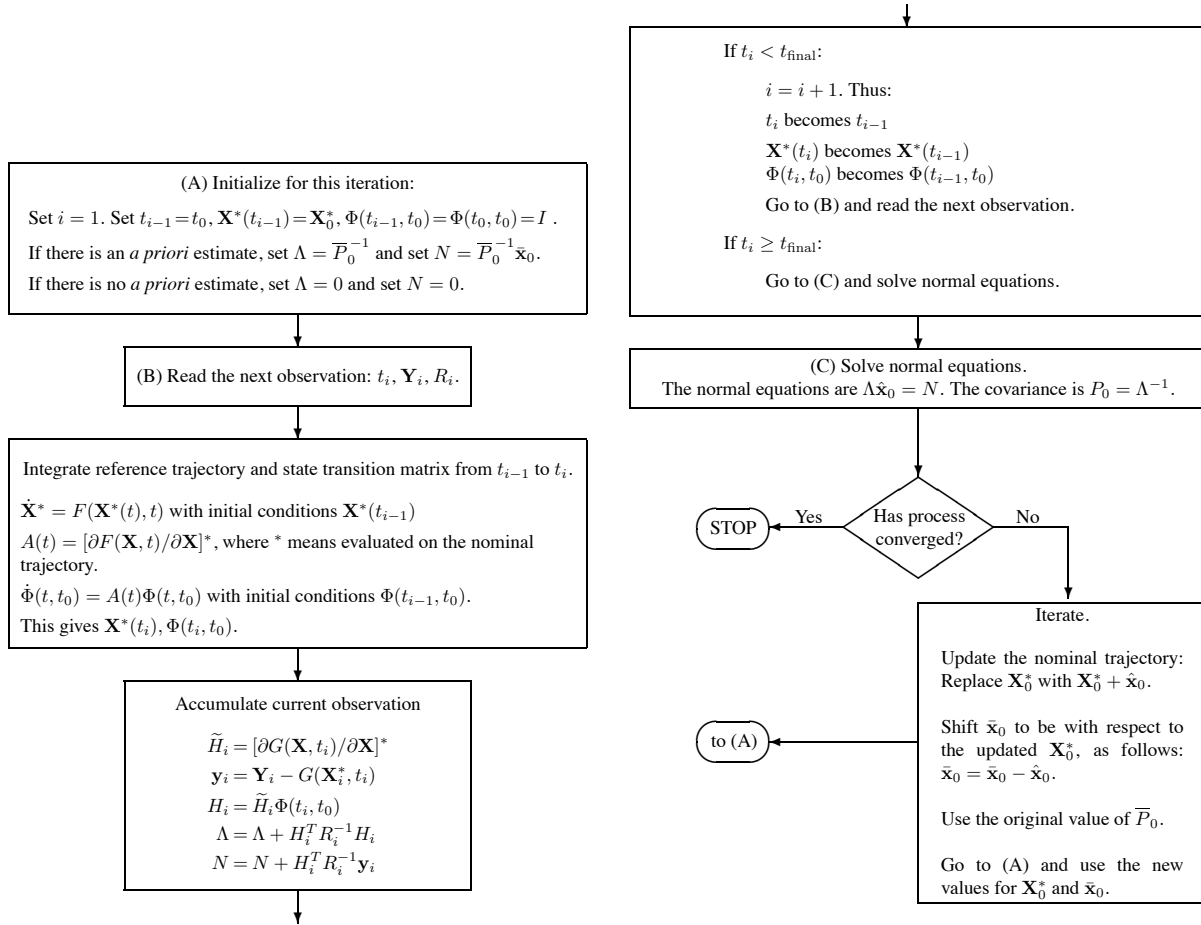


Figure 3.1: Batch processor flow chart (adapted from [83])

3.1.1 Cholesky Decomposition

The Cholesky Decomposition can be used to solve for the estimated state rather than doing an inversion. This technique is particularly useful when the number of estimated states are extremely large. An example would be the gravity field. If the Cholesky decomposition is used, the advantage

will be increased numerical accuracy since forward and backward substitutions can be used which are algebraic manipulations rather than a matrix inverse. We can decompose $\mathbf{\Lambda}$ from Eq. 3.3 as,

$$\mathbf{\Lambda} = \mathbf{R}^T \mathbf{R} \quad (3.5)$$

then,

$$\mathbf{R}^T \mathbf{R} \hat{\mathbf{x}} = \mathbf{N} \quad \rightarrow \quad \mathbf{R}^T \mathbf{z} = \mathbf{N} \quad \text{where, } \mathbf{z} = \mathbf{R} \hat{\mathbf{x}}. \quad (3.6)$$

As a result since \mathbf{R} is upper triangular \mathbf{z} can be solved for using forward substitution and $\hat{\mathbf{x}}$ can be then solved for using backward substitution, both of which are numerically stable.

3.1.2 Singular Value Decomposition (SVD)

Another method to solve for the best estimate of the state deviation without using an inverse is through SVD. The SVD of any real m by n matrix \mathbf{H} is,

$$\mathbf{H} = \mathbf{U} \mathbf{\Sigma} \mathbf{V}^T \quad \text{where, } \mathbf{U} \in \mathcal{R}^{m \times m}, \mathbf{V} \in \mathcal{R}^{n \times n}, \mathbf{\Sigma} \in \mathcal{R}^{m \times n}. \quad (3.7)$$

Where \mathbf{U} and \mathbf{V} are orthogonal matrices and $\mathbf{\Sigma}$ are singular values. An orthogonal matrix is a square matrix where $\mathbf{Q} \mathbf{Q}^T = \mathcal{I}$ and $\mathbf{Q}^T = \mathbf{Q}^{-1}$. It preserves the dot product of vectors, and therefore acts as an isometry of Euclidean space, such as a rotation or reflection. Consequently because an orthogonal matrix only rotates or reflects, we have: \forall vector \mathbf{x} , $\|\mathbf{Q} \mathbf{x}\| = \|\mathbf{x}\| = (\mathbf{x} \mathbf{x}^T)^{\frac{1}{2}}$. If \mathbf{U} and \mathbf{V} were square then instead of SVD it would be eigenvector/value decomposition. Because \mathbf{H} is not square however, Eq. 3.7 defines the pseudoinverse of \mathbf{H} . SVD like Cholesky Decomposition also increases numerical accuracy because the condition number of \mathbf{H} is not squared compared to Eq. 3.2. Now using the pseudoinverse of \mathbf{H} we have,

$$\hat{\mathbf{x}} = \mathbf{V} \mathbf{\Sigma}^+ \mathbf{U}^T \mathbf{y}, \quad (3.8)$$

which operates on \mathbf{H} directly. Solving the least-square problem using SVD arguably provides the most numerically stable solution, but is computationally intensive to compute.

3.1.3 Consider Batch Processor

The consider Batch filter is a filtering technique for including the uncertainty of unestimated parameters to improve the covariance realism. There are several reasons as to why certain parameters are simply considered over being estimated. The first reason is to reduce the computational cost and time of the filter by not estimating low impact parameters, but often times it is still a good idea to include their uncertainty. The second reason is that some parameters may not be completely observable, in that case estimating these parameters is not an option and considering them instead is the next best alternative. The state, just like in the conventional Batch processor, is \mathbf{X} , but the new consider parameters are called \mathbf{C} . The first order partials with respect to the states and consider parameters are then defined as $\mathbf{A}(t)$ and $\mathbf{B}(t)$:

$$\mathbf{A}(t) = \left[\frac{\partial F(t)}{\partial \mathbf{X}(t)} \right] \Bigg|_{\mathbf{X}_{ref}} \quad (3.9)$$

$$\mathbf{B}(t) = \left[\frac{\partial F(t)}{\partial \mathbf{C}} \right] \Bigg|_{\mathbf{C}_{ref}} \quad (3.10)$$

The STM due to the estimated states is the same as with the conventional Batch filter shown in Eq. 1.7 and is initialized using the identity matrix.

$$\dot{\Phi}(t, t_k) = \mathbf{A}(t)\Phi(t, t_k) \quad \rightarrow \quad \Phi(t, t_k) = \mathcal{I} \quad (3.11)$$

Due to the consider parameters, there is an additional STM, initialized with a zero matrix.

$$\dot{\theta}(t, t_k) = \mathbf{A}(t)\theta(t, t_k) + \mathbf{B}(t) \quad \rightarrow \quad \theta(t, t_k) = \mathbf{0} \quad (3.12)$$

We can combine the estimated states and consider parameters into one deviation vector \mathbf{z} such that $\mathbf{z} = [\mathbf{x} \ \mathbf{c}]^\top$ so that the time evolution can be expressed as,

$$\mathbf{z}(t) = \psi(t, t_k)\mathbf{z}(t_k) \quad (3.13)$$

where,

$$\psi(t, t_k) = \begin{bmatrix} \Phi(t, t_k) & \theta(t, t_k) \\ \mathbf{0} & \mathcal{I} \end{bmatrix}. \quad (3.14)$$

Next, we compute $\tilde{\mathbf{H}}_{x_k}$ with respect to the estimated states shown in Eq. 3.15,

$$\tilde{\mathbf{H}}_{x_k} = \left[\frac{\partial G(\mathbf{X}_k, t_k)}{\partial \mathbf{X}} \right] \bigg|_{\mathbf{X}_{ref}}. \quad (3.15)$$

The measurement mapping matrix $\tilde{\mathbf{H}}_{c_k}$, are the partials with respect to the consider parameters,

$$\tilde{\mathbf{H}}_{c_k} = \left[\frac{\partial G(\mathbf{X}_k, t_k)}{\partial \mathbf{C}} \right] \bigg|_{\mathbf{C}_{ref}}. \quad (3.16)$$

Given the STMs we can compute the measurement mapping matrix mapped back to epoch, where

$\mathbf{H}_{x_k} = \tilde{\mathbf{H}}_{x_k} \Phi(t, t_k)$ and $\mathbf{H}_{c_k} = \tilde{\mathbf{H}}_{x_k} \theta(t, t_k) + \tilde{\mathbf{H}}_{c_k}$. These mapping matrices are then used to compute the three different information matrices,

$$\mathbf{\Lambda}_{xx} = \sum_{k=1}^l \mathbf{H}_{x_k}^\top \mathbf{W}_k \mathbf{H}_{x_k} + \bar{\mathbf{\Lambda}}_{xx}, \quad (3.17)$$

$$\mathbf{\Lambda}_{xc} = \sum_{k=1}^l \mathbf{H}_{x_k}^\top \mathbf{W}_k \mathbf{H}_{c_k} + \bar{\mathbf{\Lambda}}_{xc}, \quad (3.18)$$

$$\mathbf{\Lambda}_{cc} = \sum_{k=1}^l \mathbf{H}_{c_k}^\top \mathbf{W}_k \mathbf{H}_{c_k} + \bar{\mathbf{\Lambda}}_{cc}. \quad (3.19)$$

After all observations are processed, the covariance, not including the consider uncertainty can be found as $\mathbf{P}_x = \mathbf{\Lambda}_{xx}^{-1}$. However, we are interested in including the consider uncertainty, therefore we compute the sensitivity matrix $\mathbf{S}_{xc} = -\mathbf{P}_x \mathbf{\Lambda}_{xc}$ which after substituting in Eq. 3.18 becomes,

$$\mathbf{S}_{xc} = -\mathbf{P}_x \mathbf{H}_x^\top \mathbf{W} \mathbf{H}_c. \quad (3.20)$$

Using the sensitivity matrix we can map the a-priori consider covariance $\bar{\mathbf{P}}_{cc}$, into the estimation space and add it to the original covariance \mathbf{P}_x to yield the new covariance \mathbf{P}_{xx} ,

$$\mathbf{P}_{xx} = \mathbf{P}_x + \mathbf{S}_{xc}\bar{\mathbf{P}}_{cc}\mathbf{S}_{xc}^\top. \quad (3.21)$$

3.2 Kalman Filter

The Kalman filter is a sequential filter, which unlike the batch processor computes the best state deviation estimate $\hat{\mathbf{x}}$ after each observation rather than all at once after all the observations have been processed. The batch processor and the Kalman filter are mathematically equivalent however and should produce the same solution. The inversion required for the Kalman filter is of a much smaller matrix compared to that of the batch processor, which could be beneficial if there are some numerical issues but could result in some minor solution differences between the two filters when put in practice. A sequential filter is ideal for real-time estimation since the new observations are immediately processed to obtain a new estimate.

Most of the equations originally introduced in chapter 1.2 are still relevant to the Kalman filter, but with a sequential filter the $\hat{\mathbf{x}}$ update is found in a different manner and the state deviations are also not mapped back to a specific epoch. The Kalman filter has two updates, first, a time update and second, a measurement update. The time update takes the last best state deviation estimate and maps it to the time of the subsequent measurement using the STM,

$$\bar{\mathbf{x}}_k = \Phi(t_k, t_{k-1})\hat{\mathbf{x}}_{k-1}. \quad (3.22)$$

The same process is used to update the covariance,

$$\bar{\mathbf{P}}_k = \Phi(t_k, t_{k-1})\mathbf{P}_{k-1}\Phi^\top(t_k, t_{k-1}). \quad (3.23)$$

Then similarly to the batch processor \mathbf{y}_k and $\tilde{\mathbf{H}}_k$ are computed, but unlike the batch processor, the computation of \mathbf{H} is unnecessary because the measurement is immediately processed rather than

accumulated. To fuse in the new information of a measurement the Kalman gain is required which is computed as follows,

$$\mathbf{K}_k = \bar{\mathbf{P}}_k \tilde{\mathbf{H}}_k^\top \left(\tilde{\mathbf{H}}_k \bar{\mathbf{P}}_k \tilde{\mathbf{H}}_k^\top + \mathbf{R}_k \right)^{-1} \quad (3.24)$$

To compute the best state deviation estimate we use the Kalman gain from Eq. 3.24 and the time updated previous best state deviation estimate from Eq. 3.22,

$$\hat{\mathbf{x}}_k = \bar{\mathbf{x}}_k + \mathbf{K}_k \left(\mathbf{y} - \tilde{\mathbf{H}}_k \bar{\mathbf{x}}_k \right). \quad (3.25)$$

Finally the covariance matrix is also updated,

$$\mathbf{P}_k = \left(\mathcal{I} - \mathbf{K}_k \tilde{\mathbf{H}}_k \right) \bar{\mathbf{P}}_k. \quad (3.26)$$

Occasionally there are problems with the covariance update, where it may become unsymmetric and/or lose its positive definiteness. The Joseph formulation may be implemented to maintain the symmetry of the covariance, but it will not mitigate a loss in positive definiteness. The Kalman filter is summarized in Figure 3.2.

3.2.1 Process Noise

Process noise is introduced in the KF to prevent saturation which could lead to filter divergence. The process noise used for the work in this dissertation is in the form of state noise compensation (SNC). The state dynamics of a linear system with process noise can be written as,

$$\dot{\mathbf{x}}(t) = \mathbf{A}(t)\mathbf{x}(t) + \mathbf{B}(t)\mathbf{u}(t) \quad (3.27)$$

Where $\mathbf{u}(t)$ is the state or process noise and is assumed to be a white noise process with,

$$E[\mathbf{u}(t)] = 0 \quad (3.28)$$

$$E[\mathbf{u}(t)\mathbf{u}^\top(\tau)] = \mathbf{Q}(t)\delta(t - \tau). \quad (3.29)$$

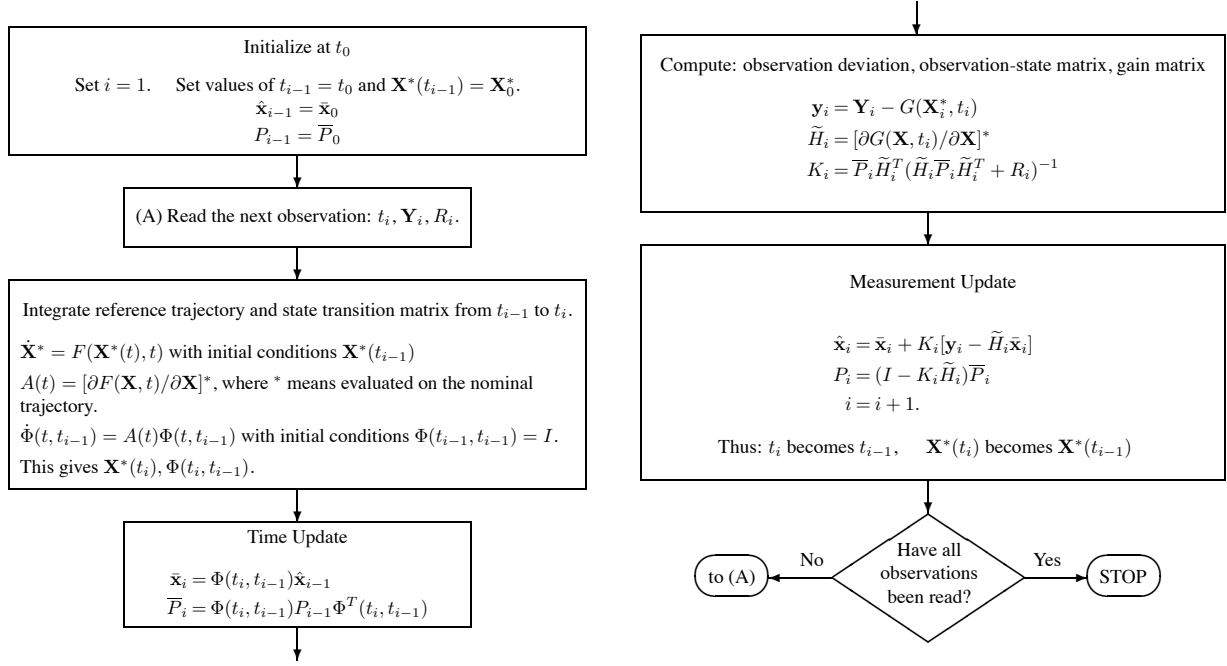


Figure 3.2: Sequential processor computational algorithm (adapted from [83])

Where $\mathbf{Q}(t)$ is the process noise covariance matrix and $\delta(t - \tau)$ is the dirac delta which ensures no correlation in time. We also assume $\mathbf{u}(t)$ is a zero-mean gaussian:

$$\mathbf{u}(t) \sim N(\mathbf{0}, \mathbf{Q}(t)). \quad (3.30)$$

The zero-mean noise process does not change the mapping of the mean state and the equation remains the same as Eq. 3.22. The process noise is added to the covariance during the time update as follows,

$$\bar{\mathbf{P}}_k = \Phi(t_k, t_{k-1})\mathbf{P}_{k-1}\Phi^\top(t_k, t_{k-1}) + \mathbf{\Gamma}(t_k, t_{k-1})\mathbf{Q}_k\mathbf{\Gamma}^\top(t_k, t_{k-1}) \quad (3.31)$$

Where, $\mathbf{\Gamma}(t_k, t_{k-1})$ is,

$$\mathbf{\Gamma}(t_k, t_{k-1}) = \int_{t_k}^{t_{k+1}} \Phi(t_{k+1}, \tau)\mathbf{B}(\tau)d\tau. \quad (3.32)$$

The process noise covariance matrix is defined in the satellite body frame so that the accelerations act in the radial, in-track and cross-track directions. Of course SNC is only one type of process noise, but there is also dynamic model compensation (DMC) which is a Gauss-Markov process (GMP). A Gauss-Markov process is one that obeys a Gaussian probability law and displays the Markov property. The Markov property describes a random (stochastic) process where knowledge of the future is only dependent on the present. In other words the probability density function (PDF) at t_n given its past history at t_{n-1}, t_{n-2}, \dots is equal to the PDF at t_n given its value at t_{n-1} . A Gauss-Markov process obeys a differential equation of the form,

$$\dot{\boldsymbol{\eta}}(t) = -\beta\boldsymbol{\eta}(t) + \mathbf{u}(t) \quad (3.33)$$

where $\mathbf{u}(t)$ is white Gaussian noise and previously defined in Eqs. 3.28 and 3.29 and the inverse of the time constant or correlation time is,

$$\beta = \frac{1}{\tau}. \quad (3.34)$$

DMC is effectively added to the filter as follows, such that the estimated state vector is defined as,

$$\mathbf{X} = \begin{bmatrix} \mathbf{r}^\top & \dot{\mathbf{r}}^\top & \boldsymbol{\eta}^\top \end{bmatrix}^\top. \quad (3.35)$$

Where, \mathbf{r} is the position vector, $\dot{\mathbf{r}}$ is the velocity vector and $\boldsymbol{\eta}$ is a stochastic acceleration term. The dynamic model is then described as follows,

$$\dot{\mathbf{X}} = F(\mathbf{X}, t) = \begin{bmatrix} \dot{\mathbf{r}} \\ \mathbf{a} + \boldsymbol{\eta} \\ \dot{\boldsymbol{\eta}} \end{bmatrix} = \begin{bmatrix} \dot{\mathbf{r}} \\ -\frac{\mu}{r^3}\mathbf{r} + \mathbf{a}_p + \boldsymbol{\eta} \\ -\beta\boldsymbol{\eta} \end{bmatrix} + \begin{bmatrix} \mathbf{0} \\ \mathbf{0} \\ \mathbf{u}(t) \end{bmatrix}. \quad (3.36)$$

Where, $\dot{\mathbf{r}}$ is the velocity, \mathbf{a} is the acceleration, $\boldsymbol{\eta}$ is the stochastic acceleration which is being estimated as the data is being processed. Then $\dot{\boldsymbol{\eta}}$ is the dynamics of the stochastic acceleration which is defined by the original ODE in equation 3.33. Then filling out the equation with a two-body force model we have the gravity acceleration and the perturbing accelerations \mathbf{a}_p . Note that

$-\beta\boldsymbol{\eta}$ is the deterministic portion of the ODE, and $\mathbf{u}(t)$ is the stochastic portion. Because there is still a random portion being added $\mathbf{u}(t)$ we still have the process noise covariance matrix \mathbf{Q} , being added to the time update equation. The \mathbf{Q} developed through DMC is also more mathematically rigorous compared to the \mathbf{Q} developed from SNC.

3.2.2 Smoothing

Smoothing algorithms, when no process noise is used, in a sequential filter produces the same results as a batch processor, using all available information to estimate the solution at one epoch. In a batch processor adding process noise is challenging and not usually done, but by smoothing a Kalman filter with process noise, the solution is the same as if it had been filtered using a batch processor with process noise. When using a sequential filter, the measurements are processed in a forward manner while the smoother goes backward from the most recent measurement back to the first measurement. We use the following notation, where $\hat{\mathbf{x}}_k^l$ is the best estimate at time t_k using observations up to time t_l . The state update using the smoothing algorithm then yields,

$$\hat{\mathbf{x}}_k^l = \hat{\mathbf{x}}_k^k + S_k \left(\hat{\mathbf{x}}_{k+1}^l - \Phi(t_{k+1}, t_k) \hat{\mathbf{x}}_k^k \right) \quad (3.37)$$

where,

$$\begin{aligned} S_k &= \mathbf{P}_k^k \Phi^\top(t_{k+1}, t_k) \left[\Phi(t_{k+1}, t_k) \mathbf{P}_k^k \Phi^\top(t_{k+1}, t_k) + \mathbf{\Gamma}(t_{k+1}, t_k) \mathbf{Q}_k \mathbf{\Gamma}^\top(t_{k+1}, t_k) \right]^{-1} \\ &= \mathbf{P}_k^k \Phi^\top(t_{k+1}, t_k) \left(\mathbf{P}_{k+1}^k \right)^{-1} \end{aligned} \quad (3.38)$$

The covariance is smoothed using,

$$\mathbf{P}_k^l = \mathbf{P}_k^k + S_k \left(\mathbf{P}_{k+1}^l - \mathbf{P}_{k+1}^k \right) S_k^\top. \quad (3.39)$$

When no process noise is present the smoother simply maps the solution back from time t_k to the epoch using the STM.

3.2.3 Extended Kalman Filter (EKF)

The conventional KF is a linearized filter about an arbitrary reference trajectory for the complete duration of the filter span. When significant non-linearities are present however, as may occur around a small body due to the large gravitational asymmetries, a linearized filter may fail. Consequently, the extended version of the Kalman filter known as the EKF can be used which handles these non-linearities more effectively because it is a non-linear filter. After each observation the reference trajectory is updated to reflect the new best estimate of the state. Therefore the a-priori state deviation $\bar{\mathbf{x}}$ will always be zero, and the state deviation update simplifies to,

$$\hat{\mathbf{x}}_k = \mathbf{K}_k \mathbf{y}_k. \quad (3.40)$$

Note that updating the reference trajectory from the start when the filter covariance has not yet had the chance to collapse could result in erroneous filter solutions. Therefore a conventional KF is usually implemented first, then after the solution has more or less stabilized the EKF can take over.

3.3 Square-Root Information Filter (SRIF)

Similar to the Cholesky decomposition of chapter 3.1.1 we define the the information matrix in terms of its square root, such that $\mathbf{\Lambda} = \mathbf{R}^\top \mathbf{R}$. The least-squares estimate is computed recursively where first the observations are pre-whitened and a time update is incurred. Then the measurement update is computed at each time k using an orthogonal transformation T to merge in new data,

$$T \begin{bmatrix} \bar{\mathbf{R}}_k & \bar{\mathbf{b}}_k \\ \tilde{\mathbf{H}}_k & \mathbf{y}_k \end{bmatrix} = \begin{bmatrix} \mathbf{R}_k & \mathbf{b}_k \\ \mathbf{0} & \mathbf{e} \end{bmatrix}. \quad (3.41)$$

The transformation used here are Householder's reflections for their efficiency. Then we solve for the best estimate, $\hat{\mathbf{x}}$ in Eq. 3.42.

$$\mathbf{R}\hat{\mathbf{x}} = \mathbf{b} \quad (3.42)$$

Since \mathbf{R} is upper triangular, $\hat{\mathbf{x}}$ can be found using backward substitution rather than inversion which may otherwise cause numerical issues. The covariance at any step is then computed as $\mathbf{P}_k = \mathbf{R}_k^{-1} \mathbf{R}_k^{-\top}$. After performing a time update on \mathbf{R}_k and \mathbf{b}_k , they become $\bar{\mathbf{R}}$ and $\bar{\mathbf{b}}$ for the following measurement update at $k + 1$. These steps are repeated from $k = 1$ to the number of measurements l . Finally the state and covariance are smoothed back to the epoch. For an in-depth look at the SRIF and its computational algorithm consult Ref. [83].

3.3.1 Process Noise

The basic SRIF algorithm as shown in chapter 3.3 does not include process noise which means that the filter can saturate when too many high precision measurements are processed. To mitigate this issue we need to modify the time update to include SNC,

$$T \begin{bmatrix} \mathbf{R}_u & \mathbf{0} & \bar{\mathbf{b}}_{u_{k-1}} \\ -\tilde{\mathbf{R}}_k \Gamma(t_k, t_{k-1}) & \tilde{\mathbf{R}}_k & \hat{\mathbf{b}}_{k-1} \end{bmatrix} = \begin{bmatrix} \bar{\mathbf{R}}_{u_k} & \bar{\mathbf{R}}_{ux_k} & \tilde{\mathbf{b}}_{u_k} \\ \mathbf{0} & \bar{\mathbf{R}}_k & \bar{\mathbf{b}}_k \end{bmatrix}. \quad (3.43)$$

Where \mathbf{R}_u is the the upper triangular Cholesky decomposition of the the process noise covariance matrix \mathbf{Q} ; and $\bar{\mathbf{b}}_{u_{k-1}} = \mathbf{R}_u \bar{\mathbf{u}}_{k-1}$; and $\tilde{\mathbf{R}}_k = \hat{\mathbf{R}}_{k-1} \Phi^{-1}(t_k, t_{k-1})$; and $\hat{\mathbf{b}}_{k-1} = \hat{\mathbf{R}}_{k-1} \hat{\mathbf{x}}_{k-1}$. Once again the transformation T in the time update also uses a Householder transformation just like the measurement update. The resulting $\bar{\mathbf{R}}_k$ and $\bar{\mathbf{b}}_k$ terms are then used in the same measurement update equation shown in Eq. 3.41. The computational algorithm for the Householder transformation can be found on pp. 316-318 of Ref. [83].

3.4 Unscented Kalman Filter (UKF)

In the field of non-linear state estimation the extended Kalman filter (EKF) has an extensive and proven history. However, while the EKF is a non-linear filter due to its continually updated reference trajectory, the standard Kalman filter linearization is still employed for the dynamics and measurement models. As a result, the EKF is not always reliable for systems which are not very linear on the time scale of the update intervals as large errors in the true posterior mean

and covariance could arise, potentially leading to divergence [43, 88]. To mitigate the linearization assumption and improve reliability for non-linear state estimation a sigma-point filter was proposed by Julier et al. [43] in 1997, the most common of which is the unscented Kalman filter (UKF). The UKF uses the full non-linear dynamics as well as measurement equations, eliminating the need for a state transition matrix or analytical Jacobians. This is achieved by using a deterministic sampling approach of a minimal number of sigma points which are propagated through the non-linear system, after which a weighted mean and covariance are computed. Further development of the UKF came in 2001 when the square-root unscented Kalman filter (SR-UKF) was developed by Van der Merwe et al. [87]. The advantages of the square-root form include numerical stability, and positive definiteness of the covariance over the non square-root implementation, for that reason we only outline the square-root form of the UKF instead of the non square-root form.

3.4.1 Square-Root Unscented Kalman Filter (SR-UKF)

A summary of the SR-UKF is shown in Algorithm 1 and is reproduced from Ref. [87]. We only show a brief overview because the subsequent section covers the SR-USKF in much greater detail.

Algorithm 1 Square-Root Unscented Kalman Filter

Initialize:

$$\hat{\mathbf{x}}_{k-1} = \bar{\mathbf{x}}$$

$$\mathbf{S}_{xx,k-1} = \text{Cholesky}(\bar{\mathbf{P}}_{xx})$$

for $k \in \{1 \dots n\}$:

$$\mathbf{X}_{k-1} = [\hat{\mathbf{x}}_{k-1} \quad \hat{\mathbf{x}}_{k-1} + \gamma \mathbf{S}_{xx,k-1} \quad \hat{\mathbf{x}}_{k-1} - \gamma \mathbf{S}_{xx,k-1}]$$

Time Update

$$\mathbf{X}_k \leftarrow \dot{\mathbf{X}}_k = \mathbf{F}(\mathbf{X}_{k-1}, t)$$

$$\hat{\mathbf{x}}_k^- = \sum_{i=0}^{2n} W_i^{(m)} X_{i,k}$$

$$\mathbf{S}_{xx,k}^- = qr \left\{ \left[\sqrt{W_{1:2n}^{(c)}} (\mathbf{X}_{1:2n,k} - \hat{\mathbf{x}}_k^-) \quad \sqrt{\mathbf{Q}_k} \right]^\top \right\}$$

$$\mathbf{S}_{xx,k}^- = cholupdate \left\{ \mathbf{S}_{xx,k}^-, \sqrt{|W_0^{(c)}|} (X_{0,k} - \hat{\mathbf{x}}_k^-), \text{sgn}(W_0^{(c)}) \right\}$$

Measurement Update (subscript k not included since all at time t_k)

$$\mathbf{Y} = \mathbf{G}(\mathbf{X}, t)$$

$$\hat{\mathbf{y}} = \sum_{i=0}^{2n} W_i^{(m)} Y_i$$

$$\mathbf{S}_{yy} = qr \left\{ \left[\sqrt{W_{1:2n}^{(c)}} (\mathbf{Y}_{1:2n} - \hat{\mathbf{y}}) \quad \sqrt{\mathbf{R}} \right]^\top \right\}$$

$$\mathbf{S}_{yy} = cholupdate \left\{ \mathbf{S}_{yy}, \sqrt{|W_0^{(c)}|} (Y_0 - \hat{\mathbf{y}}), \text{sgn}(W_0^{(c)}) \right\}$$

$$\mathbf{P}_{xy} = \sum_{i=0}^{2n} W_i^{(c)} (X_i - \hat{\mathbf{x}}^-) (Y_i - \hat{\mathbf{y}})^\top$$

$$\mathbf{K} = \mathbf{P}_{xy} (\mathbf{S}_{yy} \mathbf{S}_{yy}^\top)^{-1}$$

$$\hat{\mathbf{x}} = \hat{\mathbf{x}}^- + \mathbf{K}(\mathbf{y} - \hat{\mathbf{y}})$$

$$\mathbf{U} = \mathbf{K} \mathbf{S}_{yy}$$

$$\mathbf{S}_{xx} = cholupdate \left\{ \mathbf{S}_{xx}^-, \mathbf{U}, - \right\}$$

3.4.2 Square-Root Unscented Schmidt-Kalman Filter (SR-USKF)

Often times there are additional parameters or states in the problem which are not estimated in the filter either due to computational restrictions or observability limitations. If there is a-priori uncertainty knowledge on these parameters, they can be included in the filter as consider parameters in what is known as a Schmidt-Kalman (or consider) filter. The inclusion of consider parameters in the estimation error covariance matrix maintains covariance realism, by preventing an overly optimistic covariance from developing. It is important to note, however, that considering rather than estimating these additional parameters makes the Schmidt-Kalman filter suboptimal, but considering the states is significantly better than neglecting them all together. Considering the states may be the only viable and realistic alternative to estimating them as that is not always possible.

We follow the development of Ref. [77] by setting up the consider parameters \mathbf{c} in augmented form to the estimated parameters \mathbf{x} . The number of estimated states is n_x and the number of considered parameters is n_c for a total of n_z states in \mathbf{z} .

$$\mathbf{z} = \begin{bmatrix} \mathbf{x} \\ \mathbf{c} \end{bmatrix} \quad (3.44)$$

Likewise for the covariance, the consider covariance matrix is augmented with the state covariance with cross correlation covariances on the upper right and lower left of \mathbf{P}_{zz} . In many scenarios \mathbf{P}_{xc} and \mathbf{P}_{cx} are zeros when the filter is initialized. These cross-correlations later get populated and inflates \mathbf{P}_{xx} according to the amount of uncertainty on the consider parameters defined through \mathbf{P}_{cc} .

$$\mathbf{P}_{zz} = \begin{bmatrix} \mathbf{P}_{xx} & \mathbf{P}_{xc} \\ \mathbf{P}_{cx} & \mathbf{P}_{cc} \end{bmatrix} \quad (3.45)$$

We take the Cholesky factorization of \mathbf{P}_{zz} to obtain the square root of \mathbf{P}_{zz} in lower triangular matrix form such that $\mathbf{P}_{zz} = \mathbf{S}_{zz}\mathbf{S}_{zz}^\top$. Then as per the standard UKF we define a number of

variables pertaining to the weights of each of the sigma points. Several approaches exist, one of the simplest is weighting each of the sigma points for both the mean and covariance equally with a sum of unity as was adopted by Ref. [77]. Another approach is to use a scaling method that minimizes higher order effects such as skew and kurtosis, in this case the mean still sums up to unity, but the covariance does not necessarily [42]. The latter approach with scaled weightings is used in the development of the SRUSKF and are shown below, similar to the weights used in Refs. [87] and [42],

$$W_0^{(m)} = \frac{\lambda}{n_z + \lambda}, \quad (3.46)$$

$$W_0^{(c)} = \frac{\lambda}{n_z + \lambda} + (1 - \alpha^2 + \beta), \quad (3.47)$$

$$W_i^{(m)} = W_i^{(c)} = \frac{1}{2(n_z + \lambda)}. \quad (3.48)$$

Where superscripts m and c stand for the mean and covariance of the i^{th} sigma point. The zeroth sigma point, corresponding to the apriori mean and covariance or central point has different weights from the others as indicated by Eqs. 3.46 and 3.47. It is also possible for $W_0^{(c)}$ to be negative depending on the number of states and values of the tuning parameters which are discussed next. We define $\lambda = \alpha^2(n_z + \kappa) - n_z$, where α is a tuning parameter for the amount of spread of the sigma points from the mean, generally bounded between 10^{-4} on the low end, and 1 on the high end. Then $\kappa = 3 - n_z$ and β is used to incorporate prior information on the probability density function (PDF) of the states, if Gaussian distributions are assumed then $\beta = 2$ [87]. Finally we have $\gamma = \sqrt{n_z + \lambda}$. We compute the $2n_z + 1$ sets of sigma points where each set of n_z sigma points is contained in a column vector, $Z_{i,k-1}$ of Eq. 3.49.

$$\mathbf{Z}_{k-1} = \begin{bmatrix} \hat{\mathbf{z}}_{k-1} & \hat{\mathbf{z}}_{k-1} + \gamma \mathbf{S}_{zz,k-1} & \hat{\mathbf{z}}_{k-1} - \gamma \mathbf{S}_{zz,k-1} \end{bmatrix} \quad (3.49)$$

In the time update each set of sigma points is numerically integrated from t_{k-1} to t_k using the full non-linear dynamics \mathbf{F} .

$$\mathbf{Z}_k \leftarrow \dot{\mathbf{Z}}_k = \mathbf{F}(\mathbf{Z}_{k-1}, t) \quad (3.50)$$

We then compute the mean and covariance of the $2n_z + 1$ sets of sigma points produced from Eq. 3.50. The mean computation in square-root form is the same as for the USKF,

$$\hat{\mathbf{z}}_k^- = \sum_{i=0}^{2n_z} W_i^{(m)} Z_{i,k}. \quad (3.51)$$

The covariance calculation is not the same however, and is computed using a QR decomposition shown in Eq. 3.52 and a Cholesky factor update (downdate) of rank 1 shown in Eq. 3.54 .

$$\mathbf{S}_{zz,k}^- = qr \left\{ \left[\begin{array}{c} \sqrt{W_{1:2n_z}^{(c)}} (\mathbf{Z}_{1:2n_z,k} - \hat{\mathbf{z}}_k^-) \\ \sqrt{\mathbf{Q}_k} \end{array} \right]^\top \right\} \quad (3.52)$$

The QR decomposition is performed on the concatenated matrix of $\sqrt{W_{1:2n_z}^{(c)}} (\mathbf{Z}_{1:2n_z,k} - \hat{\mathbf{z}}_k^-)$ and the square root of the process noise \mathbf{Q}_k . The term, $\sqrt{W_{1:2n_z}^{(c)}} (\mathbf{Z}_{1:2n_z,k} - \hat{\mathbf{z}}_k^-)$ is in itself also a concatenated matrix, therefore the $qr\{\cdot\}$ operation is performed on a $n_z \times 3n_z$ matrix as illustrated in Eq. 3.53,

$$n_z \left\{ \underbrace{\left[\sqrt{W_1^{(c)}} (Z_{1,k} - \hat{z}_k^-) \right]}_1 \underbrace{\left[\sqrt{W_2^{(c)}} (Z_{2,k} - \hat{z}_k^-) \right]}_1 \cdots \underbrace{\left[\sqrt{W_{2n_z}^{(c)}} (Z_{2n_z,k} - \hat{z}_k^-) \right]}_1 \underbrace{\left[\sqrt{\mathbf{Q}_k} \right]}_{n_z}. \quad (3.53)$$

Note that the zeroth sigma point is not included in the QR decomposition since uniquely among the weights it may be negative. To add the zeroth sigma point we must perform a Cholesky update (downdate). In order for the SRUSKF to remain consistent with the USKF we deviate slightly from the implementation of the Cholesky update (downdate) used by Ref. [87] in the SRUKF algorithm. While Van Der Merwe et al. take the square root of the 1st to the n_z^{th} weight in the $qr\{\cdot\}$ operation, they do not take the square root of the zeroth weight as it may be negative. Consequently in Van Der Merwe et al.'s formulation, it is as if the W_0^c weight would be squared in the USKF, while

keeping all other weights the same. While this is simply a different approach, we aim to keep consistent with the USKF so as to make a comparison of the two filter solutions more congruent. Therefore the square-root of the absolute value of the zeroth weight is used as the multiplicative factor so that the expression to be added or subtracted to $\mathbf{S}_{zz,k}^-$ in the Cholesky update (downdate) is $\sqrt{|W_0^{(c)}|} (Z_{0,k} - \hat{\mathbf{z}}_k^-)$. Then the sign of the zeroth weight dictates whether a Cholesky update ($W_0^{(c)} > 0$) or a Cholesky downdate ($W_0^{(c)} < 0$) is performed, similar to Van Der Merwe et al.'s original approach.

$$\mathbf{S}_{zz,k}^- = cholupdate \left\{ \mathbf{S}_{zz,k}^-, \sqrt{|W_0^{(c)}|} (Z_{0,k} - \hat{\mathbf{z}}_k^-), sgn(W_0^{(c)}) \right\} \quad (3.54)$$

The SRUSKF, like the SRUKF, with a QR decomposition and a Cholesky factor update (downdate) also implements a two-step approach to compute the covariance unlike the USKF. A brief aside on the workings of the *cholupdate* algorithm for completeness. Suppose that \mathbf{P} has a Cholesky factorization of $\mathbf{S}\mathbf{S}^\top$, then $cholupdate\{\mathbf{S}, \sqrt{\nu}\mathbf{x}, \pm\}$ is equivalent to finding the square root of $\mathbf{P} \pm \nu\mathbf{x}\mathbf{x}^\top$. For additional details on the Cholesky update (downdate) of rank one consult Ref. [29] and chapter 4, section 3 of Ref. [81]. This completes the time update portion of the SRUSKF and we now move on to the measurement update.

In the measurement update all equations refer to time t_k and hence the subscript k is dropped for conciseness. Each of the sigma points in \mathbf{Z}_k , computed in the time update, are run through the non-linear measurement model \mathbf{G} to obtain the computed measurements \mathbf{Y} ,

$$\mathbf{Y} = \mathbf{G}(\mathbf{Z}, t). \quad (3.55)$$

Next we compute the mean of the measurements associated with each sigma point set. This is also the same as the USKF.

$$\hat{\mathbf{y}} = \sum_{i=0}^{2n_z} W_i^{(m)} Y_i \quad (3.56)$$

The innovation covariance, however, requires the two-step process again with the square-root of

Algorithm 2 Square-Root Unscented Schmidt-Kalman Filter

Initialize:

$$\hat{\mathbf{z}}_{k-1} = \bar{\mathbf{z}}$$

$$\mathbf{S}_{zz,k-1} = \text{Cholesky}(\bar{\mathbf{P}}_{zz})$$

for $k \in \{1 \dots n\}$:

$$\mathbf{Z}_{k-1} = [\hat{\mathbf{z}}_{k-1} \quad \hat{\mathbf{z}}_{k-1} + \gamma \mathbf{S}_{zz,k-1} \quad \hat{\mathbf{z}}_{k-1} - \gamma \mathbf{S}_{zz,k-1}]$$

Time Update

$$\mathbf{Z}_k \leftarrow \dot{\mathbf{Z}}_k = \mathbf{F}(\mathbf{Z}_{k-1}, t)$$

$$\hat{\mathbf{z}}_k^- = \sum_{i=0}^{2n_z} W_i^{(m)} Z_{i,k}$$

$$\mathbf{S}_{zz,k}^- = qr \left\{ \left[\sqrt{W_{1:2n_z}^{(c)}} (\mathbf{Z}_{1:2n_z,k} - \hat{\mathbf{z}}_k^-) \quad \sqrt{\mathbf{Q}_k} \right]^\top \right\}$$

$$\mathbf{S}_{zz,k}^- = \text{cholupdate} \left\{ \mathbf{S}_{zz,k}^-, \sqrt{|W_0^{(c)}|} (Z_{0,k} - \hat{\mathbf{z}}_k^-), \text{sgn}(W_0^{(c)}) \right\}$$

Measurement Update (subscript k not included since all at time t_k)

$$\mathbf{Y} = \mathbf{G}(\mathbf{Z}, t)$$

$$\hat{\mathbf{y}} = \sum_{i=0}^{2n_z} W_i^{(m)} Y_i$$

$$\mathbf{S}_{yy} = qr \left\{ \left[\sqrt{W_{1:2n_z}^{(c)}} (\mathbf{Y}_{1:2n_z} - \hat{\mathbf{y}}) \quad \sqrt{\mathbf{R}} \right]^\top \right\}$$

$$\mathbf{S}_{yy} = \text{cholupdate} \left\{ \mathbf{S}_{yy}, \sqrt{|W_0^{(c)}|} (Y_0 - \hat{\mathbf{y}}), \text{sgn}(W_0^{(c)}) \right\}$$

$$\mathbf{P}_{zy} = \sum_{i=0}^{2n_z} W_i^{(c)} (Z_i - \hat{\mathbf{z}}^-) (Y_i - \hat{\mathbf{y}})^\top$$

$$\mathbf{K}_z = \mathbf{P}_{zy} (\mathbf{S}_{yy} \mathbf{S}_{yy}^\top)^{-1} = \begin{bmatrix} \mathbf{K}_x \\ \mathbf{K}_c \end{bmatrix}$$

$$\hat{\mathbf{z}} = \hat{\mathbf{z}}^- + \begin{bmatrix} \mathbf{K}_x \\ \mathbf{0} \end{bmatrix} (\mathbf{y} - \hat{\mathbf{y}})$$

$$\mathbf{U}_1 = \mathbf{K}_z \mathbf{S}_{yy}$$

$$\mathbf{S}_{zz} = \text{cholupdate} \{ \mathbf{S}_{zz}^-, \mathbf{U}_1, - \}$$

$$\mathbf{U}_2 = \begin{bmatrix} \mathbf{0} \\ \mathbf{K}_c \end{bmatrix} \mathbf{S}_{yy}$$

$$\mathbf{S}_{zz} = \text{cholupdate} \{ \mathbf{S}_{zz}, \mathbf{U}_2, + \}$$

the measurement covariance matrix, \mathbf{R} appended at the end. The notation used in Eq. 3.57 and 3.58 is respectively identical to that of Eq. 3.52 and 3.54.

$$\mathbf{S}_{yy} = qr \left\{ \left[\sqrt{W_{1:2n_z}^{(c)}} (\mathbf{Y}_{1:2n_z} - \hat{\mathbf{y}}) \quad \sqrt{\mathbf{R}} \right]^\top \right\} \quad (3.57)$$

$$\mathbf{S}_{yy} = cholupdate \left\{ \mathbf{S}_{yy}, \sqrt{|W_0^{(c)}|} (Y_0 - \hat{y}), \text{sgn}(W_0^{(c)}) \right\} \quad (3.58)$$

The computation of the cross correlation covariance \mathbf{P}_{zy} is also the same as with the USKF.

$$\mathbf{P}_{zy} = \sum_{i=0}^{2n_z} W_i^{(c)} (Z_i - \hat{\mathbf{z}}^-) (Y_i - \hat{\mathbf{y}})^\top \quad (3.59)$$

Using Eqs. 3.57, 3.58 and 3.59 we can compute the augmented Kalman gain \mathbf{K}_z as follows,

$$\mathbf{K}_z = \mathbf{P}_{zy} \left(\mathbf{S}_{yy} \mathbf{S}_{yy}^\top \right)^{-1} = \begin{bmatrix} \mathbf{K}_x \\ \mathbf{K}_c \end{bmatrix}. \quad (3.60)$$

Note that we solve for \mathbf{K}_z in two steps. First we solve for $[\mathbf{S}_{yy}^\top \mathbf{K}_z^\top]$ in $\mathbf{S}_{yy} [\mathbf{S}_{yy}^\top \mathbf{K}_z^\top] = \mathbf{P}_{zy}^\top$. Since \mathbf{S}_{yy} is lower triangular, forward substitutions can be used rather than an inverse since it follows the $\mathbf{L}\mathbf{x} = \mathbf{N}$ format, where \mathbf{L} is a lower triangular matrix. Second we solve for \mathbf{K}_z^\top in $\mathbf{S}_{yy}^\top \mathbf{K}_z^\top = \mathbf{S}_{yy}^{-1} \mathbf{P}_{zy}^\top$ using backward substitutions since \mathbf{S}_{yy}^\top is an upper triangular matrix and follows the $\mathbf{U}\mathbf{x} = \mathbf{N}$ format, where \mathbf{U} is an upper triangular matrix. Finally the augmented gain matrix \mathbf{K}_z can be broken up in its respective state and consider gain matrices \mathbf{K}_x and \mathbf{K}_c .

If the consider parameters were estimated rather than considered (as it would be using a non-consider filter such as the SRUKF), the full augmented gain matrix would be used to update the complete augmented state \mathbf{z} ,

$$\hat{\mathbf{z}} = \hat{\mathbf{z}}^- + \mathbf{K}_z (\mathbf{y} - \hat{\mathbf{y}}). \quad (3.61)$$

However in the consider filter we do not update the consider parameters as that would be similar to estimating them, therefore we set $\mathbf{K}_c = 0$ such that,

$$\hat{\mathbf{z}} = \hat{\mathbf{z}}^- + \begin{bmatrix} \mathbf{K}_x \\ \mathbf{0} \end{bmatrix} (\mathbf{y} - \hat{\mathbf{y}}). \quad (3.62)$$

Likewise for the covariance (shown here in full rather than in square-root form for clarity) if the consider parameters were estimated we would have,

$$\mathbf{P}_{zz} = \mathbf{P}_{zz}^- - \mathbf{K}_z \mathbf{P}_{yy} \mathbf{K}_z^\top \quad (3.63)$$

$$= \begin{bmatrix} \mathbf{P}_{xx}^- & \mathbf{P}_{xc}^- \\ \mathbf{P}_{cx}^- & \mathbf{P}_{cc}^- \end{bmatrix} - \begin{bmatrix} \mathbf{K}_x \mathbf{P}_{yy} \mathbf{K}_x^\top & \mathbf{K}_x \mathbf{P}_{yy} \mathbf{K}_c^\top \\ \mathbf{K}_c \mathbf{P}_{yy} \mathbf{K}_x^\top & \mathbf{K}_c \mathbf{P}_{yy} \mathbf{K}_c^\top \end{bmatrix}. \quad (3.64)$$

In this Schmidt-Kalman filter however we do not want to update the consider covariance terms. In essence we need,

$$\mathbf{P}_{zz} = \begin{bmatrix} \mathbf{P}_{xx}^- & \mathbf{P}_{xc}^- \\ \mathbf{P}_{cx}^- & \mathbf{P}_{cc}^- \end{bmatrix} - \begin{bmatrix} \mathbf{K}_x \mathbf{P}_{yy} \mathbf{K}_x^\top & \mathbf{K}_x \mathbf{P}_{yy} \mathbf{K}_c^\top \\ \mathbf{K}_c \mathbf{P}_{yy} \mathbf{K}_x^\top & \mathbf{0} \end{bmatrix}. \quad (3.65)$$

It is important to note that the actual non-zero \mathbf{K}_c matrix from Eq. 3.60 is used in the covariance update unlike Eq. 3.62 for the state update. In square root form, updating the covariance without affecting \mathbf{P}_{cc} is achieved by first performing a Cholesky factor downdate and then an update as shown in Eq. 3.66.

$$\begin{bmatrix} \mathbf{K}_x \mathbf{P}_{yy} \mathbf{K}_x^\top & \mathbf{K}_x \mathbf{P}_{yy} \mathbf{K}_c^\top \\ \mathbf{K}_c \mathbf{P}_{yy} \mathbf{K}_x^\top & \mathbf{0} \end{bmatrix} = \begin{bmatrix} \mathbf{K}_x \\ \mathbf{K}_c \end{bmatrix} \mathbf{S}_{yy} \mathbf{S}_{yy}^\top \begin{bmatrix} \mathbf{K}_x \\ \mathbf{K}_c \end{bmatrix}^\top - \begin{bmatrix} \mathbf{0} \\ \mathbf{K}_c \end{bmatrix} \mathbf{S}_{yy} \mathbf{S}_{yy}^\top \begin{bmatrix} \mathbf{0} \\ \mathbf{K}_c \end{bmatrix}^\top \quad (3.66)$$

$$= \mathbf{U}_1 \mathbf{U}_1^\top - \mathbf{U}_2 \mathbf{U}_2^\top \quad (3.67)$$

Therefore,

$$\mathbf{U}_1 = \mathbf{K}_z \mathbf{S}_{yy} \quad (3.68)$$

and,

$$\mathbf{U}_2 = \begin{bmatrix} \mathbf{0} \\ \mathbf{K}_c \end{bmatrix} \mathbf{S}_{yy} \quad (3.69)$$

Then the Cholesky downdate is,

$$\mathbf{S}_{zz} = cholupdate \{ \mathbf{S}_{zz}^-, \mathbf{U}_1, - \}, \quad (3.70)$$

and the Cholesky update to add back in $\mathbf{K}_c \mathbf{P}_{cc} \mathbf{K}_c^\top$ which was originally also downdated in Eq. 3.70 is,

$$\mathbf{S}_{zz} = cholupdate \{ \mathbf{S}_{zz}, \mathbf{U}_2, + \}. \quad (3.71)$$

If \mathbf{U}_j is a matrix rather than a vector, consecutive Cholesky updates or downdates are required, one for each of the columns of \mathbf{U}_j .

Chapter 4

Absolute Dual-Satellite Orbit Determination

In this chapter we discuss the viability and results of doing dual-satellite OD using TDOA and FDOA and also compare these OD results to the more conventional range and range-rate measurements. To determine the viability, the observability of the system is analyzed using a number of different but extensive techniques. Then OD results are shown for various satellite pairings.

4.1 Observability

4.1.1 Definition of Observability

Rudolf Kalman developed the idea of observability in his 1959 paper “On the General Theory of Control Systems” with his original definition paraphrased below [46]:

A costate of a plant is said to be ‘observable’ if its exact value at any state at time 0 can be determined from measurements of the output signal over the finite interval $0 \geq t \geq t_2$. If every costate is observable we say that the plant is “completely observable.”

This concept as Kalman puts forth has corresponding mathematical tests for the observability of a system. First the observability matrix can be constructed for a discrete linear (recall that the problem is linearized) time-variant (LTV) system following Silverman et al’s convention [73]:

$$\mathcal{O} \equiv \mathbf{H} = \begin{bmatrix} \tilde{\mathbf{H}}(t_0) \\ \tilde{\mathbf{H}}(t_1)\Phi(t_1, t_0) \\ \vdots \\ \tilde{\mathbf{H}}(t_k)\Phi(t_k, t_0) \end{bmatrix}. \quad (4.1)$$

Since the observability matrix in Eq. 4.1 is not square, we can transform \mathcal{O} from \mathbf{H} to $\mathbf{H}^\top \mathbf{H}$ which ensures its squareness. This transformation is valid since the null space of \mathbf{H} is the same as the null space of $\mathbf{H}^\top \mathbf{H}$; $\mathcal{N}(\mathbf{H}) = \mathcal{N}(\mathbf{H}^\top \mathbf{H})$ [9]. Eq. 4.2 shows the final observability matrix used for an LTV system such as the orbit determination problem [9, 10, 80]:

$$\mathbf{\Lambda}(t_k, t_0) = \mathbf{H}^\top \mathbf{H} = \sum_{k=0}^l \Phi^\top(t_k, t_0) \tilde{\mathbf{H}}^\top(t_k) \tilde{\mathbf{H}}(t_k) \Phi(t_k, t_0). \quad (4.2)$$

References [28] and [83] then declare that the following statements must be true in order for the system to be observable:

- The Rank of \mathbf{H} must be n .
- \mathbf{H} must have n nonzero eigenvalues.
- The eigenvalues of $\mathbf{\Lambda}$ must be greater than zero.
- The determinant of $\mathbf{\Lambda}$ must be greater than zero.
- $\mathbf{\Lambda}$ must be positive definite; $\mathbf{x}^\top \mathbf{\Lambda} \mathbf{x} > 0, \quad \forall \mathbf{x} \in \mathcal{R}^+$.

While these tests are theoretically relatively easy to check, bear in mind that numerical errors can cause any one of the above listed tests to fail even if the system is theoretically observable. Likewise, numerical errors can cause the listed tests to pass even if the system is theoretically unobservable. Therefore there is a distinction between theoretical and numerical observability of a system. The following sections discuss the derivation of the observability matrix from which a theoretical observability analysis is setup (but not carried out) and a numerical analysis is performed using the observability matrix.

4.1.2 Observability Matrix Formulation

In this section the equations are derived to perform an observability analysis by developing the observability matrix. The approach used here is an extension of Refs. [68] and [56] which only uses 2-body dynamics. Therefore we also use a 2-body dynamics setup, but we also include SRP. If it can be shown that the problem is observable using 2-body dynamics then it will also be observable using the full ephemeris because all the additional perturbations increase the observability of the system. The time derivatives of the gravity gradient have also been broadened to now include up to order five from the previous order two, used in Ref. [68]. The newly added SRP component also has up to fifth order derivatives of the SRP gradient. Finally the measurement mapping matrix, \mathbf{C} , is significantly more involved due to the use of TDOA and FDOA instead of range measurements between the two satellites. In this section, the observability matrix is developed using the dynamics and measurements models, which are subsequently evaluated to determine the numerical observability.

We start by defining our estimated state vector in this orbit determination scenario:

$$\mathbf{X} = \left[\mathbf{r}_1^\top \quad \mathbf{v}_1^\top \quad C_{r_1} \quad \mathbf{r}_2^\top \quad \mathbf{v}_2^\top \quad C_{r_2} \right]^\top \in \mathcal{R}^{14 \times 1}. \quad (4.3)$$

Where \mathbf{r} and \mathbf{v} are the satellite position and velocity vectors with respect to the Earth and C_r is the coefficient of reflectivity. The C_r term is in fact representative of the whole Area-[times]-Gamma-over-Mass (AGOM) term found in the SRP acceleration equation shown previously. The Gamma term in AGOM is another name for C_r , as this was the original designation for the coefficient of reflectivity [51]. The subscripts indicate the state associated with satellite 1 or 2. With the state characterized, the dynamics and measurement model are illustrated in the following subsections.

4.1.2.1 Linearized Dynamics Model

The dual-satellite dynamics can be expressed in first order form as follows:

$$\dot{\mathbf{X}}(t) = F(\mathbf{X}, t) = \begin{bmatrix} \dot{\mathbf{r}}_1 \\ \dot{\mathbf{v}}_1 \\ \dot{C}_{r_1} \\ \dot{\mathbf{r}}_2 \\ \dot{\mathbf{v}}_2 \\ \dot{C}_{r_2} \end{bmatrix} = \begin{bmatrix} \mathbf{v}_1 \\ \mathbf{a}_{1_{2B}} + \mathbf{a}_{1_{SRP}} \\ 0 \\ \mathbf{v}_2 \\ \mathbf{a}_{2_{2B}} + \mathbf{a}_{2_{SRP}} \\ 0 \end{bmatrix} \in \mathcal{R}^{14 \times 1}, \quad (4.4)$$

where, $\mathbf{a}_{i_{2B}}$ and $\mathbf{a}_{i_{SRP}}$ for $i = 1, 2$ are the accelerations due to 2-body and SRP forces for both satellites 1 and 2 and are previously defined in Eqs. 2.6 and 2.15.

The orbit determination problem is non-linear in both the dynamics as well as the measurement model. To simplify the calculations significantly, the system is linearized about some reference. Notation-wise, a capitol letter signifies the actual state values, e.g., \mathbf{X} , while a lower case version of the same letter represents a deviation or perturbation from the reference, e.g., \mathbf{x} . The first order perturbations about the reference are as follows:

$$\mathbf{x} = \left[\delta \mathbf{r}_1^\top \quad \delta \mathbf{v}_1^\top \quad \delta C_{r_1} \quad \delta \mathbf{r}_2^\top \quad \delta \mathbf{v}_2^\top \quad \delta C_{r_2} \right]^\top \in \mathcal{R}^{14 \times 1}. \quad (4.5)$$

Then the first equation in the state-variable formulation for a linearized dynamic system is,

$$\dot{\mathbf{x}}(t) = \mathbf{A}(t)\mathbf{x}(t). \quad (4.6)$$

The \mathbf{A} -matrix are the partials of the dynamics from Eq. 4.4 with respect to the states from Eq. 4.3 at the reference. Eq. 4.7 shows the \mathbf{A} -matrix and also its sparsity, as there are only four

submatrices \mathbf{G}_1 , \mathbf{G}_2 , \mathbf{S}_1 and \mathbf{S}_2 that are not either zero or one:

$$\mathbf{A}(t) = \frac{\partial F(\mathbf{X}, t)}{\partial \mathbf{X}} = \begin{bmatrix} \mathbf{0}_{3 \times 3} & \mathcal{I}_{3 \times 3} & \mathbf{0}_{3 \times 1} & \mathbf{0}_{3 \times 3} & \mathbf{0}_{3 \times 3} & \mathbf{0}_{3 \times 1} \\ \mathbf{G}_1(t) & \mathbf{0}_{3 \times 3} & \mathbf{S}_1(t) & \mathbf{0}_{3 \times 3} & \mathbf{0}_{3 \times 3} & \mathbf{0}_{3 \times 1} \\ 0 & 0 & 0 & 0 & 0 & 0 \\ \mathbf{0}_{3 \times 3} & \mathbf{0}_{3 \times 3} & \mathbf{0}_{3 \times 1} & \mathbf{0}_{3 \times 3} & \mathcal{I}_{3 \times 3} & \mathbf{0}_{3 \times 1} \\ \mathbf{0}_{3 \times 3} & \mathbf{0}_{3 \times 3} & \mathbf{0}_{3 \times 1} & \mathbf{G}_2(t) & \mathbf{0}_{3 \times 3} & \mathbf{S}_2(t) \\ 0 & 0 & 0 & 0 & 0 & 0 \end{bmatrix} \in \mathcal{R}^{14 \times 14}. \quad (4.7)$$

The \mathbf{G}_i matrix is the gravity and SRP gradients, specifically,

$$\mathbf{G}_i(t) = \frac{\partial(\mathbf{a}_{i2B} + \mathbf{a}_{iSRP})}{\partial \mathbf{r}_i} \in \mathcal{R}^{3 \times 3}. \quad (4.8)$$

Upon differentiating Eq. 4.8 the gravity gradient is,

$$\frac{\partial \mathbf{a}_{i2B}}{\partial \mathbf{r}_i} = \frac{\mu_{\oplus}}{r_i^3} \left[3\hat{\mathbf{r}}_i \hat{\mathbf{r}}_i^{\top} - \mathcal{I}_{3 \times 3} \right], \quad (4.9)$$

and the SRP gradient becomes,

$$\frac{\partial \mathbf{a}_{iSRP}}{\partial \mathbf{r}_i} = -p_{SR} C_r \frac{A_{\odot}}{m} \frac{1}{r_{i,\odot}} \left[\hat{\mathbf{r}}_{i,\odot} \hat{\mathbf{r}}_{i,\odot}^{\top} - \mathcal{I}_{3 \times 3} \right]. \quad (4.10)$$

\mathbf{S}_i is the SRP partial with respect to C_{r_i} ,

$$\mathbf{S}_i(t) = \frac{\partial \mathbf{a}_{iSRP}}{\partial C_{r_i}} \in \mathcal{R}^{3 \times 1}. \quad (4.11)$$

Of course taking the partial of Eq. 4.11, results in $\frac{\partial \mathbf{a}_{iSRP}}{\partial C_{r_i}} = -p_{SR} \frac{A_{\odot}}{m} \frac{\mathbf{r}_{i,\odot}}{r_{i,\odot}^2}$. Now that an expression has been developed for the linearized dynamics, a linearized expression for the measurement model is next.

4.1.2.2 Linearized Measurement Model

The observation equation in the state-variable formulation for a linearized dynamic system is,

$$\mathbf{y}(t) = \mathbf{C}\mathbf{x}(t). \quad (4.12)$$

In this way the state deviations \mathbf{x} are mapped to the measurement deviations \mathbf{y} using the measurement mapping matrix \mathbf{C} . Rows one and two of \mathbf{C} correspond to the partials of TDOA and FDOA with respect to the state vector.

$$\mathbf{C} = \begin{bmatrix} \mathbf{T}_1 & \mathbf{0}_{1 \times 3} & 0 & \mathbf{T}_2 & \mathbf{0}_{1 \times 3} & 0 \\ \mathbf{F}_1 & \mathbf{J}_1 & 0 & \mathbf{F}_2 & \mathbf{J}_2 & 0 \end{bmatrix} \in \mathcal{R}^{2 \times 14} \quad (4.13)$$

The coefficient of reflectivity is not a parameter within the measurement model, consequently columns 3 and 6 are both zero. In addition, TDOA is not a function of the velocity, therefore those partials are also zero. While these partials are not particularly difficult they are somewhat tedious to derive. In addition, the cartesian position and velocity values need to be associated with the correct times, calculated through the light-time correction explained in chapter 2.2.2. The partials \mathbf{T} , \mathbf{F} , and \mathbf{J} have been previously defined in chapter 2.2.1.1. Armed with the linearized dynamics and measurement models, the observability matrix can be constructed and is discussed in the following section.

4.1.2.3 Observability Matrix

Continuing the approach used in Refs. [68] and [56], we can derive an equation that maps a perturbation in the state to a perturbation in the measurement and its time derivatives as shown in Eq. 4.14. Naturally if a small perturbation in the state causes a perturbation in the measurement or one of its time derivatives then that perturbation is observable. On the other hand if for all k , the measurement or its time derivatives remain zero for a perturbation in the state (i.e. a non-trivial null-space exists), then that perturbation is unobservable.

$$\begin{bmatrix} \mathbf{y} \\ \dot{\mathbf{y}} \\ \ddot{\mathbf{y}} \\ \vdots \\ d^{k-1}\mathbf{y}/dt^{k-1} \end{bmatrix} = \mathcal{O}_k \mathbf{x} \quad (4.14)$$

Another way of stating this is: a perturbation in the state is unobservable if and only if $\mathcal{O}_k \mathbf{x} = 0$, $\forall k$. Consequently if for some k , $\mathcal{O}_k \mathbf{x} \neq 0$ then it is observable. It is mathematically equivalent to show that there exists some integer k , where $k \geq 7$, for which the $2k \times 14$ observability matrix

$$\mathcal{O}_k^\top = \left[\mathbf{C}^\top \quad (\mathbf{A}^\top + d/dt)\mathbf{C}^\top \quad (\mathbf{A}^\top + d/dt)^2\mathbf{C}^\top \quad \dots \quad (\mathbf{A}^\top + d/dt)^{k-1}\mathbf{C}^\top \right], \quad (4.15)$$

is of rank 14 to show that the system is observable [56, 73]. The first condition can be used to analytically show that the orbit determination problem with TDOA and FDOA is observable. The second condition is the one used to demonstrate observability in a numerical sense. The $2k \times 14$ specification is for the one-baseline case as one baseline provides one TDOA and one FDOA measurement for a total of two measurements. If two baselines were used then two TDOA and FDOA measurements would be used which means $\mathbf{C} \in \mathcal{R}^{4 \times 14}$ and the observability matrix would be a $4k \times 14$ and so forth. If the one-baseline case is observable then the two or more baseline cases are also observable.

In the analytical observability setup, we develop necessary conditions for unobservability. If these necessary conditions cannot be met then the problem is observable. Therefore if we can show that $\mathcal{O}_k \mathbf{x} \neq 0$ for some k , it is sufficient to prove the theoretical observability. However, while some time was dedicated to solving the observability analytically, it appears not to be tractable. As a result we prove the observability numerically instead by showing that the observability matrix is full rank. Using one baseline, the minimum k required is 7 to meet the rank criterium.

The observability matrix is derived using Eqs. 4.7, 4.13 and 4.15. Equation 4.16 shows $\mathcal{O}_7 \mathbf{x}$,

$$\mathcal{O}_7 \mathbf{x} = \begin{bmatrix} \mathbf{N}_{11} & \mathbf{\Xi}_{11} & \mathbf{O}_{11} & \mathbf{N}_{12} & \mathbf{\Xi}_{12} & \mathbf{O}_{12} \\ \mathbf{N}_{21} & \mathbf{\Xi}_{21} & \mathbf{O}_{21} & \mathbf{N}_{22} & \mathbf{\Xi}_{22} & \mathbf{O}_{22} \\ \vdots & & & & & \vdots \\ \mathbf{N}_{71} & \mathbf{\Xi}_{71} & \mathbf{O}_{71} & \mathbf{N}_{72} & \mathbf{\Xi}_{72} & \mathbf{O}_{72} \end{bmatrix} \begin{bmatrix} \delta \mathbf{r}_1 \\ \delta \mathbf{v}_1 \\ \delta C_{r_1} \\ \delta \mathbf{r}_2 \\ \delta \mathbf{v}_2 \\ \delta C_{r_2} \end{bmatrix} \in \mathcal{R}^{14 \times 1}. \quad (4.16)$$

The submatrices \mathbf{N} , $\mathbf{\Xi}$, and \mathbf{O} are listed below using Eqs. 4.17 to 4.37. The first subscript

corresponds to k , while the subscript of the subscript refers to either satellite 1 or 2.

$$\mathbf{N}_{1_i} = \begin{bmatrix} \mathbf{T}_i \\ \mathbf{F}_i \end{bmatrix} \quad (4.17)$$

$$\mathbf{N}_{2_i} = \begin{bmatrix} \mathbf{0}_{1 \times 3} \\ \mathbf{J}_i \mathbf{G}_i \end{bmatrix} \quad (4.18)$$

$$\mathbf{N}_{3_i} = \begin{bmatrix} \mathbf{T}_i \mathbf{G}_i \\ \mathbf{J}_i \dot{\mathbf{G}}_i + \mathbf{F}_i \mathbf{G}_i \end{bmatrix} \quad (4.19)$$

$$\mathbf{N}_{4_i} = \begin{bmatrix} \mathbf{T}_i \dot{\mathbf{G}}_i \\ \mathbf{J}_i (\ddot{\mathbf{G}}_i + \mathbf{G}_i^2) + \mathbf{F}_i \dot{\mathbf{G}}_i \end{bmatrix} \quad (4.20)$$

$$\mathbf{N}_{5_i} = \begin{bmatrix} \mathbf{T}_i (\ddot{\mathbf{G}}_i + \mathbf{G}_i^2) \\ \mathbf{J}_i (2\mathbf{G}_i \dot{\mathbf{G}}_i + \ddot{\mathbf{G}}_i) + \mathbf{F}_i (\ddot{\mathbf{G}}_i + \mathbf{G}_i^2) \end{bmatrix} \quad (4.21)$$

$$\mathbf{N}_{6_i} = \begin{bmatrix} \mathbf{T}_i (2\mathbf{G}_i \dot{\mathbf{G}}_i + \ddot{\mathbf{G}}_i) \\ \mathbf{J}_i (\mathbf{G}_i^3 + 2\mathbf{G}_i \ddot{\mathbf{G}}_i + \dot{\mathbf{G}}_i^2 + \ddot{\mathbf{G}}_i) + \mathbf{F}_i (2\mathbf{G}_i \dot{\mathbf{G}}_i + \ddot{\mathbf{G}}_i) \end{bmatrix} \quad (4.22)$$

$$\mathbf{N}_{7_i} = \begin{bmatrix} \mathbf{T}_i (\mathbf{G}_i^3 + 2\mathbf{G}_i \ddot{\mathbf{G}}_i + \dot{\mathbf{G}}_i^2 + \ddot{\mathbf{G}}_i) \\ \mathbf{J}_i (3\mathbf{G}_i^2 \dot{\mathbf{G}}_i + 2\mathbf{G}_i \ddot{\mathbf{G}}_i + 2\dot{\mathbf{G}}_i \ddot{\mathbf{G}}_i + \dot{\mathbf{G}}_i^3) + \mathbf{F}_i (\mathbf{G}_i^3 + 2\mathbf{G}_i \ddot{\mathbf{G}}_i + \dot{\mathbf{G}}_i^2 + \ddot{\mathbf{G}}_i) \end{bmatrix} \quad (4.23)$$

$$\mathbf{E}_{1_i} = \begin{bmatrix} \mathbf{0}_{1 \times 3} \\ \mathbf{J}_i \end{bmatrix} \quad (4.24)$$

$$\mathbf{E}_{2_i} = \begin{bmatrix} \mathbf{T}_i \\ \mathbf{F}_i \end{bmatrix} \quad (4.25)$$

$$\mathbf{E}_{3_i} = \begin{bmatrix} \mathbf{0}_{1 \times 3} \\ \mathbf{J}_i \mathbf{G}_i \end{bmatrix} \quad (4.26)$$

$$\mathbf{\Xi}_{4_i} = \begin{bmatrix} \mathbf{T}_i \mathbf{G}_i \\ \mathbf{J}_i \dot{\mathbf{G}}_i + \mathbf{F}_i \mathbf{G}_i \end{bmatrix} \quad (4.27)$$

$$\mathbf{\Xi}_{5_i} = \begin{bmatrix} \mathbf{T}_i \dot{\mathbf{G}}_i \\ \mathbf{J}_i (\ddot{\mathbf{G}}_i + \mathbf{G}_i^2) + \mathbf{F}_i \dot{\mathbf{G}}_i \end{bmatrix} \quad (4.28)$$

$$\mathbf{\Xi}_{6_i} = \begin{bmatrix} \mathbf{T}_i (\ddot{\mathbf{G}}_i + \mathbf{G}_i^2) \\ \mathbf{J}_i (2\mathbf{G}_i \dot{\mathbf{G}}_i + \ddot{\mathbf{G}}_i) + \mathbf{F}_i (\mathbf{G}_i^2 + \dot{\mathbf{G}}_i) \end{bmatrix} \quad (4.29)$$

$$\mathbf{\Xi}_{7_i} = \begin{bmatrix} \mathbf{T}_i (2\mathbf{G}_i \dot{\mathbf{G}}_i + \ddot{\mathbf{G}}_i) \\ \mathbf{J}_i (\mathbf{G}_i^3 + 2\mathbf{G}_i \ddot{\mathbf{G}}_i + \dot{\mathbf{G}}_i^2 + \ddot{\mathbf{G}}_i) + \mathbf{F}_i (2\mathbf{G}_i \dot{\mathbf{G}}_i + \ddot{\mathbf{G}}_i) \end{bmatrix} \quad (4.30)$$

$$\mathbf{O}_{1_i} = \begin{bmatrix} 0 \\ 0 \end{bmatrix} \quad (4.31)$$

$$\mathbf{O}_{2_i} = \begin{bmatrix} 0 \\ \mathbf{J}_i \mathbf{S}_i \end{bmatrix} \quad (4.32)$$

$$\mathbf{O}_{3_i} = \begin{bmatrix} \mathbf{T}_i \mathbf{S}_i \\ \mathbf{J}_i \dot{\mathbf{S}}_i + \mathbf{F}_i \mathbf{S}_i \end{bmatrix} \quad (4.33)$$

$$\mathbf{O}_{4_i} = \begin{bmatrix} \mathbf{T}_i \dot{\mathbf{S}}_i \\ \mathbf{F}_i \dot{\mathbf{S}}_i + \mathbf{J}_i (\ddot{\mathbf{S}}_i + \mathbf{G}_i \mathbf{S}_i) \end{bmatrix} \quad (4.34)$$

$$\mathbf{O}_{5_i} = \begin{bmatrix} \mathbf{T}_i (\ddot{\mathbf{S}}_i + \mathbf{G}_i \mathbf{S}_i) \\ \mathbf{J}_i (\mathbf{G}_i \dot{\mathbf{S}}_i + \dot{\mathbf{G}}_i \mathbf{S}_i + \ddot{\mathbf{S}}_i) + \mathbf{F}_i (\ddot{\mathbf{S}}_i + \mathbf{G}_i \mathbf{S}_i) \end{bmatrix} \quad (4.35)$$

$$\mathbf{O}_{6_i} = \begin{bmatrix} \mathbf{T}_i (\mathbf{G}_i \dot{\mathbf{S}}_i + \dot{\mathbf{G}}_i \mathbf{S}_i + \ddot{\mathbf{S}}_i) \\ \mathbf{J}_i (\ddot{\mathbf{S}}_i + \mathbf{G}_i \ddot{\mathbf{S}}_i + \ddot{\mathbf{G}}_i \mathbf{S}_i + \dot{\mathbf{G}}_i \dot{\mathbf{S}}_i + \mathbf{G}_i^2 \mathbf{S}_i) + \mathbf{F}_i (\mathbf{G}_i \dot{\mathbf{S}}_i + \dot{\mathbf{G}}_i \mathbf{S}_i + \ddot{\mathbf{S}}_i) \end{bmatrix} \quad (4.36)$$

$$\mathbf{O}_{\tau_i} = \begin{bmatrix} \mathbf{T}_i \left(\ddot{\mathbf{S}}_i + \mathbf{G}_i \ddot{\mathbf{S}}_i + \ddot{\mathbf{G}}_i \mathbf{S}_i + \dot{\mathbf{G}}_i \dot{\mathbf{S}}_i + \mathbf{G}_i^2 \mathbf{S}_i \right) \\ \mathbf{J}_i \left(\dot{\mathbf{G}}_i \ddot{\mathbf{S}}_i + \ddot{\mathbf{G}}_i \dot{\mathbf{S}}_i + \mathbf{G}_i^2 \dot{\mathbf{S}}_i + \mathbf{G}_i \ddot{\mathbf{S}}_i + \ddot{\mathbf{G}}_i \mathbf{S}_i + 2\mathbf{G}_i \dot{\mathbf{G}}_i \mathbf{S}_i + \overset{5}{\dot{\mathbf{S}}}_i \right) + \\ \mathbf{F}_i \left(\ddot{\mathbf{S}}_i + \mathbf{G}_i \ddot{\mathbf{S}}_i + \ddot{\mathbf{G}}_i \mathbf{S}_i + \dot{\mathbf{G}}_i \dot{\mathbf{S}}_i + \mathbf{G}_i^2 \mathbf{S}_i \right) \end{bmatrix} \quad (4.37)$$

The time derivatives of both \mathbf{G} and \mathbf{S} are listed in Appendix A due to their extensive size. This completes the formulation of the observability matrix which will be evaluated numerically in the subsequent section.

4.1.3 Numerical Evaluation of the Observability Matrix

The rank of the observability matrix shown in Eq. 4.16, can be scrutinized to determine the observability of the orbit determination problem. We increase the precision from double to 50-digits of precision using Python's mpmath package to mitigate numerical issues since double precision produces an incorrect rank evaluation as a result of a condition number higher than machine precision. To calculate the rank a singular value decomposition is used to obtain the singular values of the observability matrix. The threshold for rank deficiency is by identifying those singular values less than some defined tolerance. The tolerance implemented is,

$$tol = \max(s) * \max(\text{size}(\mathcal{O}_k)) * \epsilon, \quad (4.38)$$

where, s are the singular values of \mathcal{O}_k and ϵ is machine precision [67]. The input values can be defined with 50 digits of precision, this means that a double value is padded with 0's up to the 50th digit. However, if a double value is introduced incorrectly then it is possible that rather than being padded with 0's after the double, the digits are random. The following test was performed to test whether this could have an effect on rank. A linearly dependent matrix as the one shown in Eq. 4.39 was incorrectly defined using 50 digits with correct values up to double-precision. This means that the four floats have 0's after the first decimal value up to double precision (15 digits),

but from then on have random digits up to 50.

$$\begin{bmatrix} 1.1 & 2.2 \\ 2.2 & 4.4 \end{bmatrix} \quad (4.39)$$

One might conclude that the difference in random digits would result in a rank 2 matrix. However, that is not the case; using the tolerance specified in Eq. 4.38 the rank is still only 1 as it should be. This test is important to validate the rank of the \mathcal{O}_k matrix. It confirms that the rank is real rather than a numerical artifact from using 50 digits of precision. Therefore the observability question can be answered from this numerical method.

Using one baseline, we have $2k \times 14$ for the size of the observability matrix, accordingly the minimum k for which \mathcal{O}_k can be full rank is 7. Calculating \mathcal{O}_7 as shown in Eq. 4.16 requires fifth order time derivatives of both \mathbf{G} and \mathbf{S} , these were derived and computationally verified and are laid out in Appendix A. The rank of \mathcal{O}_7 can be computed in less than one second for a single scenario, this quick computation time makes it conducive for a Monte Carlo simulation. A scenario refers to a set of orbits and satellite positions with specified station geometries.

Two Monte Carlo simulations, each with 10,000 cases were executed. The first Monte Carlo simulation is a general analysis where the input parameters can vary extensively. The 26 input parameters are shown with their low and high values in the first three columns of Table 4.1. The first two parameters relate to the time of year as well as the time of day, the ephemerii are calculated for 2015. The next four rows place the two transmitters (TX) as well as two receivers (RX) anywhere on the Earth, the difficulty of placing them in inaccessible places is not taken into account. Furthermore, it is possible that the signal is blocked by the Earth and therefore not visible to the satellite or satellites. Once again this physical restriction is ignored. Finally the last seven rows define the orbit as well as the coefficient of reflectivity for both satellites. Where a is the semi-major axis, e is the eccentricity, i is the inclination, Ω is the longitude of the ascending node, ω is the argument of periapsis and ν is the true anomaly. Notice that the two satellites can be in practically any orientation with a semi-major axis ranging from low earth orbit (LEO) to geosynchronous (GEO) and above. The purpose is to show that widely varying geometries

uniformly sampled produce an observable system if physical constraints are not an issue. In fact all 10,000 cases produced a rank 14 observability matrix with one baseline.

A second Monte Carlo was run with some limitations. The new inputs are shown as the GEO Monte Carlo in Table 4.1 which are the last three columns. In this case we have 27 input parameters, instead of specifying the true anomaly for both satellites we specify the longitude of satellite 1 and then have a longitudinal separation defined between the two satellites to place satellite 2. With the specified input bounds, the two satellites are longitudinally located over the United States with a satellite separation between 1 and 20 degrees to ensure that the signal can be acquired by both satellites. Furthermore the location of the stations are limited to roughly the contiguous United States as well. The other orbital parameters are confined for the satellites to be in the geosynchronous belt. In this second case all 10,000 cases were rank 14, and therefore full rank and observable. Thus it has been shown that the problem should always be observable with enough numerical precision. We show in section 4.1.7.1 that when using double precision however, the GEO-GEO case with one baseline is not observable.

Table 4.1: Monte Carlo simulation inputs

General Monte Carlo			GEO Monte Carlo		
Parameter	Low Value	High Value	Parameter	Low Value	High Value
Day of Year [DOY]	1	364	Day of Year [DOY]	1	364
Hour	0	23	Hour	0	23
Ref/Cal TX Lat [deg]	-90	90	Ref/Cal TX Lat [deg]	25	49
Ref/Cal TX Lon [deg]	0	359	Ref/Cal TX Lon [deg]	235	293
Ref/Cal RX Lat [deg]	-90	90	Ref/Cal RX Lat [deg]	25	49
Ref/Cal RX Lon [deg]	0	359	Ref/Cal RX Lon [deg]	235	293
Ref/Cal Freq [MHz]	14380	14390	Ref/Cal Freq [MHz]	14380	14390
a_i [km]	6578	42264	a_i [km]	41964	42364
e_i	0	0.1	e_i	0	0.1
i_i [deg]	-90	90	i_i [deg]	-5	5
Ω_i [deg]	0	359	Ω_i [deg]	0	359
ω_i [deg]	0	359	ω_i [deg]	0	359
C_{r_i}	0.001	0.1	C_{r_i}	0.001	0.1
ν_i [deg]	0	359	Sat ₁ Lon [deg]	225	283
			Sat Lon Sep [deg]	1	20

4.1.4 Condition Number

The condition number is another example to determine numerical observability of a problem [28]. The condition number is a matrix property that describes the sensitivity of \mathbf{x} in the normal equation:

$$\mathbf{\Lambda}\mathbf{x} = \mathbf{N}. \quad (4.40)$$

Solutions that are very sensitive are considered ill-conditioned and are characterized by a high condition number. From Ref. [16] it can be shown how a small change in \mathbf{N} and $\mathbf{\Lambda}$ yields a small or large change in \mathbf{x} , we show this next. First the Schwarz inequality is applied to Eq. 4.40 to yield,

$$\frac{1}{\|\mathbf{x}\|} \leq \frac{\|\mathbf{\Lambda}\|}{\|\mathbf{N}\|}. \quad (4.41)$$

This form of the normal equation will be used shortly. Next, the left column below shows the sensitivity to $\delta\mathbf{N}$ while the right column shows the sensitivity to $\delta\mathbf{\Lambda}$.

$$\delta\mathbf{x} = \mathbf{\Lambda}^{-1}\delta\mathbf{N} \quad (4.42)$$

Applying the Schwarz inequality,

$$\|\delta\mathbf{x}\| \leq \|\mathbf{\Lambda}^{-1}\| \|\delta\mathbf{N}\| \quad (4.43)$$

Merging Eq. 4.41 and Eq. 4.43,

$$\frac{\|\delta\mathbf{x}\|}{\|\mathbf{x}\|} \leq \|\mathbf{\Lambda}\| \|\mathbf{\Lambda}^{-1}\| \frac{\|\delta\mathbf{N}\|}{\|\mathbf{N}\|} \quad (4.44)$$

$$\delta\mathbf{x} = -\mathbf{\Lambda}^{-1}\delta\mathbf{\Lambda}\mathbf{x} \quad (4.45)$$

Applying the Schwarz inequality,

$$\|\delta\mathbf{x}\| \leq \|\mathbf{\Lambda}^{-1}\| \|\delta\mathbf{\Lambda}\| \|\mathbf{x}\| \quad (4.46)$$

Merging Eq. 4.41 and Eq. 4.46,

$$\frac{\|\delta\mathbf{x}\|}{\|\mathbf{x}\|} \leq \|\mathbf{\Lambda}\| \|\mathbf{\Lambda}^{-1}\| \frac{\|\delta\mathbf{\Lambda}\|}{\|\mathbf{\Lambda}\|} \quad (4.47)$$

Notice that both Eqs. 4.44 and 4.47 have $\|\mathbf{\Lambda}\|_p \|\mathbf{\Lambda}^{-1}\|_p$ which bounds the relative error and defines the condition number C of $\mathbf{\Lambda}$. However, since a matrix inverse is not always numerically stable, the condition number can also be computed by calculating the minimum and maximum

eigenvalues of $\mathbf{\Lambda}$ and hence,

$$C(\mathbf{\Lambda}) = \|\mathbf{\Lambda}\|_p \|\mathbf{\Lambda}^{-1}\|_p = \frac{\gamma_{max}}{\gamma_{min}}. \quad (4.48)$$

Where, γ are the eigenvalues. Equation 4.48 holds when $\mathbf{\Lambda}$ is square. A condition number cannot be taken at face-value however, since the eigenvalues are properties of \mathbf{H} and consequently $\mathbf{\Lambda}$. This means that the eigenvalues do not take into account the relative magnitudes of the states, measurements and measurement noise [28]. Therefore the measurement model, $\mathbf{y} = \mathbf{H}\mathbf{x} + \boldsymbol{\epsilon}$, should be normalized as follows:

$$\left(\mathbf{R}^{-1/2}\mathbf{y}\right) = \left(\mathbf{R}^{-1/2}\mathbf{H}\mathbf{D}^{-1}\right)\left(\mathbf{D}\mathbf{x}\right) + \left(\mathbf{R}^{-1/2}\boldsymbol{\epsilon}\right). \quad (4.49)$$

This is called correlation or scaled form for the minimum variance estimation methods [28, 62]. Here $\mathbf{R}^{1/2}$ is a cholesky decomposition of the measurement noise matrix \mathbf{R} , and \mathbf{D} is a diagonal matrix with each element equal to the l_2 -norm of the corresponding column of \mathbf{H} . This form of the measurement equation is used in the batch processor implementation which reduces the condition number approximately by a factor of two.

4.1.5 Degree of Observability

In Section 4.1.1 a set of tests were listed that yield a yes-no answer as to whether a system is numerically observable or not. The condition number C was also introduced and is a good metric for the degree of observability in the system. The lower the condition number the higher the observability, in fact if $C(\mathbf{\Lambda}) = 1$, then that implies the system is as observable as can be [3].

Another way to look at the observability of the dual-satellite OD problem is from an optimization perspective. A filter, in essence, is an optimization algorithm that reduces a cost function, in the case of the dual-satellite system the TDOA and FDOA RMS. The problem is 14-dimensional and impossible to visualize, as a result we can extract two estimated parameters at a time, plot those on the abscissa and ordinate with the RMS on the z axis. Intuitively we can expect at a

minimum, that the parameters from the primary satellite will be correlated with the same parameters of the secondary satellite. This is also backed up through the correlations explained in chapter 4.1.6.

In Figures 4.1 to 4.14 only two states are perturbed from a simulated truth trajectory. For example in Figures 4.13 and 4.14 only the AGOM values of satellite 1 and 2 are perturbed from the nominal 0.0625/0.0425 AGOM value cases. For each perturbed AGOM value the TDOA and FDOA RMS (the cost function of the optimizer) are displayed in a contour plot. Notice how both TDOA and FDOA display a valley rather than an obvious single minimum point. Furthermore, the noise floor for both TDOA and FDOA are $0.035 \mu s$ and 0.2 mHz . In the TDOA case, the difference in RMS value over a wide variety of AGOMs is extremely low, in fact the plot shows nearly a flat surface, making it very difficult for the filter to locate the minimum. With all estimated parameters we show that there is an extreme correlation between the corresponding estimated parameters of the two satellites, seen by the dark blue diagonal lines.

The smaller plots in the lower-right corners are identical to the main figure, with the exception of the z-axis scale. The z-axis scale is chosen to be identical to that of the AGOM plots 4.13 and 4.14, so that a relative comparison between plots can be made. Notice that in Figures 4.1 and 4.2 for example, there is indeed a minimum present made clear by the new smaller z-axis scale. Since the scale is identical in the subfigures, it is also easy to compare the relative ‘flatness’. Clearly the AGOM parameters have the least amount of change in the cost function making it more difficult to estimate properly.

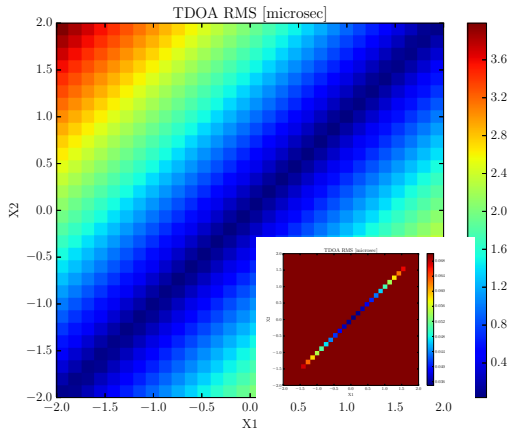


Figure 4.1: TDOA RMS for $\text{sat}_1/\text{sat}_2$ X_0 perturbation from truth in km

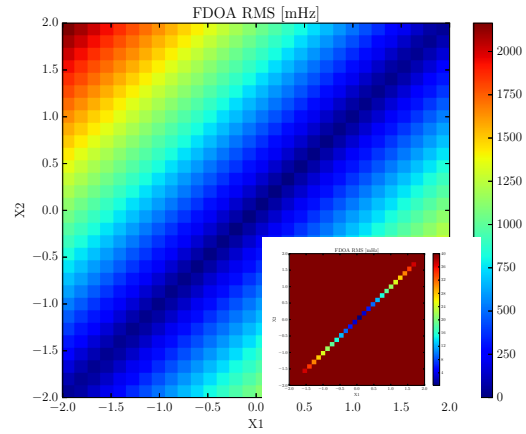


Figure 4.2: FDOA RMS for $\text{sat}_1/\text{sat}_2$ X_0 perturbation from truth in km

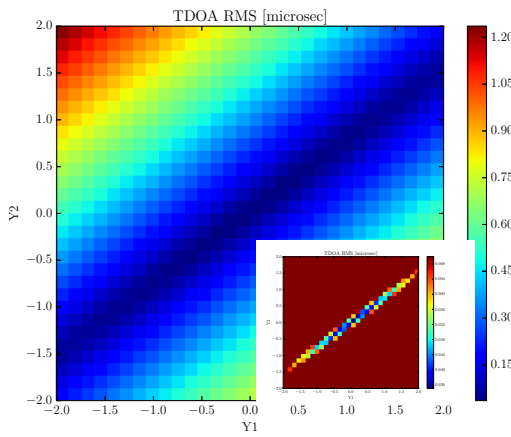


Figure 4.3: TDOA RMS for $\text{sat}_1/\text{sat}_2$ Y_0 perturbation from truth in km

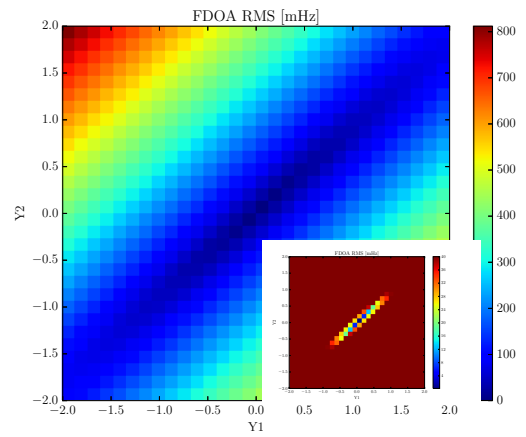


Figure 4.4: FDOA RMS for $\text{sat}_1/\text{sat}_2$ Y_0 perturbation from truth in km

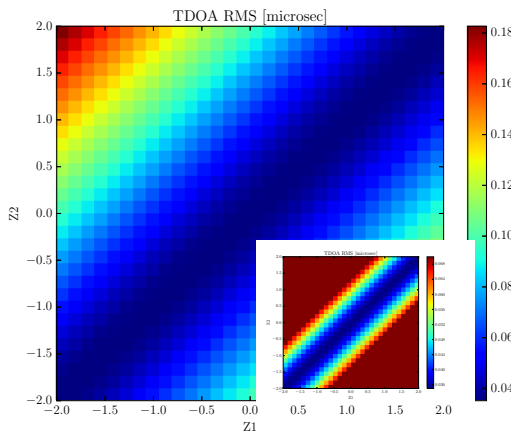


Figure 4.5: TDOA RMS for $\text{sat}_1/\text{sat}_2$ Z_0 perturbation from truth in km

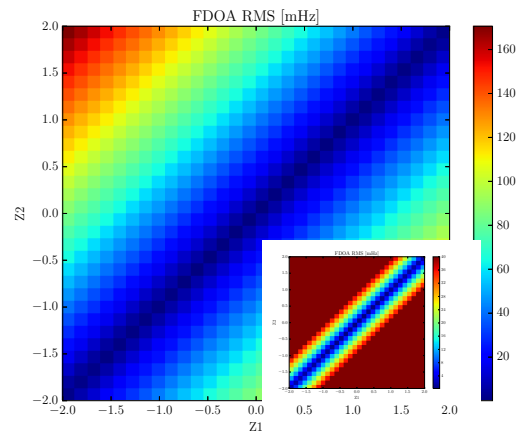


Figure 4.6: FDOA RMS for $\text{sat}_1/\text{sat}_2$ Z_0 perturbation from truth in km

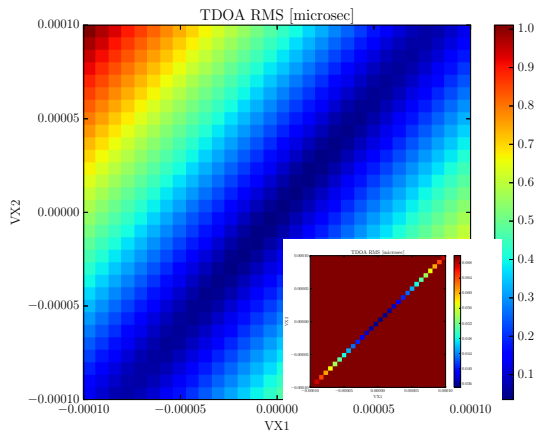


Figure 4.7: TDOA RMS for sat₁/sat₂ \dot{X}_0 perturbation from truth in km/s

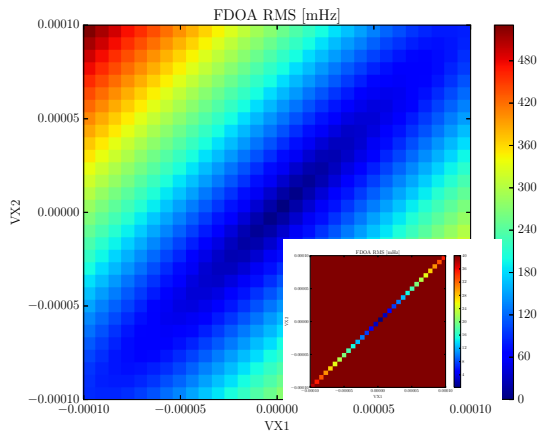


Figure 4.8: FDOA RMS for sat₁/sat₂ \dot{X}_0 perturbation from truth in km/s

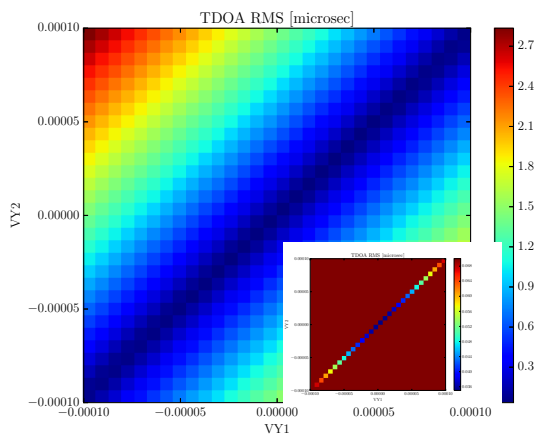


Figure 4.9: TDOA RMS for sat₁/sat₂ \dot{Y}_0 perturbation from truth in km/s

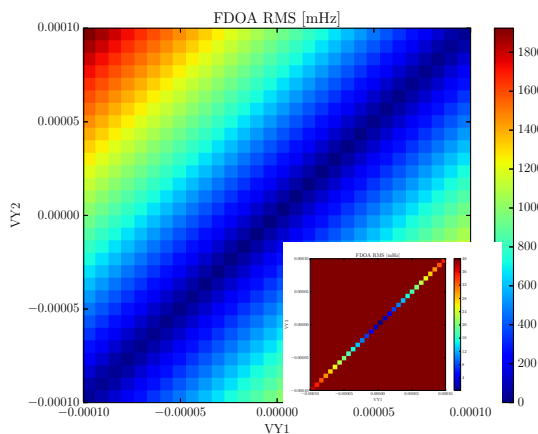


Figure 4.10: FDOA RMS for sat₁/sat₂ \dot{Y}_0 perturbation from truth in km/s

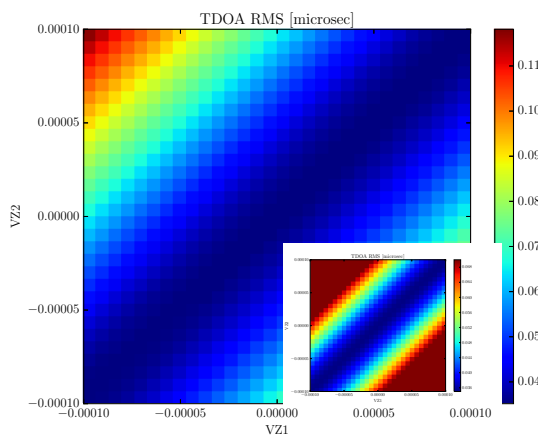


Figure 4.11: TDOA RMS for sat₁/sat₂ \dot{Z}_0 perturbation from truth in km/s

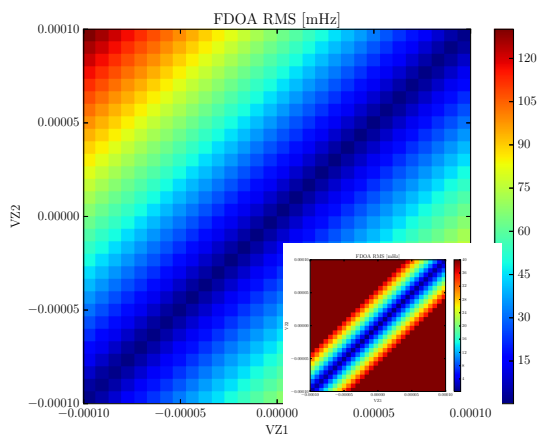


Figure 4.12: FDOA RMS for sat₁/sat₂ \dot{Z}_0 perturbation from truth in km/s

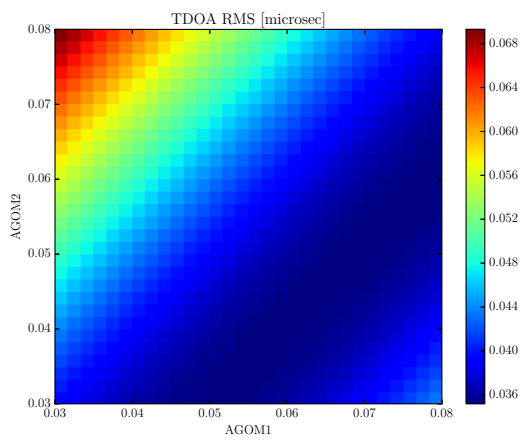


Figure 4.13: TDOA RMS for sat₁/sat₂ AGOM perturbation from truth of 0.0625/0.0425

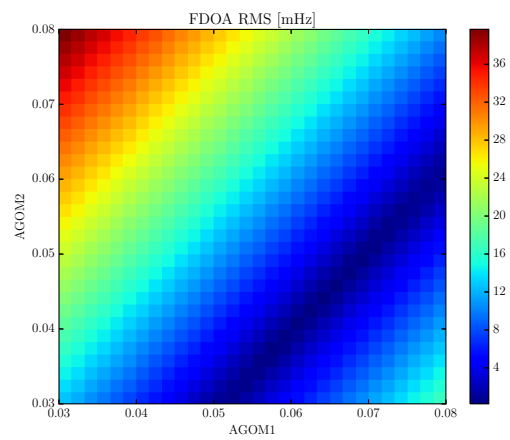


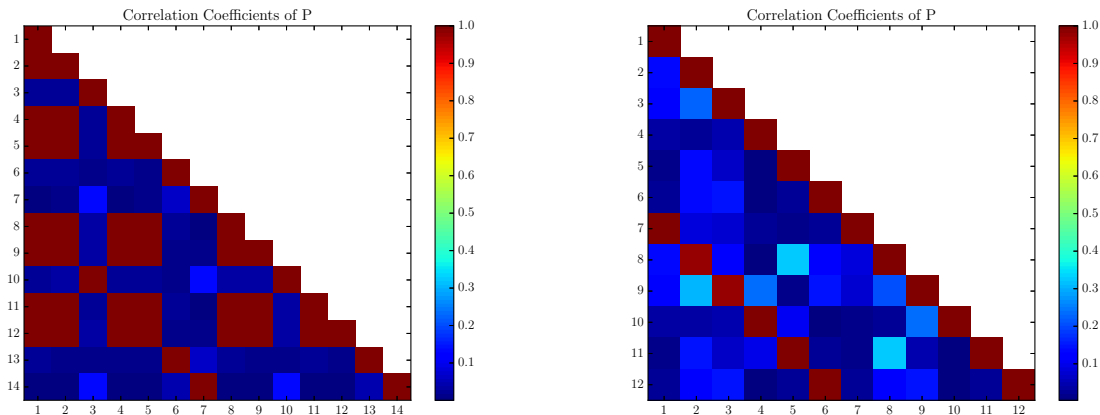
Figure 4.14: FDOA RMS for sat₁/sat₂ AGOM perturbation from truth of 0.0625/0.0425

4.1.6 Correlations

The correlation coefficient measures the degree of linear correlation between the estimated state variables and can be written as,

$$\rho_{ij} = \frac{P_{ij}}{\sigma_i \sigma_j}, \quad i \neq j. \quad (4.50)$$

Where P_{ij} is the ij^{th} element of the covariance matrix \mathbf{P} and $\sigma_{i/j}$ is the standard deviation of the corresponding i^{th} or j^{th} element in \mathbf{P} . In this definition of correlation coefficient, the lower the value the better, as that signifies orthogonality between the estimated parameters. A high correlation coefficient signifies a statistical dependence making it more difficult to separate the behavior of the estimated parameters given a set of measurements.



(a) GEO-GEO correlations in cartesian coordinates (numbers correspond to states from Eq. 4.3)

(b) GEO-GEO correlations in equinoctial elements (numbers correspond to states from Eq. 4.3 with AGOM omitted)

Figure 4.15: Correlations

Figure 4.15(a) illustrates the high correlations between the various estimated parameters. Not only between the parameters of both satellites but also with position and velocity of the same satellite. By transforming the cartesian states into equinoctial state space using an unscented transform we can significantly reduce self-correlation, meaning the states from the same satellite,

but correlation with the identical state from the other satellite is still significantly present, indicated by the 6-block diagonal red line.

4.1.7 Cramér-Rao Lower Bound (CRLB)

Another way to assess the observability of the system is by analyzing the CRLB, which establishes the optimal filter performance through enumeration of the lowest possible covariance or expected state errors. This means there exists a covariance, defined by the inverse of the Fisher information matrix \mathbf{J}_k^{-1} , for which all other realizations of the covariance \mathbf{P}_k are equal to or greater than the Fisher information matrix. The relationship is defined as the Cramér-Rao inequality,

$$\mathbf{P}_k \geq \mathbf{J}_k^{-1}. \quad (4.51)$$

Using the recursive form developed in Ref. [84], the Fisher information matrix can be written as,

$$\mathbf{J}_k = \left(\Phi^{-\top}(t_k, t_{k-1}) \mathbf{J}_{k-1} \Phi^{-1}(t_k, t_{k-1}) \right) + \tilde{\mathbf{H}}_k^\top \mathbf{W}_k \tilde{\mathbf{H}}_k. \quad (4.52)$$

Where, Φ is the state transition matrix (STM) and \mathbf{W} is the observation weighting matrix. Equation 4.52 is initialized with $\mathbf{J}_0 = \mathbf{P}_0^{-1}$. The CRLB simulations have initial 1σ state and measurement uncertainties as defined in Table 4.2.

Table 4.2: CRLB 1σ a-priori uncertainty for dual-estimated states and measurements

<i>Satellite state uncertainty</i>	
Position	100 km
Velocity	10 m/s
C_r (AGOM)	0.01
<i>Measurement uncertainty</i>	
TDOA	0.035 μ s
FDOA	0.2 mHz
Range	1 m
Range-rate	1 mm/s

Table 4.3 lists the orbit parameters of the satellites considered in the CRLB analyses. Where a is the semi-major axis, e is the eccentricity, i is the inclination, Ω is the right ascension of the ascending node, ω is the argument of periapsis, and ν is the true anomaly. The first GEO satellite listed is paired with four different LEO satellites, one MEO and another GEO satellite. For each of these cases beamwidths of 45, 60, and 75 degrees are considered with specific cases investigated in further detail.

Table 4.3: Orbit parameters of satellites in CRLB analysis

	a [km]	e	i [deg]	Ω [deg]	ω [deg]	ν [deg]	C_r
GEO -	42166.4	0	0.08	105.1	101.4	286.7	0.04
LEO 0°	8377.7	0.01	0	0	265.1	263.4	0.06
LEO 30°	8377.7	0.01	30	270.2	354.9	263.4	0.06
LEO 60°	8377.7	0.01	60	270.0	265.1	263.4	0.06
LEO 90°	8377.7	0.01	90	260.0	265.1	263.4	0.06
MEO	24926.5	0	35	110.0	289.6	122.6	0.06
GEO	42166.5	0	0.08	81.0	139.7	266.4	0.06

Table 4.4, lists the latitude, longitude and altitude of the simulated TXs and RXs. The reference TX in Boulder is paired with anyone or all of the i TXs to create a baseline.

Table 4.4: Latitude, longitude and altitude of transmitters and receivers

<i>Transmitters (TXs)</i>			
<i>Reference</i>			
Boulder	40.015° N	105.270° W	1623.72 m
i^{th}			
Boston	42.36° N	71.06° W	11.49 m
Miami	25.76° N	80.19° W	0.89 m
Houston	29.76° N	95.37° W	14.54 m
San Diego	32.72° N	117.16° W	27.91 m
Seattle	47.60° N	122.33° W	9.44 m
<i>Receivers (RXs)</i>			
Boulder 1	40.014° N	105.271° W	1625.57 m
Boulder 2	40.014° N	105.270° W	1621.13 m

4.1.7.1 Discrete Orbit Pairs with Varying Number of Baselines

The first CRLB analysis examines the observability of changing the number of baselines utilized for OD of a GEO satellite paired with six other satellites. Table 4.3 lists the orbit parameters of these satellites. The first GEO satellite listed is paired with four different LEO satellites, one MEO satellite, and another GEO satellite. For each of these cases beamwidths of 45, 60, and 75 degrees are considered with specific cases investigated in further detail.

Figure 4.16 shows the CRLBs for the GEO-LEO 30° case with a 75 degree beamwidth constraint over a 9 hour period of which 108 minutes had the correct geometry to take TDOA and FDOA measurements. The GEO satellite is shown in 4.16(a) and the LEO satellite shown in 4.16(b). The greyed out time periods are data gaps because the LEO satellite was not within the 75 degree beamwidth during those times, note that the last data gap up to the 9 hour mark was not included in the plot. The CRLBs are shown for all possible combinations of the i TXs listed in Table 4.4 with the legend colors specifying the number of baselines used to obtain that CRLB. When measurements are available there is a steady decrease in the trace of the diagonal of the covariances, except for the GEO satellite when only one baseline is used. Note that \mathbf{J}_k is only computed for regions of data, consequently the covariance over a data gap is not representative of the actual covariance, this is apparent by the occasional decreasing covariances over the data gaps in Figures 4.16 and 4.17. In the one baseline case the slow reduction in covariance indicates little information is accumulated suggesting a low degree of observability. Therefore it is recommended that a minimum of two baselines are used to maintain a higher degree of observability. In general, the more baselines that are implemented the lower the CRLB, this is predictable as there are more measurements available with an increase in TXs. When reducing the beamwidth to 60 degrees, the total span over which measurements can be taken in the 9 hour time frame is reduced to 57 minutes, the trends remain the same however, with steady reductions in the trace of the covariance except in GEO with one baseline. Due to the reduction in measurements compared to

the 75 degree beamwidth case the uncertainty does not shrink down nearly as far. Finally, using a 45 degree beamwidth, a total of 27 minutes is available for measurements, but the trends are still the same as with the other beamwidth cases. Three other inclinations for the LEO satellites were considered and their available measurement times over a 9 hour span are listed in Table 4.5. As the inclination of the LEO satellite increases, the window of available time for data acquisition reduces significantly. This reduction is due to the west-ward drift of the node which impacts a higher inclination orbit's measurement window more than a lower inclination orbit. There is one exception and that is the 30 degree LEO inclination with a 45 degree beamwidth case which has a higher available time for which the geometry is favorable to take measurements. This is simply an artifact of the geometry from the locations of the TXs listed in Table 4.4 and the orbits listed in Table 4.3.

Table 4.5: Time available to take measurements with a GEO-LEO setup in a 9 hour period [min]

Beamwidth	LEO Inclination			
	0°	30°	60°	90°
45°	18	27	12	12
60°	72	57	33	30
75°	120	108	57	51

Next we examine the CRLB for the GEO-MEO case with a 75 degree beamwidth constraint, shown in Figure 4.17. A 24 hour time span was chosen over the 9 hour span with the LEO case to ensure that two data arcs were available. Once again the one baseline case remains at a low degree of observability for the GEO satellite and the two baseline case now has a noticeable gap in performance compared to the three or more baseline cases with the MEO satellite. The reduced relative dynamics of the GEO-MEO case compared to the GEO-LEO case reduces the amount of available information. This is confirmed by the GEO-LEO OD setup having a lower magnitude of the trace of the diagonal of the covariance even while utilizing far fewer measurements. Over the 24

hour span 648 minutes can be utilized for taking measurements using a 75 degree beamwidth, this cuts down to 516 minutes with 60 degrees and finally to 381 minutes with a 45 degree beamwidth.

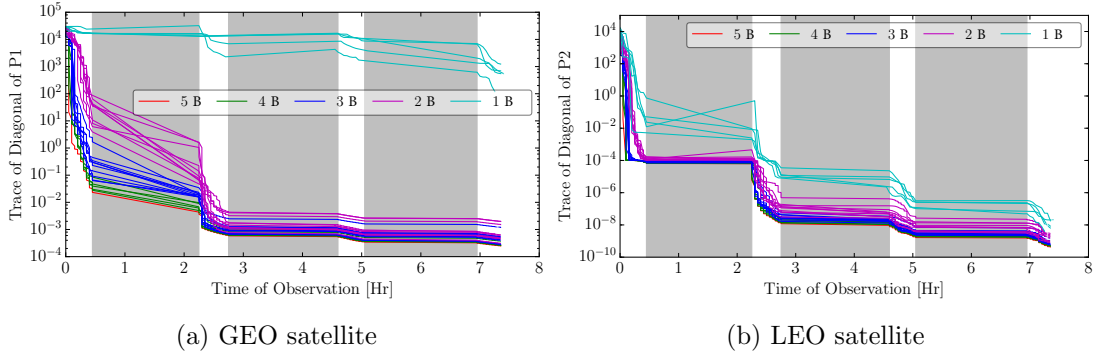


Figure 4.16: GEO-LEO CRLB: trace of covariance for TDOA/FDOA with varying number of baselines

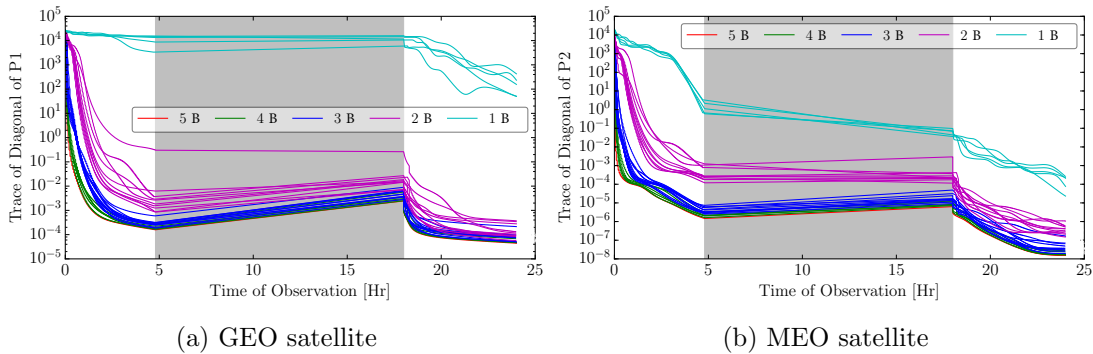


Figure 4.17: GEO-MEO CRLB: trace of covariance for TDOA/FDOA with varying number of baselines

Finally in Figure 4.18, we show the CRLBs using two GEO satellites. Naturally, both satellites are visible at all times resulting in a continuous arc of measurements. Due to the low relative dynamics, the GEO-GEO scenario performs the worst out the three orbit regimes. The one baseline case is completely unobservable with the two and three baseline cases showing low degrees of observability compared to using four or more baselines. The uncertainties on the GEO satellites while significantly reduced from the a-priori values are still high compared to the GEO uncertainties when coupled with either a LEO or MEO satellite. While OD is possible with a GEO-GEO satellite

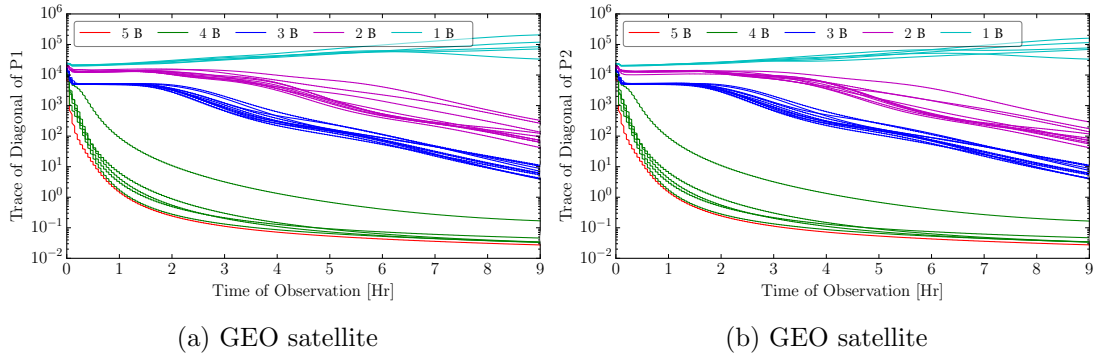


Figure 4.18: GEO-GEO CRLB: Trace of Covariance for TDOA/FDOA with varying number of baselines

setup, it is recommended that four or more baselines are utilized to obtain a good OD solution. Furthermore due the low relative dynamics of the two GEO satellites, the various beamwidth sizes do not have an affect other than constricting the maximum longitudinal separation between the satellites.

4.1.7.2 GEO Primary + LEO-to-GEO Secondary with Fixed Number of Baselines

The second component is examining the CRLB for various satellite pairs while keeping the number of baselines fixed. All i TXs listed in Table 4.4 are used in conjunction with the reference TX to create five baselines. In Figure 4.19 we show how the CRLB changes as a GEO satellite is paired with secondary satellites ranging from LEO to GEO. For conciseness we show the Root-Sum-Square (RSS) of the position and velocity components for each of the satellite CRLBs. The left column of figures are the results pertaining to the GEO primary satellite while the right column of figures are the results for the secondary satellite ranging from LEO to GEO. Of course while the primary satellite remains the same, the secondary satellite pairing affects the CRLB of the primary. The abscissa indicates the observation time span. The ordinate shows the semi-major axis of the secondary satellite as a fraction of a circular GEO orbit. The applicate indicates the RSS covariance values of position, velocity and coefficient of reflectivity. Table 4.6 lists the orbital parameters for both satellites at epoch. Recall that the dynamical models implemented are not

just that of 2-body consequently the resulting orbits will not remain circular but will be slightly perturbed.

Table 4.6: Satellite orbital elements for dual-satellite CRLB analysis

	a [km]	e	i [deg]	Ω [deg]	ω [deg]	ν [deg]	C_r
GEO	42164.14	0	0	0	0	255	0.04
LEO-GEO	6746.26 - 48910.40	0	0	0	0	260	0.06

From Figure 4.19 there are several important things that should be pointed out. First, notice that when the secondary satellite is also in a GEO orbit, denoted by the 1 on the ordinate, the covariance does not collapse significantly. This is a region of lower observability due to the low relative velocity of the satellites with respect to the stations. This affects every estimated component of both satellites. Second, we find that pairing the primary GEO satellite with a lower orbiting secondary satellite such as a LEO, the covariance drops down to very low levels for the secondary. This is shown by the light blue areas of Figures 4.19(b) and 4.19(d). The measurement equations do not directly include the coefficient of reflectivity, therefore C_r can only be measured over time as a result of the changing dynamics. We find evidence of this in Figures 4.19(e) and 4.19(f) because a significant amount of time has passed before the covariance finally starts dropping. Finally, the GEO primary satellite does not obtain covariance levels as low as the secondary in the majority of cases. Once again this is due to the low relative velocity with respect to the stations. Other cases, in which both primary and secondary satellites varied from LEO to GEO orbits, not included in this dissertation, showed significant reductions in covariance for both satellites. It is clear from this CRLB covariance analysis however, that using five baselines with any satellite pairing configuration results in an observable setup, even the GEO-GEO case, despite being less observable than the other pairings.

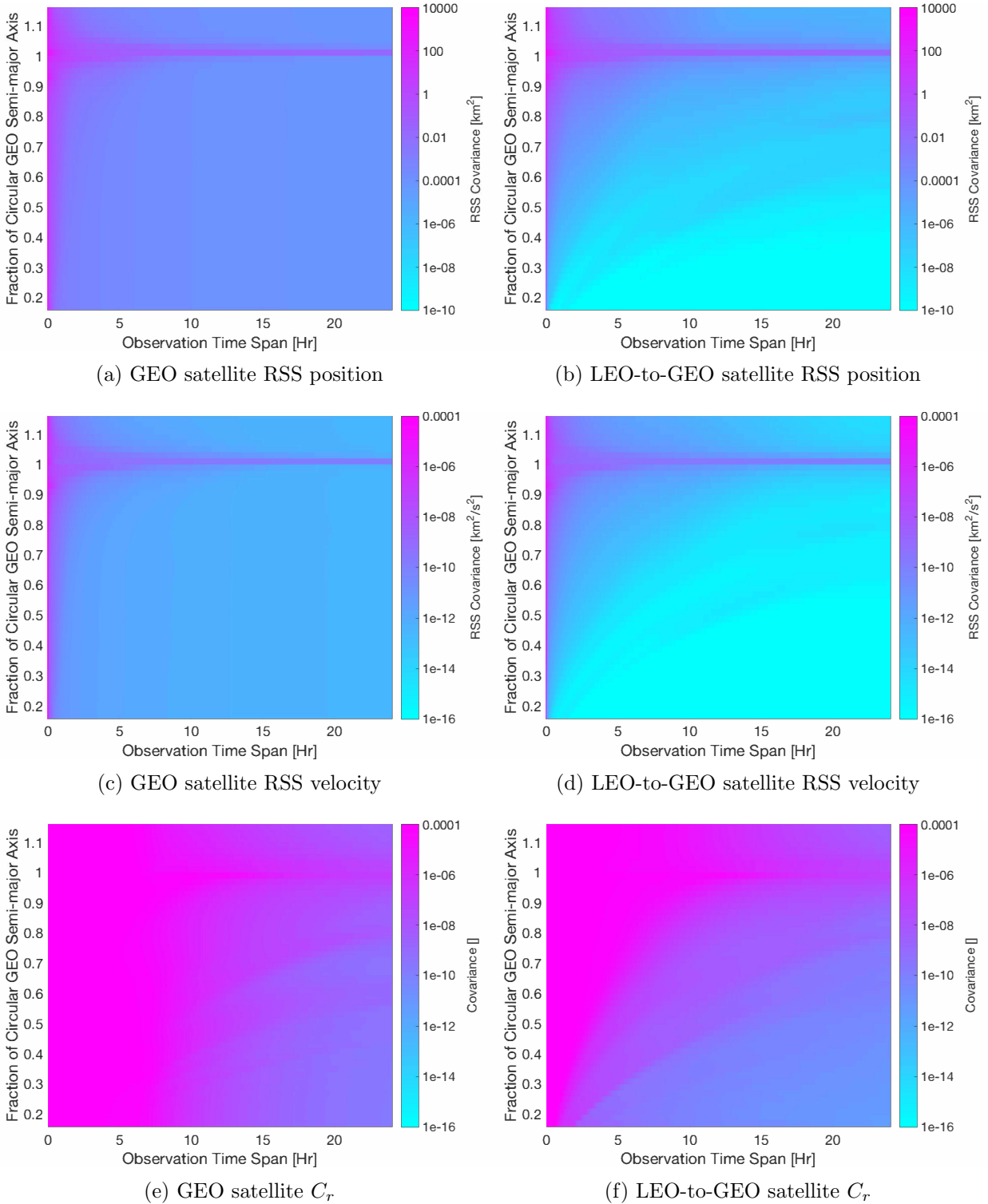


Figure 4.19: Dual-satellite CRLB of a GEO satellite (left column) paired with LEO-to-GEO secondary satellite (right column). Secondary satellite semi-major axis shown on ordinate. Showing CRLB covariance bounds using TDOA/FDOA measurements over various observation time spans shown on abscissa. Five baselines used.

4.2 Dual-Satellite Orbit Determination

In this section we show a comparison of the state uncertainty obtained with the TDOA and FDOA measurements and the state uncertainty obtained with range and range-rate measurements. This comparison covers a GEO primary paired with a secondary ranging from LEO to GEO, similar in setup to Figure 4.19 with orbits defined in Table 4.6. Then we show the state errors and covariances between TDOA/FDOA, range/range-rate, and range/range-rate with biases for three different scenarios: GEO-LEO, GEO-MEO, and GEO-GEO pairings. The biases imposed are only in range and not range-rate with a maximum bias of four meters. In reality range biases can be significantly larger but we show that even with small biases the state errors quickly exceed the covariance bounds and the TDOA/FDOA measurements become favorable even if its RSS covariance bounds are slightly larger.

The estimated states for the dual-satellite orbit determination case are,

$$\mathbf{X} = \left[\mathbf{r}_1^\top \quad \mathbf{v}_1^\top \quad C_{r_1} \quad \mathbf{r}_2^\top \quad \mathbf{v}_2^\top \quad C_{r_2} \right]^\top. \quad (4.53)$$

Equation 4.53 includes the position \mathbf{r} , and velocity \mathbf{v} , as well as the coefficient of reflectivity C_r , of both spacecraft. The time evolution of the states are given by the following dynamics shown in first-order form:

$$\dot{\mathbf{X}}(t) = F(\mathbf{X}, t) = \begin{bmatrix} \dot{\mathbf{r}}_1 \\ \dot{\mathbf{v}}_1 \\ \dot{C}_{r_1} \\ \dot{\mathbf{r}}_2 \\ \dot{\mathbf{v}}_2 \\ \dot{C}_{r_2} \end{bmatrix} = \begin{bmatrix} \mathbf{v}_1 \\ \mathbf{a}_{1_{2B}} + \mathbf{a}_{1_{NS}} + \mathbf{a}_{1_{3B}} + \mathbf{a}_{1_{SRP}} \\ 0 \\ \mathbf{v}_2 \\ \mathbf{a}_{2_{2B}} + \mathbf{a}_{2_{NS}} + \mathbf{a}_{2_{3B}} + \mathbf{a}_{2_{SRP}} \\ 0 \end{bmatrix} \quad (4.54)$$

where the accelerations are due to 2-body (\mathbf{a}_{2B}) and non-spherical (\mathbf{a}_{NS}) effects from the Earth, the Sun and Moon as 3rd bodies (\mathbf{a}_{3B}), and Solar Radiation Pressure (SRP) (\mathbf{a}_{SRP}), all previously

defined in chapter 2. The subscripts 1 and 2 refer to either the primary or secondary satellite.

4.2.1 TDOA/FDOA and Range/Range-Rate CRLB Comparison with Varying Measurement Uncertainties

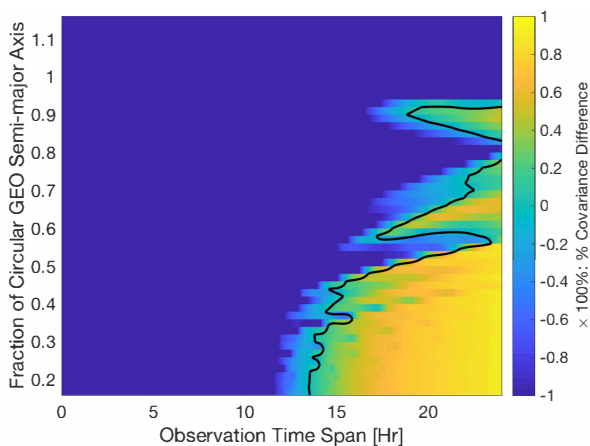
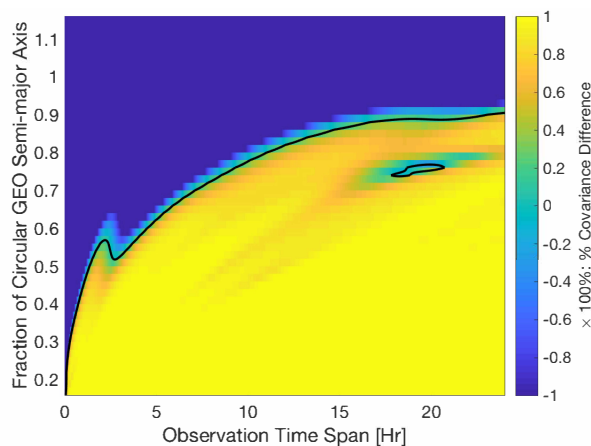
In this section we examine the effect of varying the TDOA/FDOA measurement uncertainty while holding the range and range-rate 1σ uncertainties fixed at 1 m and 1 mm/s. The default values used throughout this dissertation are listed as ‘default’ in Table 4.7 and are values obtained from real-data and an existing TDOA/FDOA hardware architecture. Two deviations from the nominal values are considered, case 1 explores measurement uncertainties 10x larger, while case 2 uses TDOA and FDOA uncertainties 10x smaller. Keep in mind that for every TDOA/FDOA measurement pair, four range and four range-rate measurements are used, this means four times as many measurements are implemented with range/range-rate. Furthermore, in some state components the uncertainties are lower with range and range-rate over all the observation time spans and semi-major axes, indicated by a solid blue panel. However, that does not mean the state uncertainties using TDOA and FDOA are not significantly reduced, which was previously demonstrated by the 3D CRLB plots. Finally, biases do not effect the uncertainties, so while some of the state uncertainty components may be lower using range and range-rate, the actual state errors due non-solved for biases could be higher than with TDOA and FDOA.

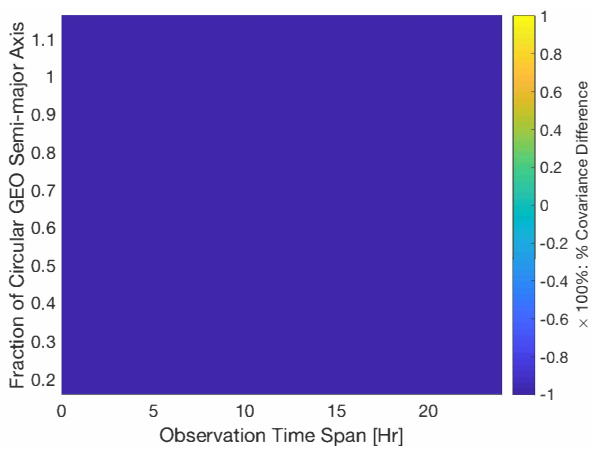
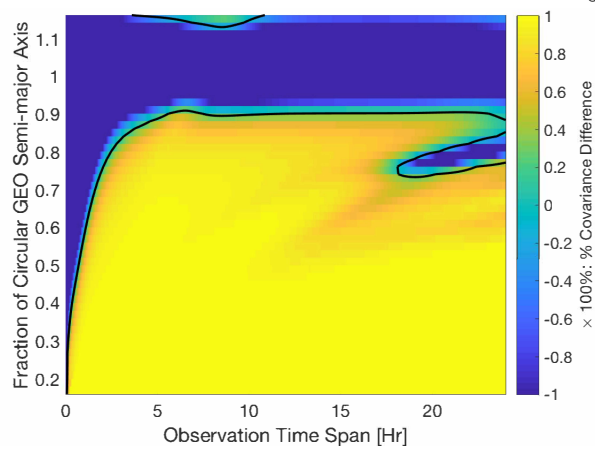
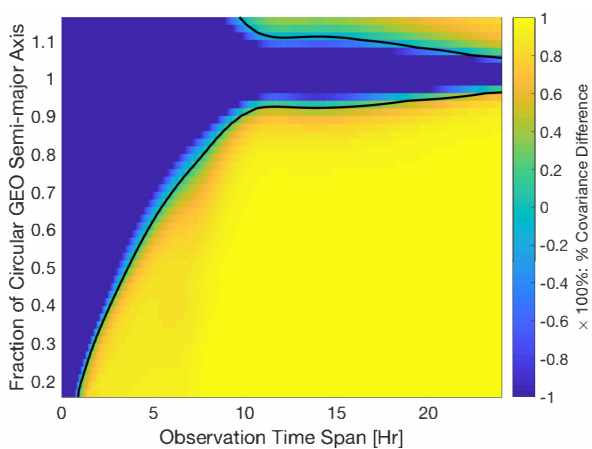
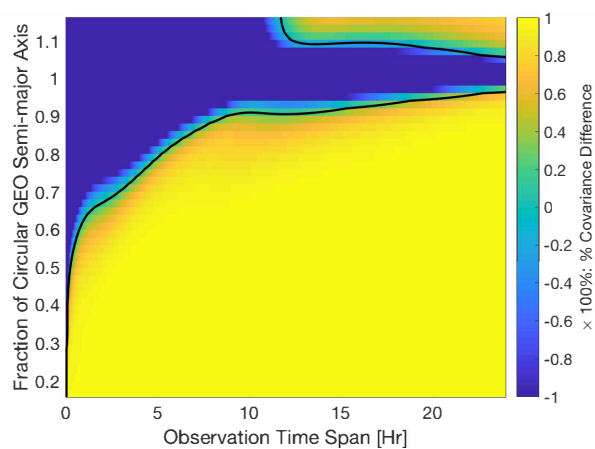
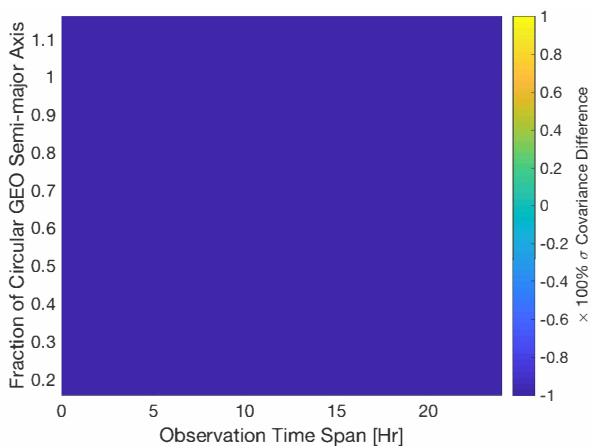
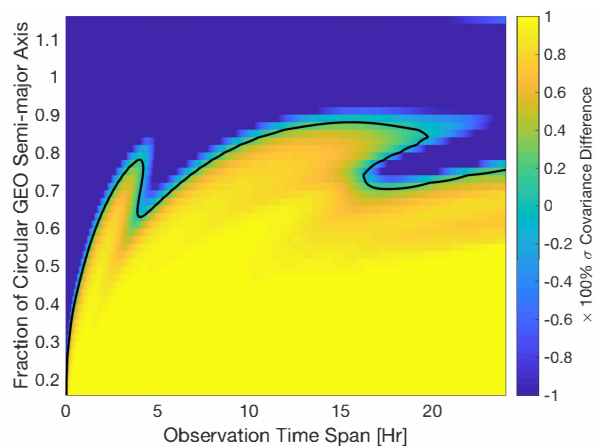
Table 4.7: Measurement Uncertainty Ranges

	TDOA [μ s]	FDOA [mHz]
default	0.035	0.2
case 1	0.35	2.0
case 2	0.0035	0.02

Figure 4.20 uses the nominal measurement uncertainties and is broken down into 14 subfigures, each one corresponding to one of the estimated states from the two satellites. The left column

corresponds to the GEO primary satellite and the right column refers to the LEO to GEO secondary satellite states. The states are presented in the RIC body frame. The z-axis or the color axis of the plots is the percent difference in the covariance between TDOA/FDOA and range/range-rate with yellow indicating a smaller uncertainty using TDOA/FDOA while blue indicates the covariance is smaller using range/range-rate. The a-priori uncertainties are the same as before and listed in Table 4.2. In a number of the states, the secondary satellite has more favorable TDOA/FDOA coverage compared to the primary satellite. A prime example of this is in the radial, in-track, and radial velocity directions in addition to the coefficient of reflectivity. This can be attributed to the primary being a GEO satellite with a very low relative velocity compared to the stations which significantly reduces the amount of information available. In general however, the secondary satellite, when not in GEO, has significantly lower uncertainties when using TDOA and FDOA compared to the range and range-rate measurements. When the secondary is in GEO, range and range-rate provide lower covariances as seen by the dark blue horizontal band, this is because it is a region of lower observability previously discussed in Figure 4.19.

(a) R_1 (b) R_2

(c) I_1 (d) I_2 (e) C_1 (f) C_2 (g) \dot{R}_1 (h) \dot{R}_2

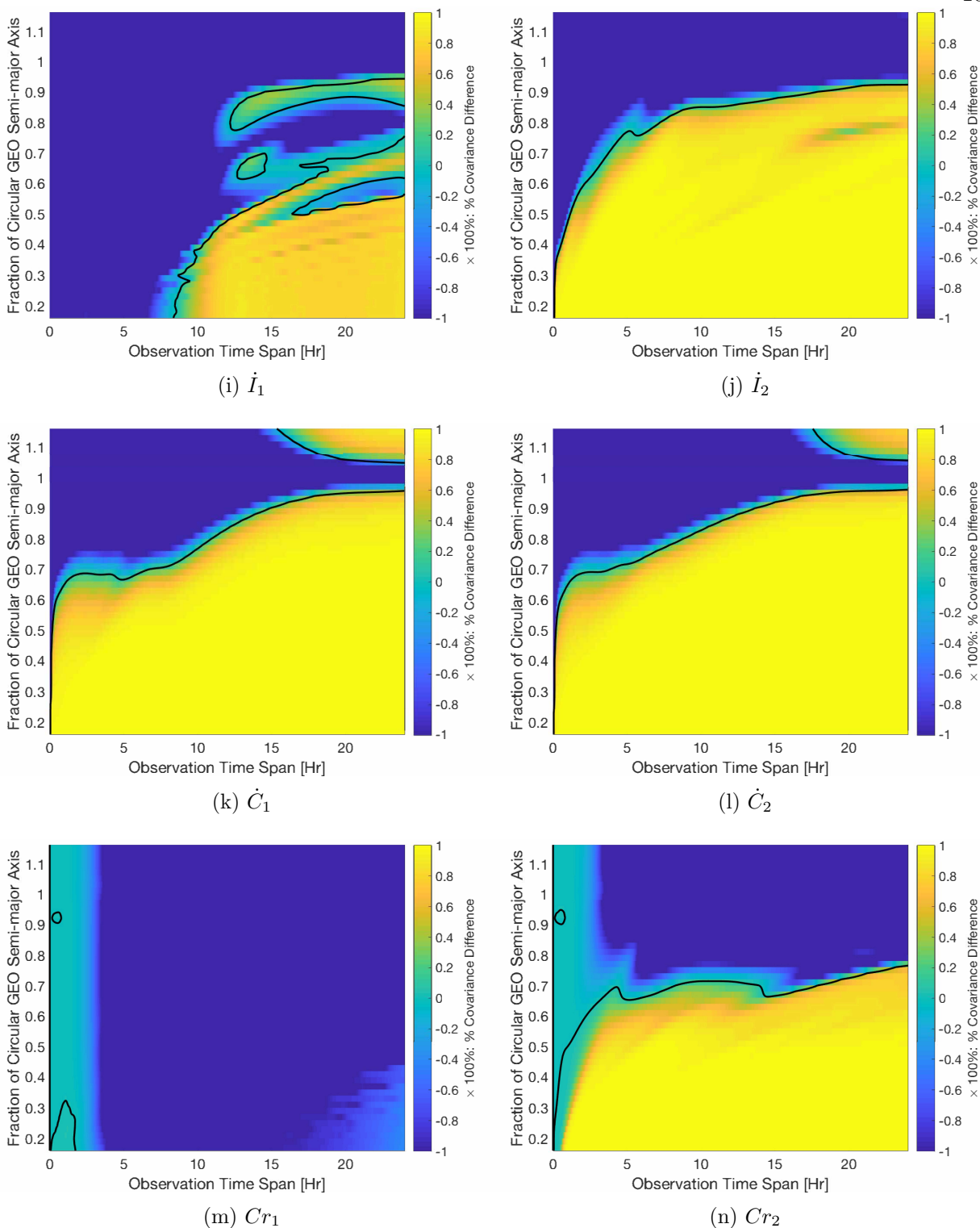
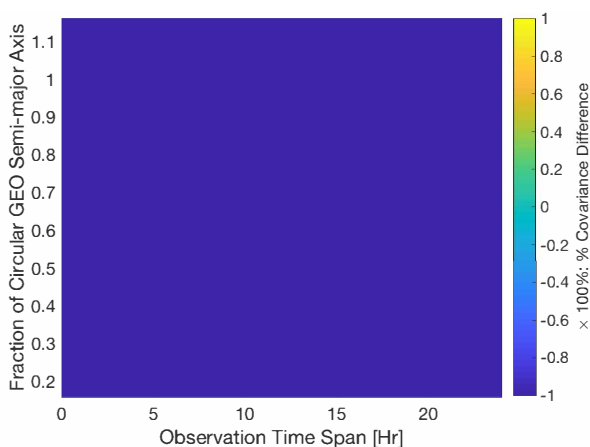
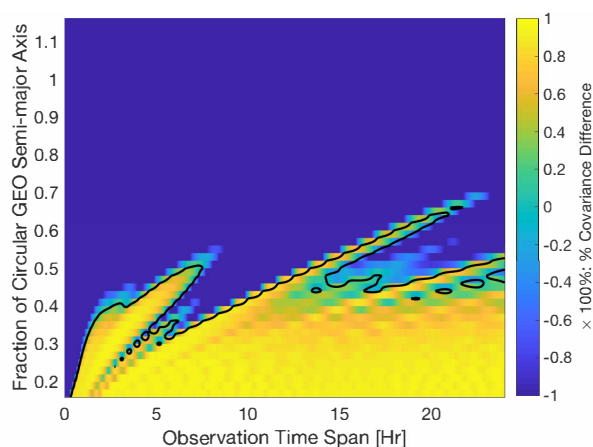
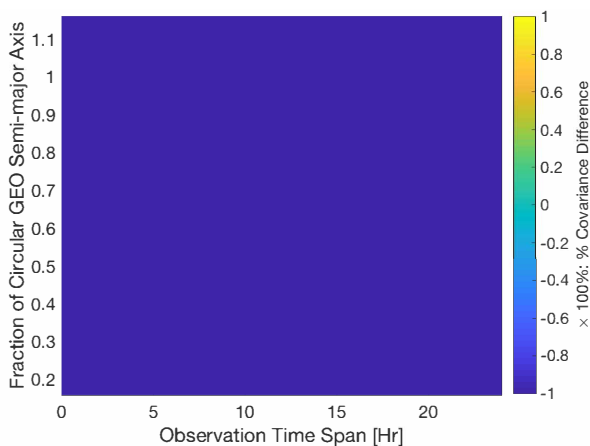
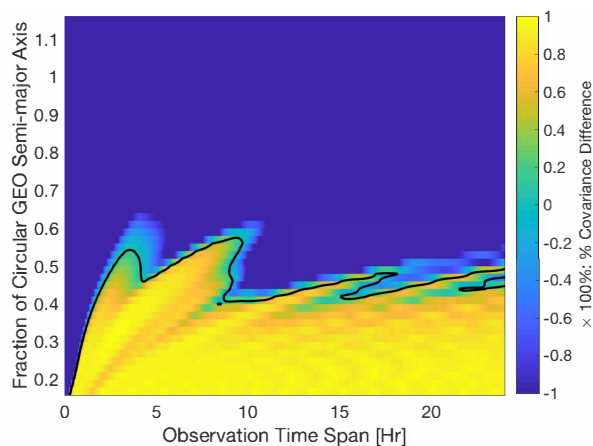
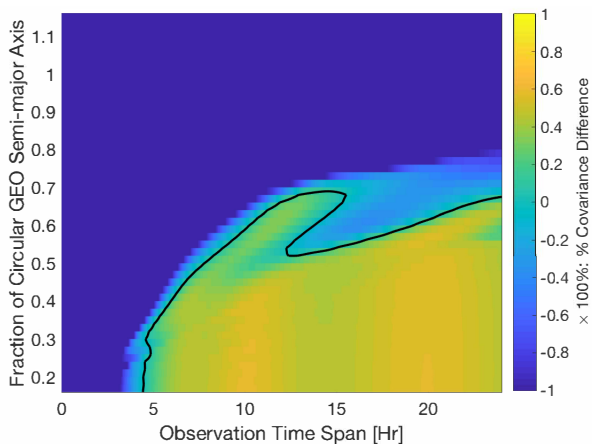


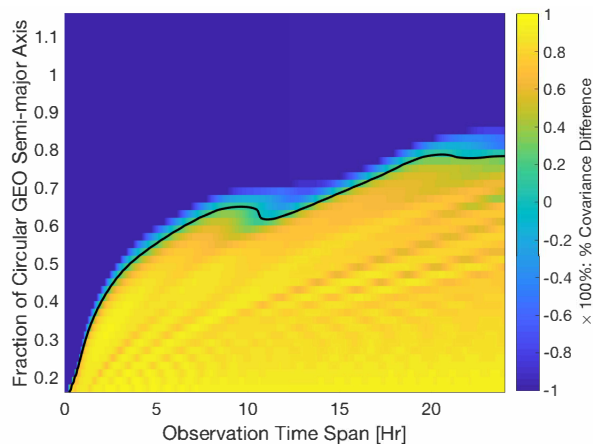
Figure 4.20: Dual-satellite estimation of a GEO satellite (left column) paired with LEO-to-GEO secondary satellite (right column). Secondary satellite semi-major axis shown on ordinate. Showing % difference of CRLB covariance bounds between TDOA/FDOA and range/range-rate measurements over various observation time spans shown on abscissa. Color values above 0 indicate a region where TDOA/FDOA has lower covariance bounds compared to range/range-rate and vice versa. Five baselines used.

In the following 14 plots, again we have the GEO satellite in the left column and the secondary satellite in the right column using TDOA and FDOA measurement uncertainties from case 1 in Table 4.7. As expected, the orbital regions where TDOA and FDOA has lower 3σ uncertainties are reduced. With the GEO primary satellite, only the cross-track direction in both position and velocity still provide lower uncertainties when MEO satellites or below are used for the secondary. When the secondary satellite is a MEO or below in semi-major axis the uncertainties of the secondary are still lower than with range and range-rate.

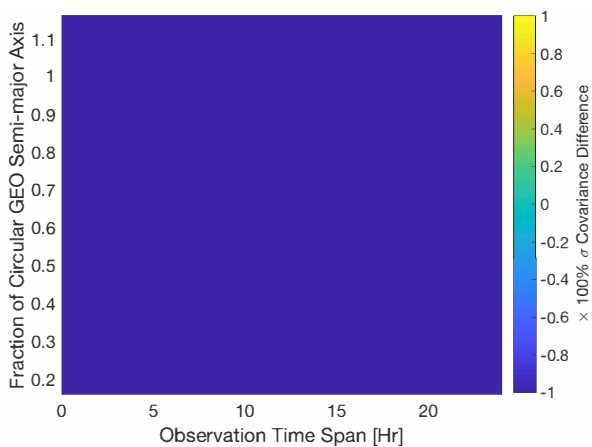
(a) R_1 (b) R_2 (c) I_1 (d) I_2



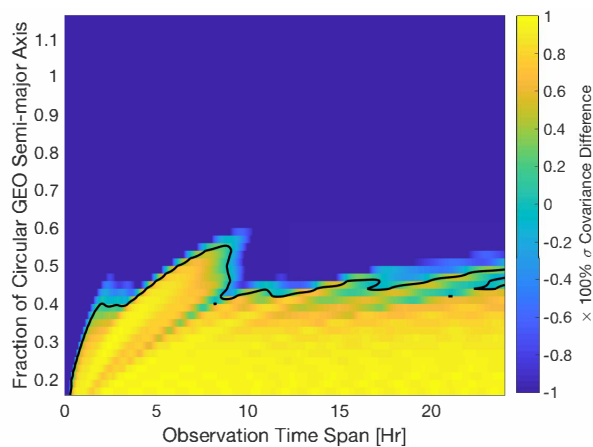
(e) C_1



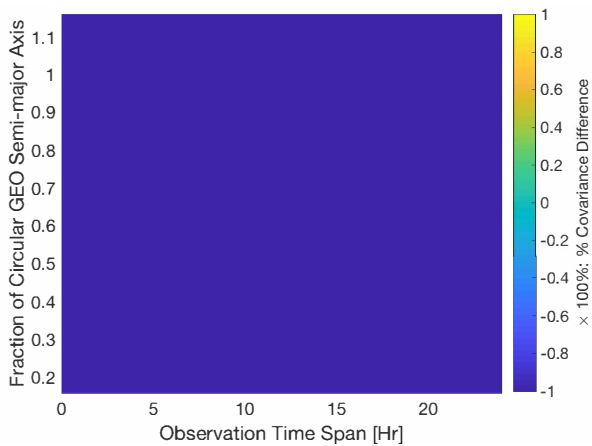
(f) C_2



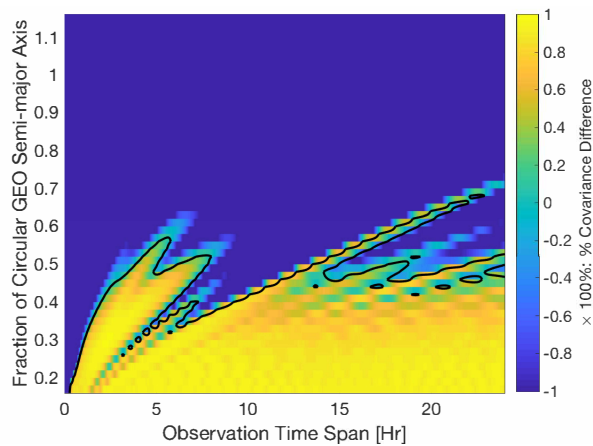
(g) \dot{R}_1



(h) \dot{R}_2



(i) \dot{I}_1



(j) \dot{I}_2

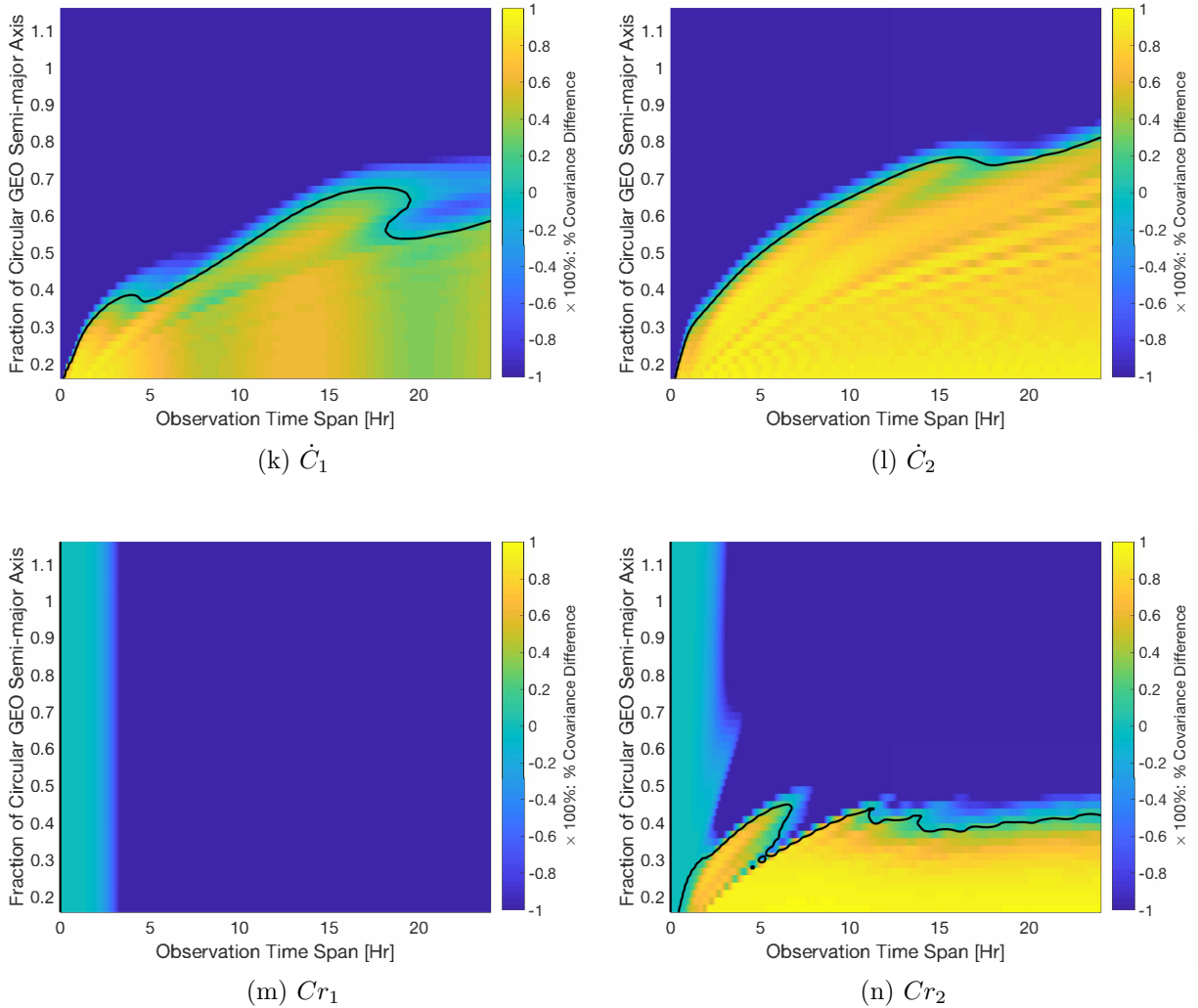
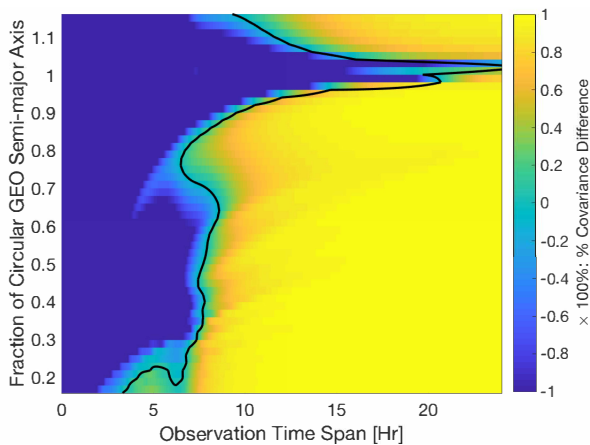
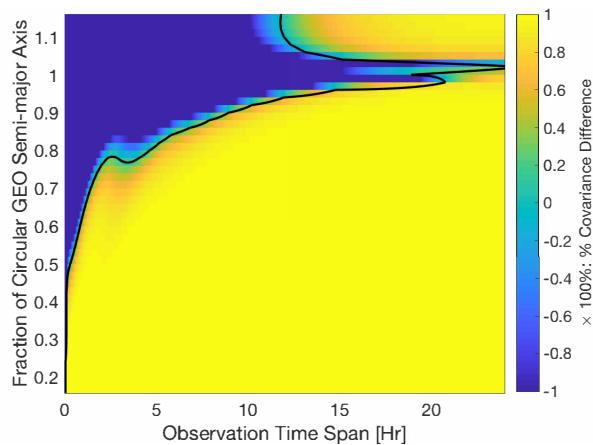
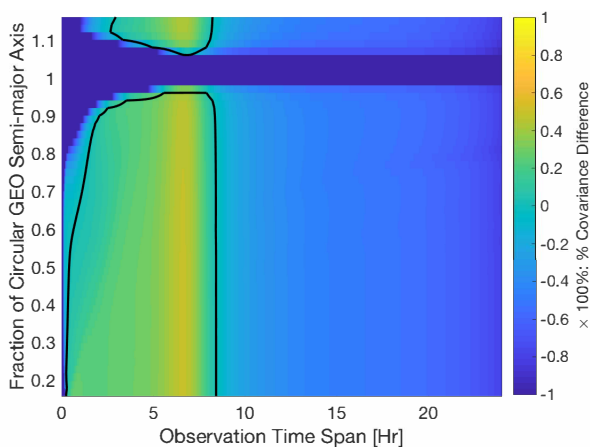
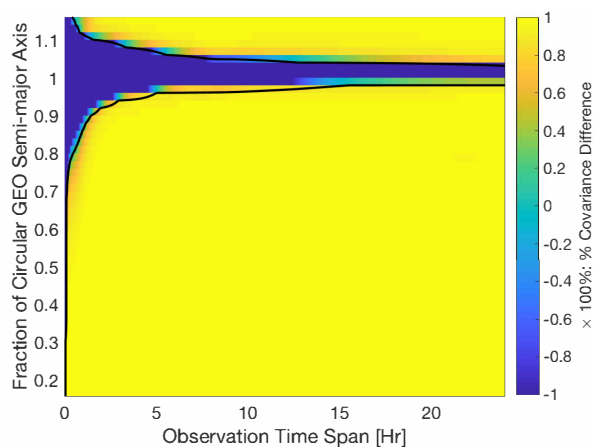


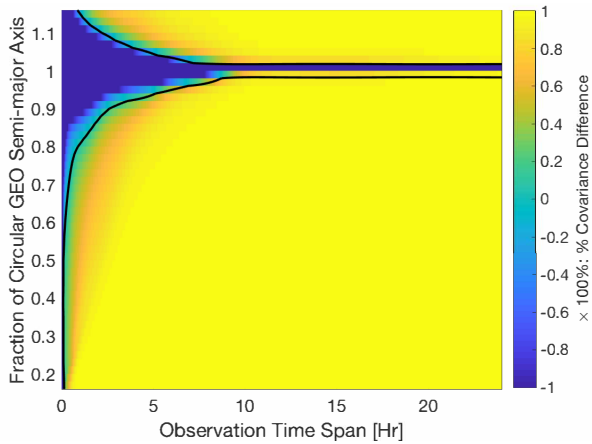
Figure 4.21: Case 1: Dual-satellite estimation of a GEO satellite (left column) paired with LEO-to-GEO secondary satellite (right column). Secondary satellite semi-major axis shown on ordinate. Showing % difference of CRLB covariance bounds between TDOA/FDOA and range/range-rate measurements over various observation time spans shown on abscissa. Color values above 0 indicate a region where TDOA/FDOA has lower covariance bounds compared to range/range-rate and vice versa. Five baselines used.

In this last scenario we use the measurement uncertainties from case 2 in Table 4.7. From Figure 4.22 we see that even the GEO primary satellite now has large regions in the components where the TDOA and FDOA uncertainties are lower than with range and range-rate. The exception includes in-track position, radial velocity, and when the secondary is also in a GEO orbit, for all state components. For the secondary satellite, only when it is in GEO, are the uncertainties larger than

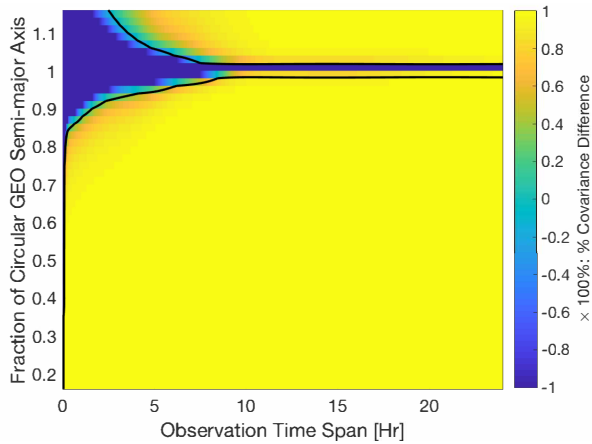
those obtained using range and range-rate. Of course, the large regions with lower uncertainties using TDOA and FDOA are expected because the uncertainty for FDOA is much lower than that of range-rate while TDOA and range are similar, even with range and range-rate having four times as many measurements.

(a) R_1 (b) R_2 (c) I_1 (d) I_2

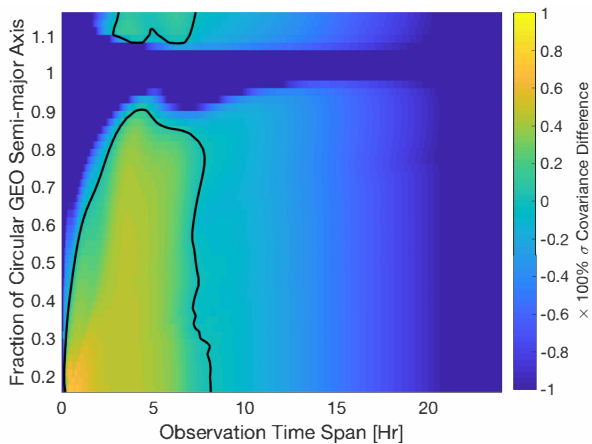
In the following three sections we look at the state error performance in addition to the covariances of three different satellite pairings.



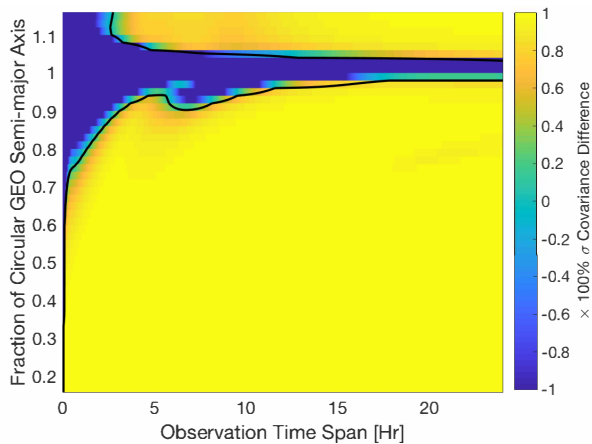
(e) C_1



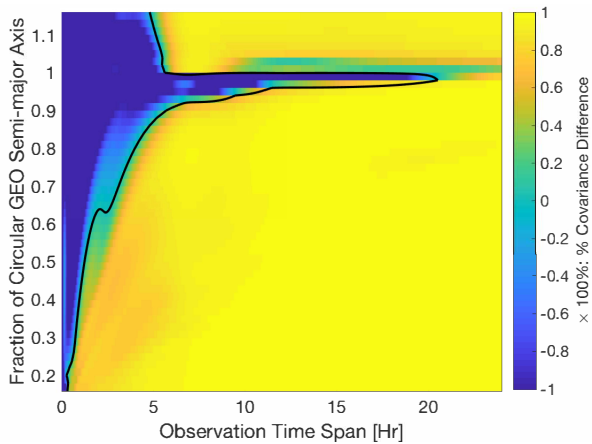
(f) C_2



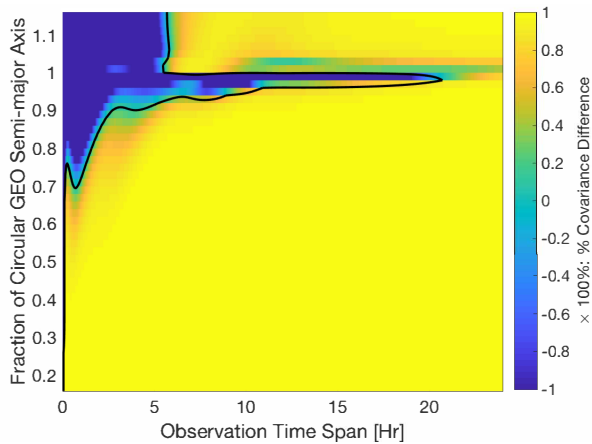
(g) \dot{R}_1



(h) \dot{R}_2



(i) \dot{I}_1



(j) \dot{I}_2

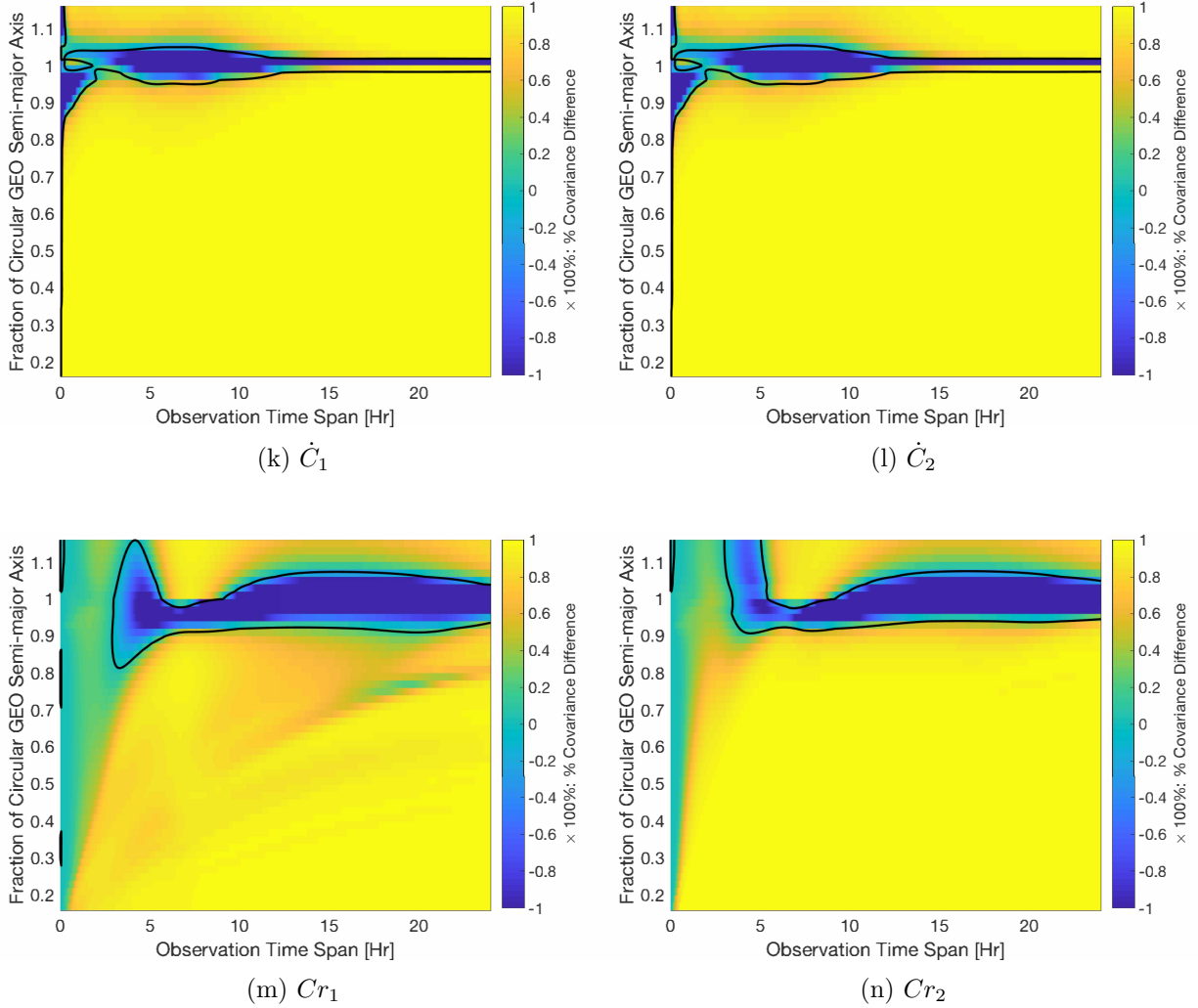


Figure 4.22: Case 2: Dual-satellite estimation of a GEO satellite (left column) paired with LEO-to-GEO secondary satellite (right column). Secondary satellite semi-major axis shown on ordinate. Showing % difference of CRLB covariance bounds between TDOA/FDOA and range/range-rate measurements over various observation time spans shown on abscissa. Color values above 0 indicate a region where TDOA/FDOA has lower covariance bounds compared to range/range-rate and vice versa. Five baselines used.

4.2.2 GEO-LEO Orbit Determination

In this section we show the state errors and covariances of doing OD on a GEO-LEO pair of satellites. The orbits are defined by the ‘GEO-’ and ‘LEO 30°’ orbital elements in Table 4.3 and reproduced in Table 4.8. Furthermore, only three baselines are used, the reference TX is linked with the Boston, Miami and San Diego secondary TXs for an observation span of 9 hours. The

last data gap, in this scenario, is not shown in Figures 4.23 - 4.25. For conciseness the RSS of the position and velocity is shown rather than each component, this can be somewhat misleading however because if one component has a large covariance or error it will dominate. Therefore we also include Table 4.9 which shows the covariance and state error at the end of the observation span for all components for TDOA/FDOA, range/range-rate, and range/range-rate with a bias. The legend for the figures is defined as: TF for TDOA/FDOA, RR for range/range-rate, and $RR + b$ for range/range-rate with a bias. In Figure 4.23(a) the state errors between TDOA/FDOA and range/range-rate are comparable after the second LEO pass but range/range-rate with a bias is outside of its covariance bounds and has significantly larger errors than TDOA and FDOA. We see that the covariance bounds for TDOA/FDOA in position, velocity, and AGOM for the GEO satellite are slightly larger than those for range and range-rate but from Table 4.9 we see that only two components of the covariance are larger using TDOA and FDOA than range and range-rate, namely the in-track position direction and the radial velocity direction. The LEO satellite, after the second pass, collapses its covariance very quickly and all components have a much lower uncertainty and state error using TDOA and FDOA.

Table 4.8: Orbit parameters of GEO-LEO satellites

	a [km]	e	i [deg]	Ω [deg]	ω [deg]	ν [deg]	C_r
GEO	42166.4	0	0.08	105.1	101.4	286.7	0.04
LEO 30°	8377.7	0.01	30	270.2	354.9	263.4	0.06

In Table 4.9 we see that 12 out of the 14 satellite state components have a lower covariance and state error using the TDOA and FDOA measurements. Furthermore the LEO satellite is down to millimeter level uncertainty in position and 10s of micrometers/second in velocity. The TDOA and FDOA measurements provide especially good information in the cross-track direction compared to the range and range-rate observables.

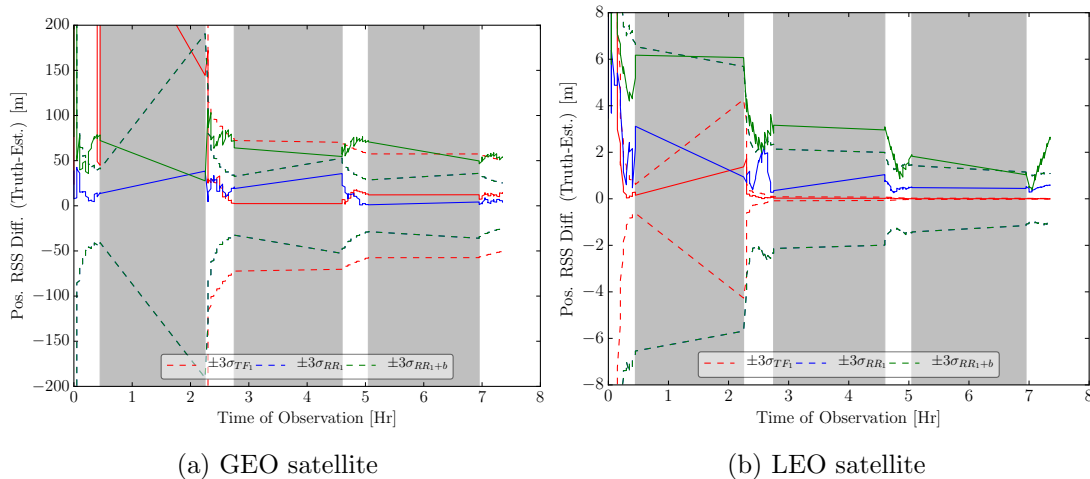


Figure 4.23: GEO-LEO: RSS position state errors and 3σ covariance for TDOA/FDOA, range/range-rate with and without bias

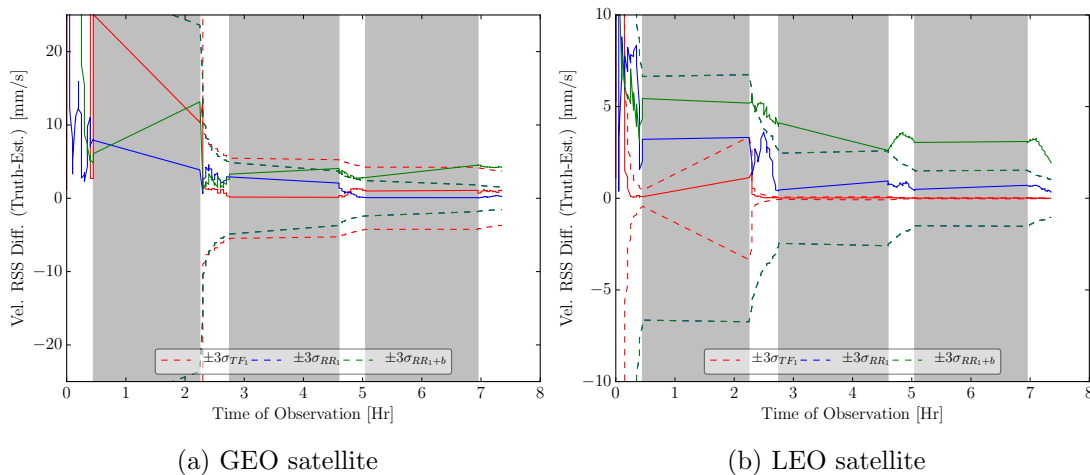


Figure 4.24: GEO-LEO: RSS velocity state errors and 3σ covariance for TDOA/FDOA, range/range-rate with and without bias

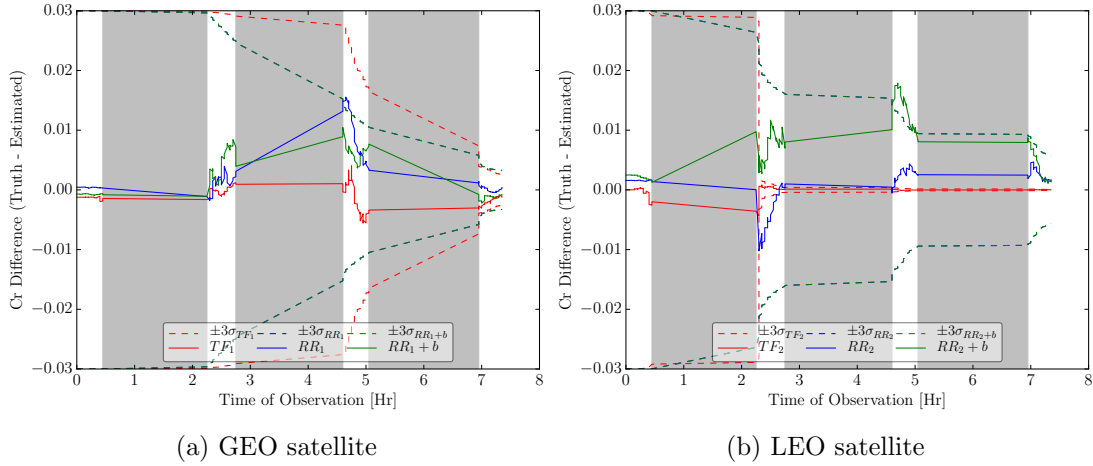


Figure 4.25: GEO-LEO: AGOM state errors and 3σ covariance for TDOA/FDOA, range/range-rate with and without bias

Table 4.9: GEO-LEO: $\pm 3\sigma$ covariance and state errors at the end of 9 hour observation span

		TDOA/FDOA		Range/Range-Rate		Range/Range-Rate + bias	
		$\pm 3\sigma$	Err.	$\pm 3\sigma$	Err.	$\pm 3\sigma$	Err.
R_{GEO}	[m]	0.5	-0.1	2.5	0.4	2.5	-6.4
R_{LEO}	[m]	0.006	-0.002	0.5	0.08	0.5	-0.6
I_{GEO}	[m]	50.4 [†]	-14.6	6.7	-2.6	6.7	4.0
I_{LEO}	[m]	0.005	-0.002	0.6	0.2	0.6	-0.08
C_{GEO}	[m]	1.3	-0.2	24.0	3.1	24.0	-53.2
C_{LEO}	[m]	0.01	-0.002	0.8	-0.5	0.8	-2.5
\dot{R}_{GEO}	[mm/s]	3.7 [†]	1.1	0.5	0.1	0.5	-0.7
\dot{R}_{LEO}	[mm/s]	0.009	0.003	0.8	-0.3	0.8	0.3
\dot{I}_{GEO}	[mm/s]	0.03	0.02	0.2	-0.02	0.2	0.4
\dot{I}_{LEO}	[mm/s]	0.004	0.002	0.4	-0.04	0.4	0.5
\dot{C}_{GEO}	[mm/s]	0.1	0.02	1.4	-0.2	1.4	-4.1
\dot{C}_{LEO}	[mm/s]	0.001	0.001	0.5	0.07	0.5	1.8
$AGOM_{GEO}$	□	0.003	-0.001	0.003	0.0004	0.003	-0.0008
$AGOM_{LEO}$	□	0.0001	0.0	0.006	0.001	0.006	0.002

[†] TDOA/FDOA 3σ covariance component worse than Range/Range-Rate

4.2.3 GEO-MEO Orbit Determination

The previous section’s analysis is repeated with a GEO-MEO pair of satellites, where the orbits are defined by the ‘GEO-’ and ‘MEO’ orbital elements in Table 4.3 and show again for convenience in Table 4.10. The same three baselines are used from the GEO-LEO case. A 24 hour observation span is used to ensure that the MEO satellite has two arcs of data. From Figures 4.26(a) and 4.27(a) we see that the RSS covariance with TDOA and FDOA is larger than with range and range-rate but from Table 4.11 only the GEO in-track position and radial velocity uncertainties are larger than those from range and range-rate. The state errors between TDOA/FDOA and range/range-rate are comparable once more, except when a bias is introduced then the state errors are off by nearly 100 m in position and 6 mm/s in velocity at their maximum during the second pass. The covariance for the MEO satellite is lower using TDOA and FDOA but the margin is not as large as with the GEO-LEO pair due to the slower relative velocity of the MEO compared to the stations.

Table 4.10: Orbit parameters of GEO-MEO satellites

	a [km]	e	i [deg]	Ω [deg]	ω [deg]	ν [deg]	C_r
GEO	42166.4	0	0.08	105.1	101.4	286.7	0.04
MEO	24926.5	0	35	110.0	289.6	122.6	0.06

Table 4.11 presents the covariances as well as the state errors for each estimated component. Twelve of the 14 states have a lower covariance and state error using the TDOA and FDOA measurements. In reality the range and range-rate measurements will likely have some biases present, in that case, the TDOA and FDOA state errors are lower in all components compared to the range and range-rate measurements with a small bias.

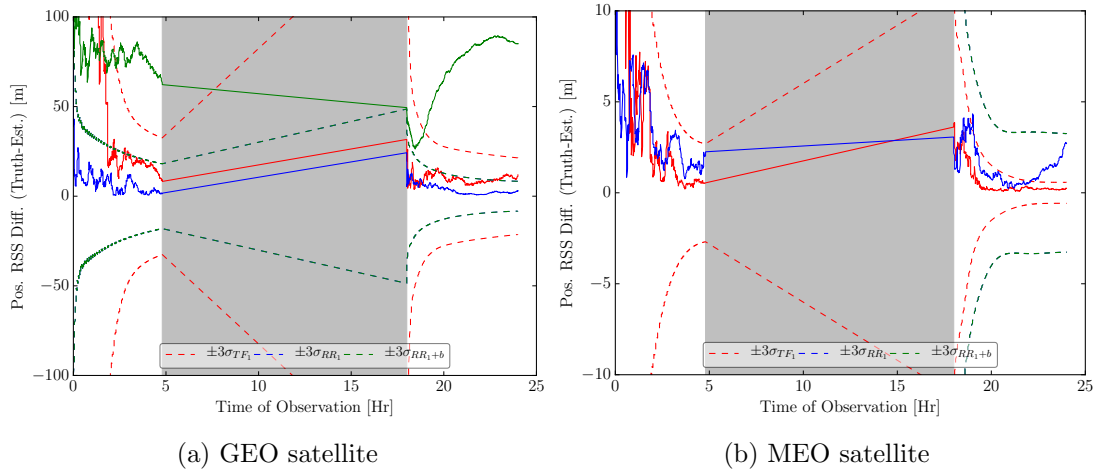


Figure 4.26: GEO-MEO: RSS position state errors and 3σ covariance for TDOA/FDOA, range/range-rate with and without bias

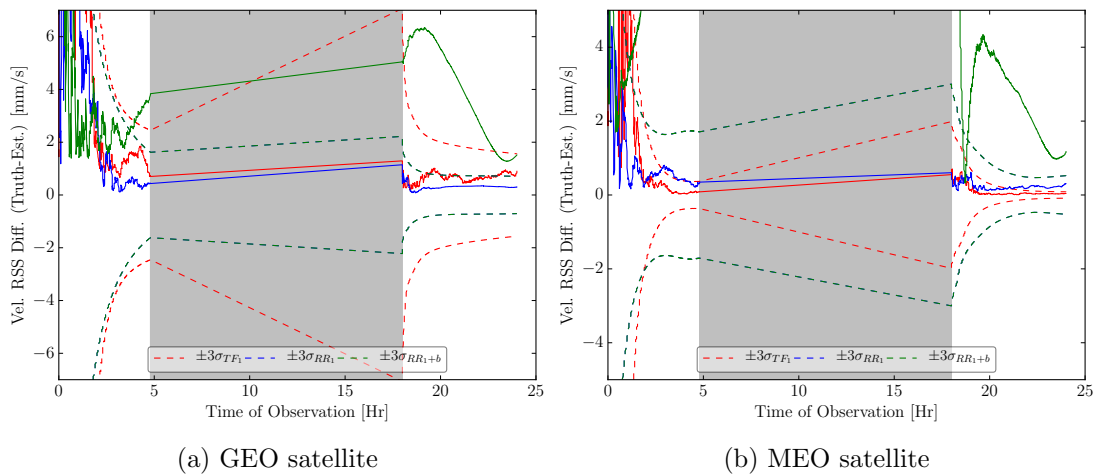


Figure 4.27: GEO-MEO: RSS velocity state errors and 3σ covariance for TDOA/FDOA, range/range-rate with and without bias

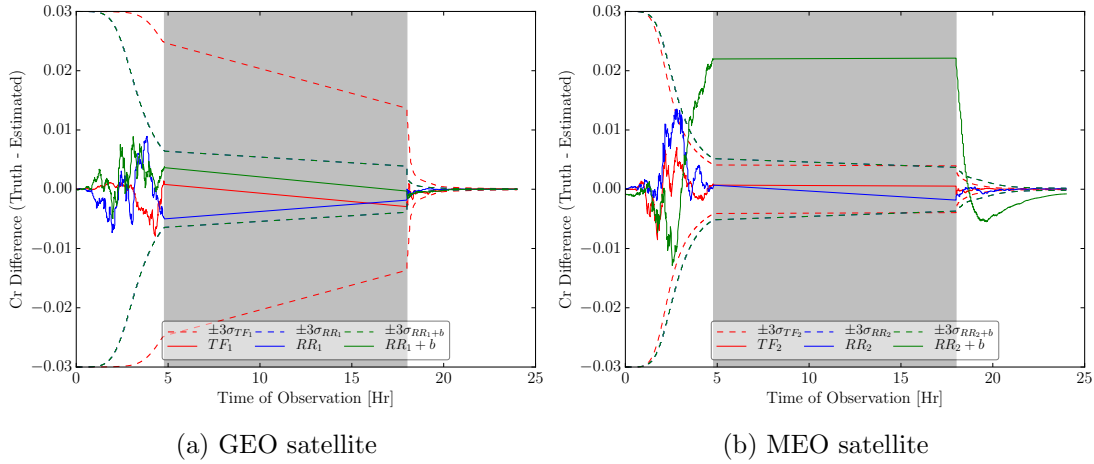


Figure 4.28: GEO-MEO: AGOM state errors and 3σ covariance for TDOA/FDOA, range/range-rate with and without bias

Table 4.11: GEO-MEO: $\pm 3\sigma$ covariance and state errors at the end of 24 hour observation span

		TDOA/FDOA		Range/Range-Rate		Range/Range-Rate + bias	
		$\pm 3\sigma$	Err.	$\pm 3\sigma$	Err.	$\pm 3\sigma$	Err.
R_{GEO}	[m]	0.5	-0.3	0.8	0.4	0.8	-9.4
R_{MEO}	[m]	0.1	0.03	0.6	-0.5	0.6	0.8
I_{GEO}	[m]	21.3 [†]	-11.9	2.6	0.9	2.6	13.1
I_{MEO}	[m]	0.5	0.2	2.3	-1.8	2.3	6.7
C_{GEO}	[m]	0.8	-0.1	7.8	2.8	7.8	-83.5
C_{MEO}	[m]	0.2	-0.03	2.2	-2.0	2.2	-16.1
\dot{R}_{GEO}	[mm/s]	1.6 [†]	0.9	0.2	-0.1	0.2	-1.0
\dot{R}_{MEO}	[mm/s]	0.08	-0.04	0.4	0.3	0.4	-1.1
\dot{I}_{GEO}	[mm/s]	0.04	0.03	0.06	-0.02	0.06	0.6
\dot{I}_{MEO}	[mm/s]	0.02	-0.004	0.09	0.07	0.09	-0.2
\dot{C}_{GEO}	[mm/s]	0.06	-0.02	0.7	-0.3	0.7	-0.9
\dot{C}_{MEO}	[mm/s]	0.02	-0.01	0.4	-0.06	0.4	-0.2
AGOM _{GEO}	□	0.0001	0.0001	0.0	-0.0	0.0	0.0
AGOM _{MEO}	□	0.0001	0.0	0.0002	0.0001	0.0002	-0.0008

[†] TDOA/FDOA 3σ covariance component worse than Range/Range-Rate

4.2.4 GEO-GEO Orbit Determination

The last case we show for completion is a GEO-GEO scenario where the orbits are defined by ‘GEO-’ and ‘GEO’ in Table 4.3 and reproduced once more in Table 4.12. All five baselines are used to ensure good observability as previously discussed for Figure 4.18. As predicted from Figure 4.20 with two satellites in GEO, the range and range-rate observables provide smaller covariances and state errors in all components compared to TDOA and FDOA. The CRLB from Figure 4.19 also showed that for GEO satellites the covariance would take a long time to drop down which is corroborated by Figures 4.29 to 4.31. Yet the a-priori 3σ uncertainty started from 300 km in position and 30 m/s in velocity in each direction as shown in Table 4.2, the covariance has dropped by a factor of a 1000 in both position and velocity over the 24 hour observation span.

Table 4.12: Orbit parameters of GEO-GEO satellites

	a [km]	e	i [deg]	Ω [deg]	ω [deg]	ν [deg]	C_r
GEO ₁	42166.4	0	0.08	105.1	101.4	286.7	0.04
GEO ₂	42166.5	0	0.08	81.0	139.7	266.4	0.06

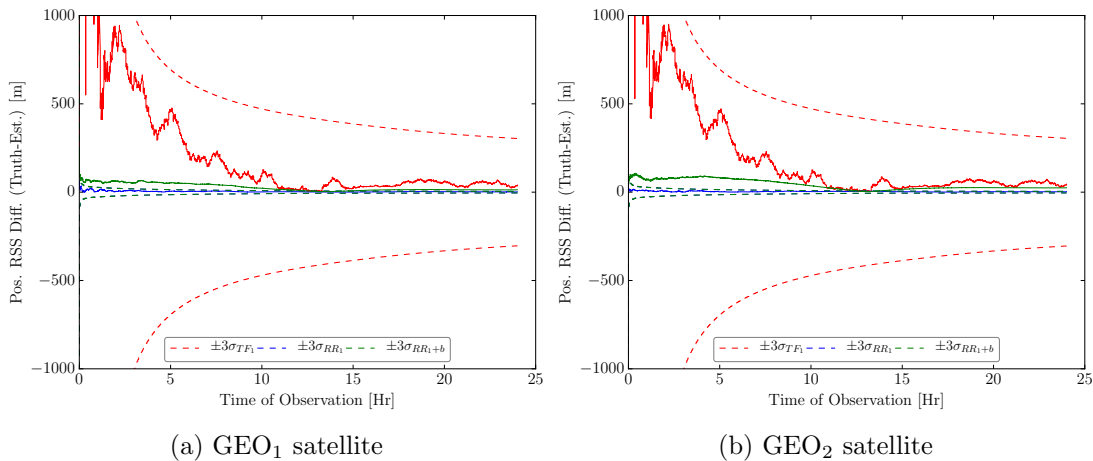


Figure 4.29: GEO-GEO: RSS position state errors and 3σ covariance for TDOA/FDOA, range/range-rate with and without bias

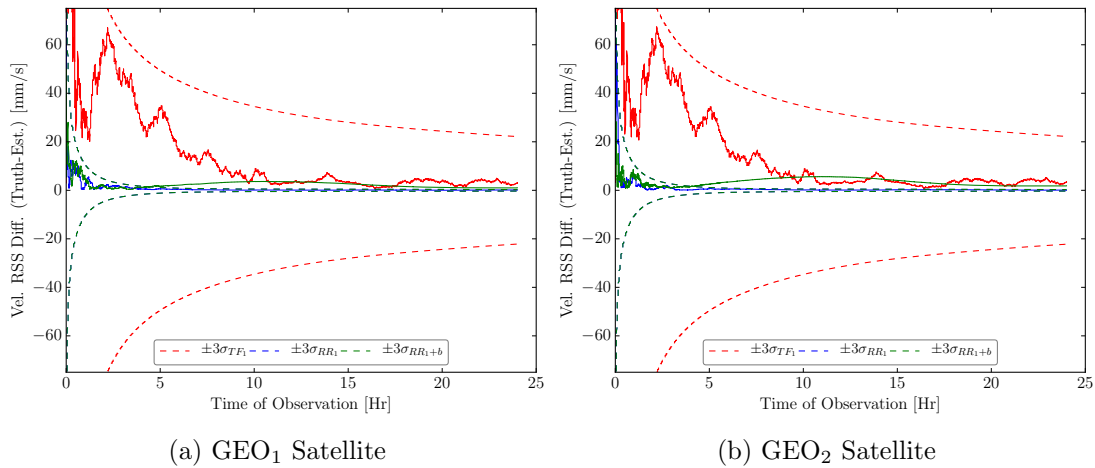


Figure 4.30: GEO-GEO: RSS velocity state errors and 3σ covariance for TDOA/FDOA, range/range-rate with and without bias

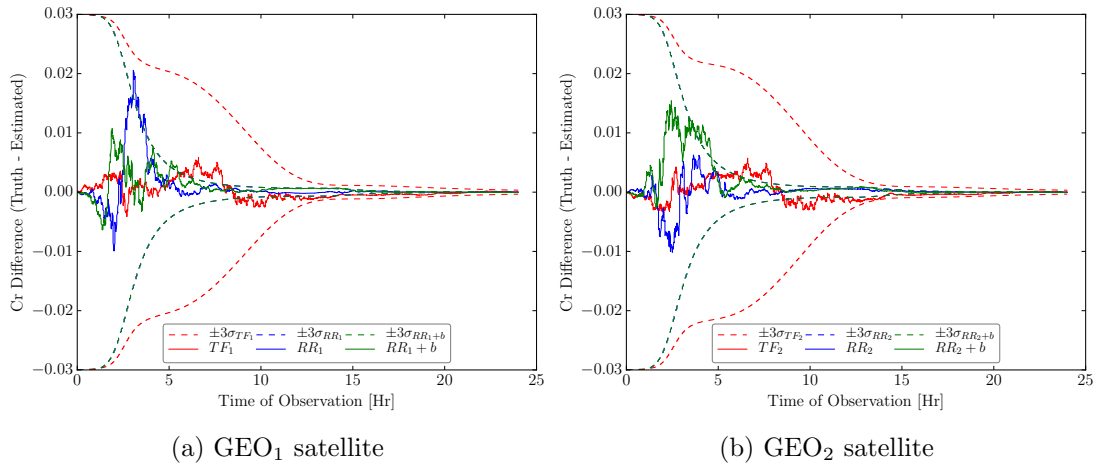


Figure 4.31: GEO-GEO: AGOM state errors and 3σ covariance for TDOA/FDOA, range/range-rate with and without bias

Table 4.13 shows the comparison of the TDOA/FDOA observables to range/range-rate with and without biases present. While the results are not as good as using range and range-rate in this case, TDOA and FDOA can still be used to reduce the state uncertainty from TLE level a-priori information. This is particularly interesting for geolocation as often times GEO communication satellites are used for dual-satellite geolocation of an unknown transmitter. The uncertainty of the satellites increases the uncertainty on the location of the transmitter so any means of reducing

the satellite uncertainty reduces the transmitter positioning covariance. Geolocation already uses TDOA and FDOA so no additional infrastructure is needed to put this to use.

Table 4.13: GEO-GEO: $\pm 3\sigma$ covariance and state errors at the end of 24 hour observation span

		TDOA/FDOA		Range/Range-Rate		Range/Range-Rate + bias	
		$\pm 3\sigma$	Err.	$\pm 3\sigma$	Err.	$\pm 3\sigma$	Err.
R_{GEO_1}	[m]	2.6 [†]	-1.4	0.4	0.1	0.4	-1.3
R_{GEO_2}	[m]	2.7 [†]	-1.3	0.4	0.3	0.4	-1.2
I_{GEO_1}	[m]	297.0 [†]	34.2	1.6	-0.04	1.6	12.7
I_{GEO_2}	[m]	297.9 [†]	39.6	1.6	0.9	1.6	24.0
C_{GEO_1}	[m]	62.7 [†]	-11.0	4.0	1.0	4.0	-3.2
C_{GEO_2}	[m]	62.9 [†]	-11.2	4.0	1.9	4.0	-4.9
\dot{R}_{GEO_1}	[mm/s]	21.7 [†]	-2.5	0.1	0.01	0.1	-1.0
\dot{R}_{GEO_2}	[mm/s]	21.7 [†]	-3.0	0.1	-0.06	0.1	-1.8
\dot{I}_{GEO_1}	[mm/s]	0.2 [†]	0.1	0.03	-0.009	0.03	0.05
\dot{I}_{GEO_2}	[mm/s]	0.2 [†]	0.09	0.03	-0.02	0.03	0.06
\dot{C}_{GEO_1}	[mm/s]	4.6 [†]	-1.5	0.3	0.1	0.3	-0.2
\dot{C}_{GEO_2}	[mm/s]	4.6 [†]	-1.5	0.3	0.04	0.3	-0.3
AGOM $_{GEO_1}$	□	0.0003 [†]	0.0	0.0	0.0	0.0	0.0
AGOM $_{GEO_2}$	□	0.0003 [†]	0.0	0.0	0.0	0.0	0.0

[†] TDOA/FDOA 3σ covariance component worse than Range/Range-Rate

Chapter 5

Relative Orbit Determination

5.1 Satellite State Dynamics

In this chapter on relative navigation we consider the simplest case of 2-body motion without any perturbing forces acting upon the two satellites. A chief and a deputy satellite are defined such that the deputy is estimated relative to the chief satellite.

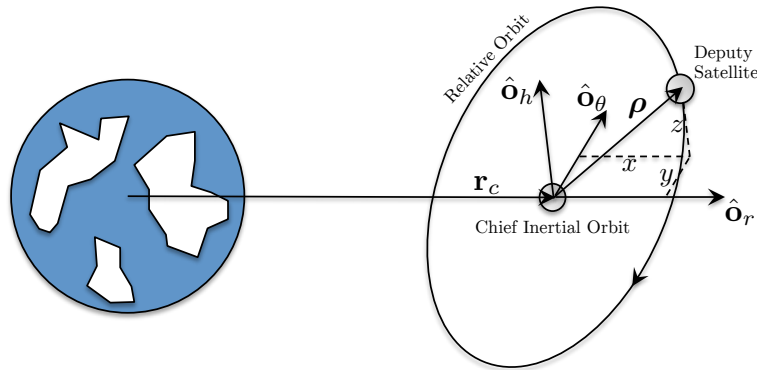


Figure 5.1: Spacecraft formation flying: chief with deputy (adapted from [71])

The relative orbit of the deputy about the chief is expressed in the Hill frame, also known as the local vertical local horizontal (LVLH) frame, defined by the vector triad $\{\hat{\mathbf{o}}_r, \hat{\mathbf{o}}_\theta, \hat{\mathbf{o}}_h\}$ using the following expressions,

$$\hat{\mathbf{o}}_r = \frac{\mathbf{r}_c}{r_c}, \quad (5.1)$$

$$\hat{\mathbf{o}}_\theta = \hat{\mathbf{o}}_h \times \hat{\mathbf{o}}_r, \quad (5.2)$$

$$\hat{\mathbf{o}}_h = \frac{\mathbf{h}}{h}. \quad (5.3)$$

Where, \mathbf{r}_c is the vector from the center of the Earth to the chief satellite and \mathbf{h} is the angular momentum vector of the chief inertial orbit, see Figure 5.1 for the diagram. The deputy inertial position vector \mathbf{r}_d is defined relative to the chief as,

$$\mathbf{r}_d = \mathbf{r}_c + [NO]\boldsymbol{\rho}. \quad (5.4)$$

Where $\boldsymbol{\rho}$ is comprised of x , y and z components in the $\hat{\mathbf{o}}_r$, $\hat{\mathbf{o}}_\theta$ and $\hat{\mathbf{o}}_h$ directions respectively and $[NO]$ is the rotation matrix from the the Hill frame \mathcal{O} to the inertial frame \mathcal{N} . The $[NO]$ rotation matrix is defined as,

$$[NO] = \begin{bmatrix} \hat{\mathbf{o}}_r & \hat{\mathbf{o}}_\theta & \hat{\mathbf{o}}_h \end{bmatrix}^\top. \quad (5.5)$$

The deputy inertial velocity vector $\dot{\mathbf{r}}_d$ is,

$$\dot{\mathbf{r}}_d = \dot{\mathbf{r}}_c + [NO] \left(\frac{{}^{\mathcal{O}}d\boldsymbol{\rho}}{dt} + \dot{f}\hat{\mathbf{o}}_h \times \boldsymbol{\rho} \right). \quad (5.6)$$

Where \dot{f} is the angular velocity of the Hill frame relative to the inertial frame. Because we are assuming 2-body Keplerian motion, the angular momentum of the orbit is constant and the angular velocity can be defined as,

$$\dot{f} = \frac{h}{r_c^2}. \quad (5.7)$$

The estimated state vector, in the Hill frame is then,

$$\mathbf{X} = \begin{bmatrix} \boldsymbol{\rho} & \dot{\boldsymbol{\rho}} \end{bmatrix} = \begin{bmatrix} x & y & z & \dot{x} & \dot{y} & \dot{z} \end{bmatrix}^\top. \quad (5.8)$$

The time evolution of the states are given by the following dynamics shown in first-order form:

$$\dot{\mathbf{X}}(t) = F(\mathbf{X}, t) = \begin{bmatrix} \dot{x} \\ \dot{y} \\ \dot{z} \\ \ddot{x} \\ \ddot{y} \\ \ddot{z} \end{bmatrix} = \begin{bmatrix} \dot{x} \\ \dot{y} \\ \dot{z} \\ 2\dot{f} \left(\dot{y} - y \frac{\dot{r}_c}{r_c} \right) + x \dot{f}^2 + \frac{\mu}{r_c^2} - \frac{\mu}{r_d^3} (r_c + x) \\ -2\dot{f} \left(\dot{x} - x \frac{\dot{r}_c}{r_c} \right) + y \dot{f}^2 - \frac{\mu}{r_d^3} y \\ -\frac{\mu}{r_d^3} z \end{bmatrix} \quad (5.9)$$

The dynamics equations shown in Eq. 5.9 are in exact non-linear form, that allows the deputy satellite to be an arbitrarily large distance away from the chief and the orbits can be eccentric as well while still describing the satellite motion accurately.

The deputy spacecraft is estimated in the Hill frame of the chief, which was up until now simply defined as the \mathcal{O} frame. But often times rotating the state and uncertainty from the chief LVLH frame to the deputy LVLH frame is more appropriate. In this way the state and uncertainty basis vectors correspond directly with the radial, velocity (for circular orbits only), and angular momentum directions of the deputy spacecraft. To perform this rotation we now discern the Hill or LVLH frame for both the chief and the deputy by using subscripts c for chief and d for deputy so that we have the \mathcal{O}_c and \mathcal{O}_d frames. The state of the deputy is initially estimated in the chief frame which is represented by ${}^{\mathcal{O}_c}\mathbf{X}_d$, instead we rotate the state into the deputy frame represented by ${}^{\mathcal{O}_d}\mathbf{X}_d$ using the LVLH to inertial rotations $[NO]$ from both the chief and the deputy resulting in the following equation,

$${}^{\mathcal{O}_d}\mathbf{X}_d = [NO]_d^T [NO]_c^{\mathcal{O}_c} \mathbf{X}_d. \quad (5.10)$$

Similarly, the covariance of the deputy is initially estimated in the chief frame represented by ${}^{\mathcal{O}_c}\mathbf{P}_d$, and is rotated into the deputy frame represented by ${}^{\mathcal{O}_d}\mathbf{P}_d$ resulting in the following equation,

$${}^{\mathcal{O}_d}\mathbf{P}_d = [NO]_d^T [NO]_c^{\mathcal{O}_c} \mathbf{P}_d [NO]_c^T [NO]_d. \quad (5.11)$$

All plots in this chapter show the state and uncertainty in the $\mathcal{O}_d \mathbf{X}_d$ and $\mathcal{O}_d \mathbf{P}_d$ frame respectively unless specified otherwise.

In the following sections we examine the effectiveness of using TDOA and FDOA by analyzing the CRLB in a number of different scenarios. The first is where a GEO chief satellite is paired with deputy satellites between LEO and GEO. Next we examine a pair of satellites in a leader-follower scenario with various semi-major axes, ranging from LEO to GEO. Finally, the last section looks at a chief and deputy satellite in bounded relative motion and also in very close proximity to each other. Once again we look at semi-major axes of the chief ranging from LEO to GEO. For the majority of these scenarios three stations are used in addition to the reference station. Table 5.1 lists the exact locations used in these simulations. Notice that the locations of the RXs are also listed but do not actually influence the solution in anyway because the frequencies used by the TXs are all the same (14.3 GHz), consequently, the downlink legs cancel in all cases.

Table 5.1: Latitude, longitude and altitude of transmitters and receivers used in relative OD cases

<i>Transmitters (TXs)</i>			
<i>Reference Station</i>			
Boulder	40.015° N	105.270° W	1623.72 m
<i>Stations</i>			
San Diego	32.72° N	117.16° W	27.91 m
Seattle	47.60° N	122.33° W	9.44 m
Houston	29.76° N	95.37° W	14.54 m
<i>Receivers (RXs)</i>			
Boulder 1	40.014° N	105.271° W	1625.57 m
Boulder 2	40.014° N	105.270° W	1621.13 m

The apriori uncertainties needed for calculating the CRLB are listed in Table 5.2. Both the TDOA/FDOA and range/range-rate uncertainties are included, the latter of which is used later on for CRLB comparison with the TDOA/FDOA results.

Table 5.2: CRLB 1σ a-priori uncertainty for relative estimated states and measurements

<i>Satellite state uncertainty</i>	
Position	10 km
Velocity	10 m/s
<i>Measurement uncertainty</i>	
TDOA	0.035 μ s
FDOA	0.2 mHz
Range	1 m
Range-Rate	1 mm/s

5.2 GEO Chief + LEO-to-GEO Deputy Satellite Pairing

The GEO chief and LEO-to-GEO Deputy pairing is specifically analyzed for the geolocation application. By pairing the GEO satellite with a deputy that has faster dynamics we find that the OD on both the chief and the deputy improves. As a result of the improved satellite states the uncertainty of the geolocation solution can be significantly reduced. Two different cases are examined, the first assumes that the chief state is known perfectly. In reality this is not possible so in the second case we consider a small but reasonable amount of uncertainty on the chief satellite state.

Table 5.3 lists the satellite orbital elements, with the satellites 5 degrees apart in longitude and starting out in longitudinal slots corresponding to those over the contiguous United States.

Table 5.3: Orbital elements for GEO chief + LEO-to-GEO deputy

	a [km]	e	i [deg]	Ω [deg]	ω [deg]	ν [deg]
Chief	42164.14	0	0	0	0	255
Deputy	6746.26 - 48910.40	0	0	0	0	260

5.2.1 Estimating the Deputy with Perfect Chief Knowledge

First the CRLB is computed using three stations and the reference station as specified in Table 5.1. The CRLB analysis spans up to a 24 hour time period with the deputy varying in

semi-major axis from LEO up to GEO. Figure 5.2 illustrates the results of the analysis by the state component of the deputy satellite. A general trend present in all states is that the covariance collapses faster with a lower semi-major axis paired deputy. The faster reduction in covariance is due the increased dynamics of the deputy at lower altitude which results in a faster accumulation of information. In all of the components we see either a faint or distinct line when the deputy is in a GEO orbit (1 on the ordinate). Because the chief is also in a GEO orbit this corresponds to the relative GEO-GEO OD case. In this case all the components except for y we see that the line is a lighter blue compared to the surrounding color, this indicates increased observability because the covariance has collapsed faster than it would have otherwise. In the case of y however, we find the opposite, and this component is barely observable with only a slight reduction in uncertainty over the 24 hour time span. When putting the deputy in a slightly lower or higher orbit than GEO however, this region of lower observability goes away. The position 1σ uncertainty can reach as low as 1 cm for the deputy while the velocity 1σ uncertainty can easily achieve a fraction of 1 mm/s.

Throughout this chapter the CRLB is plotted where striations are visible. The increase and decrease of the covariance over time is due to the changing geometry of the satellites with respect to the stations. Because a LEO deputy satellite orbits much faster than a MEO or GEO deputy satellite, the period of these striations increases. Indeed when plotting the CRLB versus orbit rather than observation time span these striations becomes almost vertical and correspond proportionally to the orbital period.

The CRLB shown in Figure 5.2 shows the absolute covariance values obtained using the TDOA and FDOA measurements. However without a baseline for comparison it can be difficult to gage how these results might stack up to other, more conventional observables. Therefore, we compare them to range and range-rate. While range and range-rate are subject to potential biases unlike TDOA and FDOA, we assume that no biases are present and show the best case scenario for range and range-rate. In Figure 5.3 we have the chief in GEO and the deputy in MEO at $0.5 \times a_{GEO}$. In all deputy state components, the 3σ covariance bounds of TDOA and FDOA (shown in the legend as $\pm 3\sigma_{TF}$) collapse much quicker than those using range and range-rate (shown in

the legend as $\pm 3\sigma_{RR}$). The initial error in the state from the truth was 10 km in each direction in position and 10 m/s in each direction in velocity. The state errors are reduced very rapidly and stay consistently within their covariance bounds. In this particular case the TDOA and FDOA OD results outperform range and range-rate by a significant margin, especially at lower observation times, but as the observation span increases, the performance gap decreases.

In Figure 5.3 we show a single comparison between TDOA/FDOA and range/range-rate of their covariances as well as state errors. Figure 5.4 on the other hand compares the TDOA/FDOA OD results with range/range-rate over a swath of orbital regimes for the deputy. The percent difference is plotted in the 3rd axis using a color gradient. Yellow indicates a lower covariance using TDOA/FDOA while blue indicates a lower covariance using range/range-rate. The black line is where the OD performance between the two measurement types are equal. In the majority of cases the TDOA/FDOA observables outperform those of range and range-rate. Notice that the y direction, equivalent to the in-track direction of the deputy, above approximately $0.9 \times a_{GEO}$ is better using range and range-rate. This is due to the lower observability issue shown previously in Figure 5.2(c). The z direction, or equivalently the cross-track direction of the deputy, is particularly good with the TDOA and FDOA measurements.

The OD of the velocity components is favorable in most cases using TDOA and FDOA which is important for the geolocation problem. This scenario suggests that if a GEO satellite is known precisely then it is best to use the geolocation observables to obtain an OD estimate for use with the geolocation problem. Even with a GEO deputy satellite, at observation spans of about 10 hours or more, the TDOA/FDOA observables provide a better OD solutions in all three velocity components compared to range and range-rate.

While this section showed some insight into using a GEO chief paired with a deputy ranging from LEO to GEO, the assumed perfect knowledge of the chief is unrealistic. In the following section, the same analyses are conducted with a small, but realistic amount of uncertainty on the chief satellite state.

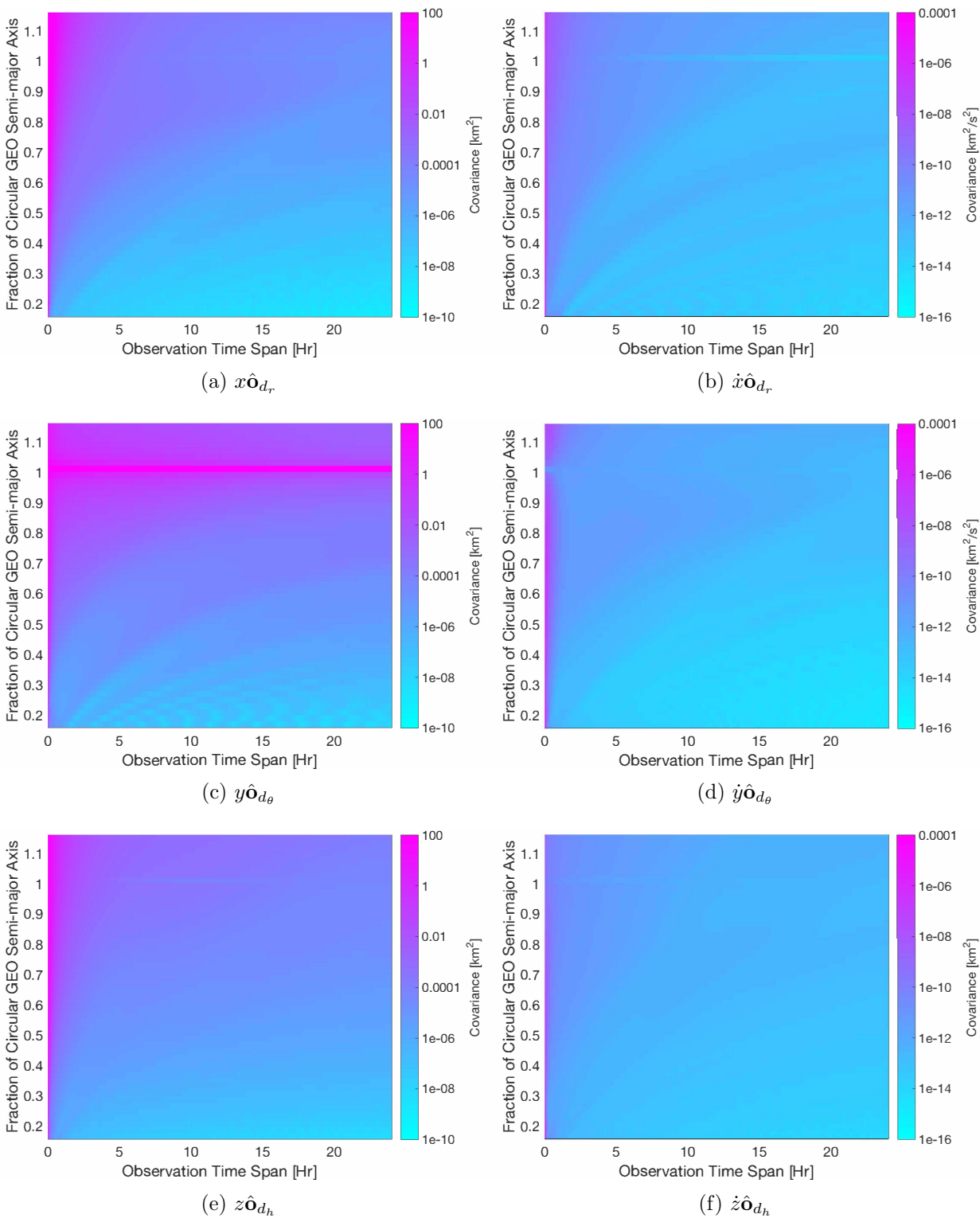


Figure 5.2: Circular GEO chief + circular deputy at various semi-major axes, shown on ordinate. Showing CRLB covariance over various observation time spans shown on abscissa. Coordinates are in the LVLH frame of the deputy. Three baselines used.

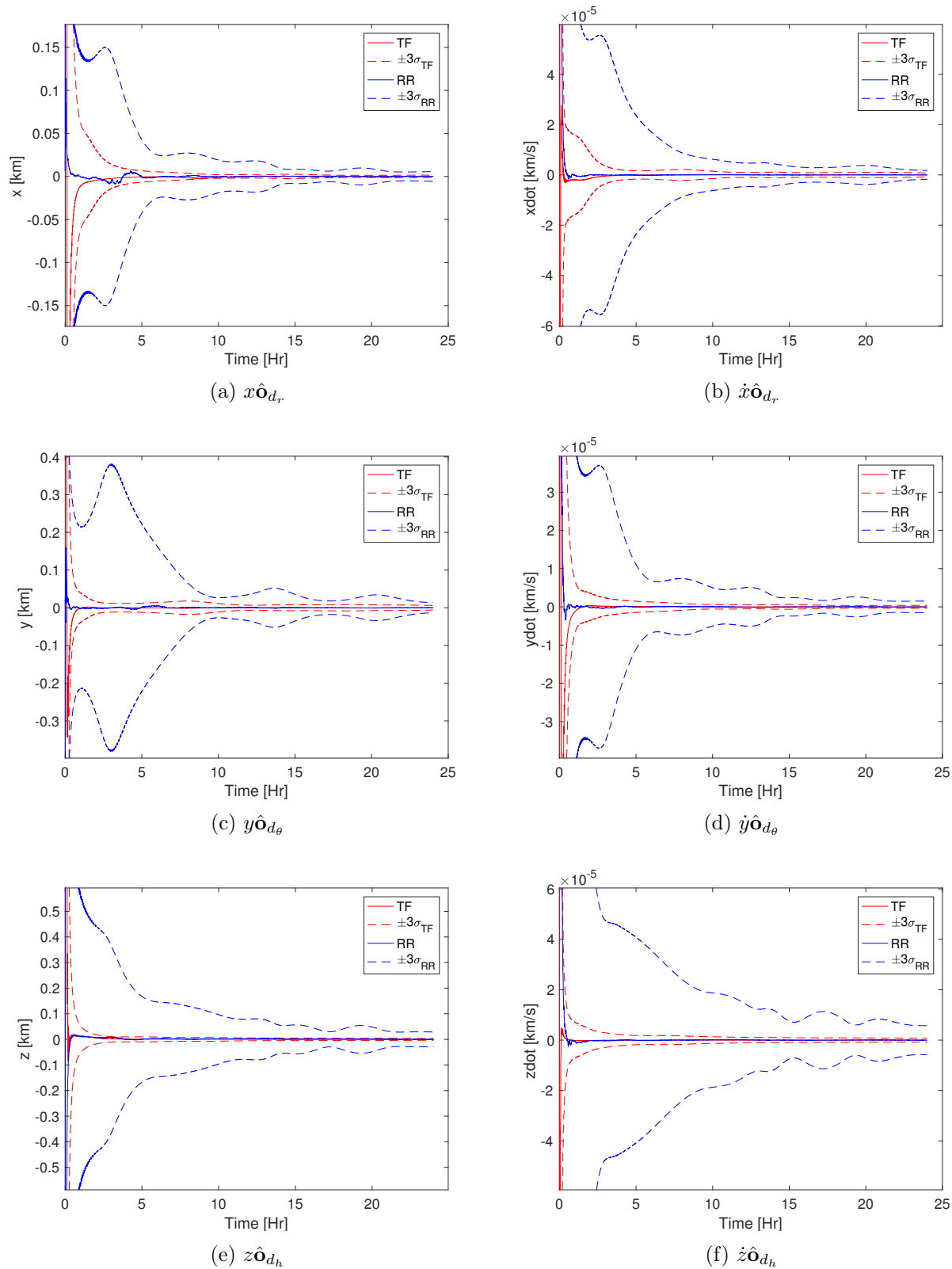


Figure 5.3: State error and 3σ covariances for circular GEO chief + circular MEO deputy ($0.5 \times a_{GEO}$) in the deputy LVLH frame. Comparison between TDOA/FDOA (TF) and range/range-rate (RR) observables. Three baselines used.

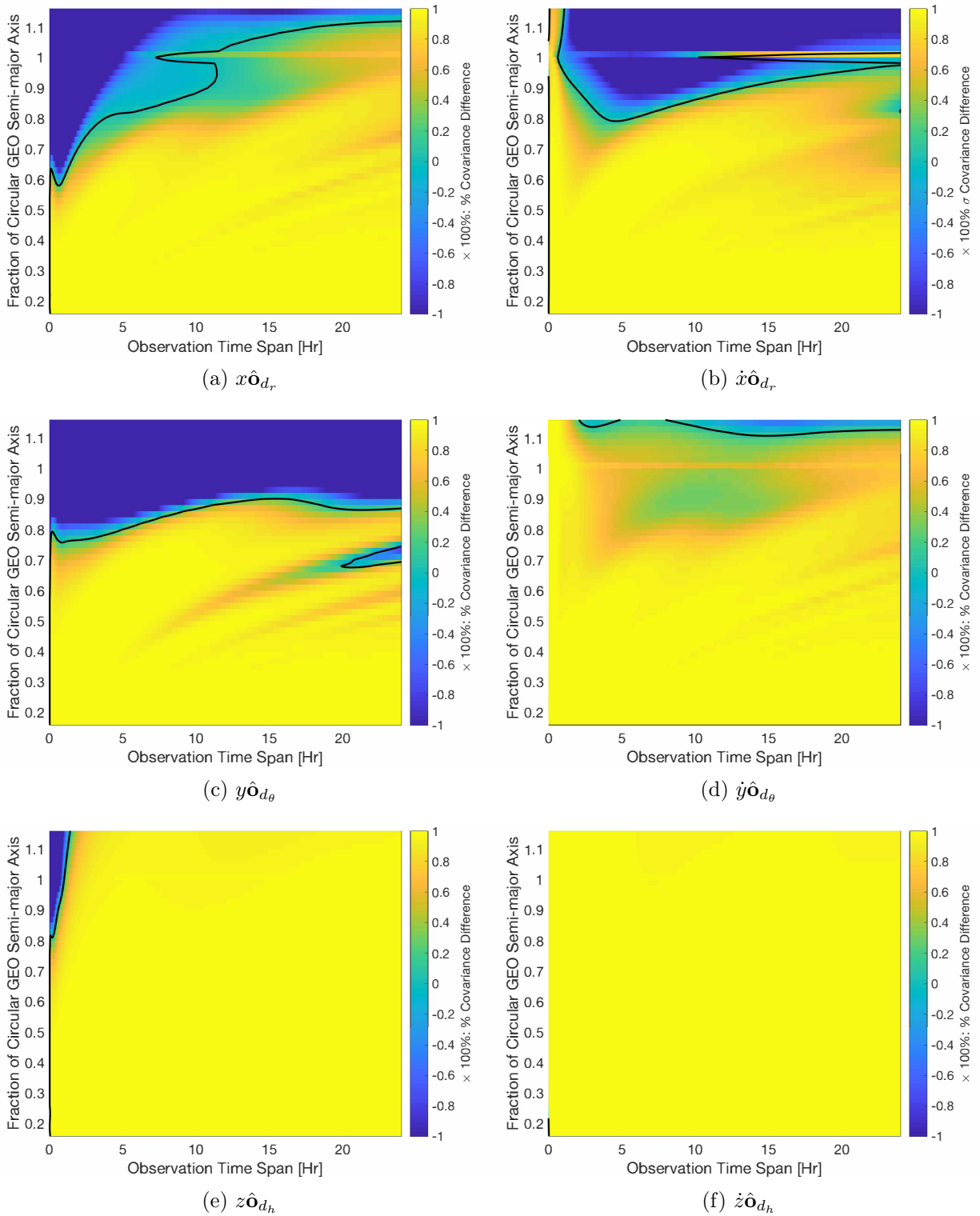


Figure 5.4: Circular GEO chief + circular deputy at various semi-major axes, shown on ordinate. Showing % difference of CRLB covariance bounds between TDOA/FDOA and range/range-rate measurements over various observation time spans shown on abscissa. Color values above 0 indicate a region where TDOA/FDOA has lower covariance bounds compared to range/range-rate and vice versa. Coordinates are in the LVLH frame of the deputy. Three baselines used.

5.2.2 Estimating the Deputy with Considered Chief Uncertainty

As a natural follow-up, we increase the realism by introducing a small amount of uncertainty on the chief satellite in GEO. A 10 m 1σ position uncertainty as well as a 1 mm/s 1σ velocity uncertainty in each basis vector direction is assumed. Once again, the CRLB is computed for a range of deputy satellite semi-major axes and is shown in Figure 5.5. It is immediately apparent that the covariance has not collapsed as quickly or as much in this case compared to the original CRLB analysis shown in Figure 5.2. As would be expected, the degree of unobservability of the in-track position y , direction of the deputy satellite at GEO is as high or higher than without any chief considered state uncertainty. Interestingly however, the in-track velocity \dot{y} , of a deputy satellite at GEO has a fast-collapsing covariance that remains low throughout the observation time span, this was also present in Figure 5.2(d). The striations are also more pronounced with large increases and decreases in covariance over time for a specified deputy orbit.

Once more, a comparison can be made between using TDOA/FDOA and range-range-rate observables. The same satellites are used as were used for Figure 5.3, a GEO chief and a MEO deputy at $0.5 \times a_{GEO}$ is shown in Figure 5.6. The considered uncertainty on the chief however has significantly reduced the advantage of using TDOA and FDOA over range and range-rate. In part this is because the TDOA/FDOA measurements are directly dependent on the two satellites while range/range-rate measure each satellite independently. Recall however, that non-biased range and range-rate are used which in reality would be unlikely and corrupt the range/range-rate solution to some extent, once again increasing the favor for TDOA/FDOA measurements.

Notice that the 3σ covariance bounds of TDOA/FDOA and range/range-rate are much closer together with regular switches, in the radial and in-track directions. In cross-track, the TDOA/FDOA covariances are significantly lower. The state-errors with both sets of observables are effectively the same however.

Finally, we show the comparison of the TDOA/FDOA with the range/range-rate CRLBs of the LEO-GEO range of the deputy satellite in Figure 5.7. The result is a significantly more chaotic

pattern with the striations coming through. Shorter observation spans of up to 5 hours with a deputy satellite between LEO and $0.8 \times a_{GEO}$ tends to favor the TDOA/FDOA measurements in all components of the estimated state of the deputy. For geolocation, the velocity OD results with a GEO deputy favor the TDOA/FDOA measurements, particularly as the observation time span increases. The cross-track direction is especially good with TDOA/FDOA measurements.

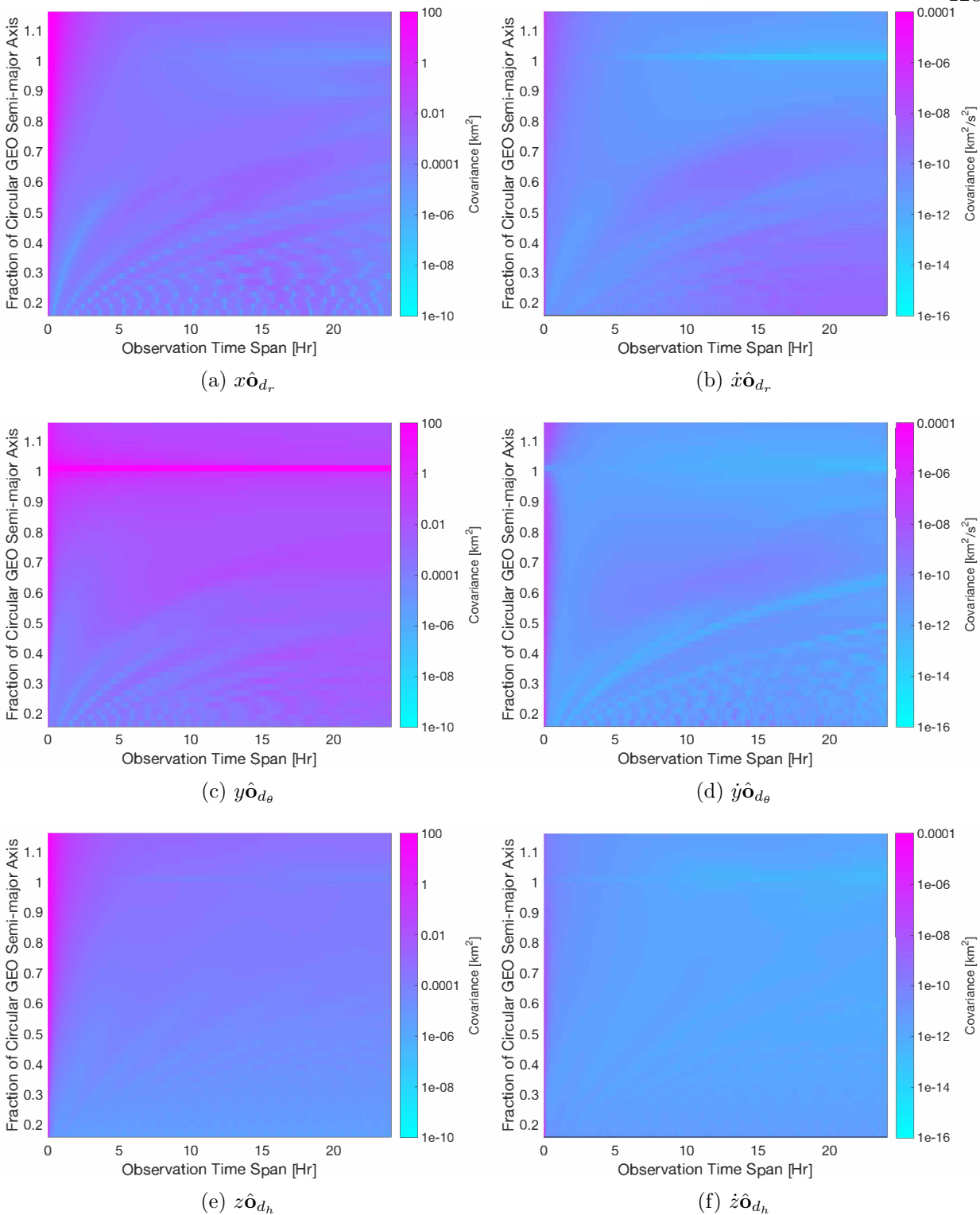


Figure 5.5: Circular GEO chief with considered 1σ position uncertainty of 10 m and 1σ velocity uncertainty of 1 mm/s in each direction + circular deputy at various semi-major axes, shown on ordinate. Showing CRLB covariance over various observation time spans shown on abscissa. Coordinates are in the LVLH frame of the deputy. Three baselines used.

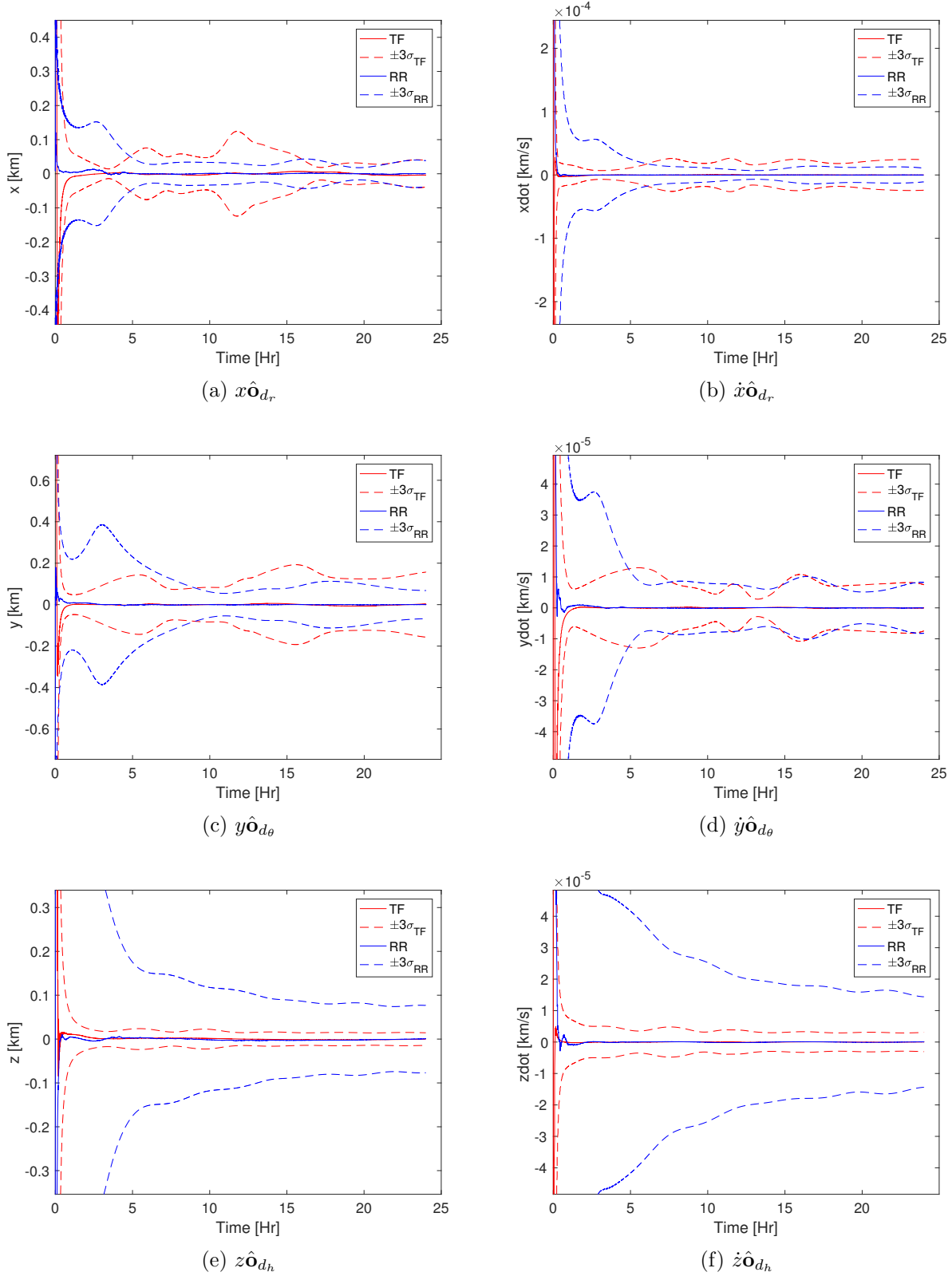


Figure 5.6: State error and 3σ covariances for circular GEO chief with considered 1σ uncertainty of 10 m and 1 mm/s in each direction + circular MEO deputy ($0.5 \times a_{GEO}$) in the deputy LVLH frame. Comparison between TDOA/FDOA (TF) and range/range-rate (RR) observables. Three baselines used.

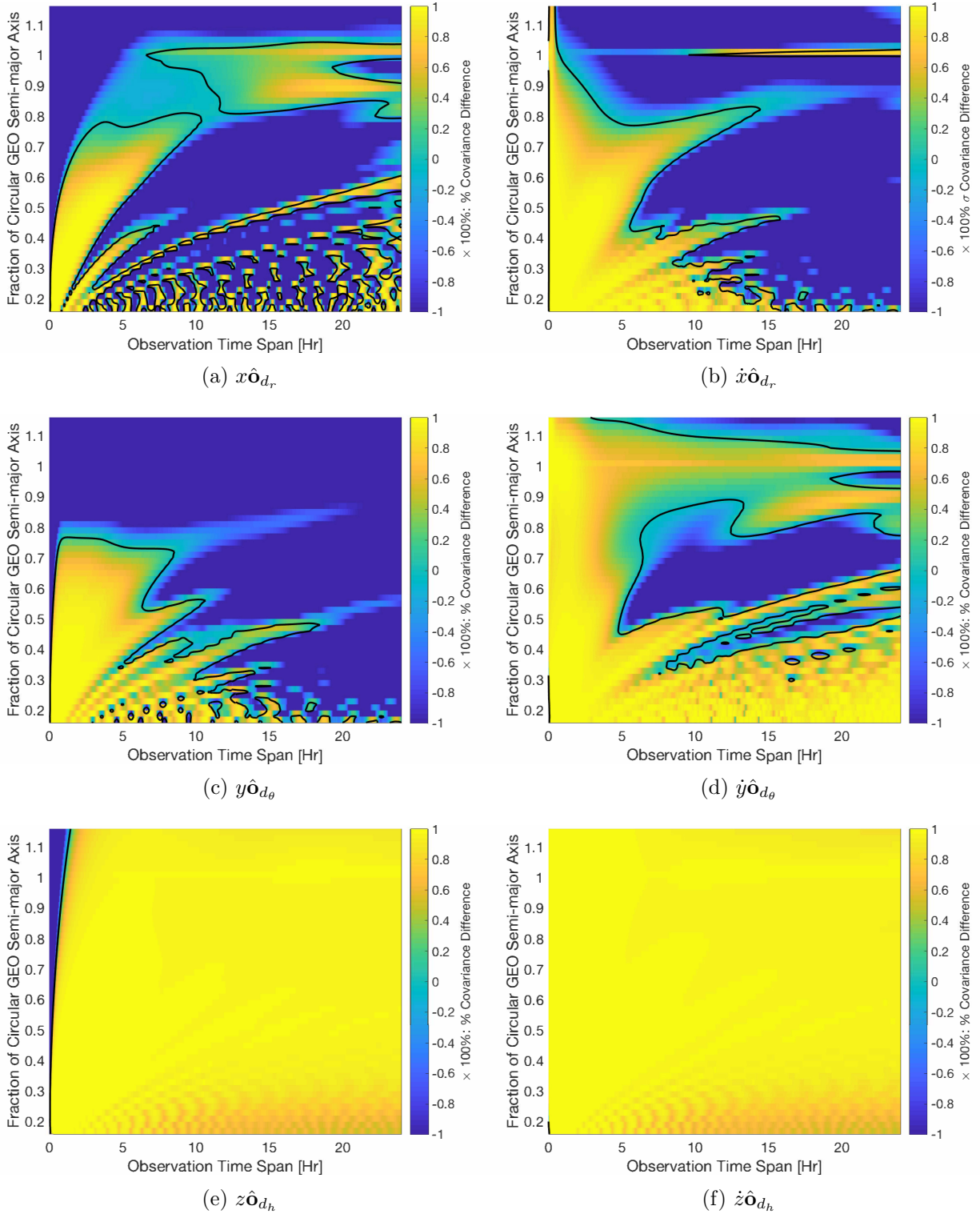


Figure 5.7: Circular GEO chief with considered 1σ position uncertainty of 10 m and 1σ velocity uncertainty of 1 mm/s in each direction + circular deputy at various semi-major axes, shown on ordinate. Showing % difference of CRLB covariance bounds between TDOA/FDOA and range/range-rate measurements over various observation time spans shown on abscissa. Color values above 0 indicate a region where TDOA/FDOA has lower covariance bounds compared to range/range-rate and vice versa. Coordinates are in the LVLH frame of the deputy. Three baselines used.

5.3 LEO-to-GEO Chief and Deputy in Leader-Follower Formation Flight

In this section we consider a leader-follower scenario of the chief and deputy, over a wide span of semi-major axes. Table 5.4 lists the satellite orbital elements, with the satellites 5 degrees apart in longitude and starting out in longitudinal slots corresponding to those over the contiguous United States.

Table 5.4: Orbital elements for LEO-to-GEO chief and deputy

	a [km]	e	i [deg]	Ω [deg]	ω [deg]	ν [deg]
Chief	6746.26 - 48910.40	0	0	0	0	255
Deputy	6746.26 - 48910.40	0	0	0	0	260

The same stations are used as those from Section 5.2 and are listed in Table 5.1. Two cases using perfect chief knowledge and a considered chief are discussed as in the previous section.

5.3.1 Estimating the Deputy with Perfect Chief Knowledge

The CRLBs in Figure 5.8 look practically identical to those from Figure 5.2 despite the difference in satellite geometries. In general the lower orbiting satellite cases tend to have lower covariances because of the faster dynamics with respect to the stations. The higher orbiting satellites, closer to GEO, tend take longer to collapse their covariances as well, for the same reason. The in-track y , direction in this scenario also has the observability problem at GEO with the covariance barely going down over time. With velocity, however, there is a faint blue line in the in-track \dot{y} , and cross-track \dot{z} , velocity directions at GEO suggesting that TDOA and FDOA are particularly suitable for accurate OD in these directions. The fact that there is a point of low observability in y at GEO, while also present in the previous case with a GEO chief and LEO-to-GEO deputy suggests that this is a consequence of the TDOA/FDOA measurement type rather than the measurement geometries between the stations and the satellites.

Figure 5.9 compares the state errors and 3σ covariance bounds of TDOA/FDOA and range/range-rate. The initial error from the truth was 10 km in position in each direction and 10 m/s in velocity in each direction. Whether TDOA/FDOA or range/range-rate are used the state errors are all driven to zero. When examining the 3σ covariance bounds however, TDOA/FDOA collapses faster and also maintains a lower level of uncertainty on the states.

Extending the results from Figure 5.9 to orbits spanning from LEO to GEO we obtain Figure 5.10. In the large majority of cases the TDOA/FDOA set of observables provide smaller uncertainties on the states than compared to range and range-rate. A leader-follower setup surrounding the GEO orbit however will produce worse results in the in-track y direction compared to range/range-rate regardless of the observation time span. This is a consequence of the low observability demonstrated with the CRLB in Figure 5.8(c). The position and velocity covariances in the cross-track direction are almost universally better using TDOA and FDOA measurements.

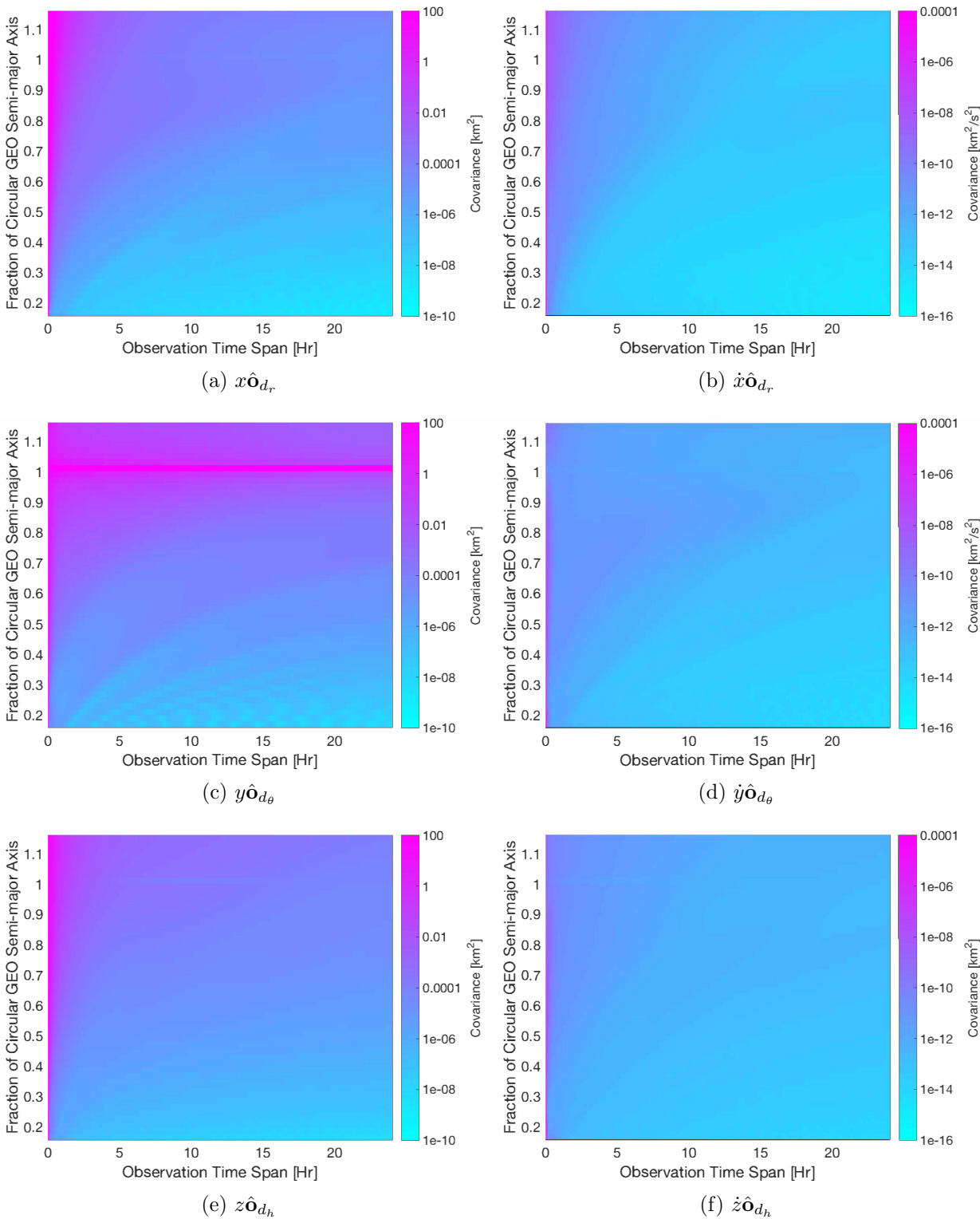


Figure 5.8: Circular chief and deputy at various semi-major axes, shown on ordinate. Showing CRLB covariance over various observation time spans shown on abscissa. Coordinates are in the LVLH frame of the deputy. Three baselines used.

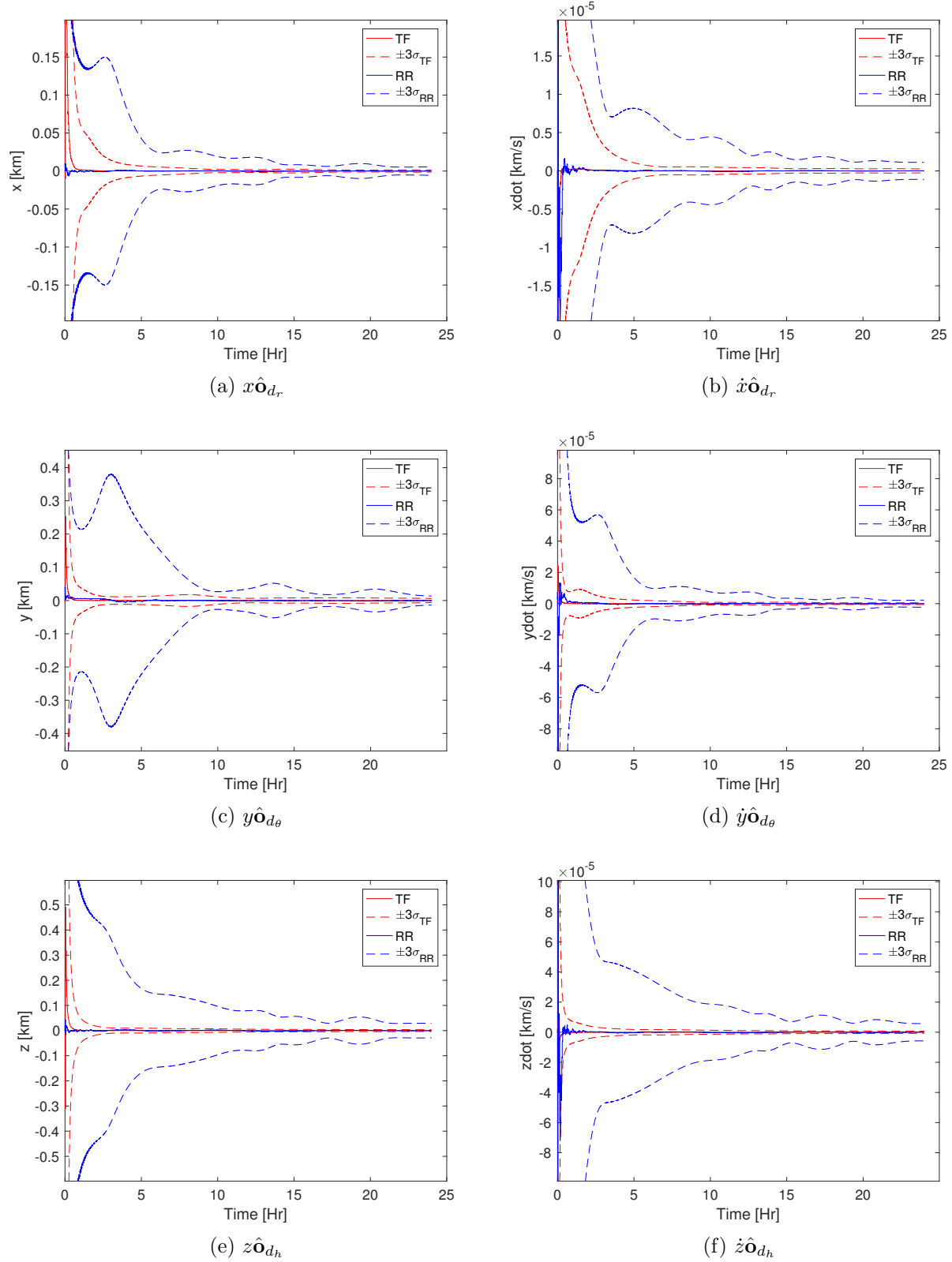


Figure 5.9: State error and 3σ covariances for circular MEO chief and deputy ($0.5 \times a_{GEO}$) in the deputy LVLH frame. Comparison between TDOA/FDOA (TF) and range/range-rate (RR) observables. Three baselines used.

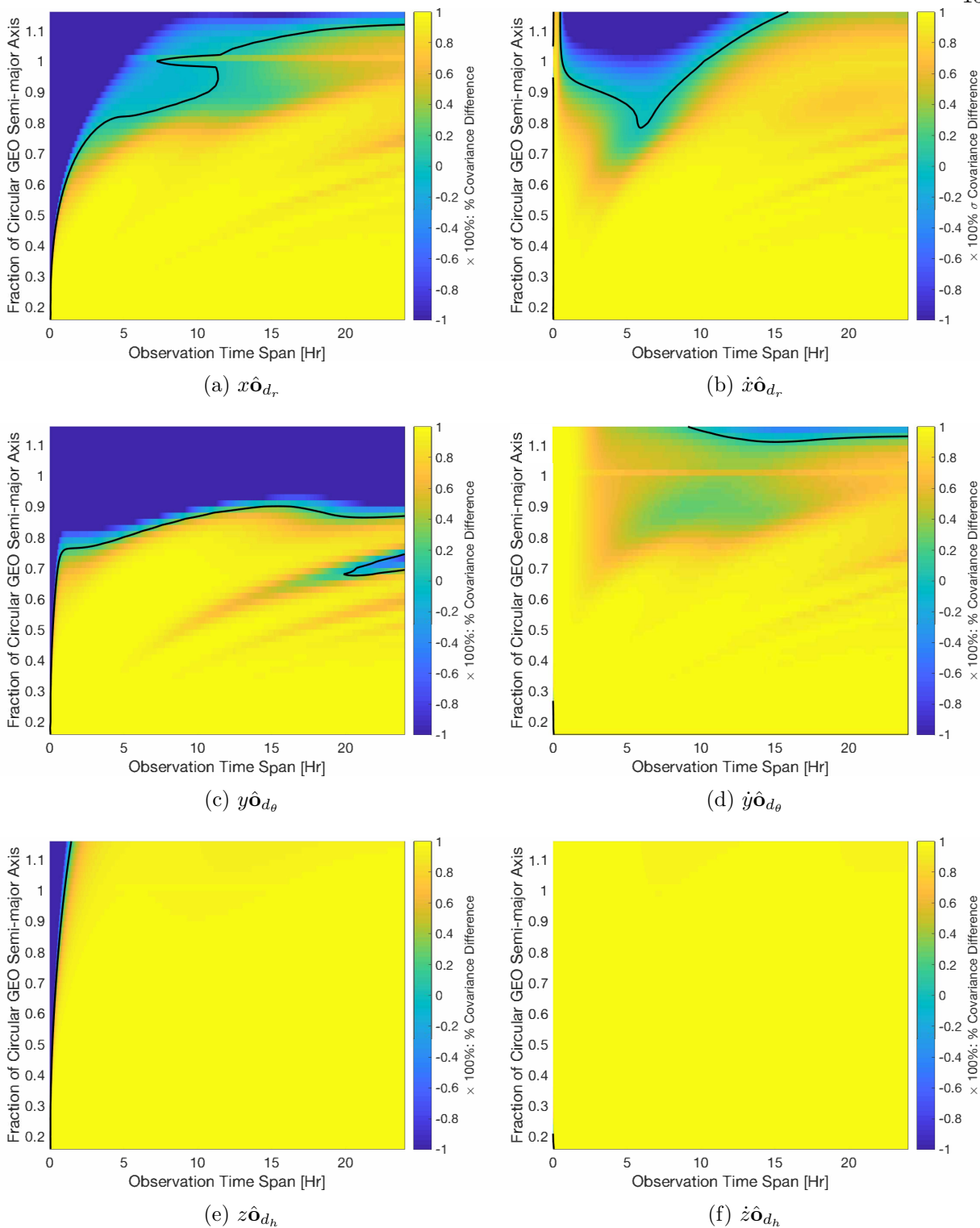


Figure 5.10: Circular chief and deputy at various semi-major axes, shown on ordinate. Showing % difference of CRLB covariance bounds between TDOA/FDOA and range/range-rate measurements over various observation time spans shown on abscissa. Color values above 0 indicate a region where TDOA/FDOA has lower covariance bounds compared to range/range-rate and vice versa. Coordinates are in the LVLH frame of the deputy. Three baselines used.

5.3.2 Estimating the Deputy with Considered Chief Uncertainty

Once more we examine the same case as presented above but with some chief uncertainty considered. The 1σ position uncertainty is 10 m in each direction and the 1σ velocity uncertainty is 1 mm/s in each direction. While the covariance in the CRLB does not quite reach the levels of perfect state knowledge on the chief, the drop in performance is less drastic than the GEO chief + LEO-to-GEO deputy case of perfect to considered chief knowledge described in chapter 5.2.

Figure 5.12 demonstrates that in the leader-follower setup with chief uncertainty considered the covariance bounds using TDOA/FDOA remain lower at all times in the case of a MEO chief and deputy. The state errors at epoch were 10 km in position in each direction and 10 m/s in velocity in each direction, only a few hours of observations are required with either TDOA/FDOA or range-rate in order to drive these errors down to zero and hone in on the truth trajectory.

The state error and covariance analysis is extended further to incorporate the whole range of Earth-orbiting satellite semi-major axes and is shown in Figure 5.13. Using this leader-follower satellite setup with chief uncertainty considered we see that TDOA/FDOA provides better OD results in the majority of cases as demonstrated by the large amount of yellow present in the plots. We find that also in this case the TDOA and FDOA measurements provide exceptionally good cross-track information in both position and velocity.

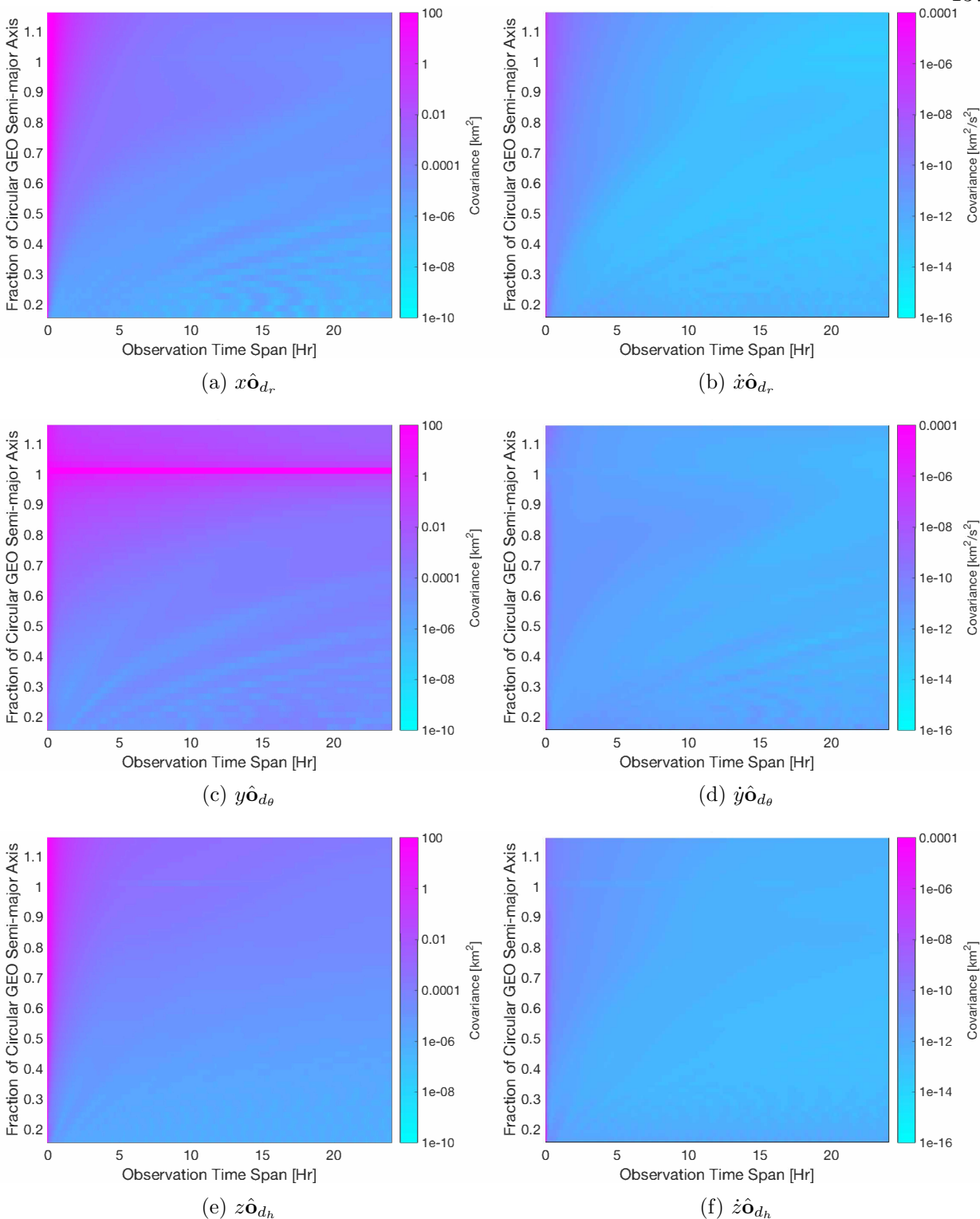


Figure 5.11: Circular chief with considered 1σ position uncertainty of 10 m and 1σ velocity uncertainty of 1 mm/s in each direction and deputy at various semi-major axes, shown on ordinate. Showing CRLB covariance over various observation time spans shown on abscissa. Coordinates are in the LVLH frame of the deputy. Three baselines used.

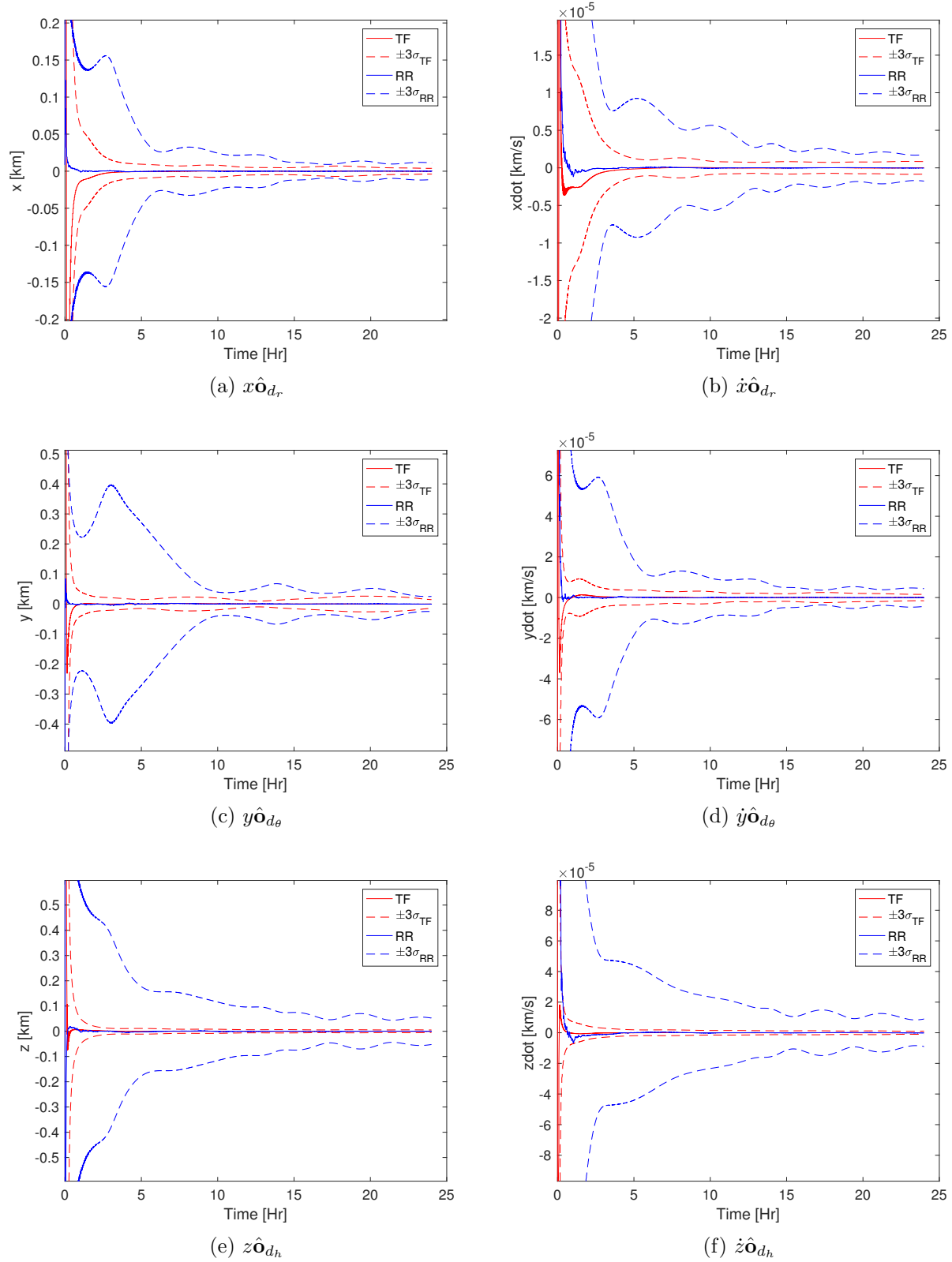


Figure 5.12: State error and 3σ covariances for circular MEO chief with considered 1σ position uncertainty of 10 m and 1σ velocity uncertainty of 1 mm/s in each direction and deputy ($0.5 \times a_{GEO}$) in the deputy LVLH frame. Comparison between TDOA/FDOA (TF) and range/range-rate (RR) observables. Three baselines used.

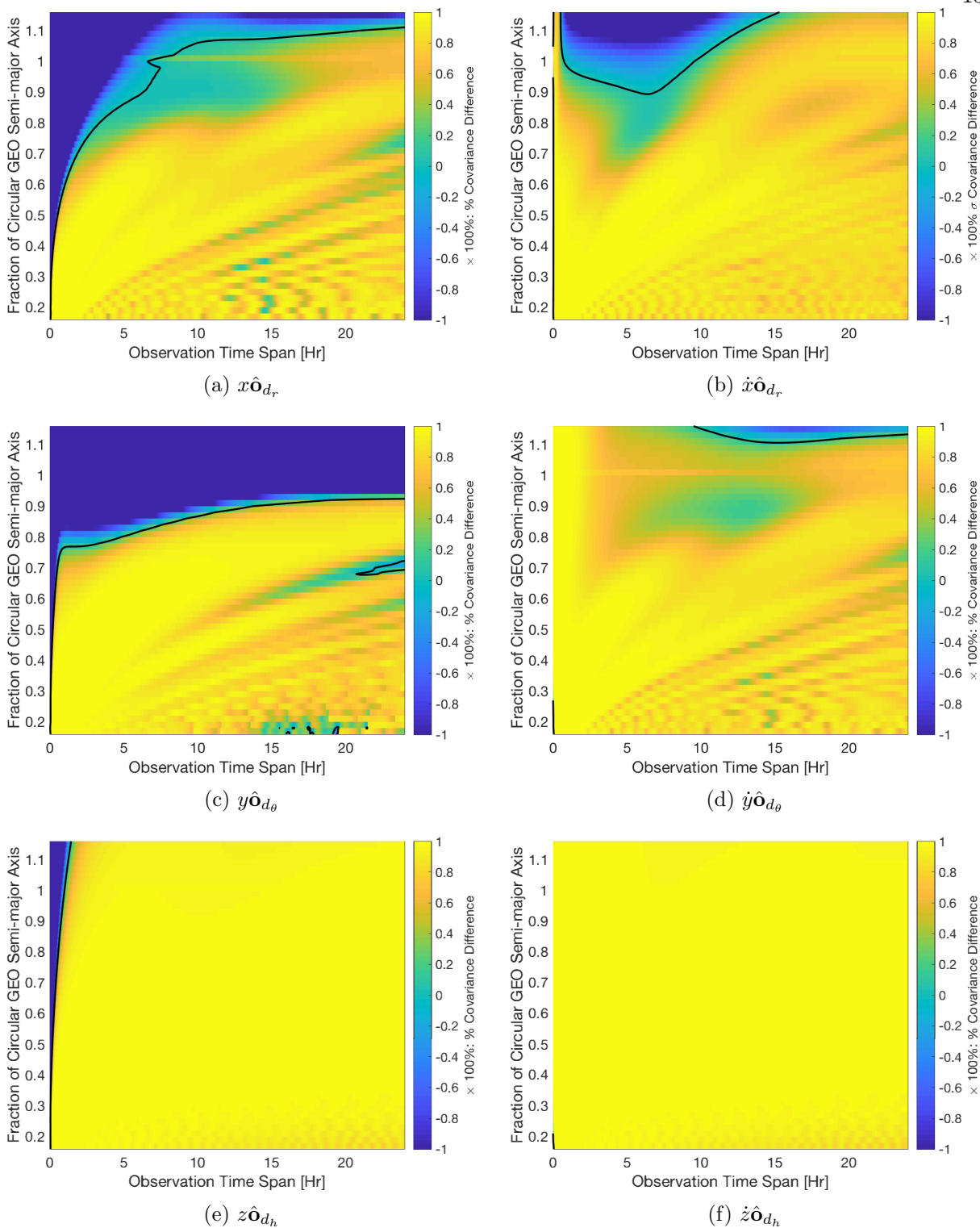


Figure 5.13: Circular chief with considered 1σ position uncertainty of 10 m and 1σ velocity uncertainty of 1 mm/s in each direction and deputy at various semi-major axes, shown on ordinate. Showing % difference of CRLB covariance bounds between TDOA/FDOA and range/range-rate measurements over various observation time spans shown on abscissa. Color values above 0 indicate a region where TDOA/FDOA has lower covariance bounds compared to range/range-rate and vice versa. Coordinates are in the LVLH frame of the deputy. Three baselines used.

5.4 Bounded Relative Motion

In the final case we examine a formation flying setup in very close proximity to each other. We show that regardless of the very small separation between the two spacecraft, the TDOA and FDOA measurements are well-suited for OD in this situation. The chief satellite orbit is the same as in the previous section and is listed in Table 5.4. The Deputy satellite orbit is described next.

5.4.1 Deputy Equations of Motion for Bounded Relative Motion

To compute a bounded relative motion trajectory of the deputy about the chief we use the following set of equations:

$$\begin{aligned}
 \mathcal{O}_c x_d &= A_0 \cos(\mathcal{O}_c \dot{f}t + \alpha) \\
 \mathcal{O}_c y_d &= -2A_0 \sin(\mathcal{O}_c \dot{f}t + \alpha) + y_{offset} \\
 \mathcal{O}_c z_d &= B_0 \cos(\mathcal{O}_c \dot{f}t + \beta) \\
 \mathcal{O}_c \dot{x}_d &= -A_0(\mathcal{O}_c \dot{f}) \sin(\mathcal{O}_c \dot{f}t + \alpha) \\
 \mathcal{O}_c \dot{y}_d &= -2A_0(\mathcal{O}_c \dot{f}) \cos(\mathcal{O}_c \dot{f}t + \alpha) \\
 \mathcal{O}_c \dot{z}_d &= -B_0(\mathcal{O}_c \dot{f}) \sin(\mathcal{O}_c \dot{f}t + \beta)
 \end{aligned} \tag{5.12}$$

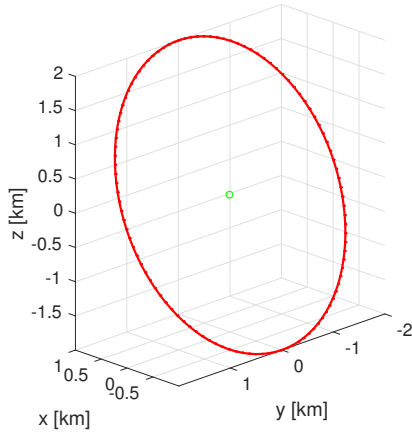
Where A_0 and B_0 are the cyclic amplitudes of the relative orbit in-plane and out-of-plane components respectively. The phase angles of the cyclic motion are defined by α and β for the in-plane and out-of-plane components correspondingly, and the along-track offset is defined by y_{offset} . The true anomaly rate of the chief is represented by \dot{f} and is previously defined by Eq. 5.7.

Table 5.5 lists two cases with a $\pi/2$ in-plane phase difference. As a consequence we obtain the two relative orbit plots shown in Figure 5.14.

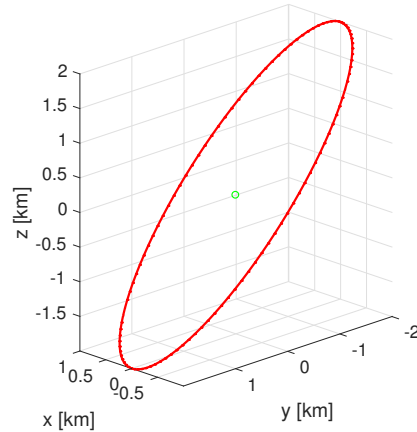
Both cases were examined, but whether the relative orbit was face-on or edge-on had no impact on the OD accuracy. Therefore we only show the OD results using the face-on (case 1) relative orbit.

Table 5.5: Relative orbit parameters for face-on and edge-on relative orbits

Case	A_0 [km]	B_0 [km]	t [s]	α [rad]	β [rad]	y_{offset} [km]
1	1	2	0	0	0	0
2	1	2	0	$\pi/2$	0	0



(a) Case 1: Face on towards Earth



(b) Case 2: Edge on towards Earth

Figure 5.14: Relative orbits of cases in Table 5.5. Green central circle is the chief, red line is relative deputy orbit. Plotted in the chief Hill frame.

5.4.2 Estimating the Deputy with Perfect Chief Knowledge

We first show the CRLBs of varying chief orbits with a tightly orbiting deputy spacecraft, assuming perfect state knowledge on the chief. The results shown in Figure 5.15 are nearly the same as those shown previously in Figures 5.2 and 5.8. In all three scenarios the static variable is the approximate location of the deputy satellite while the chief tends to be different in each case. Therefore we can conclude that the state uncertainty of the deputy is primarily dominated by the inertial geometry of the deputy with respect to the stations rather than with respect to the chief satellite as long as the state knowledge of the chief is known perfectly. Once more, as the chief and deputy satellite formation increases in semi-major axis, thereby reducing the relative velocity with respect to the stations, the amount of information content present is lower, therefore the covariance does not drop as much as with a smaller semi-major axis. The lower observability in the y direction

at GEO remains as well as the striations.

In Figure 5.16 we compare the OD results using both TDOA/FDOA and range/range-rate with the formation flight in a MEO orbit with a semi-major axis of $0.5 \times a_{GEO}$. The state errors are comparable and driven to zero from the initial state perturbation from the truth of 10 km in each direction for position and 10 m/s in each direction for velocity. The 3σ covariance bounds are significantly smaller and also driven to zero much faster using the TDOA and FDOA observables.

Expanding the comparison beyond the MEO case shown in Figure 5.16 to include semi-major axes of the formation flight pair from LEO to GEO we obtain the results shown in Figure 5.17. We find Figure 5.17 to have the same general features as those found in Figure 5.10 with the only large region of range and range-rate having an advantage occurring above a semi-major axis of $0.8 \times a_{GEO}$ in the in-track y , position direction.

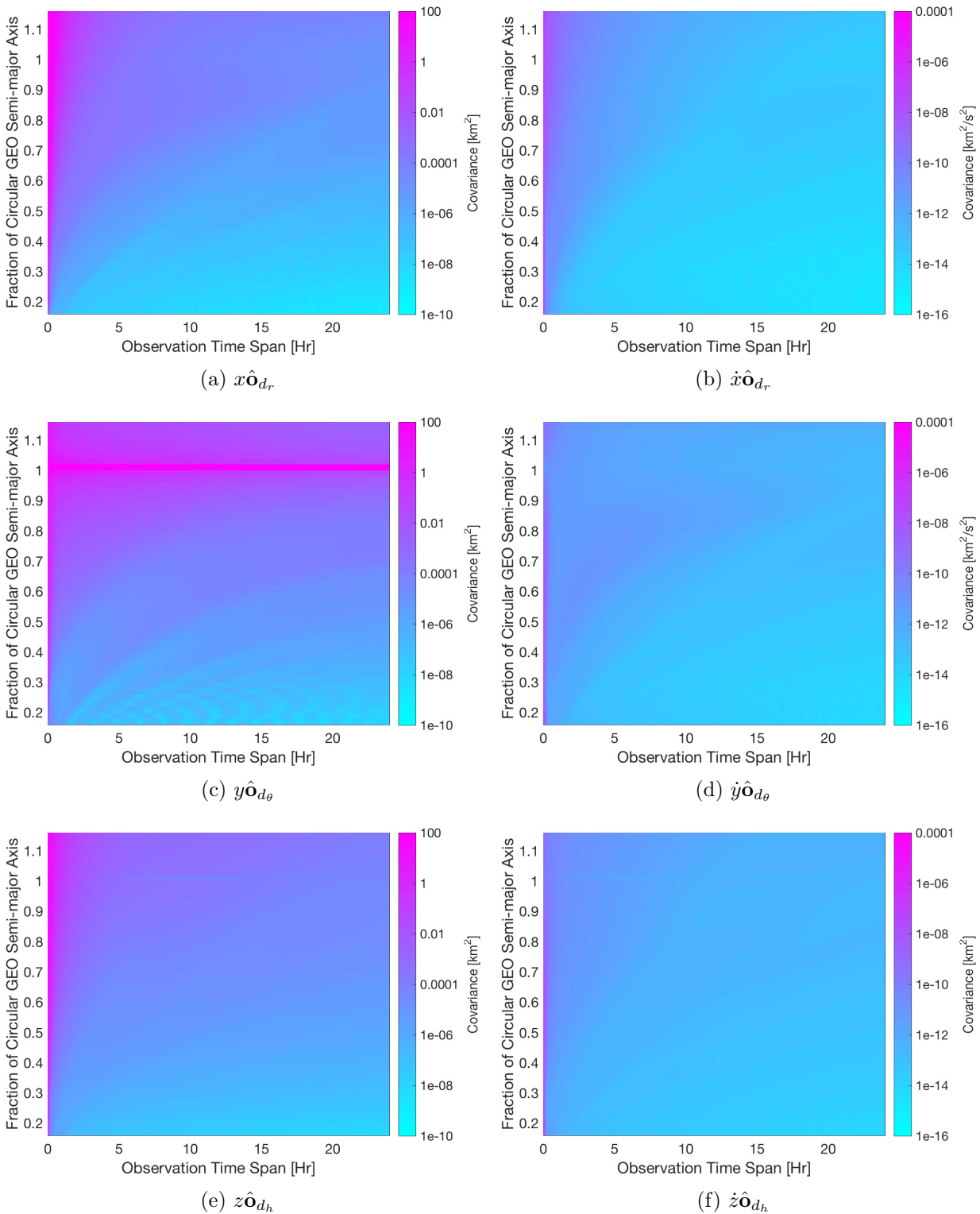


Figure 5.15: Close proximity bounded relative motion at various semi-major axes, shown on ordinate. Showing CRLB covariance over various observation time spans shown on abscissa. Coordinates are in the LVLH frame of the deputy. Three baselines used.

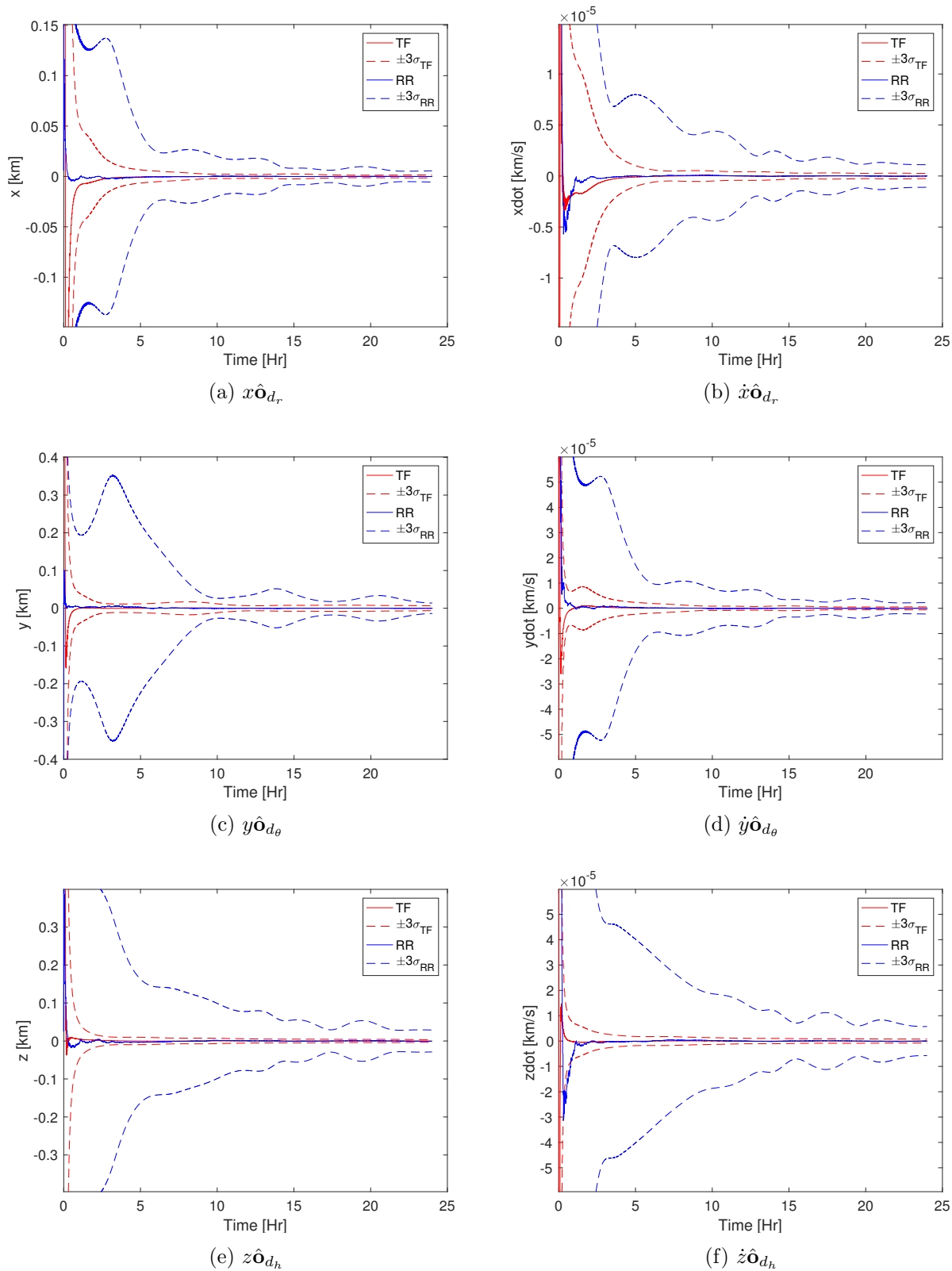


Figure 5.16: State error and 3σ covariances for close proximity bounded relative motion with chief at MEO ($0.5 \times a_{GEO}$) in the deputy LVLH frame. Comparison between TDOA/FDOA (TF) and range/range-rate (RR) observables. Three baselines used.

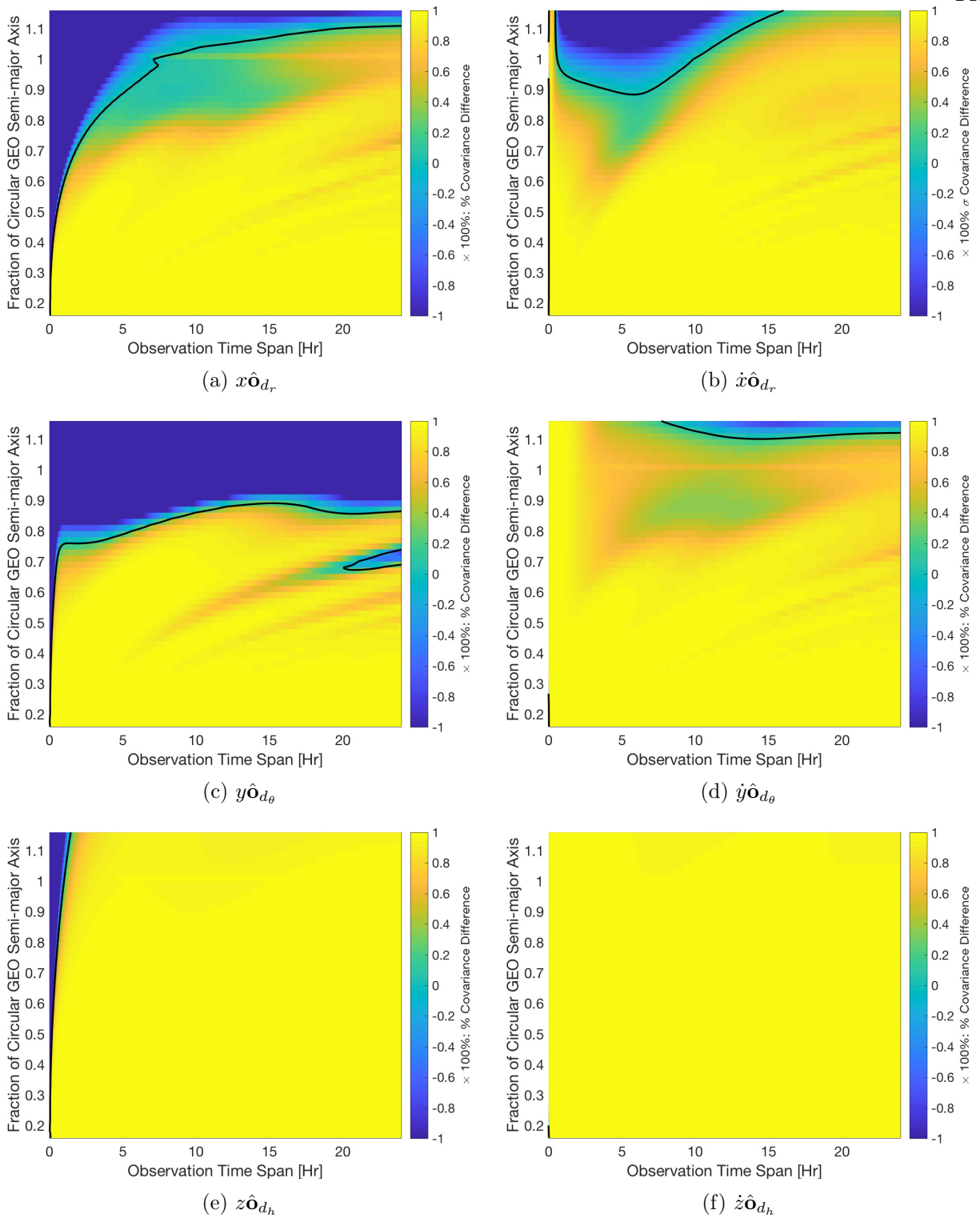


Figure 5.17: Close proximity bounded relative motion at various semi-major axes, shown on ordinate. Showing % difference of CRLB covariance bounds between TDOA/FDOA and range/range-rate measurements over various observation time spans shown on abscissa. Color values above 0 indicate a region where TDOA/FDOA has lower covariance bounds compared to range/range-rate and vice versa. Coordinates are in the LVLH frame of the deputy. Three baselines used.

5.4.3 Estimating the Deputy with Considered Chief Uncertainty

To increase the realism of the relative OD case of a close proximity satellite formation we now look at the instance where a chief position uncertainty of 10 m in each direction and velocity uncertainty of 1 mm/s in each direction is considered. The chief uncertainty effect upon the CRLBs does not change the results significantly from those found without the included uncertainty in Figure 5.17. The same features are encountered, with the low observability of the in-track position at GEO occurring once more.

We scrutinize the GEO case more closely and run a simulation case to see how the low observability in y affects the filter solution. The SR-USKF is initiated with an a-priori state off from the truth by 10 km in position in each direction and 10 m/s in velocity in each direction as well. Figure 5.19(a) shows the chief satellite in green at the origin with the deputy truth orbit shown in red. The estimated deputy orbit is shown in blue which started from the a-priori state and moved its way over to the truth trajectory in all components except for y as predicted by the CRLB. The residuals are shown in Figure 5.19(b). The TDOA residuals clearly indicate that the estimated solution is not perfect, while the FDOA residuals are fitted to the noise. A sequential filter like the SR-USKF is not generally iterated but by iterating it anyway the solution can slowly be walked over closer to the truth trajectory as indicated by the estimated trajectory and residuals shown in Figures 5.19(c) and (d) respectively. The ability to obtain a better solution after many iterations suggests that the issue is numerical and a better method to obtain the best estimate likely exists. One such a method may be to compute multiple a-priori states after the first iteration, which vary in the in-track direction, in effect using a line-search rather than waiting for the filter to slowly converge upon a solution with residuals in the noise.

The low observability in y only occurs at GEO illustrated by a satellite formation pair positioned at $0.95 \times a_{GEO}$ and not showing any symptoms of numerical problems, instead quickly snapping to the correct solution. Figure 5.20 shows this case where the estimated solution is coincident to the truth trajectory and the residuals are fitted to the noise.

Also in the bounded formation flying case with the satellite at MEO ($0.5 \times a_{GEO}$) in Figure 5.21 the TDOA/FDOA 3σ covariance bounds are much smaller than those of range and range-rate while the state errors tend to be comparable.

Finally Figure 5.7 demonstrates that also the bounded relative motion case is in most cases better with TDOA and FDOA measurements.

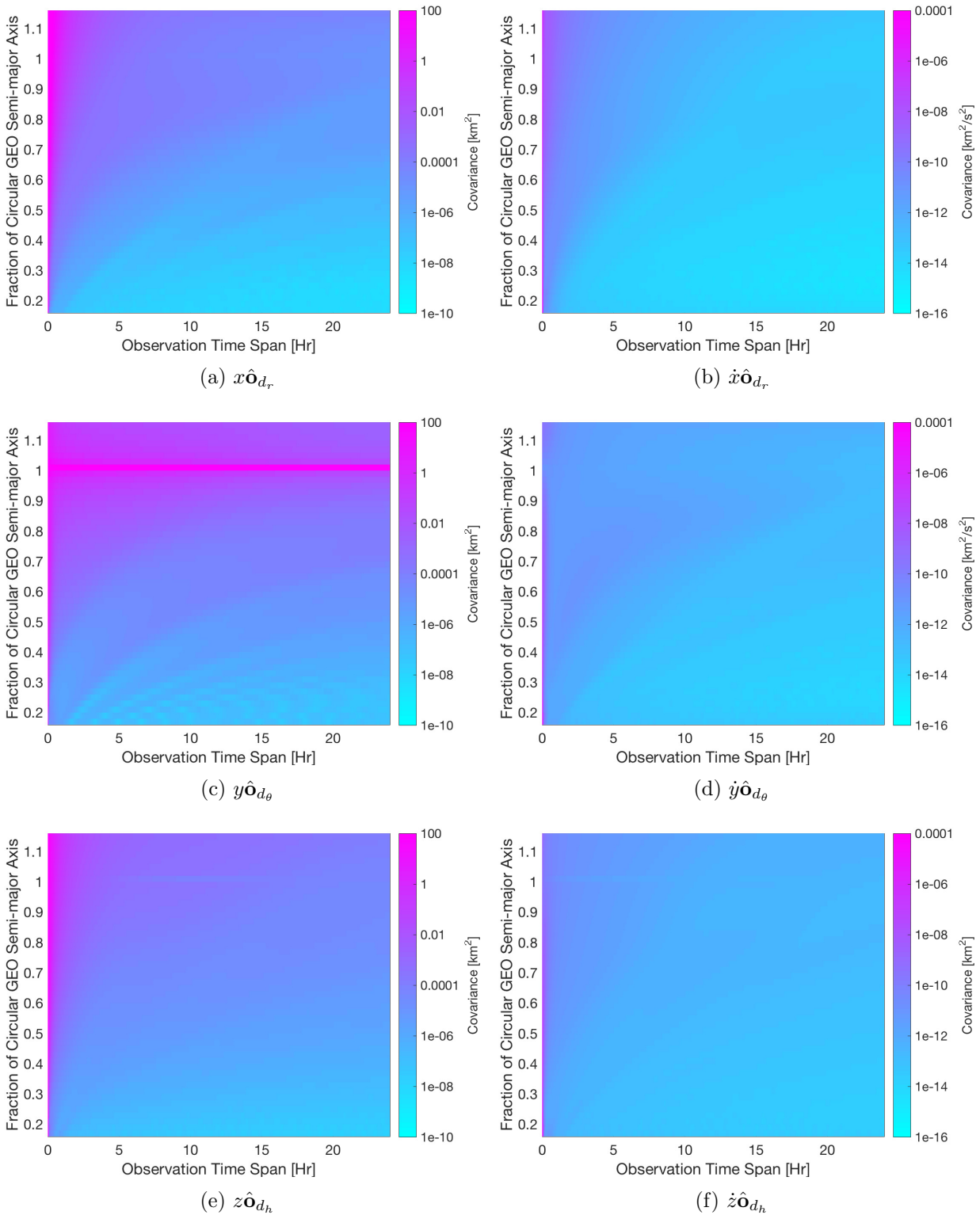


Figure 5.18: Close proximity bounded relative motion with considered 1σ position uncertainty of 10 m and 1σ velocity uncertainty of 1 mm/s in each direction of the chief at various semi-major axes, shown on ordinate. Showing CRLB covariance over various observation time spans shown on abscissa. Coordinates are in the LVLH frame of the deputy. Three baselines used.

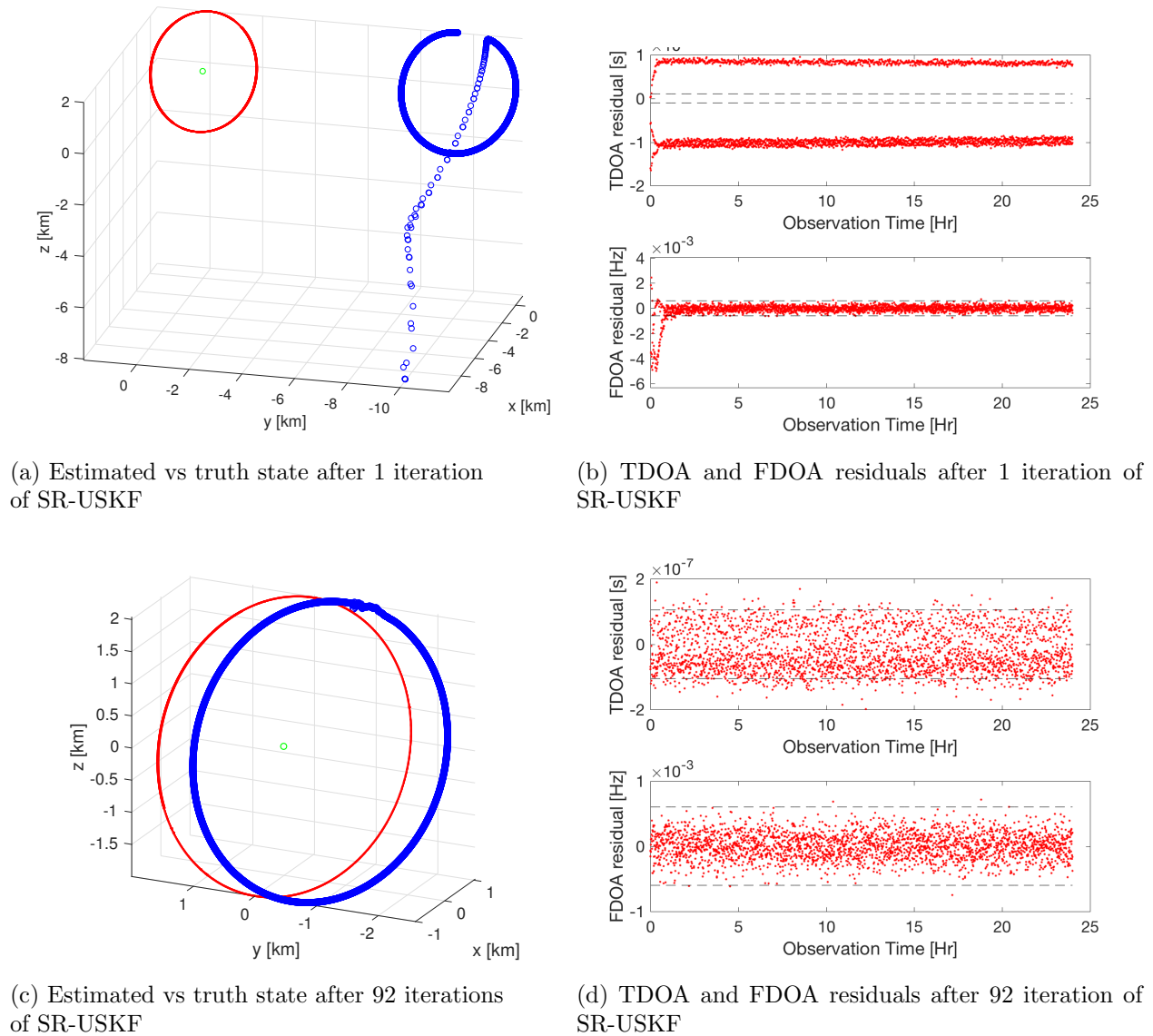
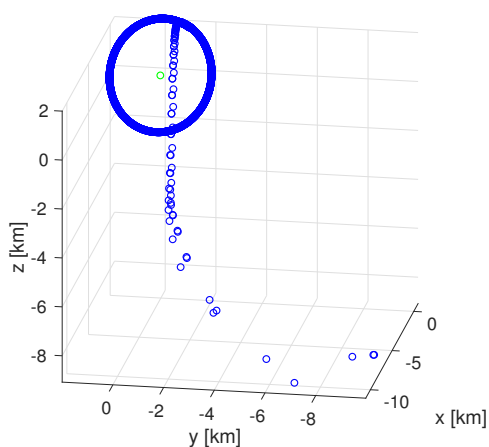
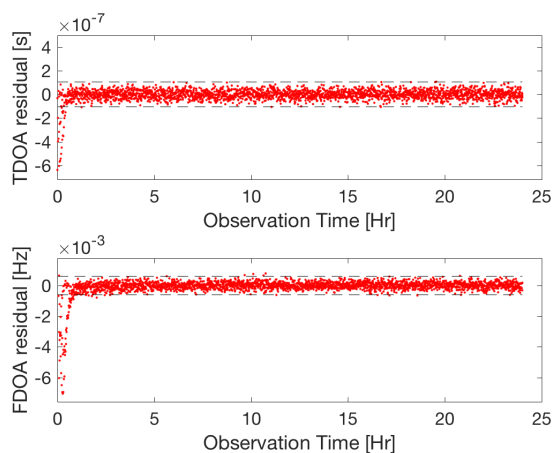


Figure 5.19: Close proximity bounded relative motion with considered 1σ position uncertainty of 10 m and 1σ velocity uncertainty of 1 mm/s in each direction of the chief. Satellite formation pair in GEO orbit resulting in low observability in the in-track y position direction of deputy. Comparing 1st to 92nd iteration.



(a) Estimated vs truth state after 1 iteration of SR-USKF



(b) TDOA and FDOA residuals after 1 iteration of SR-USKF

Figure 5.20: Close proximity bounded relative motion with considered 1σ position uncertainty of 10 m and 1σ velocity uncertainty of 1 mm/s in each direction of the chief. Chief in $0.95 \times a_{GEO}$ orbit demonstrating the low observability in the in-track y position direction is limited to GEO only and not its neighboring orbits.

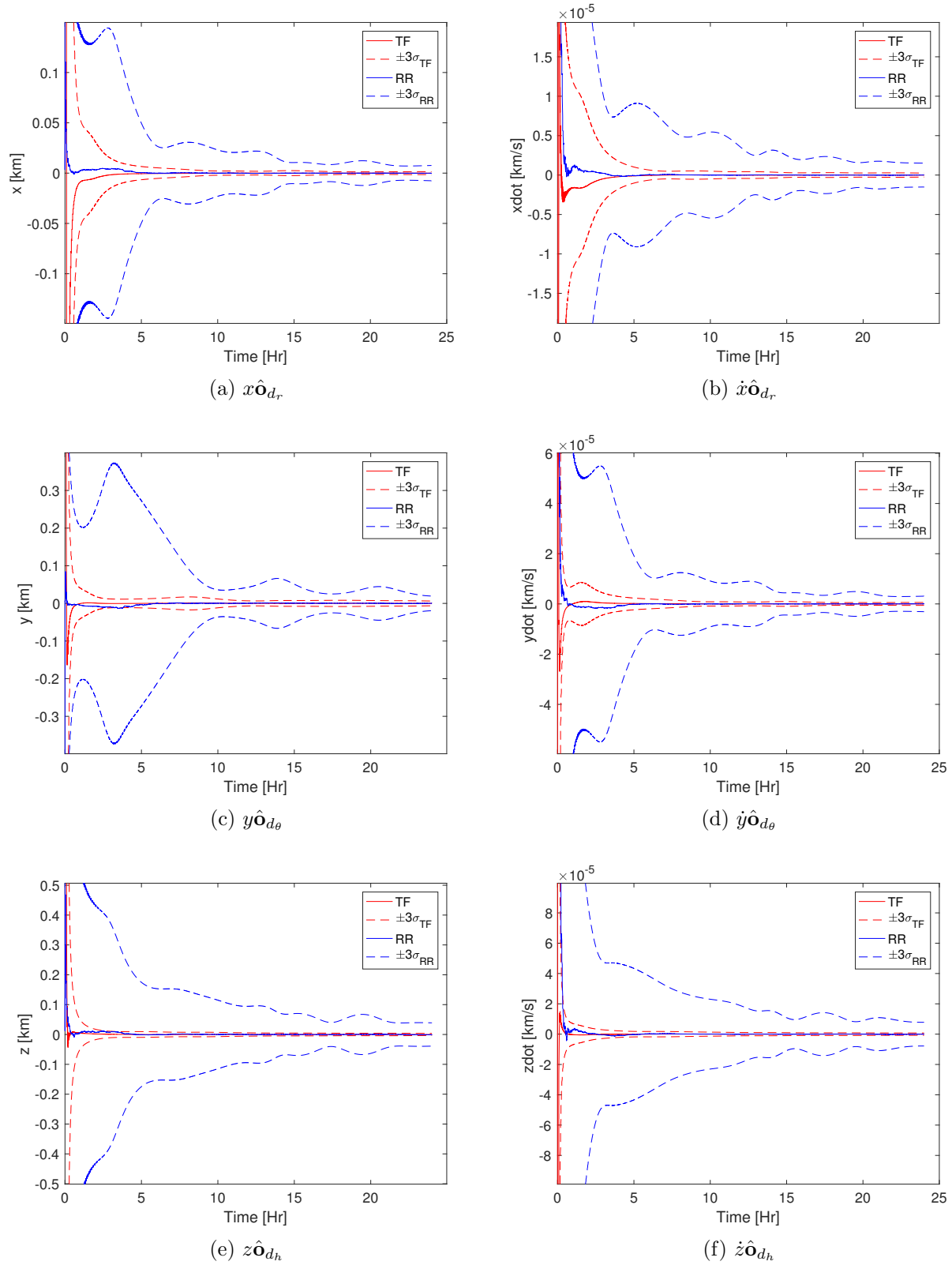


Figure 5.21: State error and 3σ covariances for close proximity bounded relative motion with considered 1σ position uncertainty of 10 m and 1σ velocity uncertainty of 1 mm/s in each direction of chief with chief at MEO ($0.5 \times a_{GEO}$) in the deputy LVLH frame. Comparison between TDOA/FDOA (TF) and range/range-rate (RR) observables. Three baselines used.

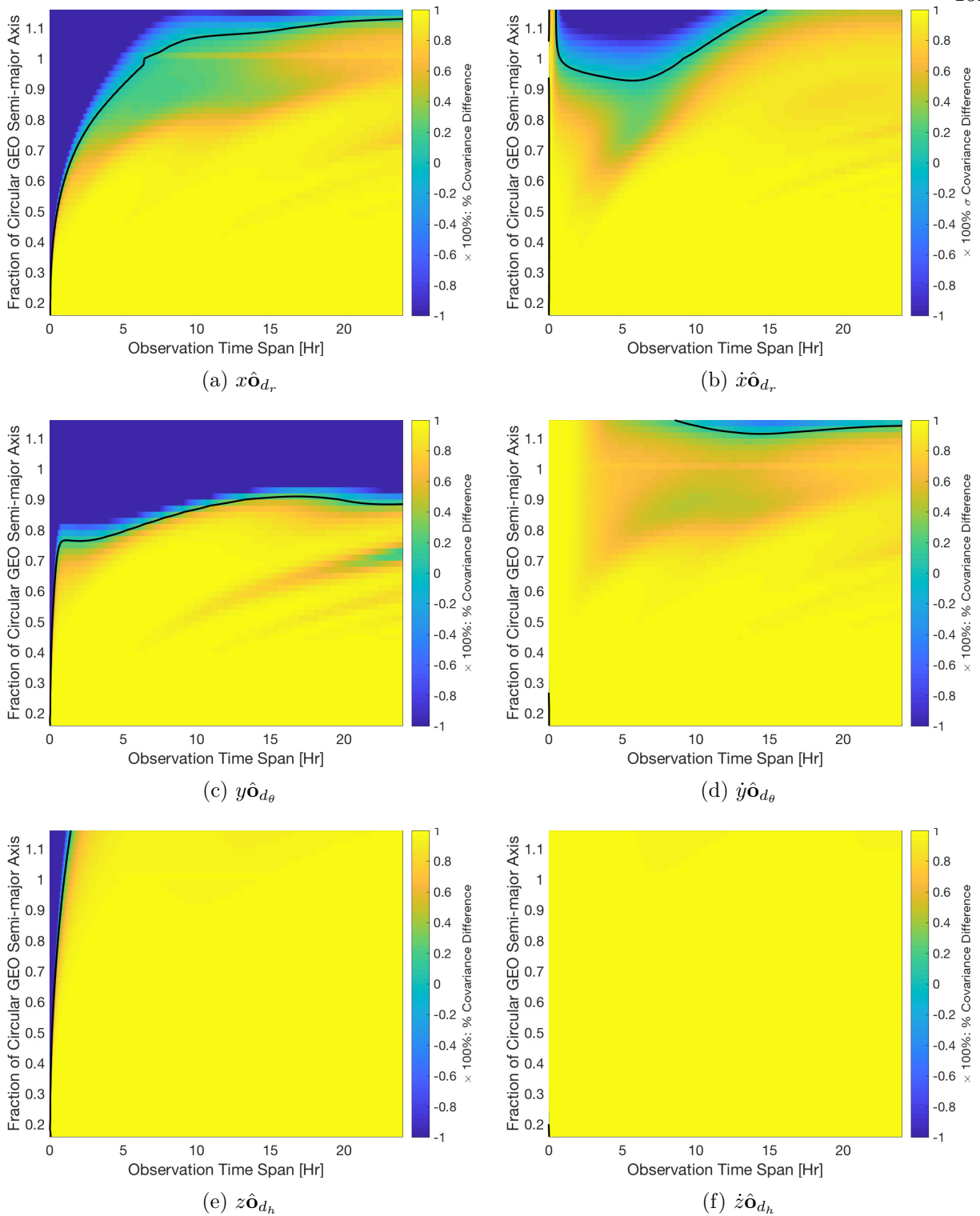


Figure 5.22: Close proximity bounded relative motion with considered 1σ position uncertainty of 10 m and 1σ velocity uncertainty of 1 mm/s in each direction of the chief at various semi-major axes, shown on ordinate. Showing % difference of CRLB covariance bounds between TDOA/FDOA and range/range-rate measurements over various observation time spans shown on abscissa. Color values above 0 indicate a region where TDOA/FDOA has lower covariance bounds compared to range/range-rate and vice versa. Coordinates are in the LVLH frame of the deputy. Three baselines used.

5.4.3.1 Estimating the Deputy with Considered Chief Uncertainty and One Station + Reference

In all previous cases in this chapter we have shown the results using three stations plus the reference to generate three baselines using the stations listed in Table 4.4. In this final scenario we take the previous bounded relative motion case and only use one station, to create one baseline, the Boulder-San Diego baseline. In this scenario there are distinct orbital regimes that would benefit from the TDOA/FDOA and the range/range-rate measurement set. More specifically, when faster dynamics, as is the case with lower orbiting satellites, are present along with longer observation times TDOA and FDOA are preferred. In the higher orbits with shorter observation spans range and range-rate has a lower CRLB.

In this chapter, three different relative navigation scenarios were investigated. They include a GEO paired with GEO-to-LEO case, a leader-follower setup with the chief and deputy ranging in semi-major axis from GEO-to-LEO, and finally a closely orbiting bounded relative motion scenario where both satellites also varied from GEO-to-LEO. In all these cases three baselines were utilized in the OD analysis. In the final relative motion case, a one-baseline setup was also examined. In all situations as the motion of the satellites increased with respect to the stations the more favorable the TDOA and FDOA measurements were compared to range and range-rate. The use of TDOA and FDOA for relative navigation is particularly good and has various applications. The first is for use in the SSA community, in order to allow close navigation of active satellites of a primary with respect to a secondary to avoid a collision. A second application could include precise orbit determination of a neighboring satellite if another satellite already has very good state information. In this last setup, doing relative OD could provide a better OD solution than simply estimating the satellite state using conventional range and range-rate measurements.

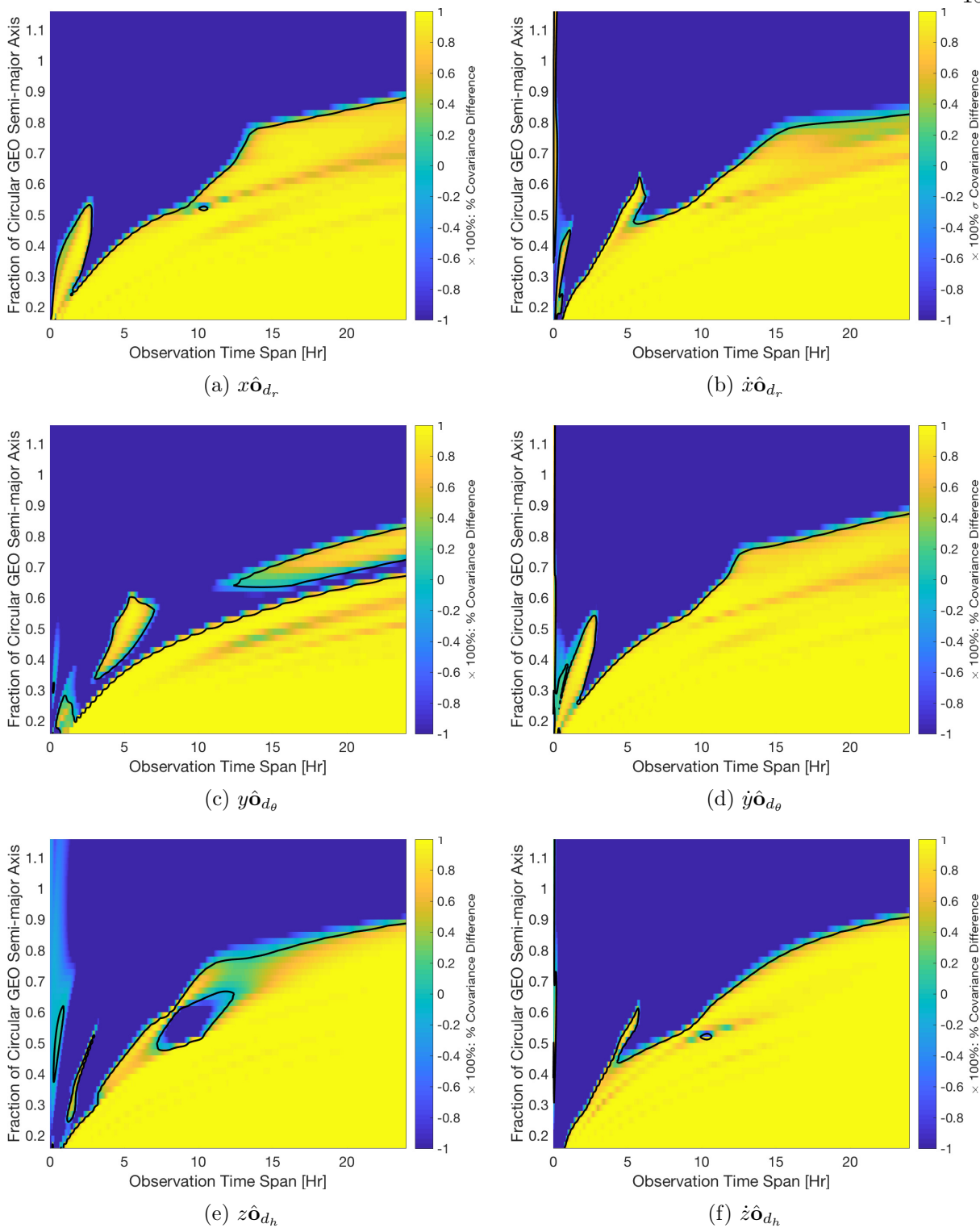


Figure 5.23: Close proximity bounded relative motion with considered 1σ position uncertainty of 10 m and 1σ velocity uncertainty of 1 mm/s in each direction of the chief at various semi-major axes, shown on ordinate. Showing % difference of CRLB covariance bounds between TDOA/FDOA and range/range-rate measurements over various observation time spans shown on abscissa. Color values above 0 indicate a region where TDOA/FDOA has lower covariance bounds compared to range/range-rate and vice versa. Coordinates are in the LVLH frame of the deputy. One baseline used.

Chapter 6

Radio Frequency Localization

In this chapter two types of localization are discussed. The first is geolocation, or the localization of a passive RF signal on the surface of the Earth. The second is the localization of a passive satellite signal in space, similar to how the tracking and data relay satellite system (TDRSS) can track satellites, but now with TDOA and FDOA. Two techniques are discussed for geolocation and one for satellite localization. The first is a two-step process which initially estimates the dual-satellite ephemeris with covariance which is then used in the second step of estimating the Earth or space-based transmitter while taking into account the uncertainty on the dual-satellite ephemeris. The second technique is simultaneous estimation of the dual-satellite ephemeris and the RF transmitter. Each of these methods have their advantages and disadvantages.

6.1 Geolocation

The accuracy of the geolocation solution is highly dependent on the knowledge and uncertainty of the satellites' orbits. A number of articles have already emphasized this importance. In Ref. [34], a prominent paper on geolocation, it was shown that the dominant cause of geolocation error was the satellite ephemeris accuracy in predicting velocity. Furthermore, Pattinson et al. [65], Sun et al. [82] and Yan et al. [89], directly or indirectly illustrate the effects of geolocation inaccuracies due to errors in the satellites' states. We demonstrate these inaccuracies next.

Often times the most recent information on geosynchronous satellite orbits are through NORAD's Two Line Element (TLE) sets. TLEs rely on the SGP4 orbit model which is based on

the analytical theory of Brouwer developed in the 1970s. Only the zonal terms J_2 , J_3 and J_4 are accounted for in the gravity field, consequently due to the low fidelity dynamics, the propagated trajectory gives rise to widely varying position errors which are commonly on the order of 2 km [60, 45]. Due to the high inaccuracies in the resulting ephemeris, extremely large errors in the geolocation solution, on the order of 100s to 1000s of km, are introduced. A 1000 point Monte Carlo simulation in Figure 6.1 illustrates a scenario where TLE-level accuracy ephemerides are used, which results in the possible geolocation solution to spread across 5 states and nearly 1000 km. It is important to note, the 3D aspect of the Monte Carlo simulation indicated by the blue and red colors. The elongated cloud of Monte Carlo points is in fact piercing the Earth at a significant angle such that the points north of Chicago can be hundreds of kilometers below the WGS84 ellipsoid, and the points south of Chicago can be up to hundreds of kilometers above this datum. At this time we simply illustrate that the geolocation solution can vary significantly in 3D space when large ephemeris uncertainties are encountered. Later in this chapter we take advantage of the knowledge that the transmitter is located on the Earth's surface, which may reduce the Monte Carlo point distribution significantly. Despite the knowledge introduced by the altitude constraint, it is still imperative that the ephemeris uncertainty be included in developing a geolocation solution as will demonstrated throughout this chapter.

A significant amount of literature exists on the geolocation process with key contributors including Smith [74, 75, 76], Ho [37, 38, 40, 39] and Chan [13, 12]. However, there is a significant gap in the literature on geolocation in the presence of ephemeris uncertainty. While Ref. [65] discusses the sensitivity to ephemeris errors on geolocation, the process by which these errors are propagated to the geolocation covariance is lacking.

In chapter 4 we show how the dual-satellite ephemeris estimate can be improved over commonly used TLEs. This was accomplished by performing OD with the TDOA and FDOA measurements that are already being gathered for geolocation. The improvements over the a-priori knowledge on the satellites were illustrated through a CRLB analysis and various other approaches. In this chapter, using either the newly corrected ephemeris or a pre-existing ephemeris with known

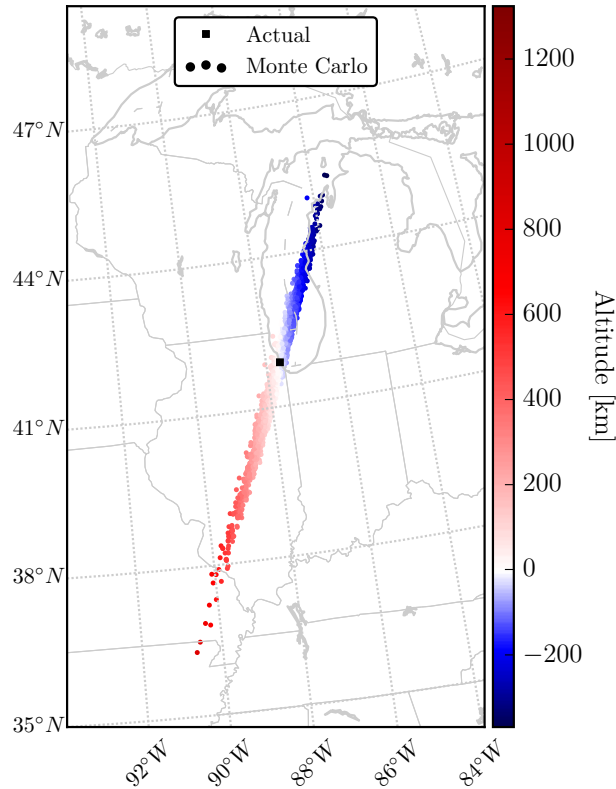


Figure 6.1: 1000 point Monte Carlo of Chicago transmitter (TX) geolocation with TLE-level ephemeris uncertainty

covariance, we derive a consider batch filter (CBF) to perform source localization of the unknown transmitter while also accounting for the ephemeris uncertainty. Including this new source of uncertainty inflates the projected covariance ellipse of the estimated transmitter position, and a Monte Carlo simulation shows the necessity of including this source of uncertainty. Then we demonstrate the addition of a probabilistic altitude constraint on the CBF computed covariance. Finally, rather than first estimating an ephemeris correction and then geolocating the unknown signal (two-steps), we show that these steps can be performed simultaneously where we estimate both the ephemeris and the unknown transmitter position together. In the following sections we demonstrate these findings.

The locations of the transmitters (TXs) and receivers (RXs) used are outlined in Table 6.1. The targets are the transmitters for which we have no prior knowledge and are geolocated in later

sections. The locations of the targets listed in the table are the truth values to compare against with the estimated values from the filter.

Table 6.1: Latitude, longitude and altitude of transmitters and receivers used in geolocation examples

<i>Transmitters (TXs)</i>			
<i>Reference station</i>			
Boulder	40.015° N	105.270° W	1623.72 m
<i>Stations</i>			
San Diego	32.72° N	117.16° W	27.91 m
Seattle	47.60° N	122.33° W	9.44 m
Houston	29.76° N	95.37° W	14.54 m
Miami	25.76° N	80.19° W	0.89 m
Boston	42.36° N	71.06° W	11.49 m
<i>Targets</i>			
Chicago	41.88° N	87.63° W	181.72 m
Prescott	34.54° N	112.47° W	1633.17 m
Atlanta	33.75° N	84.39° W	310.38 m
<i>Receivers (RXs)</i>			
Boulder 1	40.014° N	105.271° W	1625.57 m
Boulder 2	40.014° N	105.270° W	1621.13 m

6.1.1 Ephemeris Uncertainty Mapped into Geolocation Covariance

Not accounting for ephemeris uncertainty may in many cases yield a 3σ geolocation covariance that is far too optimistic. The need to include the ephemeris uncertainty for RF localization is shown in the following example. Figure 6.2 shows the location of a Chicago transmitter at the center marked ‘Actual’. Assume that the transmitter was estimated perfectly and therefore the center of the covariance ellipse is coincident with the actual transmitter location. If the ephemeris used is assumed to be without error then the only source of inaccuracy is derived from the measurement noise on TDOA and FDOA. Given that assumption, the solid ellipse provides the 3σ bound on the location of the interfering transmitter.

Notice however, when a 1000 point Monte Carlo simulation is executed including ephemeris uncertainty a non-negligible amount (if not the majority) of cases fall well outside of the original

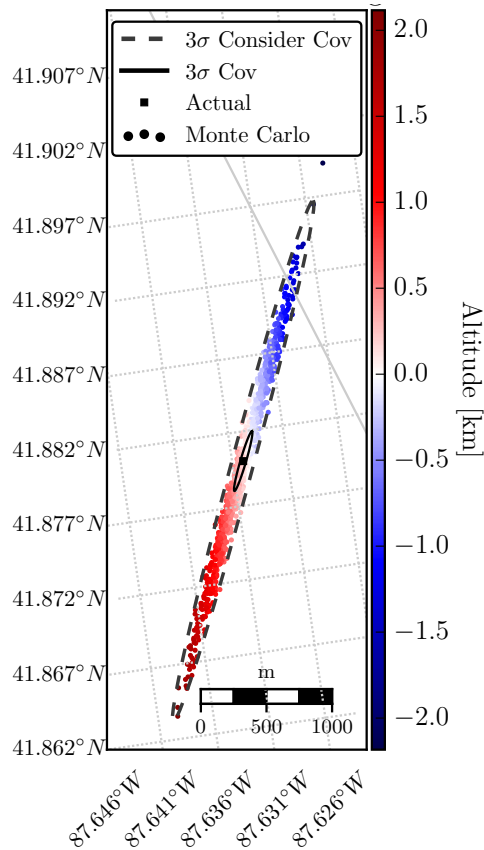


Figure 6.2: 1000 point Monte Carlo of geolocation with ephemeris uncertainty of Chicago TX

3σ ellipse. The uncertainty on the ephemeris is obtained after 9 hours of OD using four baselines. The Boston transmitter is not included in order to emphasize the ephemeris uncertainty in the geolocation solutions. Considering Figure 6.2 shows results using a corrected ephemeris, if a TLE were to be used instead, the Monte Carlo would cover a much larger area, similar to what is shown in Figure 6.1. The consequence of not including ephemeris error means the operator could be eliminating areas of potential transmitter locations due to the too optimistic covariance ellipse. We show that including the ephemeris uncertainty in the covariance calculation provides a much better representation of the actual errors. In Figure 6.2 the dashed line includes the consider parameters and captures the same results as demonstrated with the monte carlo simulation. The growth of the covariance is significant in the major axis, increasing from 470 m to 4059 m with a smaller increase in the minor axis from 43 m to 165 m. The following section derives the Consider Batch Filter

(CBF) used.

6.1.1.1 Consider Batch Filter for Ephemeris Uncertainty Inclusion in Geolocation Covariance

A CBF algorithm was previously described in chapter 3.1.3 but we modify its derivation to be used with the geolocation problem. The CBF is implemented to solve the location of the unknown transmitter while also accounting for the uncertainty in the ephemeris. The estimated states in ECEF are,

$$\mathbf{X}_{TX} = \begin{bmatrix} x_{TX}^t & y_{TX}^t & z_{TX}^t \end{bmatrix}^\top. \quad (6.1)$$

The subscript TX stands for transmitter and the superscript t is for target since this transmitter is being targeted for localization. In the CBF additional parameters are included but not estimated to more accurately represent the uncertainty of the localization problem as a whole. The consider parameters are the satellite components in position and velocity as well as the coefficients of reflectivity. Therefore there are 14 additional states,

$$\mathbf{C} = \begin{bmatrix} \mathbf{C}_1^\top & \mathbf{C}_2^\top \end{bmatrix}^\top \quad (6.2)$$

where,

$$\mathbf{C}_i = \begin{bmatrix} x_i & y_i & z_i & \dot{x}_i & \dot{y}_i & \dot{z}_i & C_{r_i} \end{bmatrix}^\top. \quad (6.3)$$

The unknown transmitter is assumed to be stationary throughout the broadcast duration. Consequently the dynamics of the transmitter are zero and the problem simplifies significantly. This is illustrated by taking the partial derivatives of the force model with respect to the estimated transmitter location,

$$\mathbf{A}_{TX}(t) = \left[\frac{\partial F(t)}{\partial \mathbf{X}_{TX}(t)} \right] \Bigg|_{\mathbf{X}_{ref}} = \mathbf{0}. \quad (6.4)$$

On the other hand the partial derivatives of the force model, described in Eq. 4.54, with respect to the consider parameters are identical to those found in chapter 4 where it was defined as the time-varying matrix $\mathbf{A}(t)$. To represent the same partials in the CBF we use the time-varying matrix $\mathbf{B}(t)$,

$$\mathbf{B}(t) = \left[\frac{\partial F(t)}{\partial \mathbf{C}} \right] \Big|_{\mathbf{C}_{ref}} = \mathbf{A}(t). \quad (6.5)$$

Furthermore the STM of the estimated states remains identity since the time evolution is also zero.

$$\dot{\Phi}(t, t_k) = \mathbf{A}_{TX}(t)\Phi(t, t_k) = \mathbf{0} \quad \rightarrow \quad \Phi(t, t_k) = \mathcal{I} \quad (6.6)$$

Due to the consider parameters, there is an additional STM defined as,

$$\dot{\theta}(t, t_k) = \mathbf{B}(t)\theta(t, t_k). \quad (6.7)$$

We can combine the estimated states and consider parameters into one deviation vector \mathbf{z} such that $\mathbf{z} = [\mathbf{x} \ \mathbf{c}]^T$ so that the time evolution is,

$$\dot{\mathbf{z}}(t) = \psi(t, t_k)\mathbf{z}(t_k) \quad (6.8)$$

where,

$$\psi(t, t_k) = \begin{bmatrix} \Phi(t, t_k) & \mathbf{0} \\ \mathbf{0} & \theta(t, t_k) \end{bmatrix} = \begin{bmatrix} \mathcal{I} & \mathbf{0} \\ \mathbf{0} & \theta(t, t_k) \end{bmatrix}. \quad (6.9)$$

Next, we compute $\tilde{\mathbf{H}}_{x_k}$ with respect to the estimated states shown in Eq. 6.10 and find a similar result to Eq. 2.43 except with reversed signs,

$$\tilde{\mathbf{H}}_{x_k} = \left[\frac{\partial G(\mathbf{X}_k, t_k)}{\partial \mathbf{X}_{TX_k}} \right] \Big|_{\mathbf{X}_{ref}}. \quad (6.10)$$

The measurement mapping matrix $\tilde{\mathbf{H}}_{c_k}$, are the partials with respect to the consider parameters and are identically the same to Eq. 2.43,

$$\tilde{\mathbf{H}}_{c_k} = \left[\frac{\partial G(\mathbf{X}_k, t_k)}{\partial \mathbf{C}} \right] \bigg|_{\mathbf{C}_{ref}}. \quad (6.11)$$

Given the STMs we can compute the measurement mapping matrix mapped back to epoch, where $\mathbf{H}_{x_k} = \tilde{\mathbf{H}}_{x_k}$ because $\Phi(t, t_k)$ is identity and $\mathbf{H}_{c_k} = \tilde{\mathbf{H}}_{c_k} \theta(t, t_k)$. These mapping matrices are then used to compute the three different information matrices,

$$\mathbf{\Lambda}_{xx} = \sum_{k=1}^l \mathbf{H}_{x_k}^\top \mathbf{W}_k \mathbf{H}_{x_k} + \bar{\mathbf{\Lambda}}_{xx}, \quad (6.12)$$

$$\mathbf{\Lambda}_{xc} = \sum_{k=1}^l \mathbf{H}_{x_k}^\top \mathbf{W}_k \mathbf{H}_{c_k} + \bar{\mathbf{\Lambda}}_{xc}, \quad (6.13)$$

$$\mathbf{\Lambda}_{cc} = \sum_{k=1}^l \mathbf{H}_{c_k}^\top \mathbf{W}_k \mathbf{H}_{c_k} + \bar{\mathbf{\Lambda}}_{cc}. \quad (6.14)$$

After all observations are processed, the covariance, not including the ephemeris uncertainty can be found as $\mathbf{P}_x = \mathbf{\Lambda}_{xx}^{-1}$. However, we are interested in including the ephemeris uncertainty, therefore we compute the sensitivity matrix $\mathbf{S}_{xc} = -\mathbf{P}_x \mathbf{\Lambda}_{xc}$ which after substituting in Eq. 6.13 becomes,

$$\mathbf{S}_{xc} = -\mathbf{P}_x \mathbf{H}_x^\top \mathbf{W} \mathbf{H}_c. \quad (6.15)$$

Using the sensitivity matrix we can map the a-priori consider covariance $\bar{\mathbf{P}}_{cc}$, into the estimation space and add it to the original covariance \mathbf{P}_x to yield the new covariance \mathbf{P}_{xx} ,

$$\mathbf{P}_{xx} = \mathbf{P}_x + \mathbf{S}_{xc} \bar{\mathbf{P}}_{cc} \mathbf{S}_{xc}^\top. \quad (6.16)$$

Both covariances \mathbf{P}_x and \mathbf{P}_{xx} are trivariate Gaussian which are projected onto the Earth's surface at the estimated position. The trivariate covariance is defined as $E[\mathbf{xx}^\top]$, but we require only the component projected onto Earth's surface which is $E[\mathbf{ss}^\top]$, see Figure 6.3.

The projection can be performed as follows,

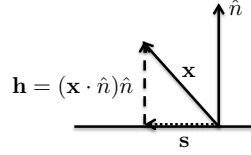


Figure 6.3: Geometry for projected covariance

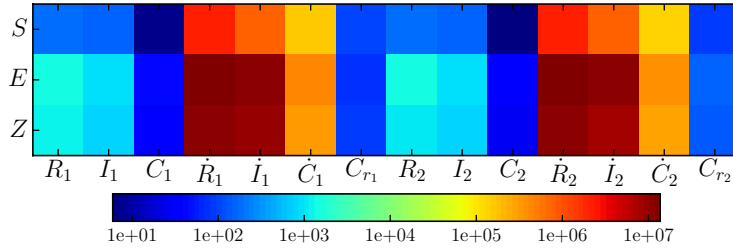
$$E[\mathbf{ss}^\top] = (\mathcal{I} - \hat{n}\hat{n}^\top)E[\mathbf{xx}^\top](\mathcal{I} - \hat{n}\hat{n}^\top)^\top \quad (6.17)$$

Where \hat{n} is the normal vector connecting Earth's CoM to \mathbf{X}_{TX} , resulting in an approximately orthogonal unit vector to the local Earth surface. Then the solid black ellipse in Figure 6.2 is the projection of \mathbf{P}_x onto Earth's surface and the dashed ellipse is the projection of \mathbf{P}_{xx} . In the next subsection we delve deeper into the sensitivity matrix.

6.1.1.2 Sensitivity Matrix

The sensitivity matrix is $\mathbf{S}_{xc} = \frac{\partial \hat{\mathbf{x}}_{TX}}{\partial \mathbf{c}}$, describing how $\hat{\mathbf{x}}_{TX}$ varies with the consider parameters \mathbf{c} . The sensitivity matrix as described in Eq. 6.15 expresses the sensitivity to the consider parameters in ECI to the estimated parameters in ECEF. Therefore by defining a rotation matrix $[T_{ECEF}^{SEZ}]$ which rotates a vector from the ECEF coordinate frame to the topocentric SEZ (south, east, zenith) and a rotation matrix $[T_{ECI}^{RIC}]$ which rotates a vector from the ECI coordinate frame to the satellite body frame (radial, in-track, cross-track) we can rotate S_{xc} so that it describes the sensitivity to the consider parameters in RIC to the estimated parameters in SEZ as $[T_{ECEF}^{SEZ}]S_{xc}[T_{ECI}^{RIC}]^\top$. Figure 6.4 visualizes the magnitude of the sensitivity matrix for the Chicago geolocation example. Blue signifies a relatively low sensitivity to the consider parameter while red is the opposite.

It is immediately apparent that the velocity components of both satellites have the highest impact on the geolocation solution. This is consistent with the claim from Ref. [34] that the primary cause of geolocation error is predominantly the satellite ephemeris accuracy in predicting velocity. For geostationary satellites the radial and in-track velocity directions are more important than the cross-track direction. Looking back to the velocity CRLBs of GEO satellites from chapter

Figure 6.4: Sensitivity matrix, S_{xc}

4 we see that while the in-track velocity direction has the most information, the radial velocity direction has poor information content. Therefore it is expected that improving the radial velocity direction information would significantly improve geolocation accuracy.

6.1.1.3 Addition of a Probabilistic Altitude Constraint

For dual-satellite geolocation with two Geostationary satellites the primary axis of the covariance ellipsoid was found to point toward the direction of the two satellites. Therefore the ellipsoid pierces the Earth's surface at a steeper and steeper angle when approaching the Equator. Consequently portions of the ellipsoid that are significantly above or below the WGS84 ellipsoid are unlikely to contain the actual transmitter location. In this subsection we leverage the fact that the transmitter is more likely to be within a certain vertical distance from the local terrain's surface. We add in a probabilistic altitude constraint thereby further reducing the size of the covariance ellipse. This new information is written in terms of a non-full rank information matrix, $\mathbf{\Lambda}_{alt}$,

$$\mathbf{\Lambda}_{alt} = \hat{n} \begin{bmatrix} 1 \\ \sigma_{alt}^2 \end{bmatrix} \hat{n}^\top. \quad (6.18)$$

Where \hat{n} is the local vertical unit vector as shown in Figure 6.3, and σ_{alt} is the standard deviation in the local vertical direction for the likelihood of the transmitter being at that height (depth) above (below) the local terrain's surface. In this research we assume $\sigma_{alt} = 75$ m, which asserts that 99.7% of all transmitters will be within ± 225 m of the local terrain which means that in almost all cases the transmitter will not be higher than a 68-story building (or in an equivalently

deep man-made depression).

Adding in this additional altitude information is done after the CBF has completed locating the RF signal. We use the output of the CBF, which is the best estimate of the position of the transmitter, $\hat{\mathbf{X}}_{CBF}$ with an associated covariance, \mathbf{P}_{CBF} . Since we have two independent Probability Density Functions (PDFs) we can mix the information into a single covariance matrix, \mathbf{P}_{tot} as shown in Eq. 6.19 [83],

$$\mathbf{P}_{tot} = (\mathbf{P}_{CBF}^{-1} + \mathbf{\Lambda}_{alt})^{-1}. \quad (6.19)$$

Then a new optimal estimate can be obtained by weighting the best estimate from the CBF and also the point about which the altitude constraint is applied, $\hat{\mathbf{X}}_{alt}$, by their respective information matrices as displayed in Eq. 6.20,

$$\hat{\mathbf{X}}_{tot} = \mathbf{P}_{tot} (\mathbf{P}_{CBF}^{-1} \hat{\mathbf{X}}_{CBF} + \mathbf{\Lambda}_{alt} \hat{\mathbf{X}}_{alt}). \quad (6.20)$$

The only unknown is $\hat{\mathbf{X}}_{alt}$. We designate $\hat{\mathbf{X}}_{alt}$ as the center of the ellipse defined by the intersection of the covariance ellipsoid, \mathbf{P}_{CBF} , and the plane representing the local Earth's surface, using the approach from Ref. [50]. This is the point about which the Gaussian distribution in altitude is centered, since we assume that the transmitter can be located on top of a building equally as likely as in a man-made depression. Computing this point requires an iterative approach and is somewhat involved, see Figure 6.5 for reference.

First, the plane is defined to be orthogonal to \hat{n} , but one additional point is required to fix the plane in 3D space as per definition of a plane. We need to sample points along \hat{n} that are also contained within the projection of the ellipsoid onto \hat{n} . Therefore we project the ellipsoid onto \hat{n} and sample the resulting line segment for points. This line segment is represented by $E[\mathbf{h}\mathbf{h}^\top]$, where \mathbf{h} is the projection of the random variable \mathbf{x} onto the normal, similar to the approach used to obtain Eq. 6.17,

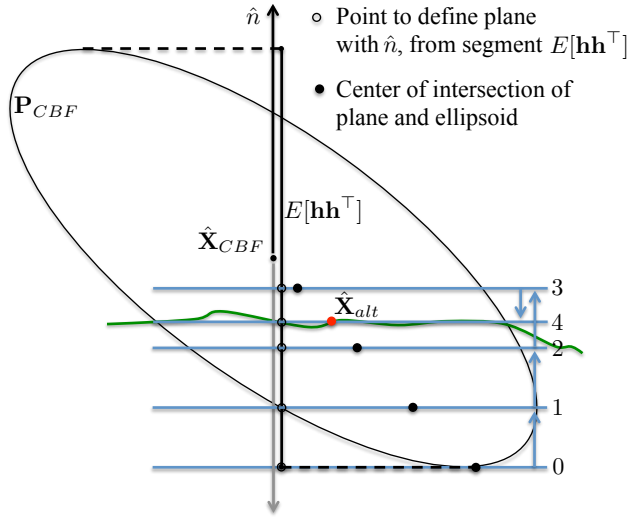


Figure 6.5: 2D side view of iterative computation of $\hat{\mathbf{X}}_{alt}$

$$E[\mathbf{h}\mathbf{h}^\top] = \hat{n}\hat{n}^\top E[\mathbf{x}\mathbf{x}^\top]\hat{n}\hat{n}^\top. \quad (6.21)$$

Iteratively sampling points along the \hat{n} line segment allows the plane to be defined and the center of the ellipse of intersection between the ellipsoid and plane to be computed. This center point is computed in ECEF which is then converted to latitude, longitude and altitude. The altitude is called the computed altitude. For the given latitude and longitude the actual terrain elevation is queried from a database (in this research we use the Google elevation api¹) which is called the observed altitude. We continue sampling points along \hat{n} , there by moving the plane, until the computed altitude and the observed altitude are within some tolerance, in our case we use 10 m. When the tolerance is met, we have effectively found $\hat{\mathbf{X}}_{alt}$, or the point about which to apply the probabilistic altitude constraint, shown with a red dot in Figure 6.5.

While 75 m for the σ_{alt} is chosen, another value could be used instead if it is deemed more appropriate. A larger value of σ_{alt} provides a weaker constraint and vice versa. From Eq. 6.20 we also see that a different σ_{alt} will change the solution. With a larger σ_{alt} the solution will tend to be closer to $\hat{\mathbf{X}}_{CBF}$ while a smaller σ_{alt} will result in a solution approaching $\hat{\mathbf{X}}_{alt}$.

¹ <https://developers.google.com/maps/documentation/elevation/start>

6.1.1.4 Geolocation Simulations

Provided with an ephemeris and associated covariance either through the approach from chapter 4 or a pre-existing one, in addition to the CBF and the altitude constraint, we demonstrate several geolocation examples using simulated data.

In Figure 6.6, first notice the solid black ellipse, this is the projected 3σ covariance without the inclusion of ephemeris uncertainty or an altitude constraint and spans 470 m by 43 m. The actual location of the Chicago transmitter shown with the black square is well outside of this covariance and is 376 m from its center, re-iterating the importance of including ephemeris uncertainty. By including the ephemeris uncertainty we obtain the large black dashed ellipse which spans 4059 m by 165 m and is consistent as it includes the actual location. Recall however, that this is a projection of a 3D covariance ellipsoid which may pierce the Earth's surface at a rather steep angle. This means that part of the consider projection is very unlikely to contain the actual location of the transmitter. Therefore we apply the probabilistic altitude constraint to both the 3σ covariance as well as the 3σ consider covariance. With the applied altitude constraint the new best estimate of the transmitter location is shown with the 'Estimated' point at the center of both the blue solid and dashed ellipses. This solution is off from the actual transmitter by 100 m, a significant reduction from the previous 376 m error. Notice however, that ephemeris uncertainty inclusion is still required in order to maintain consistency as the actual transmitter location is still outside of the solid blue 3σ covariance but well within the new dashed blue 3σ consider covariance.

We show two more geolocation examples, they include a transmitter in Prescott AZ and a transmitter in Atlanta GA. In Figure 6.7 the 3σ ellipse is 382 m by 39 m which blows up to 620 m by 49 m with ephemeris uncertainty. Then applying the altitude constraint we obtain a 3σ ellipse of 248 m by 39 m and 299 m by 48 m with ephemeris uncertainty. The altitude constraint improves the geolocation error from 104 m to 31 m.

Finally in Figure 6.8 the 3σ ellipse is 400 m by 46 m which with ephemeris uncertainty increases to 2076 m by 154 m. Applying the altitude constraint results in a 3σ ellipse of 268 m by

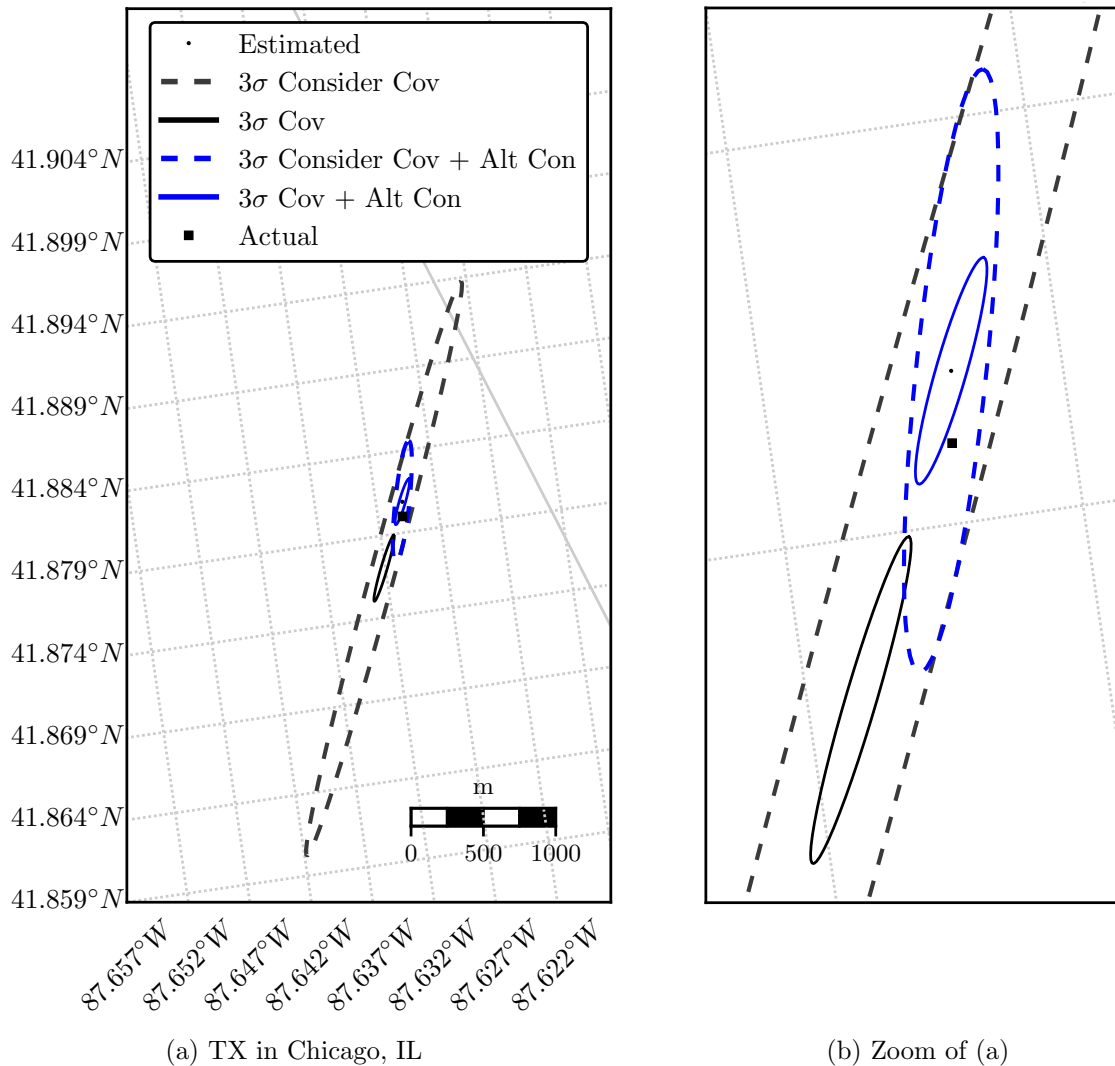


Figure 6.6: Geolocation of a Chicago, IL based TX

46 m and a 500 m by 112 m ellipse with ephemeris uncertainty. The altitude constraint improves the geolocation error from 115 m to 29 m. We summarize the results in Table 6.2 for convenience.

It is interesting to note that if the major axes of the projected 3σ geolocation covariances (without altitude constraint) were extended they would approximately intersect the projection of the simulated satellites' longitudinal slots of 99° W and 105° W longitude. Furthermore, TDOA and FDOA provide lines of positioning (LOPs) with TDOA constraining the E-W direction and FDOA constraining the N-S direction [34]. One might expect that decreasing the uncertainty on

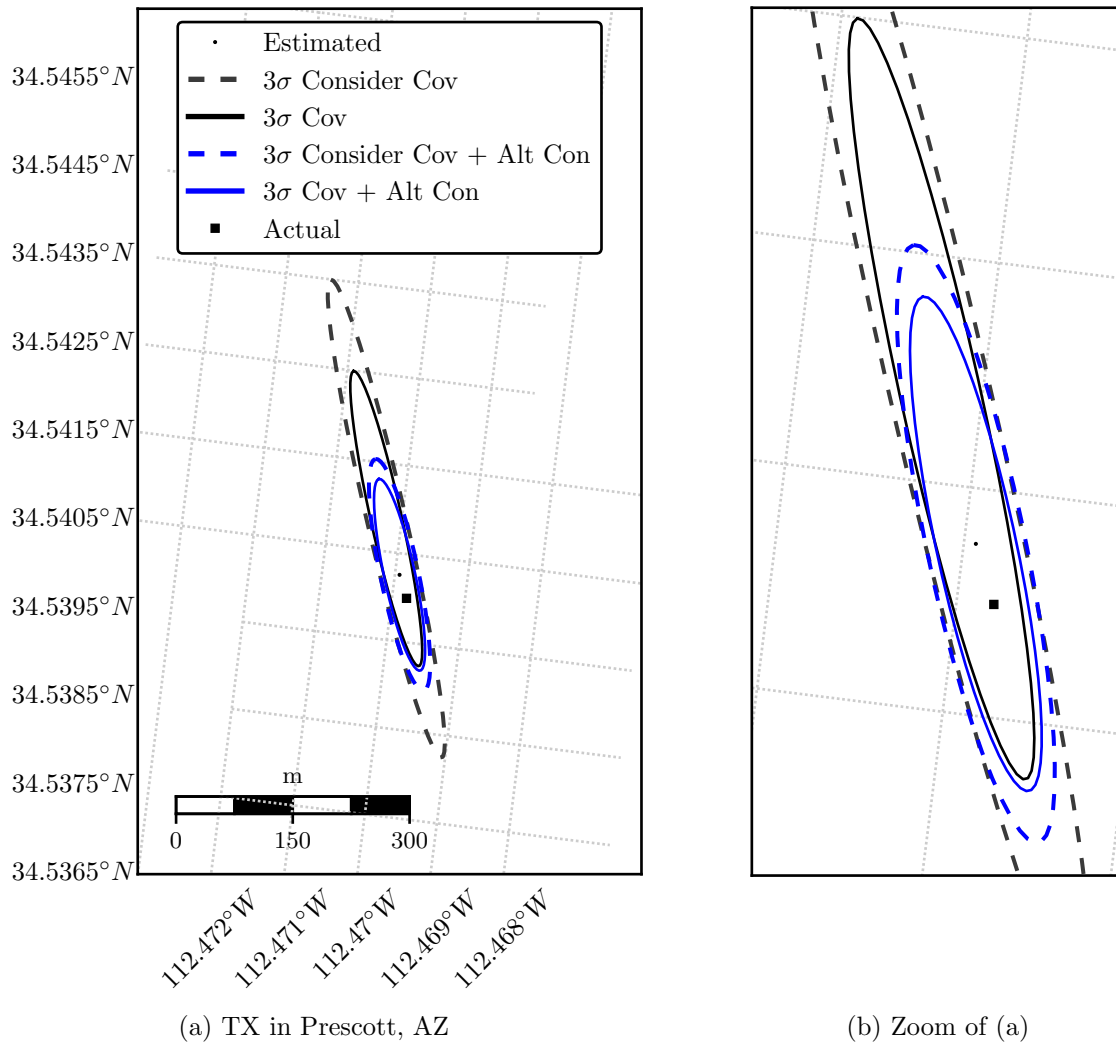


Figure 6.7: Geolocation of a Prescott, AZ based TX

the FDOA measurement would decrease the major axis of the geolocation covariance ellipse making the ellipse more circular. While it does indeed decrease the major axis, the effect is coupled and also reduces the minor axis thereby maintaining its elliptical shape.

6.1.2 Simultaneous Ephemeris Correction and Geolocation

Previous sections illustrated the process for estimating an improved ephemeris followed by localizing the interference source with accurate covariance information, this is referred to as the

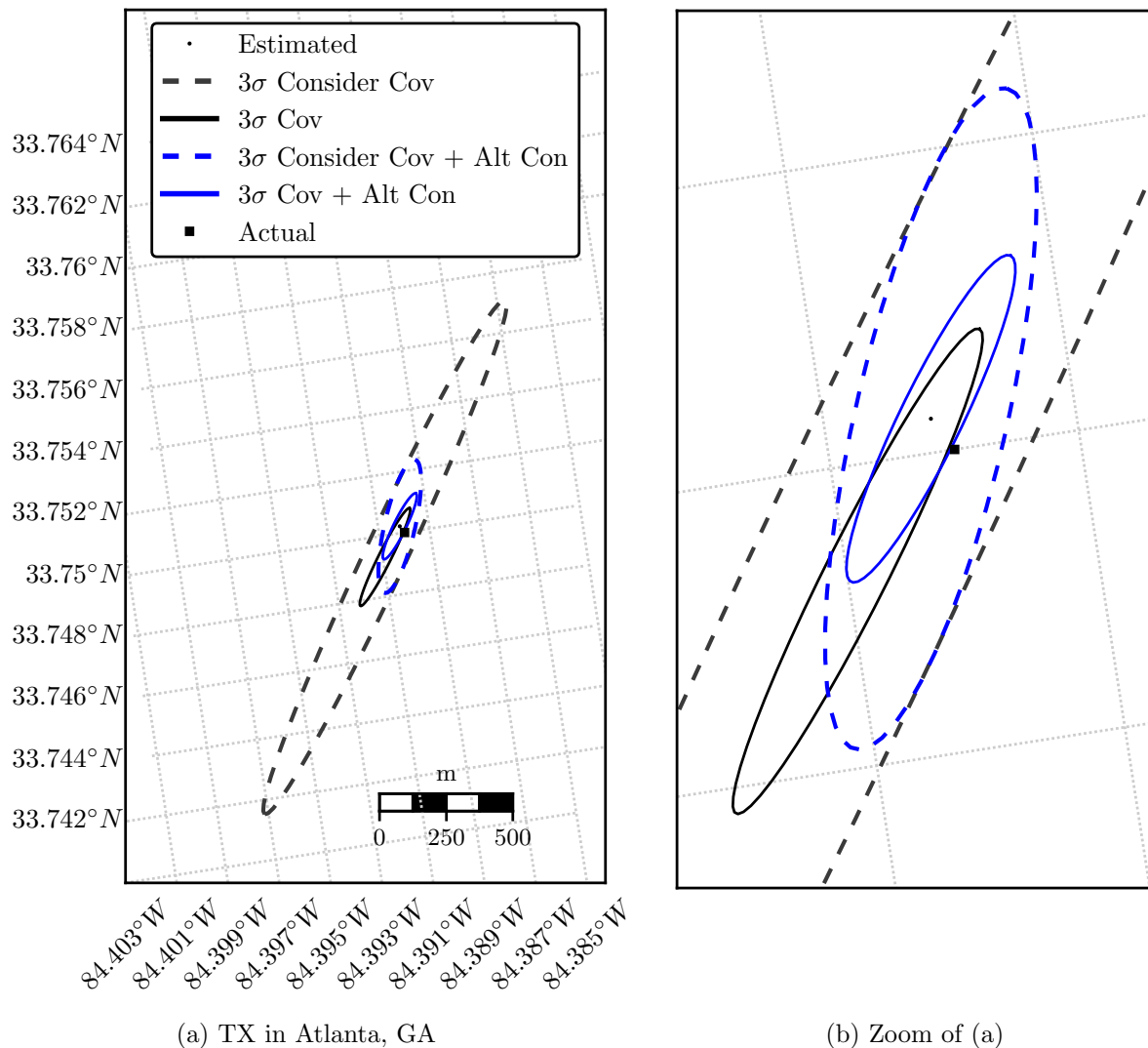


Figure 6.8: Geolocation of a Atlanta, GA based TX

Table 6.2: Summary of covariance ellipses (major axis \times minor axis) and errors [m]

	Chicago	Prescott	Atlanta
3σ Cov	$470 \times 43^\dagger$	382×39	$400 \times 46^\dagger$
3σ Consider Cov	4059×165	620×49	2076×154
3σ Cov + Alt Con	$325 \times 43^\dagger$	248×39	$268 \times 46^\dagger$
3σ Consider Cov + Alt Con	837×97	299×48	500×112
Error	376	104	115
Error with Alt Con	100	31	29

 † Truth/actual TX location is outside of covariance ellipse.

two-step process. Separating the ephemeris estimation side from the geolocation side has its advantages and disadvantages. The most important advantage is the flexibility provided to transmitter time scheduling for OD of the satellites. In other words the transmitters (other than the reference) do not necessarily need to be available for OD while geolocating the interfering RF source. OD can be performed at anytime, the solution can then be propagated to the time span of the measurements obtained from the interfering transmitter. Of course the closer the OD is performed to the time span of the geolocating process the smaller the associated ephemeris covariance and the smaller the chance that a maneuver occurred during that period. The disadvantage is the increased ephemeris covariance if propagated over longer time periods and the fact that two steps are required. Furthermore, considering the dual-satellite ephemeris while estimating the target transmitter is not optimal as some of the correlations are lost. It is possible however, if the circumstances permit, to merge this two-step process into one step by simultaneously estimating the interfering transmitter along with the dual-satellite ephemeris. Not only does this reduce the OD and geolocating steps into one estimation step, the correlations are also maintained between the targeted transmitter and the dual-satellite ephemeris. In that case, the newly estimated state vector is equivalent to that shown in Eq. 4.53 with the exception of the added position term of the estimated transmitter, \mathbf{r}_{TX}^t ,

$$\mathbf{X} = \left[\mathbf{r}_1^\top \quad \mathbf{v}_1^\top \quad C_{r_1} \quad \mathbf{r}_2^\top \quad \mathbf{v}_2^\top \quad C_{r_2} \quad \mathbf{r}_{TX}^{t\top} \right]^\top. \quad (6.22)$$

While the satellite states are estimated in the cartesian Earth Centered Inertial (ECI) frame, the transmitter position is estimated in the Earth Centered Earth Fixed (ECEF) frame. The ECEF position is then easily converted to latitude, longitude and altitude based on the WGS84 datum.

Despite the preserved correlations, the solution as well as the covariance for the target transmitter were effectively the same compared to the two-step process, with differences below the millimeter level for the cases examined. The reason for the nearly identical solution is that the target transmitter did not decidedly improve or degrade the estimated ephemeris. The added transmitter moved the dual-satellite ephemeris solution on the centimeter and meter level in position and on

the order of one tenth of a millimeter per second in velocity, too small to affect the geolocation solution and covariance. While in these cases the results are effectively the same between the 2-step and 1-step methods, it is possible for an estimated transmitter to considerably improve the OD solution of the satellites depending on the location of the transmitter. While not discussed in this chapter, it was observed that the location of certain transmitters have a higher impact on the OD solution than others depending on the geometry created. If the interfering transmitter improves the dual-satellite ephemeris, then naturally, the geolocation accuracy would also improve compared to the two-step process which keeps both the OD and geolocation steps independent.

6.2 Satellite Localization

The passive localization of a transmitter need not be limited to a stationary source on the surface of the Earth. In this section, the feasibility of localizing a satellite using two Geostationary satellites is examined. The setup of this scenario has similarities to TDRSS. Furthermore this technique can be particularly useful for locating a satellite in a GPS denied environment, or in a situation where the satellite is not operated by the analysts trying to obtain its orbit information. A requirement however, is that the satellite must be emitting an RF signal that can be picked up by two neighboring satellites. The geometry of this setup is illustrated in Figure 6.9.

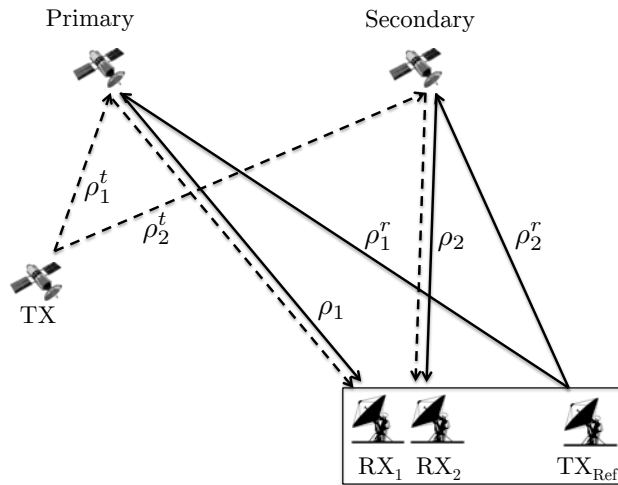


Figure 6.9: Satellite localization geometry

Similar to the two-step process used in geolocation, when applied to satellite localization the process estimates the dual-satellite ephemeris with covariance which is then used with a CBF to estimate the state of the RF source satellite. While the CBF is similar to the one shown in chapter 6.1.1.1, the dynamics are no longer zero due to the orbital motion of the satellite, this new CBF derivation is not shown.

6.2.1 Ephemeris Uncertainty Mapped into Satellite Localization Covariance

The orbital elements of the three satellites used in the satellite localization case are outlined in Table 6.3, these satellites have previously been used in a number of other simulations as well.

Table 6.3: Orbit parameters of satellites used in satellite localization

	a [km]	e	i [deg]	Ω [deg]	ω [deg]	ν [deg]	C_r
GEO ₁	42166.4	0	0.08	105.1	101.4	286.7	0.04
GEO ₂	42166.5	0	0.08	81.0	139.7	266.4	0.06
LEO	8377.7	0.01	30	270.2	354.9	263.4	0.03

We first demonstrate a case without measurement noise, but with an initial a-priori deviation from the truth. In this way, we show the sensitivity to small deviations in the dual-satellite ephemeris from the truth on the localized satellite estimate. Even very small deviations result in a signature of the localized satellite FDOA residuals.

6.2.1.1 No-Noise on Measurements

Figures 6.10 to 6.12 shows the state error in position, velocity and, AGOM as well as the 3σ covariance bounds respectively for the first step (figure a) and second step (figure b) of the two-step process. As expected the state error is nearly zero as demonstrated by the flat lines in the figures. In step 1, the covariance bounds decrease over time because a sequential SRIF was used for the estimation, while in step 2 a CBF was used instead resulting in the final covariance bounds being

mapped back to the epoch. The covariance bounds of step 2 are quite large, this is a consequence of the step 1 (dual-satellite covariance) being considered. Recall that GEO-GEO pairings have reduced observability with TDOA and FDOA observables thereby also having larger uncertainties which get mapped into the covariance of the localized RF satellite. If another satellite pair with faster dynamics were used, its covariance would be lower, thereby also reducing the localized RF satellite covariance. The advantage of using a GEO-GEO pair however is the constant visibility from the stations, but also higher visibility of the RF satellite from the GEO satellites.

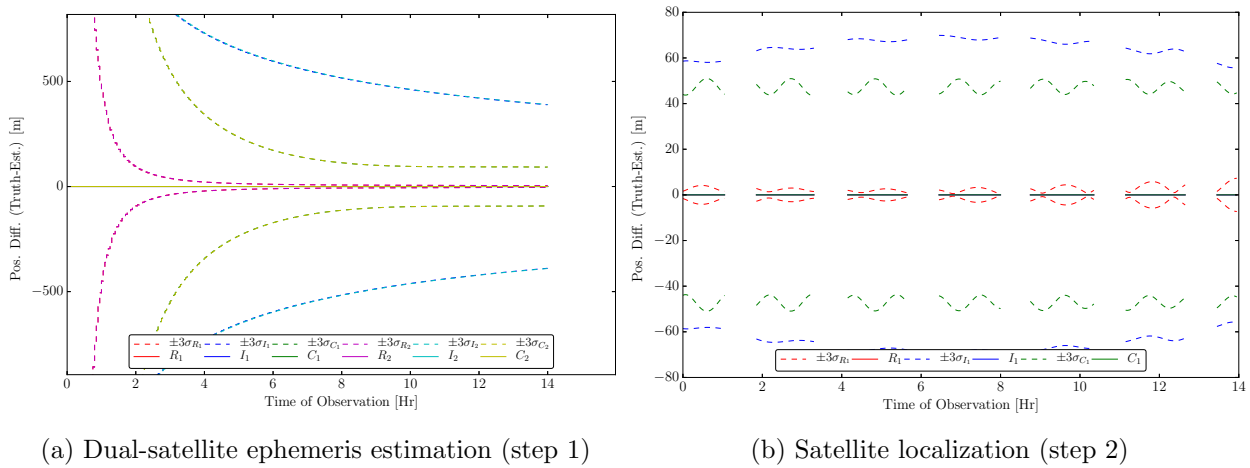


Figure 6.10: Position state error and 3σ covariance bounds. Step 1 uses SRIF, while step 2 uses CBF, no noise

Note that the satellite localization plots have brief interruptions where no data is available. This is due to the occultation of the satellite by the Earth from the vantage point of the GEO satellites. Once every period, the LEO satellite disappears behind the Earth and when it reappears measurements can be taken once more. The dual-satellite first iteration prefit and last iteration postfit residuals are shown in Figure 6.13. Of course the lines are nearly flat due to the lack of noise on the measurements. Figure 6.14 also shows the first iteration prefit and last iteration postfit residuals for the localized satellite. Notice however that the FDOA postfit residuals show some small deviations, this is due the sensitivity to the (very small) state error in the estimated dual-satellite ephemeris. This would potentially lead one to conclude that simultaneous estimation

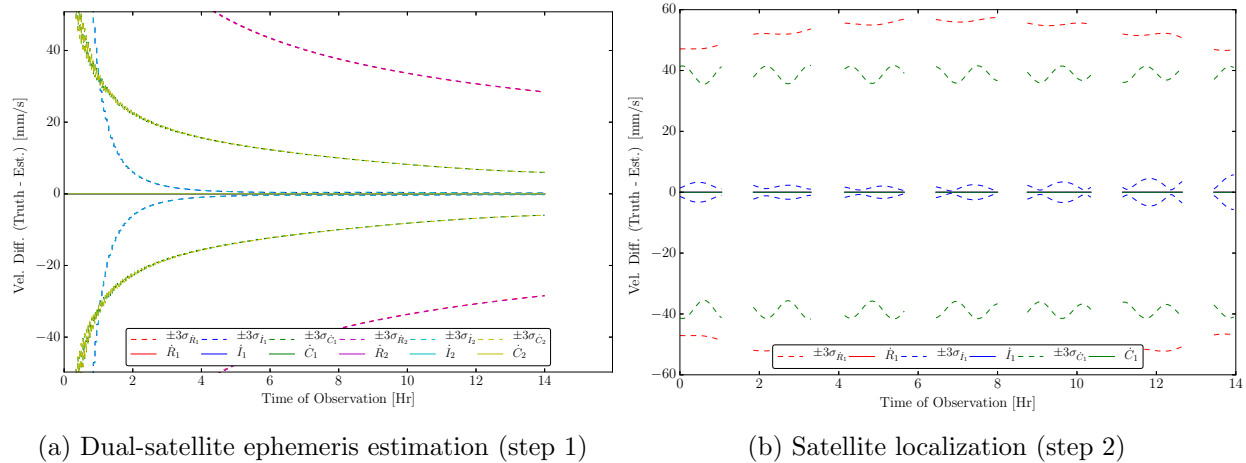


Figure 6.11: Velocity state error and 3σ covariance bounds. Step 1 uses SRIF, while step 2 uses CBF, no noise

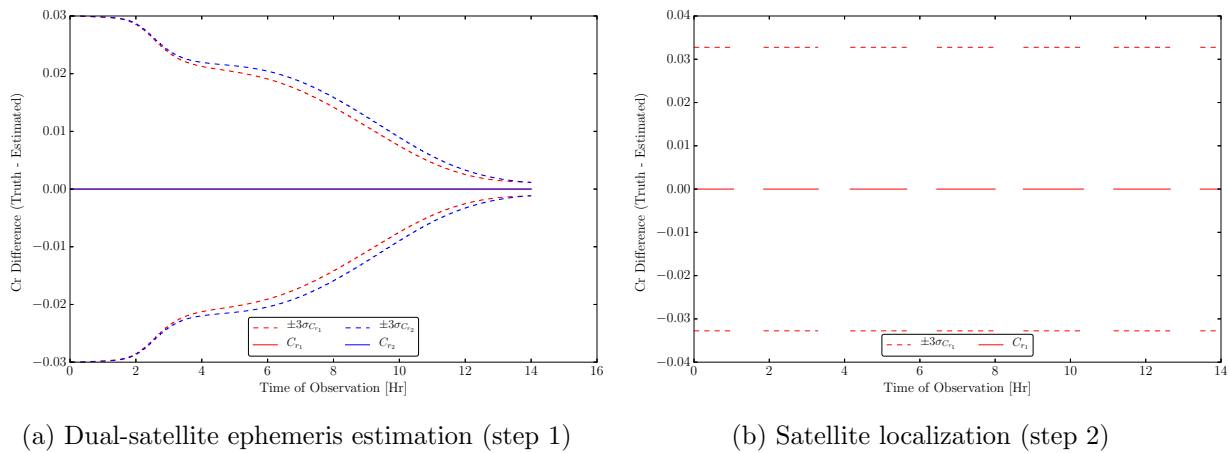


Figure 6.12: AGOM state error and 3σ covariance bounds. Step 1 uses SRIF, while step 2 uses CBF, no noise

would be better so as to leverage this additional information present in the localized satellite when estimating the dual-satellite ephemeris.

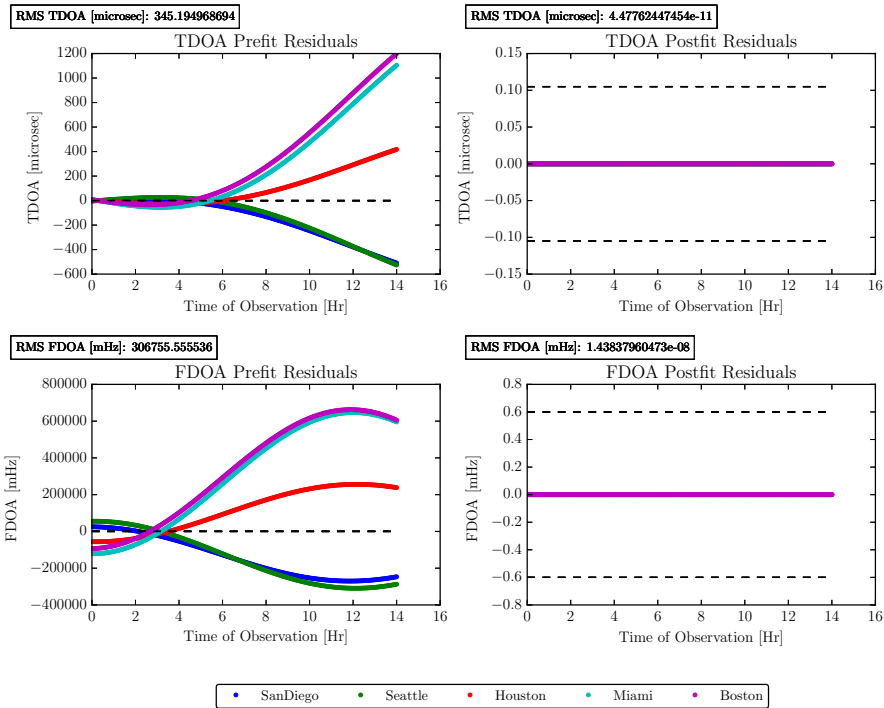


Figure 6.13: Dual-satellite TDOA/FDOA prefit residuals of first iteration and postfit residuals of last iteration, no noise

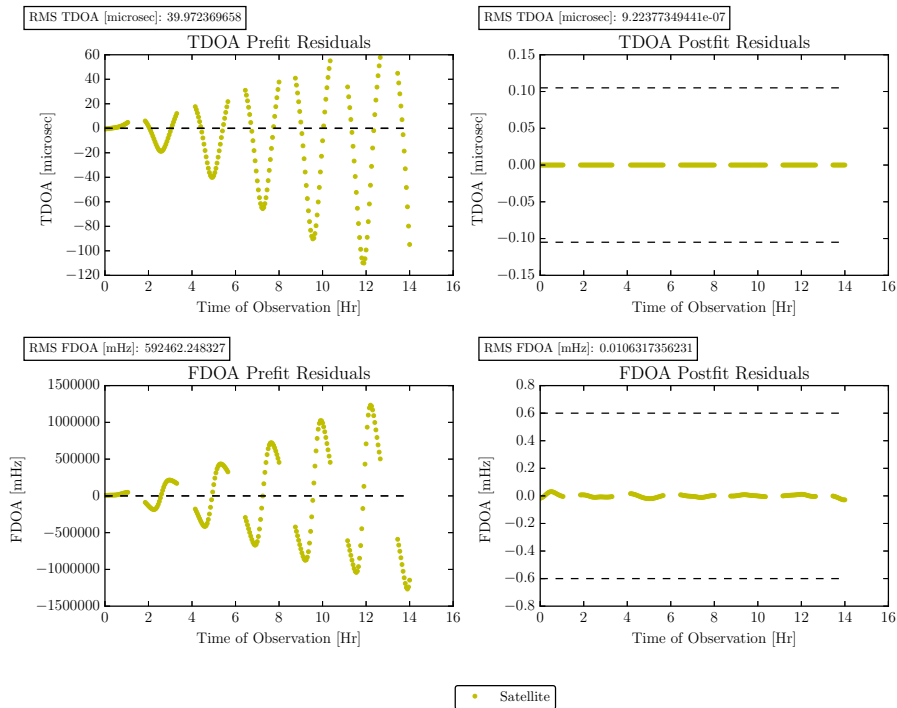


Figure 6.14: Localized satellite TDOA/FDOA prefit residuals of first iteration and postfit residuals of last iteration, no noise

6.2.1.2 Noise on Measurements

The exact same setup as the previous section is used, but now noise on the measurements is included. Due to the noise, the solution of the dual-satellite ephemeris is off by several hundred meters from the truth. The state errors are still within their covariance bounds however, consequently due to the use of the CBF the state errors from satellite localization are also consistent and within their covariance bounds. If a regular batch filter was implemented the state errors would have exceeded the covariance bounds. While the uncertainties on the localized LEO satellite are on the order of 10s of meters, this may in certain situations be sufficient. Notice that the errors in the dual-satellite ephemeris are reflected in the errors found with the satellite localization. For example, the dual-satellite ephemeris is biased in the in-track position, looking at the satellite localization position, we see that it is also biased in the in-track direction. The same is true for the radial velocity errors.

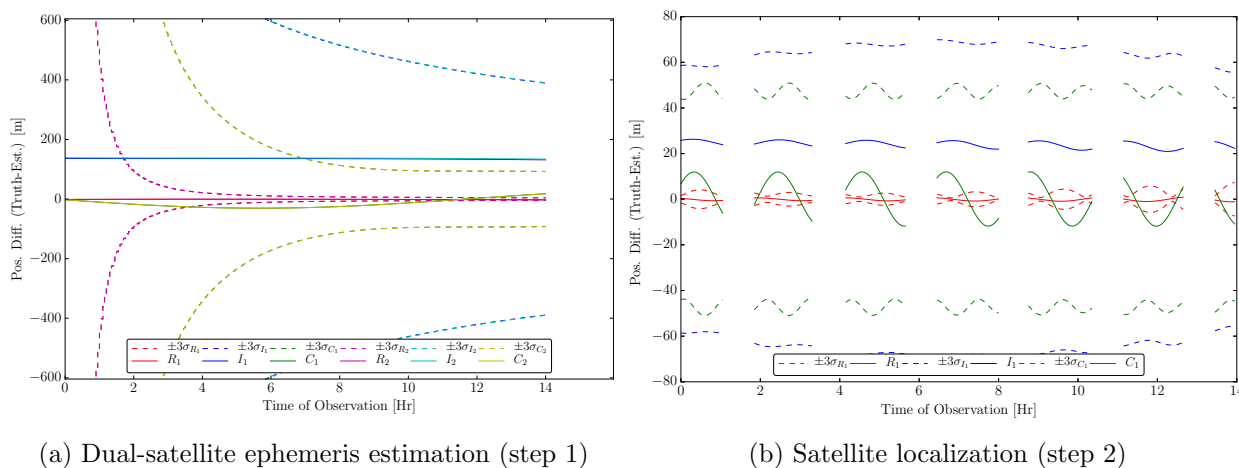


Figure 6.15: Position state error and 3σ covariance bounds. Step 1 uses SRIF, while step 2 uses CBF

From Figure 6.18 we see that the trajectory is fitted to the noise of the measurements. Despite this however, we still have dual-satellite state errors which are apparent when looking at the FDOA post-fit residuals of the satellite localization. The TDOA residuals are significantly less affected

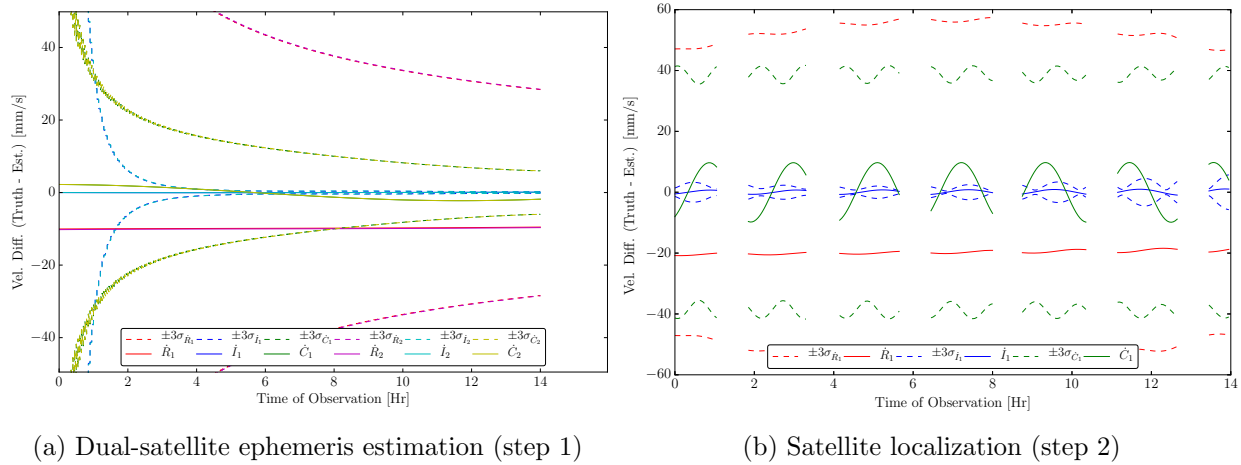


Figure 6.16: Velocity state error and 3σ covariance bounds. Step 1 uses SRIF, while step 2 uses CBF

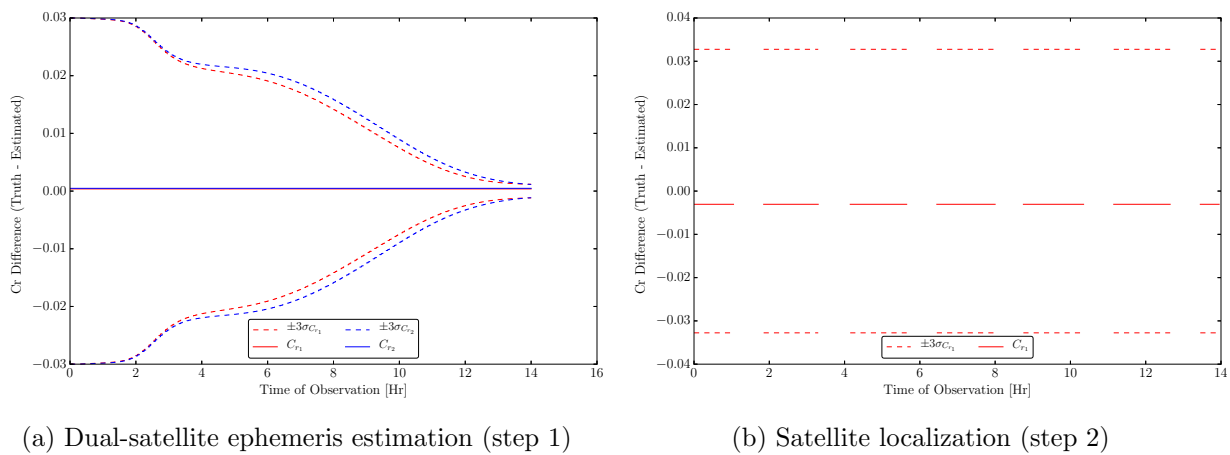


Figure 6.17: AGOM state error and 3σ covariance bounds. Step 1 uses SRIF, while step 2 uses CBF

because the radial position component of the dual-satellite estimation shown in Figure 6.15(a) is known accurately.

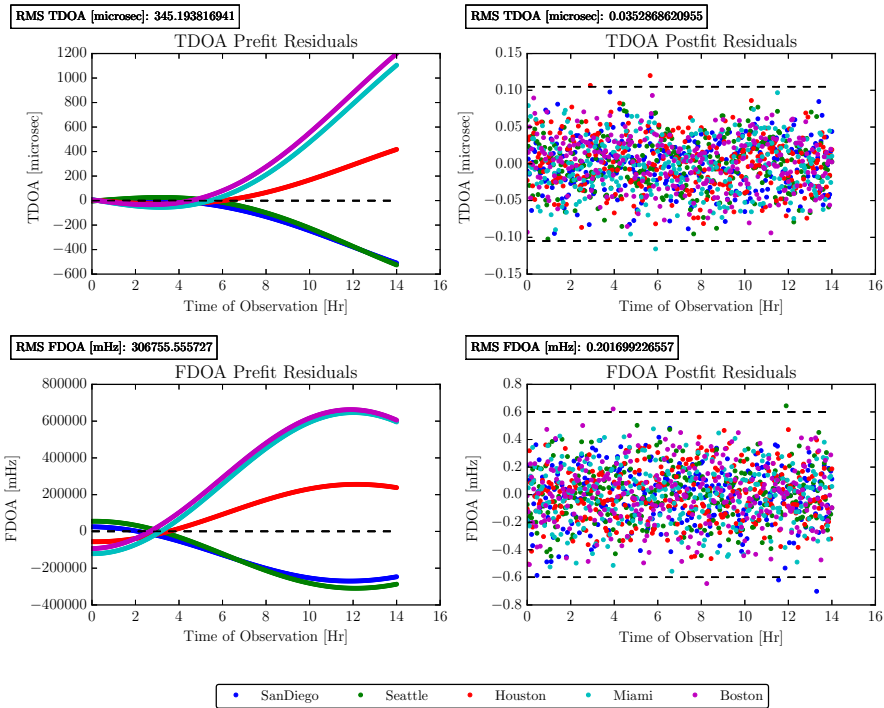


Figure 6.18: Dual-satellite TDOA/FDOA prefit residuals of first iteration and postfit residuals of last iteration

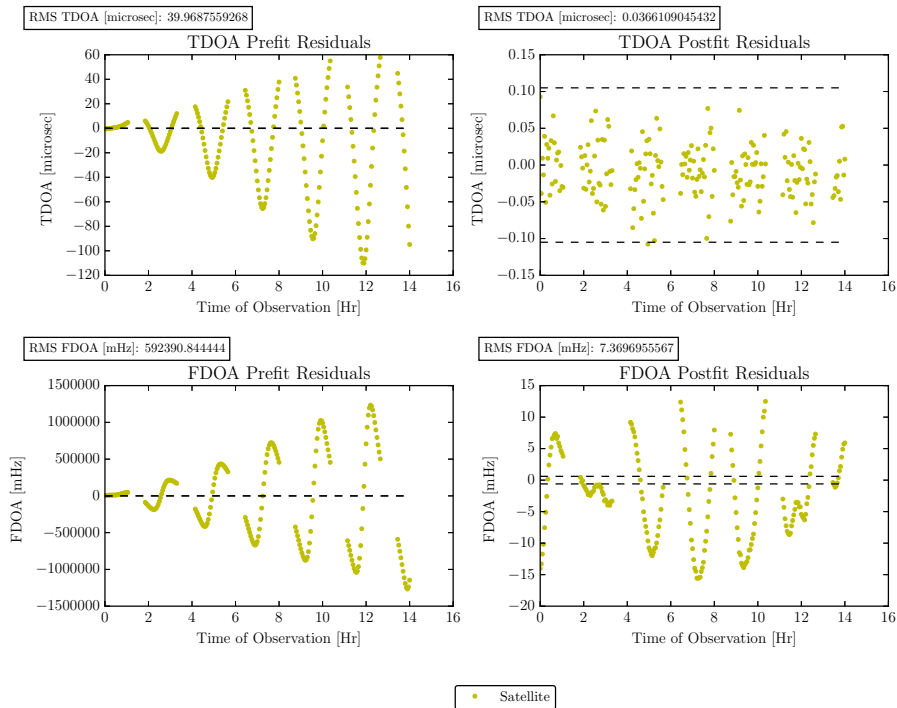


Figure 6.19: Localized satellite TDOA/FDOA prefit residuals of first iteration and postfit residuals of last iteration

Chapter 7

GEO-GEO Orbit Determination and Geolocation with Real Data

This chapter is in part a verification of the previous topics introduced in this dissertation. In previous chapters, simulated data was primarily used to demonstrate the proof of concept, here we use a 45 hour arc of real data to show the efficacy of OD with TDOA and FDOA. The data arc is for a GEO-GEO case involving the Galaxy-16 and SES-1 satellites, as demonstrated throughout this thesis, the GEO-GEO case for OD has the lowest observability compared to other scenarios. As a consequence by showing that we can indeed get an OD solution using TDOA and FDOA in this worst case scenario, the real-data results in other dual-satellite setups looks to be promising. After an OD scenario we also look at several geolocation examples using the same data set.

The measurement uncertainty for a real data set is computed from Eqs. 15 and 16 in Ref. [78]. However, in the data used here the measurement uncertainty appears to be too optimistic because the weighted RMS value is quite large while maintaining close to Gaussian residuals when doing a preliminary fit. Therefore the TDOA measurement uncertainty has been increased by a factor of 1.8 while the FDOA uncertainty was increased by a factor of 10. In general, it is possible that the FDOA measurement uncertainty is so low due to the high transmitted power of the signal while having systematic errors significantly larger than this.

7.1 GEO-GEO Orbit Determination

The developed OD framework is meant to handle real data, all that is required is an input file that includes, among other inputs, all the measurements, times, frequencies, and transmitters

used. The a-priori information is automatically obtained through a query service that pulls the TLEs closest in time to the first measurement. Naturally real data has outliers therefore a data editor is included to remove data points that exceed a certain predefined threshold. The threshold is kept quite large, to remove only the largest outliers, it could be reduced further to remove other points which could also be considered outliers particularly in the FDOA residuals. Figure 7.1 illustrates the first iteration TDOA and FDOA prefit residuals on the left with the last iteration postfit residuals on the right.

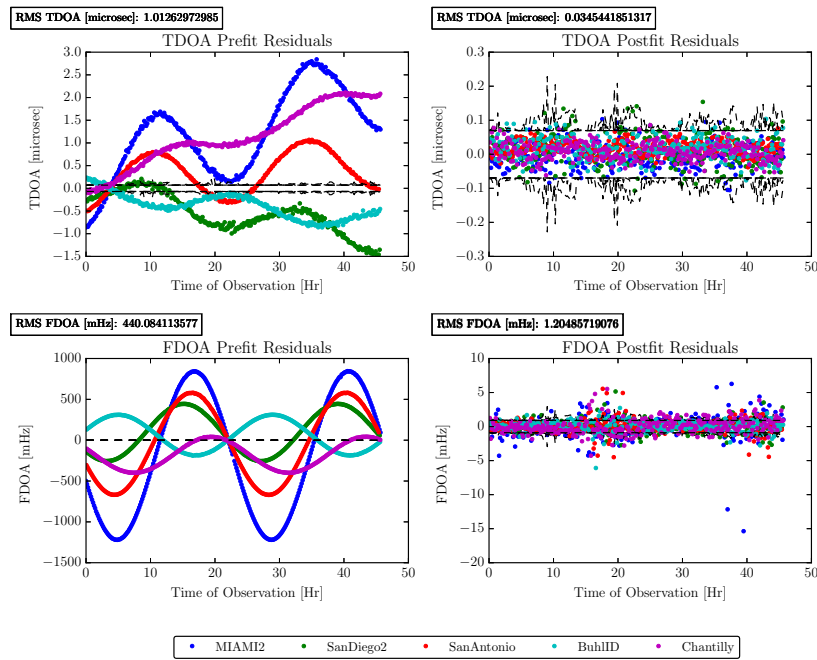


Figure 7.1: Complete arc: prefit and postfit residuals

Five baselines were used with the secondary transmitter city listed in the legend by color. The reference transmitter is located in Colorado Springs. The black dashed lines indicate the measurement uncertainty, in the TDOA postfit residuals we find that the uncertainty varies over time demonstrated by the occasional spikes. The largest source of error is most likely attributed to having used a cannonball model rather than the Fourier model, because we in effect estimated an averaged AGOM value over the 45 hour time span for both satellites of 0.049 and 0.026 for Galaxy-16 and SES-1 respectively. Because no truth state is available for comparison we look at a

prediction as well as two different overlap studies in the subsequent sections.

7.1.1 Prediction Analysis

In the prediction analysis we filter the first half of the long-arc data set, then use the second half of the data to do a pass-through. In this method we can determine whether we have simply fitted to the data and have poor orbit predictability or if we have fitted to the data but are also able to accurately predict a future satellite state. Of course the second case is desired and is proof that the models accurately represent reality. Figure 7.2 shows the first iteration prefit residuals on the left and the last iteration postfit residuals on the right. The postfit RMS values for TDOA and FDOA using half of the data is approximately the same as the RMS values obtained using the full long-arc data set shown in Figure 7.1.

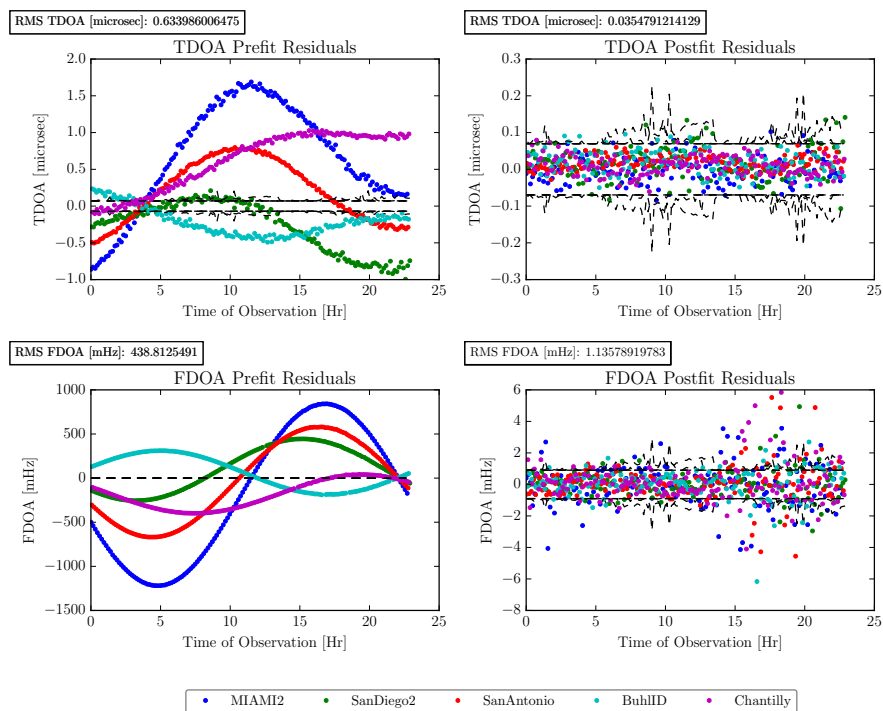


Figure 7.2: First half of data processed in filter

Figure 7.3 shows the pass-through residuals using the remainder of the data. We find that the residuals fit quite well with the original estimated trajectory with RMS values only slightly

larger than the full arc. Because the pass-through performs nearly as well as using the data to fit the trajectory we have good predictability of future satellite states.

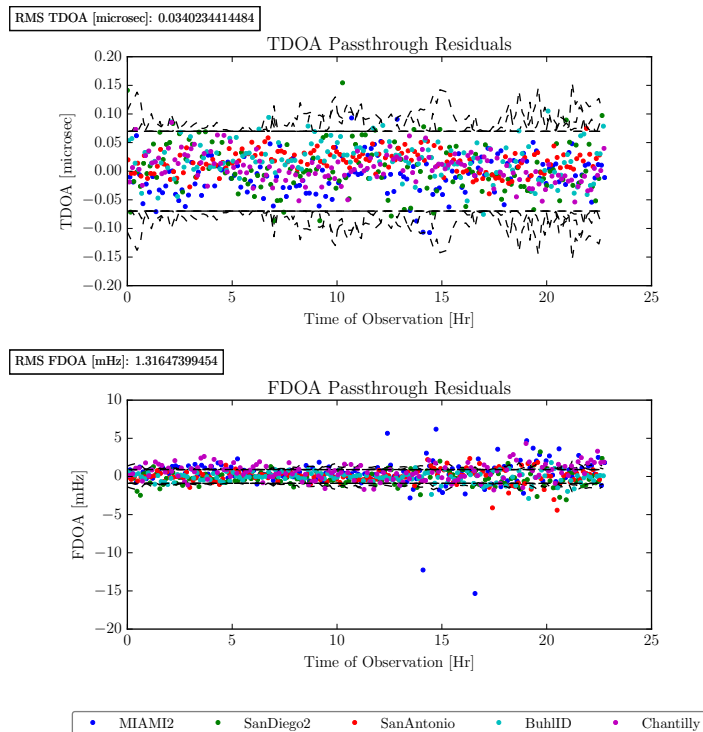


Figure 7.3: Passthrough of second half of data

7.1.2 Long-Arc Overlap Analysis

The long-arc overlap analysis consists of two data arcs each 30 hours long. The left data arc covers data from 0 to 30 hours, while the right data arc covers data from 15 hours to 45 hours. As a result, there is a period of 15 hours that overlaps between the two data arcs. The estimated ephemeris over this overlapped period is differenced between the two arcs to obtain a sense of the magnitude of the errors. The smaller the errors the better, but as long as the errors are within their expected covariance bounds the errors are acceptable.

The 15 hour overlapped ephemeris segments are rotated into the RIC frame and then differenced. The mean of the errors per satellite component are shown in row 1 of Table 7.1 in meters for position and millimeters per second for velocity. The standard deviation of the errors are shown

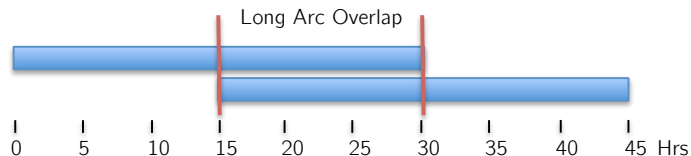


Figure 7.4: Long arc overlap: 15 hrs

in the second row. The third and fourth row are the mean 3σ values obtained from the filter covariance, where ‘L’ and ‘R’ refer to the left and right arc respectively. We can take the mean of the filter covariance when it is presented in the RIC frame due to the nearly unchanging uncertainty levels for each component (after smoothing). The error in R_i and C_i for both satellites exceeds the covariance bounds, while the other components remain consistent and below the expected error levels. One likely reason for the higher error levels is due to the use of the cannonball model over a long data arc span. The SRP effect changes depending on satellite orientation with respect to the Sun, but using a single AGOM value to capture this effect merely provides an average rather than an accurate representation. Therefore it is expected that using a shorter data span (but not too short where AGOM cannot be estimated) would provide a more accurate AGOM value because it covers a shorter time span where AGOM would have less chance to change significantly.

Table 7.1: 15 hr overlap analysis: errors and covariance [m & mm/s]

	R_1	I_1	C_1	\dot{R}_1	\dot{I}_1	\dot{C}_1	R_2	I_2	C_2	\dot{R}_2	\dot{I}_2	\dot{C}_2
\bar{x} Err.	-28.7	661.8	470.6	-48.2	1.6	-11.7	-28.1	663.7	470.5	-48.3	1.6	-11.7
Err. σ	18.5	77.3	555.9	3.6	1.6	61.4	17.8	76.2	555.4	3.5	1.5	61.4
L \bar{x} 3σ	25.9	1482.0	376.1	108.0	1.7	27.5	26.0	1480.6	376.4	107.9	1.7	27.5
R \bar{x} 3σ	26.1	1494.4	378.0	108.9	1.7	27.6	26.3	1489.0	378.2	108.5	1.7	27.6

7.1.3 Short-Arc Overlap Analysis

The short-arc overlap is conceptually the same as the long-arc overlap but rather than using two 30 hour arcs we use two 9 hour arcs with a 4.5 hour overlap as shown by Figure 7.5.



Figure 7.5: Short arc overlap: 4.5 hrs

The two 4.5 hour overlapped ephemerii are differenced in the RIC frame with the errors of position in meters and the errors of velocity in millimeters per second listed in the first row of Table 7.2. The second row is the standard deviation of those errors. Once more, the third and fourth rows provide the expected 3σ uncertainties, which is averaged over the 9 hour time span of the left and right arc respectively. The errors in this short-arc overlap are larger than those from the long-arc overlap, this is expected because fewer measurements are incorporated into the solution. However the errors in the short-arc overlap analysis are entirely consistent with their 3σ covariance values. This is likely due to the estimated AGOM value being more appropriate for a shorter span of data rather than a span of more than a day.

Table 7.2: 4.5 hr overlap analysis: errors and covariance [m & mm/s]

	R_1	I_1	C_1	\dot{R}_1	\dot{I}_1	\dot{C}_1	R_2	I_2	C_2	\dot{R}_2	\dot{I}_2	\dot{C}_2
\bar{x} Err.	10.1	1919.9	1001.4	-139.2	1.1	-59.5	9.7	1929.2	999.9	-139.9	0.8	-59.5
Err. σ	4.0	2.7	289.3	0.9	0.3	25.7	4.1	1.6	289.2	0.8	0.3	25.7
L \bar{x} 3σ	53.2	2704.7	1241.3	197.4	3.9	83.8	53.5	2701.5	1241.9	197.1	3.9	83.4
R \bar{x} 3σ	54.9	2721.7	1317.4	198.2	4.1	89.8	55.4	2718.3	1317.9	197.9	4.1	89.9

To verify the changing AGOM over a long arc of 45 hours we break up the 45 hour arc into five 9-hour segments. With each arc estimated independently we obtain the AGOM values listed in Table 7.3.

Table 7.3: Evolving AGOM over 45 hour long-arc data span

	Arc 1	Arc 2	Arc 3	Arc 4	Arc 5
AGOM ₁	0.051	0.057	0.039	0.052	0.060
AGOM ₂	0.031	0.022	0.023	0.025	0.033

7.2 Geolocation

Using the first 9-hour arc of the 45 hour long-arc data set we geolocate each of the five transmitters separately. In this way we use the four remaining transmitters (baselines) to estimate the dual-satellite ephemeris and finally geolocate the omitted transmitter. The technique used here is identical to the one described in chapter 6. Using four baselines for GEO-GEO estimation is acceptable as previously shown in Figure 4.18, but the ephemeris is not as good as using all five baselines. Because the locations of all five transmitters are known precisely we can compare our geolocated solution using real-data with the known location. The errors, in kilometers, are shown for each of the stations in Table 7.4.

Table 7.4: Real-data geolocation error [km]

Miami	San Diego	San Antonio	Buhl	Chantilly
0.180	2.090	0.275	0.232	1.172

In the following two subsections we go through a more detailed process of the Miami and Chantilly geolocation steps. The two-step process of first estimating the ephemeris (step 1) and then geolocating the unknown RF source (step 2) is implemented. The a-priori ephemeris information is obtained from two TLEs, one for each satellite, which as shown in chapter 6.1, results in extremely large geolocation errors if the ephemeris uncertainties are not reduced further.

7.2.1 Geolocate Miami Transmitter

The prefit and postfit residuals of estimating the dual-satellite ephemeris are shown in Figure 7.6, where the measurements are fitted to the noise. The estimated ephemeris and uncertainty is then used for the geolocation step.

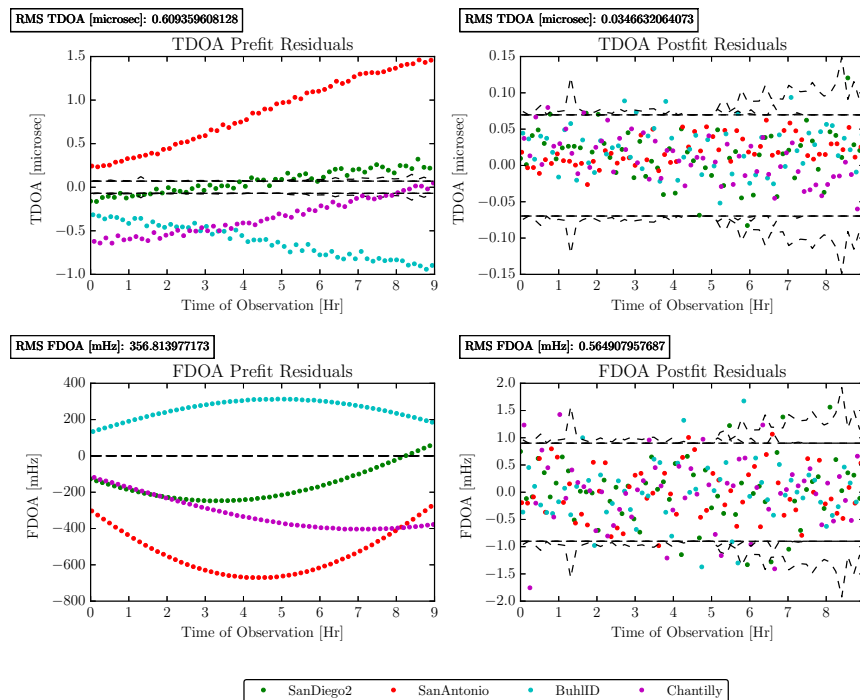


Figure 7.6: Dual-satellite ephemeris estimation without Miami baseline: first iteration prefit and last iteration postfit residuals (step 1)

Using the CBF, the Miami transmitter is estimated with the prefit and postfit residuals shown in Figure 7.7. We see that the TDOA RMS value is slightly lower than the ephemeris estimation side, while the FDOA RMS is larger. The FDOA residuals on the geolocation side absorb the ephemeris errors because the CBF is a sub-optimal filter since the ephemeris is only considered rather than estimated simultaneously.

The projected geolocation ellipses are shown in Figure 7.8. From Figure 7.8 (a) it is difficult to distinguish all the various ellipses and even the actual location of the Miami transmitter, that is why Figure 7.8 (b) shows a zoomed in area. For reference the transmitter true location is 38.816656°

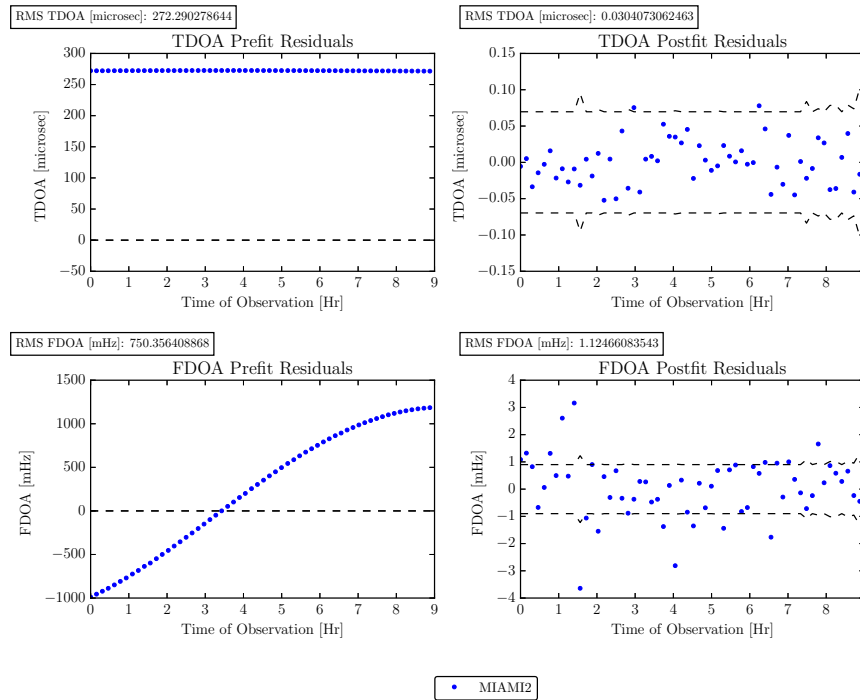


Figure 7.7: Geolocation of Miami transmitter: first iteration prefit and last iteration postfit residuals (step 2)

in latitude, -104.760277° in longitude and 1850.3 m in altitude. The largest ellipse which is the 3σ consider covariance spans 31.638 km in the long axis and 227 m in the short axis, the long axis points to the direction of the two satellites. When applying the probabilistic altitude constraint the 3σ consider covariance shrinks to 386 m by 130 m, with a final geolocation error of 180 m. Notice that the considered covariance ellipse is significantly larger than what was previously demonstrated using simulated data, but recall that the measurement uncertainty in this chapter was inflated to better represent the actual errors. This increase in measurement uncertainty accounts for the larger covariances.

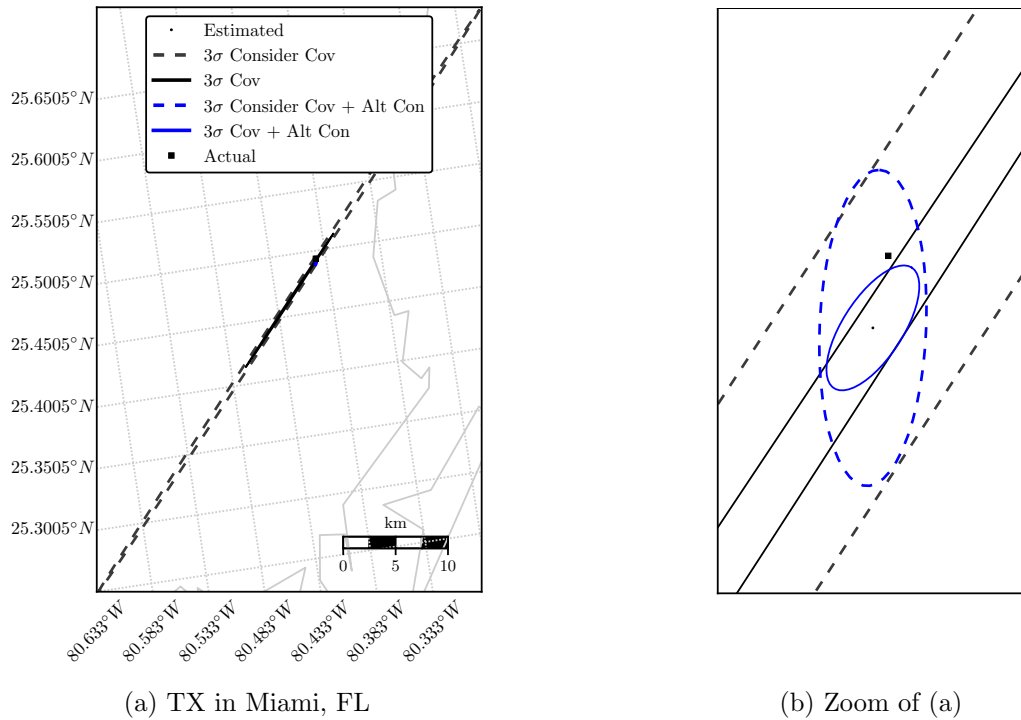


Figure 7.8: Geolocation of a Miami, FL based TX

7.2.2 Geolocate Chantilly Transmitter

The previous geolocation process is repeated with the Chantilly transmitter. The ephemeris is estimated using all baselines with the exception of the Chantilly baseline, where the prefit and postfit residuals are illustrated in Figure 7.9. Once more we are able to estimate the ephemeris down to the measurement noise with no structure present in the residuals.

The residuals for estimating the Chantilly transmitter location are shown in Figure 7.10 where we find that the TDOA postfits have a downward trend over the observation time span. This downward trend is indicative of an ephemeris position error from step 1, while the FDOA residuals appear normally distributed about zero in a Gaussian fashion.

Figure 7.11 demonstrates how good the geolocation solution is compared to the actual transmitter location. Once again in 7.11(a) we find that the 3σ consider covariance ellipse is extremely elongated towards the direction of the satellites with a 158.2 km long axis and 270 m short axis.

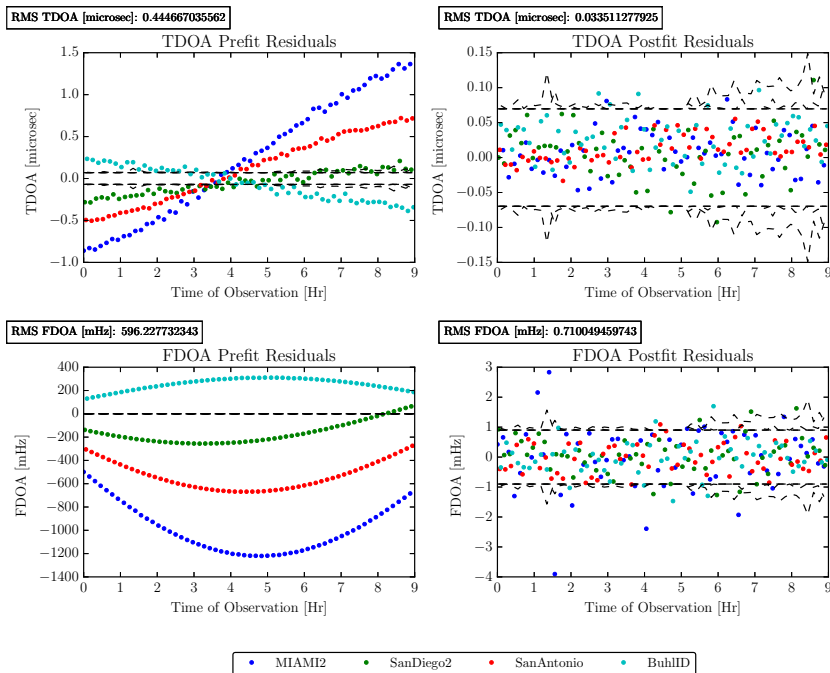


Figure 7.9: Dual-satellite ephemeris estimation without Chantilly baseline: first iteration prefit and last iteration postfit residuals (step 1)

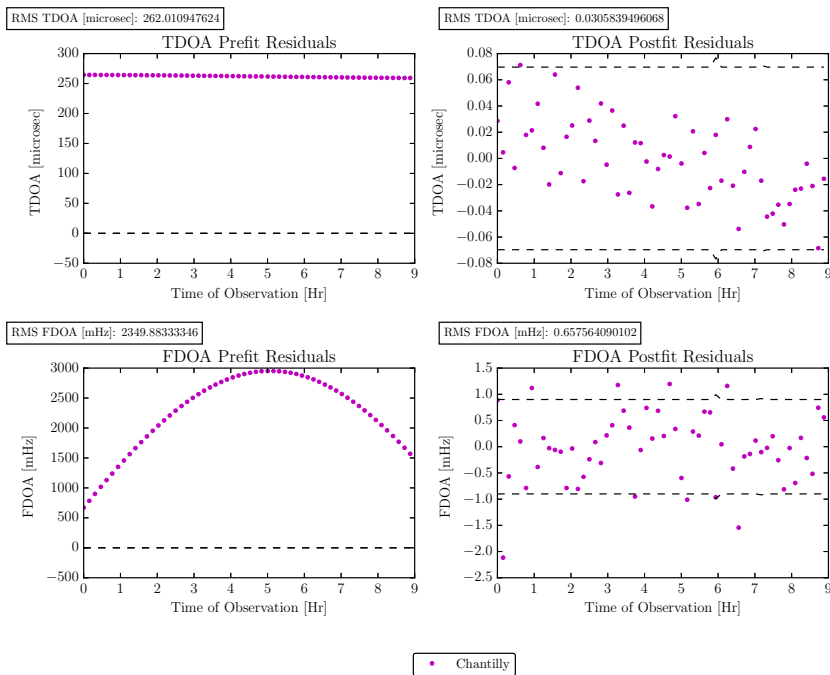


Figure 7.10: Geolocation of Chantilly transmitter: first iteration prefit and last iteration postfit residuals (step 2)

The magnitude of the long axis is simply due to the uncertainty of the considered ephemeris because the long axis of the 3σ covariance is only 9.5 km. The true location of the transmitter is 38.816656° in latitude, -104.760277° in longitude, and 1850.3 m in altitude for reference as it is difficult to see in 7.11(a). Figure 7.11(b) shows a closeup, where the 3σ consider covariance with probabilistic altitude constraint is shown with a dashed blue line and is 937.5 m by 104.7 m. Notice that the actual station location is outside of this covariance however, this is most likely due to two factors. The first is the ephemeris error as previously evidenced by the down-trending TDOA residuals. The second is likely due to the resolution of the elevation profile used to generate the ‘computed altitude’ (see chapter 6.1.1.3), if a finer mesh is used the solution could move South closer to the true transmitter location.

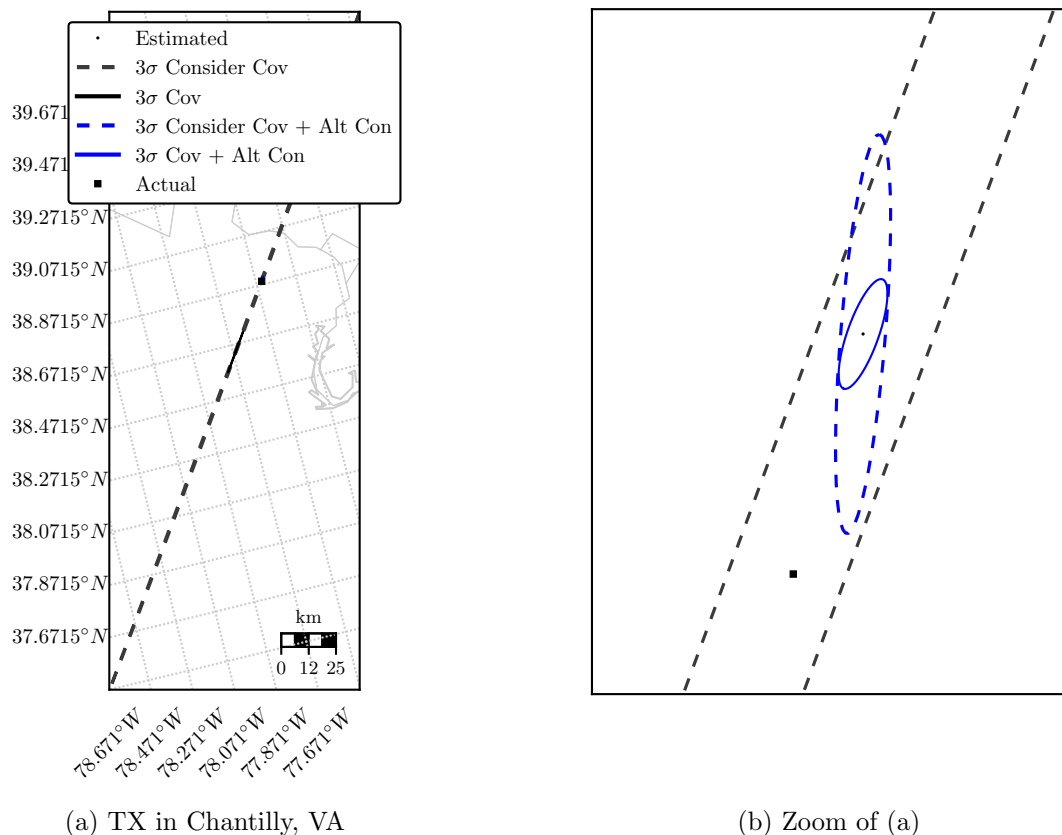


Figure 7.11: Geolocation of a Chantilly, VA based TX

Chapter 8

Small Body Navigation and Gravity Estimation

The following decade of NASA missions include a strong emphasis on asteroids, with the recently launched OSIRIS-REx spacecraft attempting a sample return by 2023 in addition to two other recently announced proposals. The first of the new missions is Lucy, a reconnaissance mission to the Jupiter Trojan asteroids which is expected to launch in 2021 [53, 63]. The second is Psyche, a mission to the 16 Psyche asteroid, of great scientific interest due to its metal composition which is expected to launch in 2023 [4, 63]. The continued interest in asteroids means new research opportunities for better and cheaper methods to navigate about these small bodies. The accuracy to which the gravity field of the asteroid is known directly impacts navigation and science goals as well. Of course many of the parameters such as the asteroid shape, spin rate and gravity field are not known to a high degree of confidence upon arrival at the asteroid. Consequently these must be determined through estimation techniques in-situ.

In this chapter we present a proof of concept for gravity recovery requiring two beacons in close proximity to the asteroid and one main spacecraft predominantly outside the asteroid's gravitational influence. The proposed measurement types are angles as well as FDOA. The motivation for using FDOA as a small-body navigation observable is for the cancellation of common error as discussed throughout this dissertation. For example if the beacons have an oscillator error or bias, the FDOA measurement would be unaffected because the errors are differenced. Furthermore main satellite receiver errors would cancel as well [34]. Consequently the beacons would not require expensive hardware, and could be made cheaper since the tolerances do not need to be as high as with other

observables such as range or range-rate. While biases can of course be estimated, FDOA eliminates the need for that entirely.

In this study we use asteroid 433 Eros for simulation purposes because its parameters are well known due to the NEAR-Shoemaker mission. NEAR orbit operations commenced in February of 2000 with an insertion orbit about Eros of 320×360 km. Over the course of a year NEAR subsequently went into lower and lower orbits eventually allowing a 15×15 gravity field to be determined [59]. This gravity field of Eros is used as truth in the analyses and simulations to follow. The studies presented here are an extension of previous work done by Refs. [35] and [52] which also used Eros' data and gravity field from the NEAR mission.

The chapter is laid out in the following manner. We first present the high level dynamics and setup used to generate the truth trajectories. These truth trajectories are used for comparison to the estimated states of the filter as a performance metric. These truth trajectories are also used to generate the truth measurements, uncorrupted by noise or bias. Second, we introduce the dynamical model used in the filter and third the measurement model in the filter. Then we present a number of covariance analyses using the CRLB to compare the performance of using FDOA versus range-rate in addition to the angle observables. We then show the viability of using angles and FDOA to perform small body navigation and gravity recovery in a navigation simulation and repeat this simulation with range-rate as a comparison benchmark. Finally we introduce a bias in the beacon translation oscillator and show the affect on the angles and range-rate simulation since the angles and FDOA simulation remains unaffected.

8.1 Navigation Truth Models

In this section, the parameters and setup to create the simulations are discussed. There are three satellites involved in this study. The primary is the main satellite which contains all the instruments and computing power necessary for the mission. The main satellite is in a heliocentric orbit, trailing Eros' orbit at a distance of approximately 1500 km. While the gravitational effect of Eros on the main satellite is not negligible it is minimal and time scales of several months are

required before the main satellite would move significantly from its original relative position to Eros. It is assumed that no corrective maneuvers are performed by the main satellite in order to maintain its original position, as a result it moves only under the influence of gravity and SRP. In this study, the state of the main satellite is assumed to be known precisely as is the ephemeris of Eros. Furthermore the main satellite attitude is also assumed to be known exactly and error free. The two additional satellites are in fact simple beacons orbiting at close range to Eros. Beacon 1 has a semi-major axis of 35.75 km and an inclination of 105° , Beacon 2 has a semi-major axis of 31.56 km and an inclination of 134° . Each satellite has an initial position \mathbf{r} , and velocity \mathbf{v} , in the Asteroid Centered Inertial (ACI) frame as well as coefficient of reflectivity C_r . We assume that the gravity coefficients \mathbf{C} do not change over the time scale of the simulation. Equation 8.1 shows the first order differential equations that describe the truth dynamics in the simulations.

$$\dot{\mathbf{X}}_{truth}(t) = F(\mathbf{X}, t) = \begin{bmatrix} \dot{\mathbf{r}}_1 \\ \dot{\mathbf{v}}_1 \\ \dot{C}_{r1} \\ \dot{\mathbf{r}}_2 \\ \dot{\mathbf{v}}_2 \\ \dot{C}_{r2} \\ \dot{\mathbf{r}}_m \\ \dot{\mathbf{v}}_m \\ \dot{C}_{rm} \\ \dot{\mathbf{C}} \end{bmatrix} = \begin{bmatrix} \mathbf{v}_1 \\ \mathbf{a}_{1_{2B}} + \mathbf{a}_{1_{NS}} + \mathbf{a}_{1_{NB}} + \mathbf{a}_{1_{SRP}} \\ 0 \\ \mathbf{v}_2 \\ \mathbf{a}_{2_{2B}} + \mathbf{a}_{2_{NS}} + \mathbf{a}_{2_{NB}} + \mathbf{a}_{2_{SRP}} \\ 0 \\ \mathbf{v}_m \\ \mathbf{a}_{m_{2B}} + \mathbf{a}_{m_{NS}} + \mathbf{a}_{m_{NB}} + \mathbf{a}_{m_{SRP}} \\ 0 \\ 0 \end{bmatrix} \quad (8.1)$$

The subscripts 1, 2 and m refer to the two beacons and the main satellite correspondingly. The four accelerations included in the dynamics are from 2-body (\mathbf{a}_{2B}) and non-spherical (\mathbf{a}_{NS}) accelerations from Eros, the Sun as a 3rd body (\mathbf{a}_{NB}), and SRP (\mathbf{a}_{SRP}). The equations describing these accelerations are shown in the ‘‘Filter Dynamical Model’’ section as the dynamics used are the same. The time histories of these states are integrated using a DOPRI(8)7 integrator scheme

from the TurboProp orbit integration package developed at CU Boulder, for an 8 day time frame [36]. The spherical harmonics of Eros are given by the NEAR15A model from which the 15×15 gravity field was used. Two views of the integrated truth trajectories of the beacons about Eros are shown in Figure 8.1. The trajectory of the main spacecraft is not shown due to scale and lack of movement over the 8 day period.

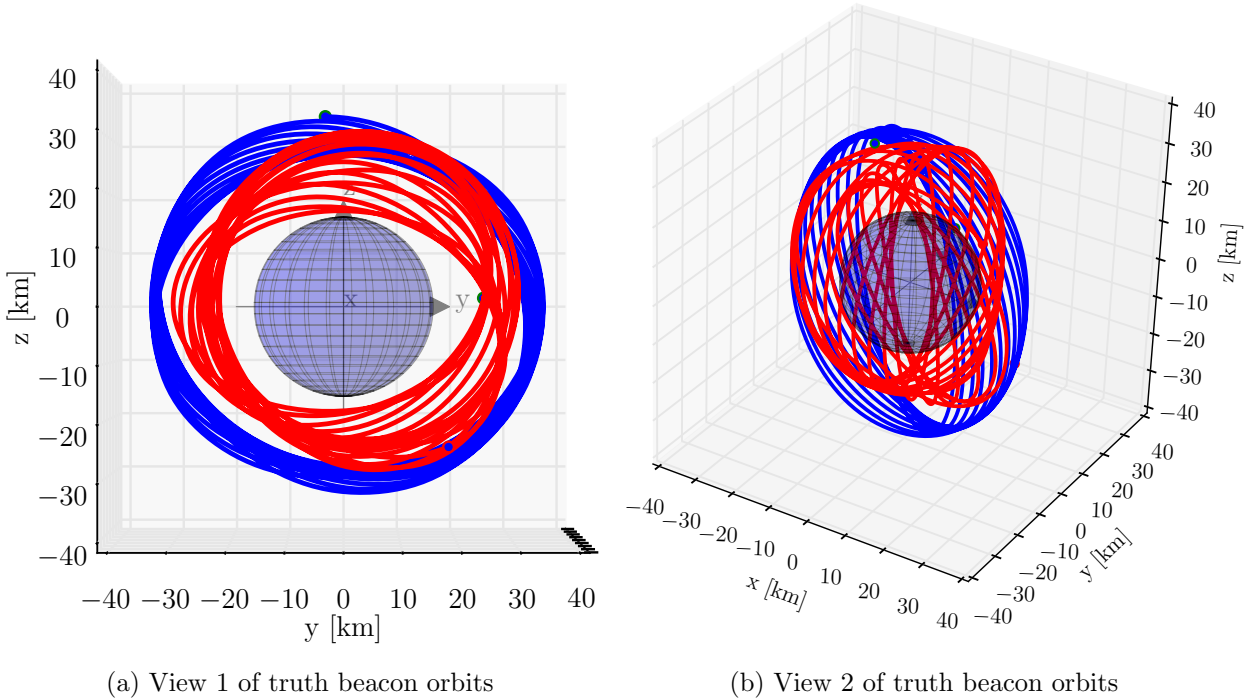


Figure 8.1: Truth beacon orbits over 8 day span with EROS reference sphere: beacon 1 in blue, beacon 2 in red

The axes shown in Figure 8.1 are in ACI, it is assumed that Eros' spin is about the z-axis at a rate of 0.00033116596755685 rad/s and is known precisely. The blue opaque sphere marks the 16 km radius reference sphere of Eros. The reference sphere is simply a sphere that marks the farthest point of Eros from its CoM, which is not representative of Eros' shape. Note that from view 1 shown in Figure 8.1(a) the beacon orbits are not occulted by Eros, this is a similar view that the main satellite has of both beacons and consequently measurements are recorded for 8 days without interruption.

Using the truth trajectories of the main spacecraft and the two beacons the truth measurements are generated, uncorrupted by noise. The measurements are generated at a frequency of once every 2 minutes. In this chapter there are two different simulation types each one using a distinct measurement set. The first uses angles in addition to FDOA and the second uses angles with two range-rate measurements. This means that every 2 minutes there is a set of truth measurements which includes angles, FDOA and range-rate. The appropriate measurements are chosen depending on which simulation is executed. Table 8.1 summarizes the parameters used in this study and is based upon the parameters used in Ref. [35]. Note that there are several FDOA parameters listed in Table 8.1. The first is Transmitter (TX) separation, this is because two TXs are used and the separation matters, the reference and secondary TXs each with their own frequency as well. Under the beacon parameters the FDOA translation frequency is the change in signal frequency by the beacon before being downlinked back to the main satellite. While the translation frequency is shown, it has no effect on the filter performance since it cancels in the FDOA measurement type.

In the following two sections the filter dynamics and measurement models are presented. While the models themselves are equivalent to those used to generate the truth trajectories, the values in some cases are different. Hence why a filter is implemented to try to recover the truth trajectory as best as possible. An Extended Kalman Filter (EKF) is used which is initialized with a Conventional Kalman Filter (CKF). Due to the high non-linearities present at Eros a non-linear filter was chosen over others such as the CKF or Batch.

Table 8.1: Truth model parameters

<i>Ephemerides</i>	
Ephemeris	DE421
Epoch	01/01/2020 00:00:00 TDB
<i>Reference Frame</i>	
Main Satellite	EROS Centered Inertial
Beacons	EROS Centered Inertial
Coordinate Center	EROS Center of Mass
Eros Spin Rate	0.00033116596755685 rad/s
<i>Force Model</i>	
Central Body	433 Eros
Non-Spherical Gravity Field	15×15 from NEAR15A
3rd Body	Sun
Solar Radiation Pressure	101,304,639.46 kg-km ³ /m ² s ² at 1 AU
<i>Main Satellite Parameters</i>	
Reflective Area to Mass Ratio, A_{\odot}/m	0.025 m ² /kg
Coefficient of Reflectivity, C_r	2.0
FDOA Baseline	10 m
FDOA Reference TX Frequency	14,385,775,000 Hz
FDOA Secondary TX Frequency	14,387,375,000 Hz
<i>Beacon Parameters</i>	
Reflective Area to Mass Ratio, A_{\odot}/m	0.025 m ² /kg
Coefficient of Reflectivity, C_r	1.5
FDOA Translation Frequency	2,300,000,000 Hz

8.2 Filter Dynamical Model

In this navigation scenario there are 14 estimated states; seven for each beacon plus the gravity coefficients, recall that the main satellite state is known exactly and therefore not estimated. They include position \mathbf{r} , velocity \mathbf{v} in the ACI frame and the coefficient of reflectivity C_r . If a 15×15 gravity field is estimated an additional 252 gravity coefficients are added alongside the original 14 for a total of 266. The estimated state vector \mathbf{X} can be represented as

$$\mathbf{X} = \left[\mathbf{r}_1^{\top} \quad \mathbf{v}_1^{\top} \quad C_{r_1} \quad \mathbf{r}_2^{\top} \quad \mathbf{v}_2^{\top} \quad C_{r_2} \quad \mathbf{C}^{\top} \right]^{\top}, \quad (8.2)$$

where,

$$\mathbf{C} = \begin{bmatrix} C_{2,0} & C_{2,1} & S_{2,1} & C_{2,2} & S_{2,2} & \cdots & C_{l,m} & S_{l,m} \end{bmatrix}^\top. \quad (8.3)$$

In Eq. 8.3 the subscripts l and m refer to the degree and order of the spherical harmonics respectively. The states evolve due to 2-body, non-spherical, 3rd body and SRP accelerations. These dynamics can be written as first order differential equations, and are the same as Eq. 8.1 except that the main satellite state is not re-integrated since the truth states are used for that instead.

$$\dot{\mathbf{X}}(t) = F(\mathbf{X}, t) = \begin{bmatrix} \dot{\mathbf{r}}_1 \\ \dot{\mathbf{v}}_1 \\ \dot{C}_{r_1} \\ \dot{\mathbf{r}}_2 \\ \dot{\mathbf{v}}_2 \\ \dot{C}_{r_2} \\ \dot{\mathbf{C}} \end{bmatrix} = \begin{bmatrix} \mathbf{v}_1 \\ \mathbf{a}_{12B} + \mathbf{a}_{1NS} + \mathbf{a}_{1NB} + \mathbf{a}_{1SRP} \\ 0 \\ \mathbf{v}_2 \\ \mathbf{a}_{22B} + \mathbf{a}_{2NS} + \mathbf{a}_{2NB} + \mathbf{a}_{2SRP} \\ 0 \\ 0 \end{bmatrix}. \quad (8.4)$$

These dynamics are linearized about a reference trajectory for use in the EKF described in chapter 3.2.3. The Jacobian is given by the sparse matrix shown in Eq. 8.5 where n is the length of the spherical harmonics vector \mathbf{C} given in Eq. 8.3,

$$\mathbf{A}(t) = \frac{\partial F(\mathbf{X}, t)}{\partial \mathbf{X}} = \begin{bmatrix} \mathbf{0}_{3 \times 3} & \mathcal{I}_{3 \times 3} & \mathbf{0}_{3 \times 1} & \mathbf{0}_{3 \times 3} & \mathbf{0}_{3 \times 3} & \mathbf{0}_{3 \times 1} & \mathbf{0}_{3 \times n} \\ \mathbf{G}_1(t) & \mathbf{0}_{3 \times 3} & \mathbf{S}_1(t) & \mathbf{0}_{3 \times 3} & \mathbf{0}_{3 \times 3} & \mathbf{0}_{3 \times 1} & \mathbf{B}_1 \\ 0 & 0 & 0 & 0 & 0 & 0 & \mathbf{0}_{1 \times n} \\ \mathbf{0}_{3 \times 3} & \mathbf{0}_{3 \times 3} & \mathbf{0}_{3 \times 1} & \mathbf{0}_{3 \times 3} & \mathcal{I}_{3 \times 3} & \mathbf{0}_{3 \times 1} & \mathbf{0}_{3 \times n} \\ \mathbf{0}_{3 \times 3} & \mathbf{0}_{3 \times 3} & \mathbf{0}_{3 \times 1} & \mathbf{G}_2(t) & \mathbf{0}_{3 \times 3} & \mathbf{S}_2(t) & \mathbf{B}_2 \\ 0 & 0 & 0 & 0 & 0 & 0 & \mathbf{0}_{1 \times n} \\ \mathbf{0}_{n \times 3} & \mathbf{0}_{n \times 3} & \mathbf{0}_{n \times 1} & \mathbf{0}_{n \times 3} & \mathbf{0}_{n \times 3} & \mathbf{0}_{n \times 1} & \mathbf{0}_{n \times n} \end{bmatrix}. \quad (8.5)$$

The \mathbf{G} , \mathbf{S} and \mathbf{B} submatrices are shown below. Specifically,

$$\mathbf{G}_i(t) = \frac{\partial(\mathbf{a}_{i2B} + \mathbf{a}_{iNS} + \mathbf{a}_{iNB} + \mathbf{a}_{iSRP})}{\partial \mathbf{r}_i} \in \mathcal{R}^{3 \times 3} \quad (8.6)$$

and,

$$\mathbf{S}_i(t) = \frac{\partial \mathbf{a}_{iSRP}}{\partial C_{r_i}} \in \mathcal{R}^{3 \times 1} \quad (8.7)$$

and,

$$\mathbf{B}_i = \frac{\partial(\mathbf{a}_{i2B} + \mathbf{a}_{iNS} + \mathbf{a}_{iNB} + \mathbf{a}_{iSRP})}{\partial \mathbf{C}} \in \mathcal{R}^{3 \times n}. \quad (8.8)$$

Next we examine the measurement models used in this study.

8.3 Filter Measurement Model

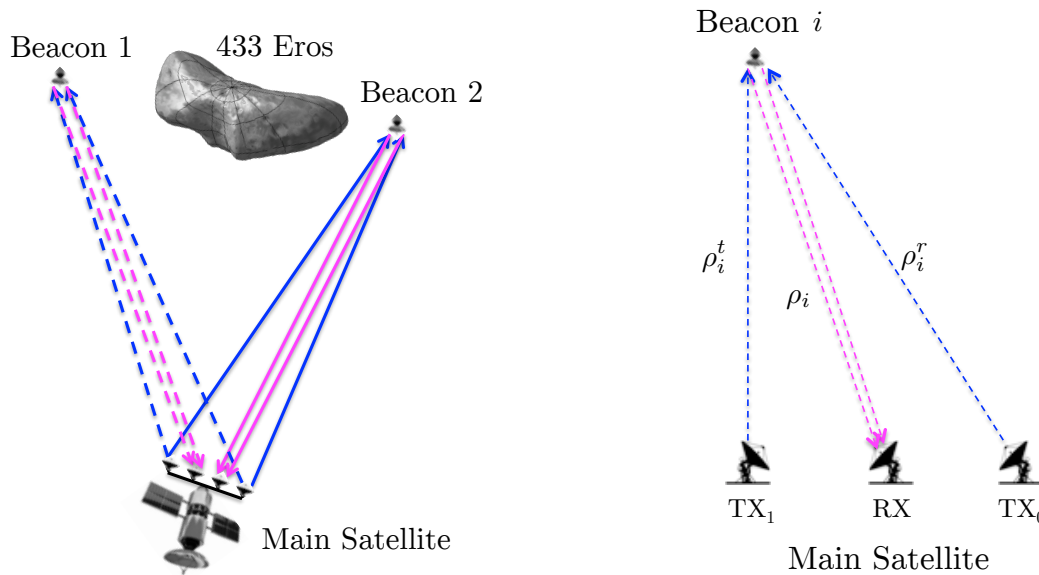
In this proof of concept study three different measurement types are implemented, either angles with FDOA or angles with range-rate. Angles provide plane-of-sky information in terms of azimuth and elevation angles from the camera line-of-sight (LOS) which is along the main satellite - Eros CoM vector. The final non-linear measurement equations $G(\mathbf{X}(t), t)$, for both setups are shown here,

$$G(\mathbf{X}(t), t) = \left[Az_1 \quad El_1 \quad Az_2 \quad El_2 \quad FDOA \right]^T, \quad (8.9)$$

or

$$G(\mathbf{X}(t), t) = \left[Az_1 \quad El_1 \quad Az_2 \quad El_2 \quad \dot{\rho}_1 \quad \dot{\rho}_2 \right]^T. \quad (8.10)$$

The actual measurement equations of angles, FDOA and range-rate are described in chapter 2.2. Figure 8.2 illustrates how the FDOA measurement is used in the context for asteroid navigation, because in this dissertation it has only been described for use with stations on the Earth.



(a) FDOA Geometry: blue lines are emitted signals and magenta lines are received at the main satellite (b) Differential Doppler geometry: half of an FDOA measurement

Figure 8.2: Differential Doppler and FDOA geometries: two differenced differential Doppler measurements generates the FDOA measurement

8.4 Simulation Results

The results are broken down into two sections, first the Cramér-Rao analyses and second two filter runs comparing the use of FDOA with two range-rate observables and finally a simulation which includes a range-rate bias representative of beacon oscillator errors.

8.4.1 Cramér-Rao Lower Bound (CRLB) Analyses

The CRLB is used extensively in the following analysis in order to assess the viability of using angles with an FDOA measurement for gravity estimation. Furthermore, angles with range-rate are also analyzed to set a benchmark for comparison with the FDOA results. Table 8.2 summarizes the a-priori uncertainties on the state as well as the measurement uncertainties used in the CRLB covariance analyses.

Table 8.2: CRLB 1σ a-priori uncertainty for estimated states and measurements

<i>Beacons</i>	
Position	200 m
Velocity	2 cm/s
Coefficient of Reflectivity	0.01
<i>433 Eros</i>	
Gravity Coefficients (normalized)	0.01
<i>Measurements</i>	
Angles	2e-5 rad \approx 30 m at 1500 km
Range-rate	1 cm/s and 1 mm/s
FDOA	0.1, 0.2 and 0.01 mHz

The purpose of this proof of concept is to determine how well FDOA can recover the gravity field and how this compares to better known measurements such as range-rate since FDOA has some advantages. The uncertainty on the measurements has a large effect on the final results, consequently we examine a number of different uncertainties. In Figure 8.3 the abscissa shows the degree of the gravity coefficients. On the ordinate in a log scale is the RMS value of the harmonics [59]. The black dashed line with ‘x’s indicate the RMS of the truth values of the spherical harmonics. For example for degree 2, the RMS value is computed as $\sqrt{\frac{1}{5}(C_{2,0}^2 + C_{2,1}^2 + S_{2,1}^2 + C_{2,2}^2 + S_{2,2}^2)}$. Then we can plot the uncertainty for each of these harmonics determined from the CRLB. If the uncertainty is lower than the actual value then those gravity coefficients can be accurately estimated. On the other hand if the uncertainty is much larger than the value of the gravity coefficients itself, there is not much information to be gained on those coefficients. We first examine the case of angles only, meaning no range-rate or FDOA measurements are included to establish a baseline. Using an angle uncertainty of 2e-5 rad we obtain the purple line in Figure 8.3. The uncertainty of the first three gravity coefficients are well below their values, therefore a 4×4 gravity field could be estimated in this configuration. Then we add FDOA with a $\sigma = 0.2$ mHz shown in blue with diamond markers. This sigma value was chosen because it is realistic and already used in certain other applications such as geolocation. Given the added measurement type we can now estimate up to a 5×5 gravity field since the uncertainty at the 5 degree harmonics mark is a magnitude smaller than its gravity coefficient value.

Next we examine two other scenarios, the first of which is FDOA with a $\sigma = 0.1$ mHz and the second is range-rate with a $\sigma = 1$ cm/s. The CRLB for those two simulations are shown in yellow with triangle markers and red with '+' markers respectively. Note that they overlap almost identically, in fact the gravity coefficient uncertainties using range-rate and FDOA with the specified measurement uncertainties are within only a few percent difference. The angles and FDOA measurement setup is marginally better than the angles and range-rate setup with these specified σ s, as the red line is somewhat lower than the yellow line. The second scenario are the CRLB analyses with FDOA $\sigma = 0.01$ mHz and range-rate $\sigma = 1$ mm/s. These are shown in cyan with circle markers and green with square markers, also in Figure 8.3. Once again these two simulations are within a few percent difference and the uncertainty is low enough to estimate a 6×6 gravity field while not quite sufficient to estimate the 7×7 field as the uncertainty is on the same level as the degree 7 coefficients values. Therefore including FDOA can increase the gravity field estimate by at least 2 degrees and orders over angles alone.

8.4.2 Navigation Results

In this section the simulations are not just covariance analyses but rather examinations of filter performance under realistic conditions with simulated measurements. This means the EKF started off with an initial reference trajectory deviated from the truth. Furthermore, the 15×15 gravity field has also been corrupted to determine how well the truth gravity field can be recovered. We show the results from the angles and FDOA measurements first, where sigmas of $2e-5$ rad and 0.1 mHz are used respectively. Then we analyze the same scenario but replace the FDOA measurement with two range-rate measurements, one for each beacon, with a sigma of 1 cm/s. These two cases correspond to the red and yellow lines in Figure 8.3. The last simulation we present is the case of a bias caused by, for example, an oscillator error in the beacons. Only the angles and range-rate with a bias are shown as angles with FDOA are unaffected by those types of errors, a potentially useful result of using differenced measurements.

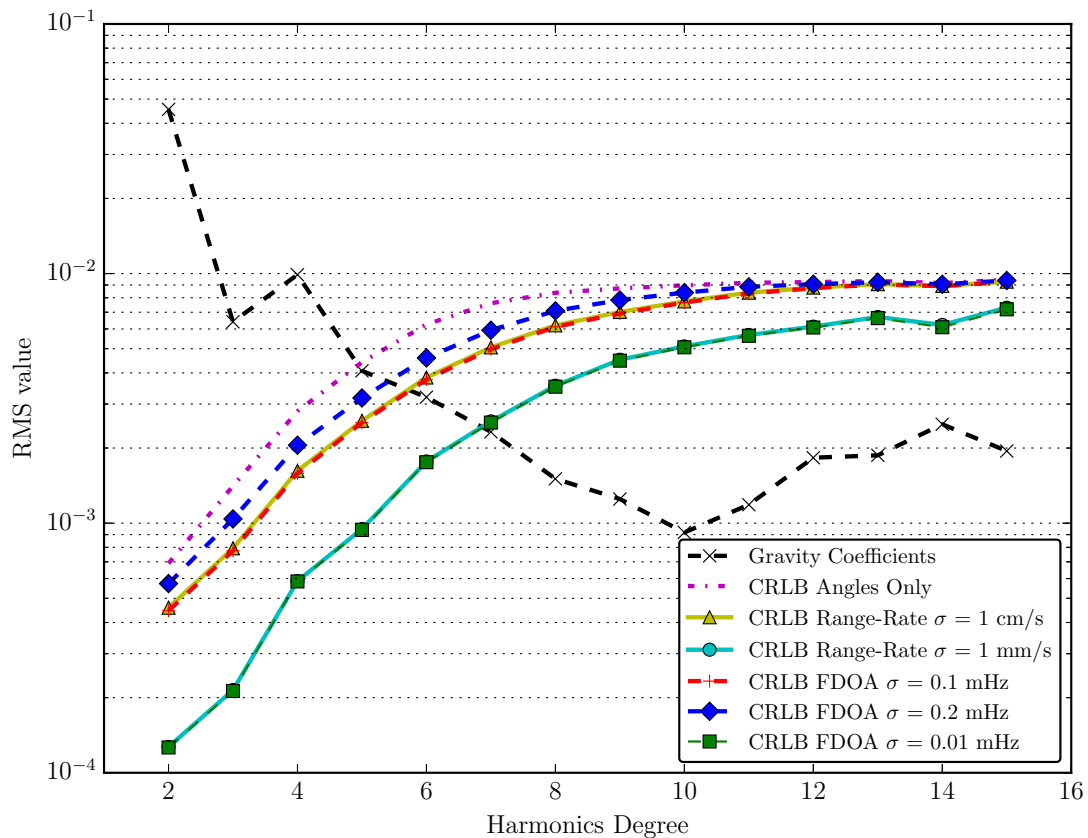


Figure 8.3: Cramér-Rao Lower Bounds for angles ($\sigma = 2e-5$ rad) with either range-rate or FDOA for various σ s

8.4.2.1 Angles and FDOA

Figures 8.4 and 8.5 illustrate the time evolution of the state errors, specifically position and velocity. The ACI x , y and z positions and velocities are shown for both beacons with the subscript indicating beacon 1 or 2. The figures are cropped in the y -axis to better show detail of how the errors are reduced over time, after about 15 hours of measurement processing the state errors have diminished to less than ± 40 m and ± 30 mm/s. The 3σ covariance bounds for the 6 states are shown with the dashed lines progressively decreasing over time. Note that the covariance for beacon 1 is lower than beacon 2 despite starting with the same a-priori covariance and deviation from the truth.

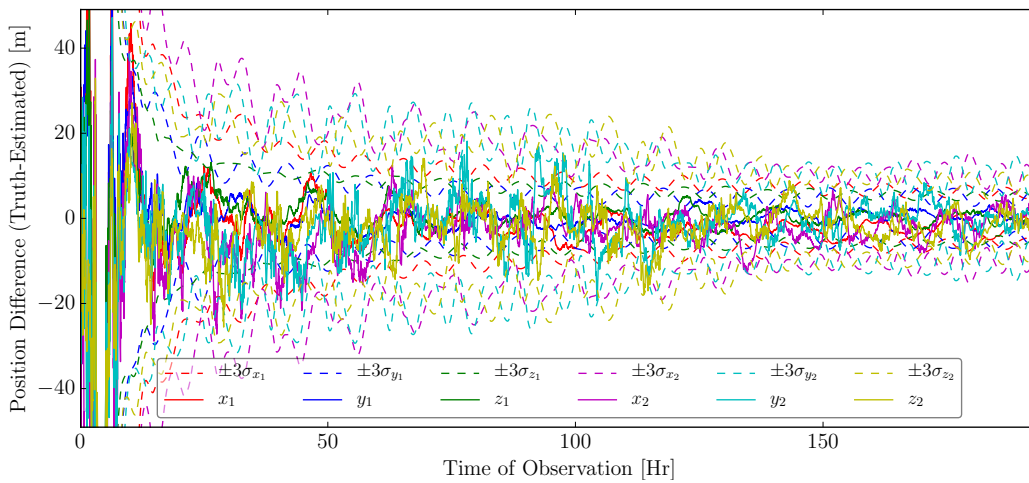


Figure 8.4: Angles and FDOA: position state errors with 3σ bounds

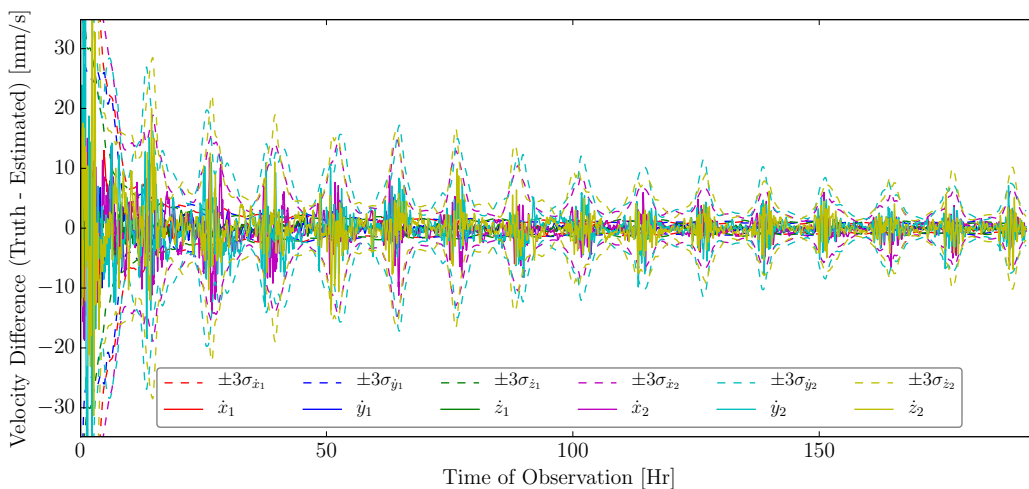


Figure 8.5: Angles and FDOA: velocity state errors with 3σ bounds

In Figure 8.5 the velocity state errors as well the covariance bounds for beacon 2 have a very noticeable and repeatable pattern of increasing and decreasing at a rate of approximately twice per day. This pattern is due to the orbital orientation with respect to the main satellite. After 8 days of measurement processing the 1σ 3D RMS uncertainty for position and velocity of beacon 1 is 1.89 m and 0.26 mm/s respectively and 3.17 m and 0.74 mm/s for beacon 2. With these measurement sigmas for the angles and FDOA the gravity field can be estimated up to degree and order 5 as

indicated by the corresponding CRLB. Figure 8.10 shows the gravity coefficient errors over time as well as the 3σ covariance bounds from degree 2 to 5. There is a rapid drop in the uncertainty over the first 24 hours and then the filter gradually continues to improve its estimate over the following week.

8.4.2.2 Angles and Range-Rate

Angles and FDOA observables have not been previously used for gravity estimation about asteroids, as a result we show a comparison with angle and two range-rate measurements. The covariance bound evolution in both the beacon states as well as the gravity coefficients match closely to that of FDOA. Again we find that the covariance for beacon 1 is lower than that of beacon 2. The pattern in the velocity of beacon 2 is still present with the same magnitude as well. After 8 days of measurement processing the 1σ 3D RMS uncertainty for position and velocity of beacon 1 is 1.91 m and 0.27 mm/s respectively and 3.21 m and 0.77 mm/s for beacon 2. These uncertainties are marginally larger than those found with the FDOA observable.

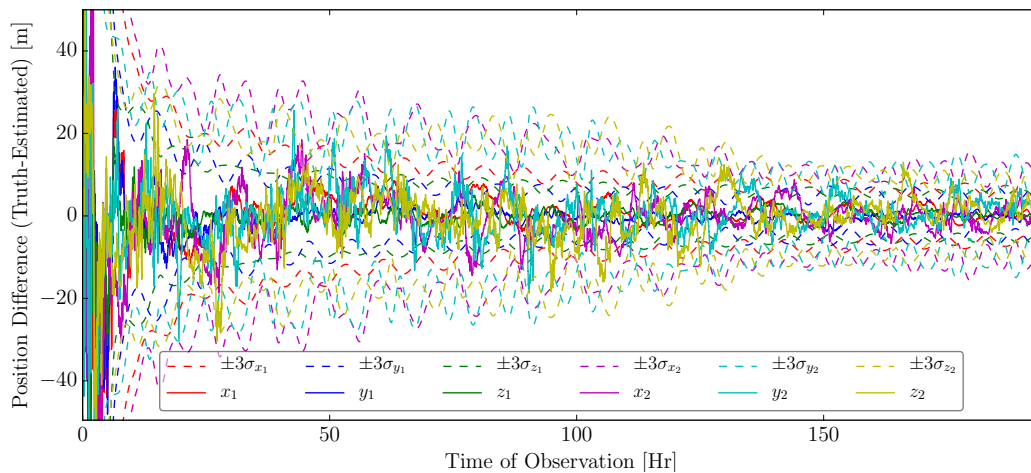


Figure 8.6: Angles and range-rate: position state errors with 3σ bounds

The gravity coefficients are also able to be estimated up to degree and order 5. The results of which are illustrated in Figure 8.11. The $S_{5,3}$ coefficient has significantly worse error over the 8 day

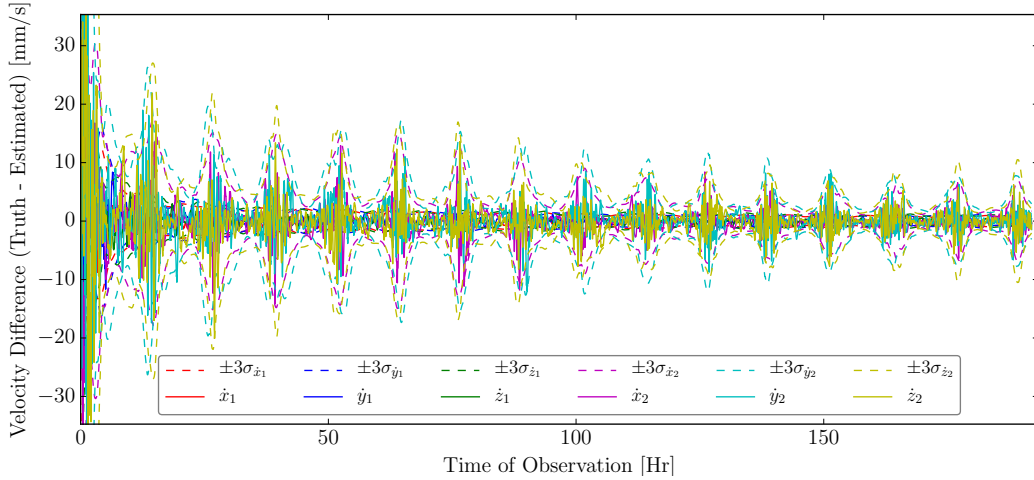


Figure 8.7: Angles and range-rate: velocity state errors with 3σ bounds

observation period despite being initiated with the same error as with FDOA but also converges by the end of the 8 days. In general, however, the FDOA results with 0.1 mHz σ show a barely perceptible improvement over range-rate with 1 cm/s σ s. This of course assumes no errors or biases are present in the system. In the next section we introduce a bias which emphasizes the potential strength of FDOA.

8.4.2.3 Angles and Range-Rate with Bias

In the following scenario we introduce a range-rate bias of +1 cm/s in beacon 1 and -1 cm/s in beacon 2. A bias like this could occur if the translation oscillator frequency of the beacons were in error. As shown by the position and velocity plots of the beacons in Figures 8.8 and 8.9 there is a significant bias present. Furthermore, this error propagates to the estimation of the gravity field as shown by Figure 8.12. While not immediately obvious in the degree 2 coefficients, degrees 3, 4 and 5 show large biases and often exceed their 3σ covariance bounds. The advantage of using the FDOA observable instead is that these common errors cancel and despite a large bias like this, the results are identical to those shown previously.

In these three cases of angles with FDOA and angles with range-rate the state errors of the

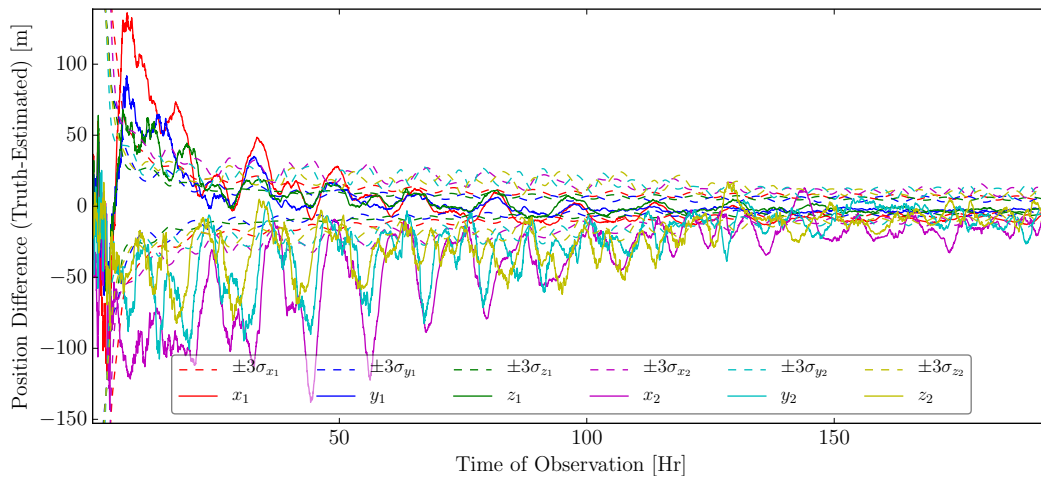


Figure 8.8: Angles and range-rate with bias: position state errors with 3σ bounds

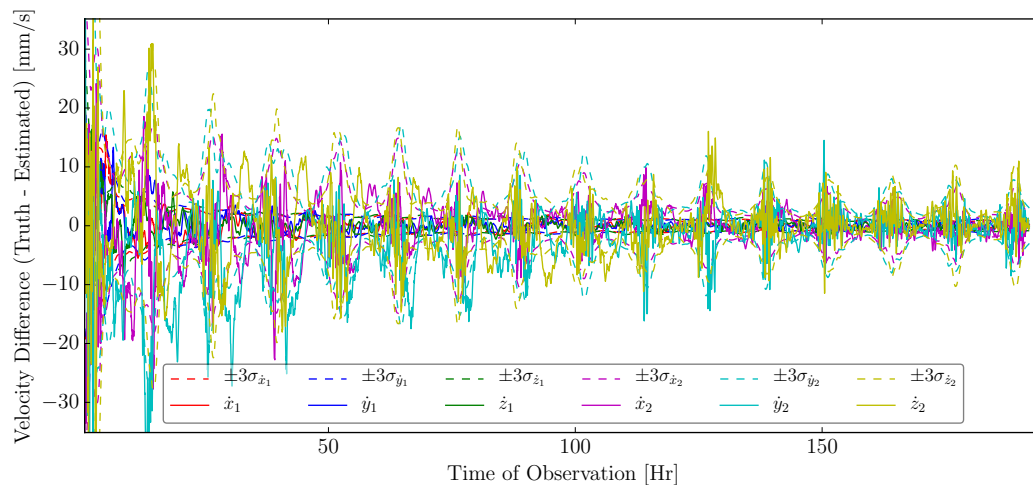


Figure 8.9: Angles and range-rate with bias: velocity state errors with 3σ bounds

coefficient of reflection were not shown. The plots simply showed a reduction in the covariance bounds but since the initial bounds were quite large with an a-priori $\sigma = 0.01$, 8 days was not sufficient to lock down on the truth value. In the simulation with the bias the coefficient of reflection estimate also diverged and slightly exceed the covariance bounds.

In this chapter we have shown the viability of using angles in conjunction with the FDOA measurement type to perform state estimation on two beacons in close proximity to a small body.

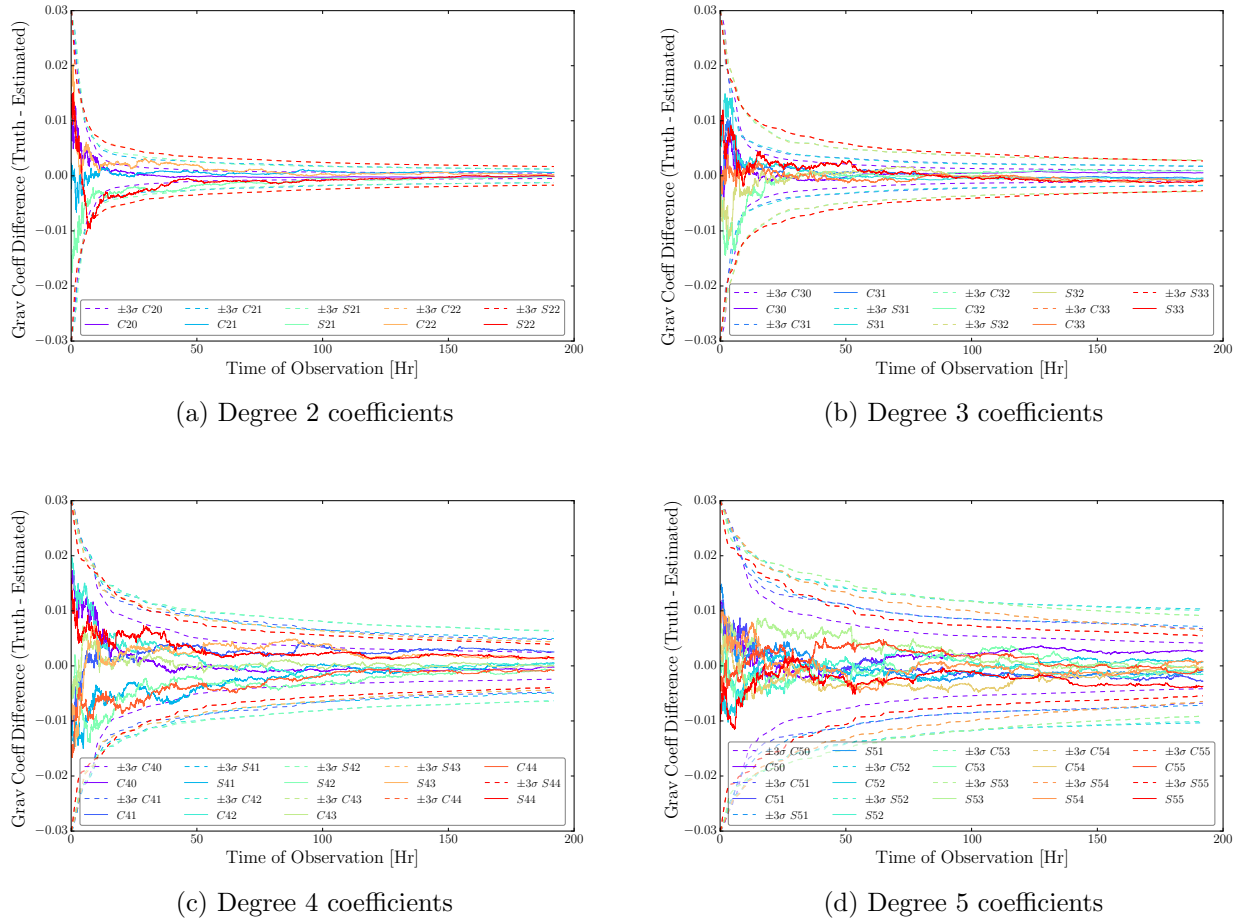


Figure 8.10: Angles and FDOA: gravity coefficient errors and 3σ bounds shown for coefficients where coefficient value RMS is less than its coefficient RMS uncertainty

More importantly we have shown that gravity field recovery is possible within just a few days. For comparison with the FDOA observable we have also conducted simulations using two range-rate measurements, one for each of the beacons. An FDOA measurement uncertainty of 0.1 mHz equates approximately to a range-rate sigma of 1 cm/s and 0.01 mHz to 1 mm/s. The motivation for exploring the use of FDOA as a navigation data type is for its resilience against certain common errors. Due to the double differenced nature of FDOA, any translation oscillation errors in the beacons and receiver errors in the main satellite cancel. As a result, cheaper hardware may be viable since the high standards required by other data types such as range and range-rate or

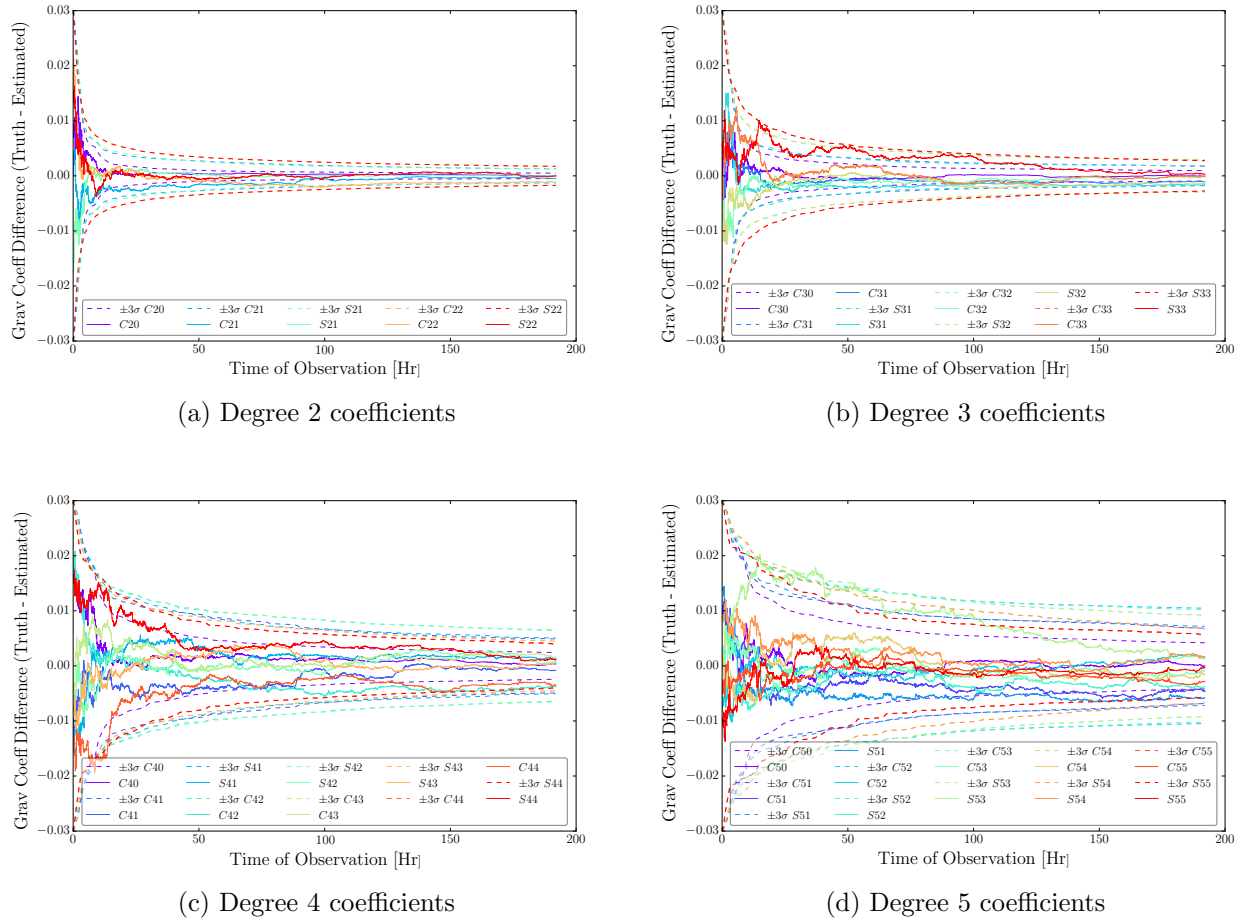


Figure 8.11: Angles and range-rate: gravity coefficient errors and 3σ bounds shown for coefficients where coefficient value RMS is less than its coefficient RMS uncertainty

Doppler are not necessary to produce the same results. While these errors could in some cases be estimated, FDOA removes the need for that entirely. The feasibility has been demonstrated in this chapter but a number of assumptions need to be addressed in the future to make this study more realistic. The first of which is the absolute knowledge of the state of the main spacecraft. In reality this spacecraft too will need to be estimated as there will be some uncertainty in its state. With limited Deep Space Network (DSN) measurements as well as optical navigation of landmark tracking as was previously shown in Ref. [35] could be a possibility. Another approach is to perform a consider covariance analysis that takes into account some uncertainty of the main spacecraft state

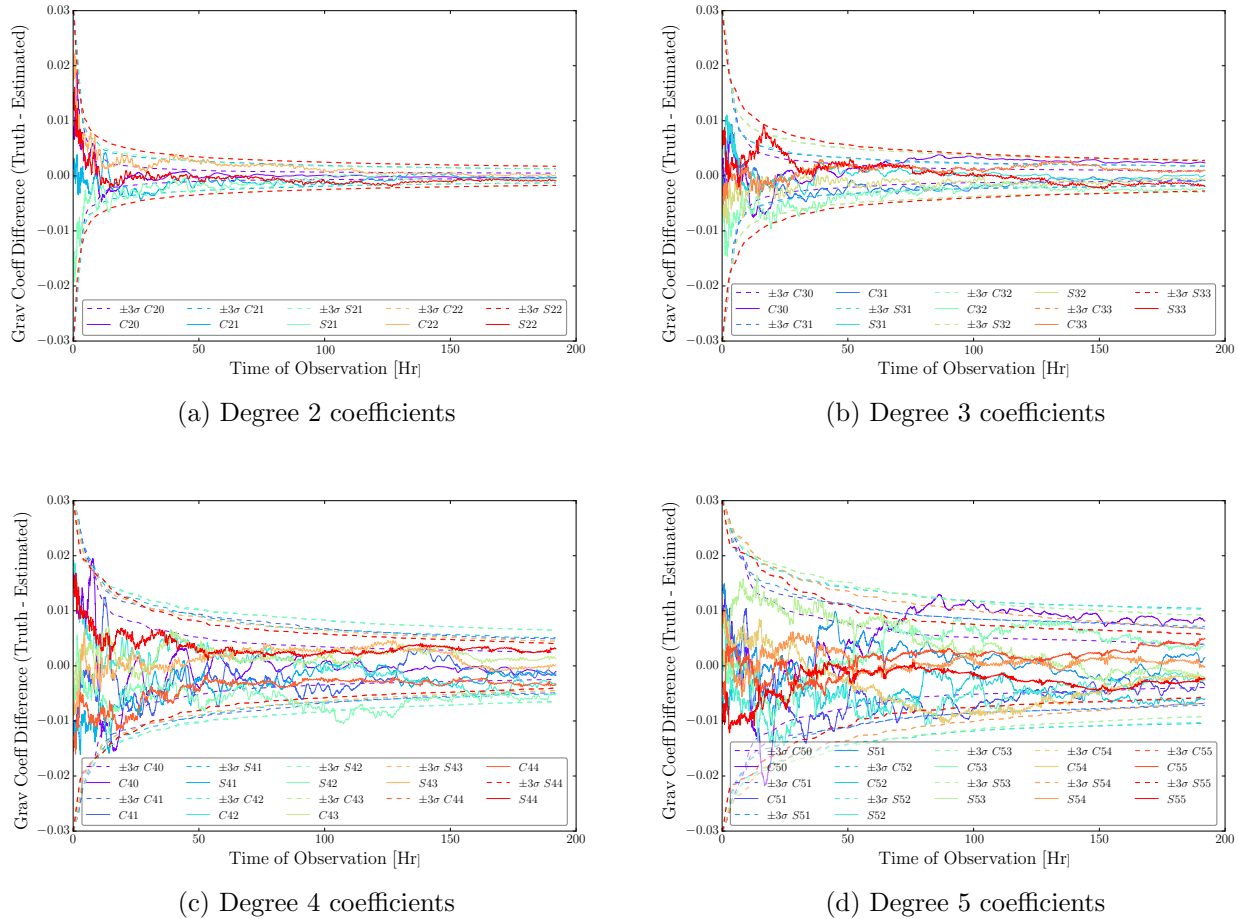


Figure 8.12: Angles and range-rate with bias: gravity coefficient errors and 3σ bounds shown for coefficients where coefficient value RMS is less than its coefficient RMS uncertainty

to see how that affects the beacon state and gravity estimation. The second assumption that needs to be addressed is the absolute knowledge of the main spacecraft attitude with the LOS vector pointing exactly at Eros' CoM, some bias or offset within the pointing would affect primarily the angles measurements. Once more a consider covariance analysis could be performed on this as well to determine the sensitivity of these errors on the final results.

Chapter 9

Conclusion and Future Work

This dissertation presents a novel technique for multi-satellite OD of active Earth-orbiting satellites. The approach is a combination of two existing, but not previously combined fields. On the one hand we have the well developed field of very long baseline interferometry (VLBI) for interplanetary navigation, specifically the technique of same beam interferometry (SBI) which estimates a set of relative satellite states. On the other hand we have the field of dual-satellite geolocation which focuses on the localization of a radio frequency (RF) source somewhere on the Earth visible to both satellites. By using the geolocation observables of time difference of arrival (TDOA) and frequency difference of arrival (FDOA) in an SBI setup, the dual satellite state vector can be estimated in an absolute sense while simultaneously canceling many common errors.

This is the first published instance of this technique, consequently we first explored the observability to determine when it is appropriate to use TDOA and FDOA. Two key factors were analyzed: the number of baselines, and the orbit regimes of the two satellites. As expected, increasing the number of baselines improves the solution quality due to the increased number of measurements but also due the additional geometrical diversity. Three different orbit regimes were explored, a GEO-GEO, GEO-MEO, and GEO-LEO setup. The use of TDOA and FDOA becomes more favorable as faster dynamics, i.e. lower orbiting satellites such as the GEO-LEO configuration are used. It should be noted that the one particular case of two geostationary satellites, meaning slow dynamics, with one baseline has a low degree of observability to the point of not being practical for real-world implementation. Indeed when the number of baselines are increased from one to two

or more, the problem does become increasingly more tractable. We also illustrate under what circumstances TDOA and FDOA observables perform better than the classical use of range and range-rate. In a strong majority of cases TDOA and FDOA have a more favorable OD result with lower uncertainties and smaller state errors. The benefit of TDOA and FDOA, over range and range-rate, is further exacerbated if biases are present which often times leaves the former unaffected yet negatively affects the latter.

In addition to dual-satellite OD, we also investigated relative satellite OD of a chief and deputy satellite with the TDOA and FDOA observables. The full non-linear equations are implemented therefore no restrictions on the satellite separation are in place other than still being within the same beamwidth of the transmitting antenna. Because only one satellite is estimated, rather than both, the estimated satellite uncertainty can attain exceptionally low levels. Three different scenarios were investigated, a GEO chief satellite paired with a deputy ranging from LEO-to-GEO, a leader-follower scenario with a chief and deputy in the same orbits ranging from LEO-to-GEO, and finally a tightly orbiting relative bounded motion case with the orbit regimes ranging from LEO-to-GEO as well. Once more the OD results were compared to the classical range and range-rate measurements where in all three scenarios TDOA and FDOA were more favorable with the exception when both satellites were in GEO. Two types of analyses were conducted, one where the chief knowledge was assumed perfect, and second where some small amount of chief uncertainty was considered when estimating the deputy in order to maintain better covariance realism. The results demonstrate that using TDOA and FDOA in a relative navigation sense could provide better uncertainty quantification than traditional methods if the state knowledge of one satellite is already very accurate. This is particularly useful for a space situational awareness (SSA) application.

This dissertation did not only focus on OD however, but also on the estimation of RF sources both ground and space-based. Research was conducted on mapping the ephemeris uncertainty to the geolocation covariance to provide a more realistic covariance. Furthermore, the geolocation solution was improved by appending a probabilistic altitude constraint to the posterior covariance, significantly reducing the projected geolocation uncertainty ellipse. The localization of a sub-GEO

satellite, in this work a LEO satellite, by two GEO satellites was also examined. This setup resembles the tracking and data relay satellite system (TDRSS) to track lower Earth orbiting satellites, with the benefit that any higher-orbiting satellite capable of repeating a signal can be used rather than a limited number of TDR satellites. By tracking a high LEO satellite from GEO, approximately 75% of the orbit is visible allowing long arcs of tracking.

The results in this dissertation were verified by a long-arc of real data. The measurements are from the Galaxy-16 and SES-1 communication satellites in geostationary orbit. Both the OD and geolocation aspects were evaluated. Note that dual-satellite geolocation often takes place using geostationary satellites which is the worst spot for the satellites due to the low relative motion with respect to the ground stations. If a transmitter interferes with a communication satellite in GEO then it should ideally be paired with a LEO rather than another GEO. In this way, the OD on both satellites would be better than in the GEO-GEO setup, which reduces the mapped ephemeris uncertainty into the projected geolocation covariance.

Finally, the use of double differenced measurements has additional benefits that are not restricted to Earth orbiting satellites. FDOA was shown to be a suitable measurement in addition to optical measurements for small-body navigation of multiple beacons or cubesats and gravity recovery.

Future work includes additional dual-satellite configurations. In the current body of research on dual-satellite estimation the case of a GEO satellite paired with a secondary ranging in orbit from LEO-to-GEO was considered. However it is likely, because of the results shown with relative navigation, that lower-orbit configurations would yield favorable OD results compared to range and range-rate as well. Further research needs to be conducted on the inclusion of additional satellites, so as to determine the advantage of using TDOA and FDOA for formations and constellations. Continued development of the Fourier SRP model is required when longer data arcs are processed and should be incorporated in the Python framework developed for this dissertation. While preliminary research was conducted on the location and orientation of the baselines, no conclusive arguments could be established other than the number of baselines should be maximized.

Currently the relative OD research was conducted in a two-body environment, not the full ephemeris as was used for the dual-satellite OD problem. The full dynamics and measurement models need to be extended to the relative case as well. The increased dynamics are expected to improve the results rather than degrade them however, because the additional perturbations increase the observability which would be beneficial for relative OD in the GEO belt. On the geolocation research side, the benefits of doing geolocation with sub-GEO satellites needs to be investigated to quantify the geolocation solution improvement due to the faster dynamics.

Bibliography

- [1] Navigation Data - Definitions and Conventions. (May), 2010.
- [2] COSPAS-SARSAT 406 MHz MEOSAR Implementation Plan. Technical Report 1, 2013.
- [3] Henry Louis Ablin. Criteria for degree of observability in a control system. PhD thesis, 1967.
- [4] ASU. Psyche: Journey to a Metal World, January 2017. Available at <https://sese.asu.edu/research/psyche>.
- [5] Riccardo Bardelli, David Haworth, and Nigel Smith. Interference Localisation for the Eutelsat Satellite System. IEEE, pages 1641–1651, 1995.
- [6] Roger R. Bate, Donald D. Mueller, and Jerry E. White. Fundamentals of Astrodynamics. Dover Publications, Inc., New York, 1971.
- [7] J S Border and E R Kursinski. Deep space tracking and frequency standards. Frequency Control, 1991., Proceedings of the 45th Annual Symposium on, pages 594–607, 1991.
- [8] James S. Border, William M. Folkner, Robert D. Kahn, and Karen S. Zukor. Precise tracking of the Magellan and pioneer venus orbiters by same-beam interferometry Part I: Data Accuracy Analysis. TDA Progress Report 42-110, Apr-Jun:1–20, 1992.
- [9] William L. Brogan. Modern Control Theory. Prentice Hall, 3rd edition, 1991.
- [10] Arthur E. Jr. Bryson and Yu-Chi Ho. Applied Optimal Control. Taylor & Francis, revised pr edition, 1975.
- [11] Yalu Cao, Li Peng, Jinzhou Li, Le Yang, and Fucheng Guo. A new iterative algorithm for geolocating a known altitude target using TDOA and FDOA measurements in the presence of satellite location uncertainty. Chinese Journal of Aeronautics, 28(5):1510–1518, 2015.
- [12] M H Chan. Application of a Dual Satellite Geolocation System on Locating Sweeping Interference. In World Academy of Science, Engineering and Technology, volume 6, pages 939–944, 2012.
- [13] Y. T. Chan and K. C. Ho. A Simple and Efficient Estimator for Hyperbolic Location. IEEE Transactions on Signal Processing, 42(8):1905–1915, 1994.
- [14] Paul Chestnut. Emitter Location Accuracy Using TDOA and Differential Doppler. IEEE Transactions on Aerospace and Electronic Systems, AES-18(2):214–218, 1982.

- [15] C. C. Counselman III, H. F. Hinteregger, and I. I. Shapiro. Astronomical Applications of Differential Interferometry A Scanning X-Ray Microscope Using Synchrotron Radiation. Science, 178(November):607–608, 1972.
- [16] J. E. Dennis and R. B. Schnabel. Numerical Linear Algebra Background. In Numerical Methods for Unconstrained Optimization and Nonlinear Equations, pages 40–68. 1996.
- [17] Leonhard Euler and Anders Johan Lexell. Recherches et calculs sur la vraie orbite elliptique de la comete de l’an 1769 et son tems périodique. 1770.
- [18] W. M. Folkner, J. S. Border, and Sumita Nandi. Orbit determination for Magellan and Pioneer 12 using same-beam interferometry. Advances in the Astronautical Sciences, 76(pt 2):909–918, 1992.
- [19] W. M. Folkner and J.S. Border. TDA Progress Report 42-109. Orbiter-Orbiter and Orbiter-Lander Tracking Using Same-Beam Interferometry. Technical report, NASA, 1992.
- [20] William M. Folkner, James S. Border, Sumita Nandi, and Karen S. Zukor. Precise tracking of the Magellan and pioneer venus orbiters by same-beam interferometry Part II: Orbit Determination Analysis. TDA Progress Report 42-113, Jan-Mar:22–36, 1993.
- [21] Jeroen L. Geeraert, Brandon A. Jones, and Jay W. McMahon. Improving Geolocation Accuracy Through Refined Satellite Ephemeris Estimation in an Ill-Conditioned. In AIAA/AAS Astroynamics Specialist Conference, pages 1–20, 2015.
- [22] Jeroen L Geeraert and Jay W McMahon. Dual-Satellite Geolocation with Ephemeris Correction and Uncertainty Mapping. IEEE Transactions on Aerospace and Electronic Systems, pages 1–13.
- [23] Jeroen L Geeraert and Jay W McMahon. Dual-Satellite Orbit Determination with Time and Frequency Difference of Arrival. Journal of Guidance, Control, and Dynamics, 2017.
- [24] Jeroen L Geeraert and Jay W McMahon. Relative Orbit Determination of Multiple Satellites Using Double Differenced Measurements. In Advanced Maui Optical and Space Surveillance Technologies Conference, 2017.
- [25] Jeroen L. Geeraert and Jay W. McMahon. Square-Root Unscented Schmidt-Kalman Filter. Journal of Guidance, Control, and Dynamics, 2017.
- [26] Jeroen L Geeraert, Jay W McMahon, and Siamak G Hesar. Small Body Navigation and Gravity Estimation Using Angle and FDOA Observables. In AIAA/AAS Spaceflight Mechanics Meeting, pages 1–18, 2017.
- [27] Jeroen L. Geeraert, Jay W McMahon, and Brandon A Jones. Orbit Determination Observability of the Dual-Satellite Geolocation System with TDOA and FDOA. AIAA/AAS Astroynamics Specialist Conference, pages 1–21, 2016.
- [28] Bruce P. Gibbs. Advanced Kalman Filtering, Least-Squares and Modeling. John Wiley & Sons, 2011.
- [29] P. E. Gill, G. H. Golub, W. Murray, and M. a. Saunders. Methods for modifying matrix factorizations. Mathematics of Computation, 28(126):505–535, 1974.

- [30] Jon Giorgini, Eric Graat, Tung-Han You, Mark Ryne, S.K. Wong, and John McNamee. Magellan navigation using X-band differenced Doppler during Venus mapping phase. AIAA-92-4521 Astrodynamics Conference, 1992.
- [31] Robert G. Gottlieb. Fast gravity, gravity partials, normalized gravity, gravity gradient torque and magnetic field: derivation, code and data. Technical report, 1993.
- [32] Fucheng Guo, Yun Fan, Yiyu Zhou, Caigen Zhou, and Qiang Li. Space Electronic Reconnaissance, Localization Theories and Methods. John Wiley & Sons, 1 edition, 2014.
- [33] Jianying Han, Ying Liu, and Daochao Huang. Research on Satellite Interference Geolocation based on Satellite Systems. In IEEE, 2009.
- [34] D. P. Haworth, N. G. Smith, R. Bardelli, and T. Clement. Interference localization for EU-TELSAT satellites-the first European transmitter location system. International Journal of Satellite Communications, 15(4):155–183, 1997.
- [35] Siamak G Hesar, Jeffrey S Parker, Jay McMahon, and George H Born. Small Body Gravity Field Estimation Using Liaison Supplemented Optical Navigation. AAS, pages 41–54, 2015.
- [36] K Hill and Brandon A. Jones. TurboProp Version 4.0.
- [37] K. C. Ho and Y. T. Chan. Solution and Performance Analysis of Geolocation by TDOA. IEEE Transactions on Aerospace and Electronic Systems, 29(4):1311–1322, 1993.
- [38] K. C. Ho and Y. T. Chan. Geolocation of a known altitude object from TDOA and FDOA measurements. IEEE Transactions on Aerospace and Electronic Systems, 33(3):770–783, 1997.
- [39] K. C. Ho, Xiaoning Lu, and L. Kovavisaruch. Source localization using TDOA and FDOA measurements in the presence of receiver location errors: Analysis and solution. IEEE Transactions on Signal Processing, 55(2):684–696, 2007.
- [40] K. C. Ho and Wenwei Xu. An accurate algebraic solution for moving source location using TDOA and FDOA measurements. IEEE Transactions on Signal Processing, 52(9):2453–2463, 2004.
- [41] Brandon A Jones. Development of Signal and Spacecraft Ephemeris Propagation Tools for Geolocation : RF Propagator Overview Nomenclature / Definitions. Technical report, 2014.
- [42] Simon J. Julier. The scaled unscented transformation. Proceedings of the 2002 American Control Conference (IEEE Cat. No.CH37301), (2):4555–4559 vol.6, 2002.
- [43] Simon J Julier and Jeffrey K Uhlmann. New extension of the Kalman filter to nonlinear systems. The 11th International Symposium on Aerospace/Defence, Sensing, Simulation and Controls, 3:182, 1997.
- [44] R. D. Kahn, W. M. Folkner, and C. D. Edwards. Position Determination of a Lander and Rover at Mars With Earth-Based Differential Tracking. TDA Progress Report 42-108, Oct–Dec:279–293, 1992.
- [45] Erin Kahr, Oliver Montenbruck, and Kyle P G O’Keefe. Estimation and Analysis of Two-Line Elements for Small Satellites. Journal of Spacecraft and Rockets, 50(2):433–439, 2013.

- [46] R Kalman. On the general theory of control systems. IEEE Transactions on Automatic Control, 4(3):110–110, 1959.
- [47] R. E. Kalman. A New Approach to Linear Filtering and Prediction Problems. Journal of Basic Engineering, 82(1):35, 1960.
- [48] Johannes Kepler. Astronomia Nova. 1609.
- [49] Johannes Kepler. Harmonices Mundi. 1619.
- [50] P. P. Klein. On the Ellipsoid and Plane Intersection Equation. Applied Mathematics, 3(November):1634–1640, 2012.
- [51] P. Koskela. Orbital Effects of Solar radiation Pressure on an Earth Satellite. The Journal of the Astronautical Sciences, IX(3), 1962.
- [52] Jason Leonard, Brandon Jones, Eduardo Villalba, and George H Born. Absolute Orbit Determination and Gravity Field Recovery for 433 Eros Using Satellite-to-Satellite Tracking. AIAA/AAS Astrodynamics Specialist Conference, (August):1–17, 2012.
- [53] H. F. Levison. Lucy: Surveying the Diversity of the Trojan Asteroids: The Fossils of Planet Formation. SwRI, 2016. Available at <http://www.hou.usra.edu/meetings/lpsc2016/pdf/2061.pdf>.
- [54] Anders Johan Lexell. Reflexions sur le temps periodique des cometes EN general. Impr. de l'Academie imperiale des sciences, 1778.
- [55] M.J. Marcus. Satellite security: legacy of Captain Midnight. Telecommunications, 21:61–62, 1987.
- [56] F Markley. Autonomous navigation using landmark and intersatellite data. In AIAA-84-1987 Astrodynamics Conference, 1984.
- [57] Robert A. McDonald and Sharon K. Moreno. Grab and Poppy: America's Early ELINT Satellites. Technical report, National Reconnaissance Office, 2005.
- [58] J. W. McMahon. An Analytical Theory for the Perturbative Effect of Solar Radiation Pressure on Natural and Artificial Satellites. PhD thesis, 2011.
- [59] D. J. Miller, J. K., Konopliv, A. S., Antreasin, P. G., Bordi, J. J., Chesley, S., Helfrich, C. E., Owen, W. M., Wang, T. C., Williams, B. G., Yeomans, D. K., Scheeres. Determination of Shape, Gravity, and Rotational State of Asteroid 433 Eros. Icarus, 155:3–17, 2002.
- [60] Oliver Montenbruck. An epoch state filter for use with analytical orbit models of low earth satellites. Aerospace Science and Technology, 4:277–287, 2000.
- [61] Oliver Montenbruck and Eberhard Gill. Satellite Orbits: Models, Methods and Applications. Springer-Verlag Berlin Heidelberg, 2012.
- [62] Kevin M Moran and David A Cicci. Sensitivity of ridge-type estimation methods to condition number. Applied Mathematics and Computation, 112:143–159, 2000.

- [63] NASA JPL. NASA Selects Two Missions to Explore the Early Solar System, January 2017. Available at <http://www.jpl.nasa.gov/news/news.php?feature=6713>.
- [64] Isaac Newton. Philosophiæ Naturalis Principia Mathematica. 1687.
- [65] Tim Pattison and S. I. Chou. Sensitivity analysis of dual-satellite geolocation. IEEE Transactions on Aerospace and Electronic Systems, 36(1):56–71, 2000.
- [66] Gerard Petit and Brian Luzum. IERS Conventions (2010). Technical report, 2010.
- [67] William H. Press, Saul A. Teukolsky, William T. Vetterling, and Brian P. Flannery. Numerical Recipes: The Art of Scientific Computing. Number 1. Cambridge University Press, third edition, 2007.
- [68] Mark L. Psiaki. Absolute Orbit and Gravity Determination Using Relative Position Measurements Between Two Satellites. Journal of Guidance, Control, and Dynamics, 34(5):1285–1297, 2011.
- [69] RZ Sagdeyev. Differential VLBI measurements of the Venus atmosphere dynamics by balloons-VEGA Project. Astronomy and Astrophysics, 254:387, 1992.
- [70] Walter C Scales and Richard Swanson. Air and sea rescue via satellite systems. IEEE Spectrum, Mar:48–52, 1984.
- [71] Hanspeter Schaub and John L. Junkins. Analytical Mechanics of Space Systems. American Institute of Aeronautics and Astronautics, second edition, 2009.
- [72] D. J. Scheeres. The dynamical evolution of uniformly rotating asteroids subject to YORP. Icarus, 188(2):430–450, 2007.
- [73] L. M. Silverman and H. E. Meadows. Controllability and Observability in Time-Variable Linear Systems. Control, 5(1):64–73, 1967.
- [74] Julius O. Smith and Jonathan S. Abel. Closed-Form Least-Squares Source Location Estimation from Range-Difference Measurements. IEEE Transactions on Acoustics, Speech, and Signal Processing, 35(12):1661–1669, 1987.
- [75] William W. Smith and Paul G. Steffes. Time Delay Techniques for Satellite Interference Location System. IEEE Transactions on Aerospace and Electronic Systems, 25(2):224–231, 1989.
- [76] William Whitfield Smith and Paul G Steffes. Differential Time and Phase Measurement Techniques. IEEE AES Systems Magazine, (March):3–7, 1991.
- [77] Jason Stauch and Moriba Jah. Unscented SchmidtKalman Filter Algorithm. Journal of Guidance, Control, and Dynamics, 38(1):117–123, 2015.
- [78] Seymour Stein. Algorithms for Ambiguity Function Processing. IEEE Transactions on Acoustics, Speech, and Signal Processing, 29(3):588–599, 1981.
- [79] Johan Carl-Erik Stén and Per Pippin Aspaas. Anders Johan Lexell ’ s Role in the Determination of the Solar Parallax. The Journal of Astronomical Data, pages 71–82, 2013.

- [80] Robert F. Stengel. Optimal Control and Estimation. Dover, 1994.
- [81] G. W. Stewart. Matrix Algorithms: Volume 1: Basic Decompositions. 1998.
- [82] Zheng-bo Sun and Shang-fu Ye. Analysis on Parameter Error of Satellite Interference Location. In Asia-Pacific Radio Science Conference, pages 265–268, 2004.
- [83] Byron D Tapley, Bob E Schutz, and George H Born. Statistical Orbit Determination. Elsevier Academic Press, 2004.
- [84] James H Taylor. The Cramer Rao Estimation Error Lower Bound Computation for Deterministic Nonlinear Systems. IEEE Transactions on Automatic Control, AC-24(2):343–344, 1979.
- [85] Catherine L Thornton and James S Border. Radiometric Tracking Techniques for Deep - Space Navigation. Technical report, Jet Propulsion Laboratory, California Institute of Technology, 2000.
- [86] David A Vallado. Fundamentals of Astrodynamics and Applications. Space Technology Library, 4th edition, 2013.
- [87] Ronell Van Der Merwe and Eric a. Wan. The square-root unscented Kalman filter for state and parameter-estimation. Acoustics, Speech, and Signal Processing, 2001. Proceedings. (ICASSP -01). 2001 IEEE International Conference on, 6:3461–3464, 2001.
- [88] E.A. Wan and R Van Der Merwe. The unscented Kalman filter for nonlinear estimation. Proceedings of the IEEE 2000 Adaptive Systems for Signal Processing, Communications, and Control Symposium (Cat. No.00EX373), pages 153–158, 2002.
- [89] Hang Yan, Jin Cao, and Lei Chen. Study on Location Accuracy of Dual-Satellite Geolocation System. In 10th International Conference on Signal Processing, pages 107–110, 2010.

Appendix A

Observability Matrix Time Derivatives

A.1 Gravity Gradient Time Derivatives

The equations below are part of the observability matrix shown in Eq. 4.16. These equations were evaluated during the numerical analysis to show full system observability. Equations A.1 to A.6 lists the gravity gradient and its five time derivatives. Vectors \mathbf{r} and \mathbf{v} refer to the position and velocity of the satellite with respect to the Earth.

$$\mathbf{G}_{2B} = \frac{\mu}{r^3} \left[3\hat{\mathbf{r}}\hat{\mathbf{r}}^\top - \mathcal{I} \right] \quad (\text{A.1})$$

$$\dot{\mathbf{G}}_{2B} = \frac{3\mu}{r^4} \left[\mathbf{v}\hat{\mathbf{r}}^\top + \hat{\mathbf{r}}\mathbf{v}^\top - (\hat{\mathbf{r}}^\top \mathbf{v})(5\hat{\mathbf{r}}\hat{\mathbf{r}}^\top - \mathcal{I}) \right] \quad (\text{A.2})$$

$$\ddot{\mathbf{G}}_{2B} = \frac{3\mu}{r^5} \left[5(\hat{\mathbf{r}}^\top \mathbf{v})^2(7\hat{\mathbf{r}}\hat{\mathbf{r}}^\top - \mathcal{I}) - 10(\hat{\mathbf{r}}^\top \mathbf{v})(\mathbf{v}\hat{\mathbf{r}}^\top + \hat{\mathbf{r}}\mathbf{v}^\top) + 2\mathbf{v}\mathbf{v}^\top - (\mathbf{v}^\top \mathbf{v})(5\hat{\mathbf{r}}\hat{\mathbf{r}}^\top - \mathcal{I}) + \frac{\mu}{r}(3\hat{\mathbf{r}}\hat{\mathbf{r}}^\top - \mathcal{I}) \right] \quad (\text{A.3})$$

$$\begin{aligned} \ddot{\mathbf{G}}_{2B} = \frac{3\mu}{r^6} \left[-35(\hat{\mathbf{r}}^\top \mathbf{v})^3(9\hat{\mathbf{r}}\hat{\mathbf{r}}^\top - \mathcal{I}) + 105(\hat{\mathbf{r}}^\top \mathbf{v})^2(\mathbf{v}\hat{\mathbf{r}}^\top + \hat{\mathbf{r}}\mathbf{v}^\top) - 30(\hat{\mathbf{r}}^\top \mathbf{v})(\mathbf{v}\mathbf{v}^\top) + 15(\hat{\mathbf{r}}^\top \mathbf{v})(\mathbf{v}^\top \mathbf{v})(7\hat{\mathbf{r}}\hat{\mathbf{r}}^\top - \mathcal{I}) \right. \\ \left. - 15(\mathbf{v}^\top \mathbf{v})(\mathbf{v}\hat{\mathbf{r}}^\top + \hat{\mathbf{r}}\mathbf{v}^\top) + \frac{11\mu}{r}(\mathbf{v}\hat{\mathbf{r}}^\top + \hat{\mathbf{r}}\mathbf{v}^\top) - \frac{2\mu}{r}(\hat{\mathbf{r}}^\top \mathbf{v})(32\hat{\mathbf{r}}\hat{\mathbf{r}}^\top - 7\mathcal{I}) \right] \quad (\text{A.4}) \end{aligned}$$

$$\begin{aligned}
\ddot{\mathbf{G}}_{2B} = \frac{3\mu}{r^7} & \left[315(\hat{\mathbf{r}}^\top \mathbf{v})^4(11\hat{\mathbf{r}}\hat{\mathbf{r}}^\top - \mathcal{I}) - 210(\hat{\mathbf{r}}^\top \mathbf{v})^2(\mathbf{v}^\top \mathbf{v})(9\hat{\mathbf{r}}\hat{\mathbf{r}}^\top - \mathcal{I}) + \frac{\mu}{r}(\hat{\mathbf{r}}^\top \mathbf{v})^2(1165\hat{\mathbf{r}}\hat{\mathbf{r}}^\top - 187\mathcal{I}) \right. \\
& - 1260(\hat{\mathbf{r}}^\top \mathbf{v})^3(\mathbf{v}\hat{\mathbf{r}}^\top + \hat{\mathbf{r}}\mathbf{v}^\top) - \frac{302\mu}{r}(\hat{\mathbf{r}}^\top \mathbf{v})(\mathbf{v}\hat{\mathbf{r}}^\top + \hat{\mathbf{r}}\mathbf{v}^\top) + 420(\hat{\mathbf{r}}^\top \mathbf{v})^2(\mathbf{v}\mathbf{v}^\top) \\
& - 60(\mathbf{v}^\top \mathbf{v})(\mathbf{v}\mathbf{v}^\top) + \frac{52\mu}{r}(\mathbf{v}\mathbf{v}^\top) + 420(\hat{\mathbf{r}}^\top \mathbf{v})(\mathbf{v}^\top \mathbf{v})(\mathbf{v}\hat{\mathbf{r}}^\top + \hat{\mathbf{r}}\mathbf{v}^\top) + 15(\mathbf{v}^\top \mathbf{v})^2(7\hat{\mathbf{r}}\hat{\mathbf{r}}^\top - \mathcal{I}) \\
& \left. - \frac{\mu}{r}(\mathbf{v}^\top \mathbf{v})(139\hat{\mathbf{r}}\hat{\mathbf{r}}^\top - 29\mathcal{I}) + \frac{14\mu^2}{r^2}(3\hat{\mathbf{r}}\hat{\mathbf{r}}^\top - \mathcal{I}) \right] \quad (\text{A.5})
\end{aligned}$$

$$\begin{aligned}
\dot{\mathbf{G}}_{2B}^5 = \frac{3\mu}{r^8} & \left[-3465(\hat{\mathbf{r}}^\top \mathbf{v})^5(13\hat{\mathbf{r}}\hat{\mathbf{r}}^\top - \mathcal{I}) + 3150(\hat{\mathbf{r}}^\top \mathbf{v})^3(\mathbf{v}^\top \mathbf{v})(11\hat{\mathbf{r}}\hat{\mathbf{r}}^\top - \mathcal{I}) - \frac{10\mu}{r}(\hat{\mathbf{r}}^\top \mathbf{v})^3(2154\hat{\mathbf{r}}\hat{\mathbf{r}}^\top - 271\mathcal{I}) \right. \\
& + 17325(\hat{\mathbf{r}}^\top \mathbf{v})^4(\mathbf{v}\hat{\mathbf{r}}^\top + \hat{\mathbf{r}}\mathbf{v}^\top) + \frac{6705\mu}{r}(\hat{\mathbf{r}}^\top \mathbf{v})^2(\mathbf{v}\hat{\mathbf{r}}^\top + \hat{\mathbf{r}}\mathbf{v}^\top) - 6300(\hat{\mathbf{r}}^\top \mathbf{v})^3(\mathbf{v}\mathbf{v}^\top) \\
& + 2100(\hat{\mathbf{r}}^\top \mathbf{v})(\mathbf{v}^\top \mathbf{v})(\mathbf{v}\mathbf{v}^\top) - \frac{1740\mu}{r}(\hat{\mathbf{r}}^\top \mathbf{v})(\mathbf{v}\mathbf{v}^\top) - 9450(\hat{\mathbf{r}}^\top \mathbf{v})^2(\mathbf{v}^\top \mathbf{v})(\mathbf{v}\hat{\mathbf{r}}^\top + \hat{\mathbf{r}}\mathbf{v}^\top) \\
& - 525(\hat{\mathbf{r}}^\top \mathbf{v})(\mathbf{v}^\top \mathbf{v})^2(9\hat{\mathbf{r}}\hat{\mathbf{r}}^\top - \mathcal{I}) + \frac{6\mu}{r}(\hat{\mathbf{r}}^\top \mathbf{v})(\mathbf{v}^\top \mathbf{v})(1040\hat{\mathbf{r}}\hat{\mathbf{r}}^\top - 161\mathcal{I}) - \frac{2\mu^2}{r^2}(\hat{\mathbf{r}}^\top \mathbf{v})(955\hat{\mathbf{r}}\hat{\mathbf{r}}^\top - 221\mathcal{I}) \\
& \left. - \frac{801\mu}{r}(\mathbf{v}^\top \mathbf{v})(\mathbf{v}\hat{\mathbf{r}}^\top + \hat{\mathbf{r}}\mathbf{v}^\top) + \frac{292\mu^2}{r^2}(\mathbf{v}\hat{\mathbf{r}}^\top + \hat{\mathbf{r}}\mathbf{v}^\top) + 525(\mathbf{v}^\top \mathbf{v})^2(\mathbf{v}\hat{\mathbf{r}}^\top + \hat{\mathbf{r}}\mathbf{v}^\top) \right] \quad (\text{A.6})
\end{aligned}$$

A.2 SRP Gradient Time Derivatives

Equations A.8 to A.13 lists the SRP gradient and its five time derivatives. Vectors \mathbf{r} and \mathbf{v} refer to the position and velocity of the Sun with respect to the satellite.

$$\psi = -P_{SR}C_r \frac{A_\odot}{m} \quad (\text{A.7})$$

$$\mathbf{G}_{SRP} = \frac{\psi}{r} \left(\hat{\mathbf{r}}\hat{\mathbf{r}}^\top - \mathcal{I} \right) \quad (\text{A.8})$$

$$\dot{\mathbf{G}}_{SRP} = \frac{\dot{\psi}}{r^2} \left[(\mathbf{v}\hat{\mathbf{r}}^\top + \hat{\mathbf{r}}\mathbf{v}^\top) - (\hat{\mathbf{r}}^\top \mathbf{v})(3\hat{\mathbf{r}}\hat{\mathbf{r}}^\top - \mathcal{I}) \right] \quad (\text{A.9})$$

$$\ddot{\mathbf{G}}_{SRP} = \frac{\psi}{r^2} \left[-\frac{6}{r}(\hat{\mathbf{r}}^\top \mathbf{v})(\mathbf{v}\hat{\mathbf{r}}^\top + \hat{\mathbf{r}}\mathbf{v}^\top) + 2\psi(\hat{\mathbf{r}}\hat{\mathbf{r}}^\top) + \frac{2}{r}(\mathbf{v}\mathbf{v}^\top) + \frac{3}{r}(\hat{\mathbf{r}}^\top \mathbf{v})^2(5\hat{\mathbf{r}}\hat{\mathbf{r}}^\top - \mathcal{I}) \right. \\ \left. - \frac{1}{r}(\mathbf{v}^\top \mathbf{v})(3\hat{\mathbf{r}}\hat{\mathbf{r}}^\top - \mathcal{I}) - \psi(\hat{\mathbf{r}}^\top \hat{\mathbf{r}})(3\hat{\mathbf{r}}\hat{\mathbf{r}}^\top - \mathcal{I}) \right] \quad (\text{A.10})$$

$$\ddot{\mathbf{G}}_{SRP} = \frac{\psi}{r^3} \left[\frac{45}{r}(\hat{\mathbf{r}}^\top \mathbf{v})^2(\mathbf{v}\hat{\mathbf{r}}^\top + \hat{\mathbf{r}}\mathbf{v}^\top) - \frac{9}{r}(\mathbf{v}^\top \mathbf{v})(\mathbf{v}\hat{\mathbf{r}}^\top + \hat{\mathbf{r}}\mathbf{v}^\top) - 9\psi(\hat{\mathbf{r}}^\top \hat{\mathbf{r}})(\mathbf{v}\hat{\mathbf{r}}^\top + \hat{\mathbf{r}}\mathbf{v}^\top) \right. \\ \left. - \frac{18}{r}(\hat{\mathbf{r}}^\top \mathbf{v})(\mathbf{v}\mathbf{v}^\top) - 20\psi(\hat{\mathbf{r}}^\top \mathbf{v})(\hat{\mathbf{r}}\hat{\mathbf{r}}^\top) + 4\psi(\mathbf{v}\hat{\mathbf{r}}^\top + \hat{\mathbf{r}}\mathbf{v}^\top) - \frac{15}{r}(\hat{\mathbf{r}}^\top \mathbf{v})^3(7\hat{\mathbf{r}}\hat{\mathbf{r}}^\top - \mathcal{I}) \right. \\ \left. + \frac{9}{r}(\hat{\mathbf{r}}^\top \mathbf{v})(\mathbf{v}^\top \mathbf{v})(5\hat{\mathbf{r}}\hat{\mathbf{r}}^\top - \mathcal{I}) + 2\psi(\hat{\mathbf{r}}^\top \mathbf{v})(\hat{\mathbf{r}}^\top \hat{\mathbf{r}})(24\hat{\mathbf{r}}\hat{\mathbf{r}}^\top - 5\mathcal{I}) - 4\psi(\hat{\mathbf{r}}^\top \mathbf{v})(3\hat{\mathbf{r}}\hat{\mathbf{r}}^\top - \mathcal{I}) \right] \quad (\text{A.11})$$

$$\ddot{\mathbf{G}}_{SRP} = \frac{\psi}{r^3} \left[-\frac{420}{r^2}(\hat{\mathbf{r}}^\top \mathbf{v})^3(\mathbf{v}\hat{\mathbf{r}}^\top + \hat{\mathbf{r}}\mathbf{v}^\top) + \frac{180}{r^2}(\hat{\mathbf{r}}^\top \mathbf{v})(\mathbf{v}^\top \mathbf{v})(\mathbf{v}\hat{\mathbf{r}}^\top + \hat{\mathbf{r}}\mathbf{v}^\top) \right. \\ \left. + \frac{192\psi}{r}(\hat{\mathbf{r}}^\top \mathbf{v})(\hat{\mathbf{r}}^\top \hat{\mathbf{r}})(\mathbf{v}\hat{\mathbf{r}}^\top + \hat{\mathbf{r}}\mathbf{v}^\top) + \frac{180}{r^2}(\hat{\mathbf{r}}^\top \mathbf{v})^2(\mathbf{v}\mathbf{v}^\top) + \frac{18\psi}{r}(\hat{\mathbf{r}}^\top \mathbf{v})^2(26\hat{\mathbf{r}}\hat{\mathbf{r}}^\top - 3\mathcal{I}) \right. \\ \left. - \frac{102\psi}{r}(\hat{\mathbf{r}}^\top \mathbf{v})(\mathbf{v}\hat{\mathbf{r}}^\top + \hat{\mathbf{r}}\mathbf{v}^\top) - \frac{36}{r^2}(\mathbf{v}^\top \mathbf{v})(\mathbf{v}\mathbf{v}^\top) - \frac{\psi}{r}(\mathbf{v}^\top \mathbf{v})(5\hat{\mathbf{r}}\hat{\mathbf{r}}^\top - 4\mathcal{I}) - \frac{18\psi}{r}(\hat{\mathbf{r}}^\top \hat{\mathbf{r}})(\mathbf{v}\mathbf{v}^\top) \right. \\ \left. - 2\psi^2(\hat{\mathbf{r}}^\top \hat{\mathbf{r}})(15\hat{\mathbf{r}}\hat{\mathbf{r}}^\top - 2\mathcal{I}) - \frac{10\psi}{r}(\mathbf{v}\mathbf{v}^\top) - 12\psi^2(\hat{\mathbf{r}}\hat{\mathbf{r}}^\top) + \frac{105}{r^2}(\hat{\mathbf{r}}^\top \mathbf{v})^4(9\hat{\mathbf{r}}\hat{\mathbf{r}}^\top - \mathcal{I}) \right. \\ \left. - \frac{90}{r^2}(\hat{\mathbf{r}}^\top \mathbf{v})^2(\mathbf{v}^\top \mathbf{v})(7\hat{\mathbf{r}}\hat{\mathbf{r}}^\top - \mathcal{I}) - \frac{3\psi}{r}(\hat{\mathbf{r}}^\top \mathbf{v})^2(\hat{\mathbf{r}}^\top \hat{\mathbf{r}})(233\hat{\mathbf{r}}\hat{\mathbf{r}}^\top - 35\mathcal{I}) + \frac{9}{r^2}(\mathbf{v}^\top \mathbf{v})^2(5\hat{\mathbf{r}}\hat{\mathbf{r}}^\top - \mathcal{I}) \right. \\ \left. + \frac{\psi}{r}(\mathbf{v}^\top \mathbf{v})(\hat{\mathbf{r}}^\top \hat{\mathbf{r}})(48\hat{\mathbf{r}}\hat{\mathbf{r}}^\top - 19\mathcal{I}) + 2\psi^2(\hat{\mathbf{r}}^\top \hat{\mathbf{r}})^2(24\hat{\mathbf{r}}\hat{\mathbf{r}}^\top - 5\mathcal{I}) \right] \quad (\text{A.12})$$

$$\begin{aligned}
\dot{\mathbf{G}}_{SRP}^5 = & \frac{\psi}{r^4} \left[\frac{4725}{r^2} (\hat{\mathbf{r}}^\top \mathbf{v})^4 (\mathbf{v} \hat{\mathbf{r}}^\top + \hat{\mathbf{r}} \mathbf{v}^\top) - \frac{3150}{r^2} (\hat{\mathbf{r}}^\top \mathbf{v})^2 (\mathbf{v}^\top \mathbf{v}) (\mathbf{v} \hat{\mathbf{r}}^\top + \hat{\mathbf{r}} \mathbf{v}^\top) \right. \\
& - \frac{3495\psi}{r} (\hat{\mathbf{r}}^\top \mathbf{v})^2 (\hat{\mathbf{r}}^\top \hat{\mathbf{r}}) (\mathbf{v} \hat{\mathbf{r}}^\top + \hat{\mathbf{r}} \mathbf{v}^\top) - \frac{2100}{r^2} (\hat{\mathbf{r}}^\top \mathbf{v})^3 (\mathbf{v} \mathbf{v}^\top) - \frac{102\psi}{r} (\hat{\mathbf{r}}^\top \mathbf{v})^3 (71 \hat{\mathbf{r}} \hat{\mathbf{r}}^\top - 7\mathcal{I}) \\
& + \frac{225}{r^2} (\mathbf{v}^\top \mathbf{v})^2 (\mathbf{v} \hat{\mathbf{r}}^\top + \hat{\mathbf{r}} \mathbf{v}^\top) + \frac{420\psi}{r} (\hat{\mathbf{r}}^\top \hat{\mathbf{r}}) (\mathbf{v}^\top \mathbf{v}) (\mathbf{v} \hat{\mathbf{r}}^\top + \hat{\mathbf{r}} \mathbf{v}^\top) + \frac{2004\psi}{r} (\hat{\mathbf{r}}^\top \mathbf{v})^2 (\mathbf{v} \hat{\mathbf{r}}^\top + \hat{\mathbf{r}} \mathbf{v}^\top) \\
& + \frac{900}{r^2} (\hat{\mathbf{r}}^\top \mathbf{v}) (\mathbf{v}^\top \mathbf{v}) (\mathbf{v} \mathbf{v}^\top) + \frac{18\psi}{r} (\hat{\mathbf{r}}^\top \mathbf{v}) (\mathbf{v}^\top \mathbf{v}) (89 \hat{\mathbf{r}} \hat{\mathbf{r}}^\top - 11\mathcal{I}) + 240\psi^2 (\hat{\mathbf{r}}^\top \hat{\mathbf{r}})^2 (\mathbf{v} \hat{\mathbf{r}}^\top + \hat{\mathbf{r}} \mathbf{v}^\top) \\
& + \frac{852\psi}{r} (\hat{\mathbf{r}}^\top \mathbf{v}) (\hat{\mathbf{r}}^\top \hat{\mathbf{r}}) (\mathbf{v} \mathbf{v}^\top) + 2\psi^2 (\hat{\mathbf{r}}^\top \mathbf{v}) (\hat{\mathbf{r}}^\top \hat{\mathbf{r}}) (909 \hat{\mathbf{r}} \hat{\mathbf{r}}^\top - 103\mathcal{I}) - \frac{143\psi}{r} (\mathbf{v}^\top \mathbf{v}) (\mathbf{v} \hat{\mathbf{r}}^\top + \hat{\mathbf{r}} \mathbf{v}^\top) \\
& - 150\psi^2 (\hat{\mathbf{r}}^\top \hat{\mathbf{r}}) (\mathbf{v} \hat{\mathbf{r}}^\top + \hat{\mathbf{r}} \mathbf{v}^\top) - \frac{272\psi}{r} (\hat{\mathbf{r}}^\top \mathbf{v}) (\mathbf{v} \mathbf{v}^\top) - 2\psi^2 (\hat{\mathbf{r}}^\top \mathbf{v}) (107 \hat{\mathbf{r}} \hat{\mathbf{r}}^\top - 8\mathcal{I}) \\
& - 22\psi^2 (\mathbf{v} \hat{\mathbf{r}}^\top + \hat{\mathbf{r}} \mathbf{v}^\top) - \frac{945}{r^2} (\hat{\mathbf{r}}^\top \mathbf{v})^5 (11 \hat{\mathbf{r}} \hat{\mathbf{r}}^\top - \mathcal{I}) + \frac{1050}{r^2} (\hat{\mathbf{r}}^\top \mathbf{v})^3 (\mathbf{v}^\top \mathbf{v}) (9 \hat{\mathbf{r}} \hat{\mathbf{r}}^\top - \mathcal{I}) \\
& + \frac{30\psi}{r} (\hat{\mathbf{r}}^\top \mathbf{v})^3 (\hat{\mathbf{r}}^\top \hat{\mathbf{r}}) (359 \hat{\mathbf{r}} \hat{\mathbf{r}}^\top - 42\mathcal{I}) - \frac{225}{r^2} (\hat{\mathbf{r}}^\top \mathbf{v}) (\mathbf{v}^\top \mathbf{v})^2 (7 \hat{\mathbf{r}} \hat{\mathbf{r}}^\top - \mathcal{I}) \\
& \left. - \frac{18\psi}{r} (\mathbf{v}^\top \mathbf{v}) (\hat{\mathbf{r}}^\top \mathbf{v}) (169 \hat{\mathbf{r}} \hat{\mathbf{r}}^\top - 28\mathcal{I}) - 10\psi^2 (\hat{\mathbf{r}}^\top \mathbf{v}) (\hat{\mathbf{r}}^\top \hat{\mathbf{r}})^2 (183 \hat{\mathbf{r}} \hat{\mathbf{r}}^\top - 28\mathcal{I}) \right] \quad (\text{A.13})
\end{aligned}$$

A.3 SRP Partial with Respect to Coefficient of Reflectivity Time Derivatives

Equations A.14 to A.19 lists the SRP partial with respect to C_r and its five time derivatives.

Vectors \mathbf{r} and \mathbf{v} refer to the position and velocity of the Sun with respect to the satellite.

$$\mathbf{S} = \gamma \hat{\mathbf{r}} \quad \text{where,} \quad \gamma = -P_{SR} \frac{A_{\odot}}{m} \quad \text{and,} \quad \psi = -P_{SR} C_r \frac{A_{\odot}}{m} \quad (\text{A.14})$$

$$\dot{\mathbf{S}} = \frac{\gamma}{r} \left[\mathbf{v} - (\hat{\mathbf{r}}^\top \mathbf{v}) \hat{\mathbf{r}} \right] \quad (\text{A.15})$$

$$\ddot{\mathbf{S}} = -\frac{2\gamma}{r^2} (\hat{\mathbf{r}}^\top \mathbf{v}) \left(\mathbf{v} - (\hat{\mathbf{r}}^\top \mathbf{v}) \hat{\mathbf{r}} \right) + \frac{\gamma\psi}{r} \hat{\mathbf{r}} - \frac{\gamma}{r^2} \left(\mathbf{v}^\top \mathbf{v} - (\hat{\mathbf{r}}^\top \mathbf{v})^2 \right) \hat{\mathbf{r}} - \frac{\gamma\psi}{r} (\hat{\mathbf{r}}^\top \hat{\mathbf{r}}) \hat{\mathbf{r}} \quad (\text{A.16})$$

$$\begin{aligned}
\ddot{\mathbf{S}} = & \frac{9\gamma}{r^3} (\hat{\mathbf{r}}^\top \mathbf{v})^2 \mathbf{v} - \frac{3\gamma}{r^3} (\mathbf{v}^\top \mathbf{v}) \mathbf{v} - \frac{3\gamma\psi}{r^2} (\hat{\mathbf{r}}^\top \hat{\mathbf{r}}) \mathbf{v} - \frac{8\gamma\psi}{r^2} (\hat{\mathbf{r}}^\top \mathbf{v}) \hat{\mathbf{r}} + \frac{\gamma\psi}{r^2} \mathbf{v} - \frac{15\gamma}{r^3} (\hat{\mathbf{r}}^\top \mathbf{v})^3 \hat{\mathbf{r}} \\
& + \frac{9\gamma}{r^3} (\hat{\mathbf{r}}^\top \mathbf{v}) (\mathbf{v}^\top \mathbf{v}) \hat{\mathbf{r}} + \frac{10\gamma\psi}{r^2} (\hat{\mathbf{r}}^\top \mathbf{v}) (\hat{\mathbf{r}}^\top \hat{\mathbf{r}}) \hat{\mathbf{r}} \quad (\text{A.17})
\end{aligned}$$

$$\begin{aligned}
\ddot{\mathbf{S}} = & -\frac{60\gamma}{r^4}(\hat{\mathbf{r}}^\top \mathbf{v})^3 \mathbf{v} + \frac{36\gamma}{r^4}(\hat{\mathbf{r}}^\top \mathbf{v})(\mathbf{v}^\top \mathbf{v}) \mathbf{v} + \frac{40\gamma\psi}{r^3}(\hat{\mathbf{r}}^\top \mathbf{v})(\hat{\mathbf{r}}^\top \hat{\mathbf{r}}) \mathbf{v} + \frac{79\gamma\psi}{r^3}(\hat{\mathbf{r}}^\top \mathbf{v})^2 \hat{\mathbf{r}} - \frac{22\gamma\psi}{r^3}(\hat{\mathbf{r}}^\top \mathbf{v}) \mathbf{v} \\
& - \frac{11\gamma\psi}{r^3}(\mathbf{v}^\top \mathbf{v}) \hat{\mathbf{r}} - \frac{11\gamma\psi^2}{r^2}(\hat{\mathbf{r}}^\top \hat{\mathbf{r}}) \hat{\mathbf{r}} + \frac{\gamma\psi^2}{r^2} \hat{\mathbf{r}} + \frac{105\gamma}{r^4}(\hat{\mathbf{r}}^\top \mathbf{v})^4 \hat{\mathbf{r}} - \frac{90\gamma}{r^4}(\hat{\mathbf{r}}^\top \mathbf{v})^2 (\mathbf{v}^\top \mathbf{v}) \hat{\mathbf{r}} \\
& - \frac{105\gamma\psi}{r^3}(\hat{\mathbf{r}}^\top \mathbf{v})^2 (\hat{\mathbf{r}}^\top \hat{\mathbf{r}}) \hat{\mathbf{r}} + \frac{9\gamma}{r^4}(\mathbf{v}^\top \mathbf{v})^2 \hat{\mathbf{r}} + \frac{19\gamma\psi}{r^3}(\hat{\mathbf{r}}^\top \hat{\mathbf{r}})(\mathbf{v}^\top \mathbf{v}) \hat{\mathbf{r}} + \frac{10\gamma\psi^2}{r^2}(\hat{\mathbf{r}}^\top \hat{\mathbf{r}})^2 \hat{\mathbf{r}} \quad (\text{A.18})
\end{aligned}$$

$$\begin{aligned}
\overset{5}{\mathbf{S}} = & \frac{525\gamma}{r^5}(\hat{\mathbf{r}}^\top \mathbf{v})^4 \mathbf{v} - \frac{450\gamma}{r^5}(\hat{\mathbf{r}}^\top \mathbf{v})^2 (\mathbf{v}^\top \mathbf{v}) \mathbf{v} - \frac{525\gamma\psi}{r^4}(\hat{\mathbf{r}}^\top \mathbf{v})^2 (\hat{\mathbf{r}}^\top \hat{\mathbf{r}}) \mathbf{v} - \frac{924\gamma\psi}{r^4}(\hat{\mathbf{r}}^\top \mathbf{v})^3 \hat{\mathbf{r}} + \frac{45\gamma}{r^5}(\mathbf{v}^\top \mathbf{v})^2 \mathbf{v} \\
& + \frac{95\gamma\psi}{r^4}(\hat{\mathbf{r}}^\top \hat{\mathbf{r}})(\mathbf{v}^\top \mathbf{v}) \mathbf{v} + \frac{319\gamma\psi}{r^4}(\hat{\mathbf{r}}^\top \mathbf{v})^2 \mathbf{v} + \frac{312\gamma\psi}{r^4}(\hat{\mathbf{r}}^\top \mathbf{v})(\mathbf{v}^\top \mathbf{v}) \hat{\mathbf{r}} + \frac{50\gamma\psi^2}{r^3}(\hat{\mathbf{r}}^\top \hat{\mathbf{r}})^2 \mathbf{v} \\
& + \frac{331\gamma\psi^2}{r^3}(\hat{\mathbf{r}}^\top \hat{\mathbf{r}})(\hat{\mathbf{r}}^\top \mathbf{v}) \hat{\mathbf{r}} - \frac{33\gamma\psi}{r^4}(\mathbf{v}^\top \mathbf{v}) \mathbf{v} - \frac{33\gamma\psi^2}{r^3}(\hat{\mathbf{r}}^\top \hat{\mathbf{r}}) \mathbf{v} - \frac{69\gamma\psi^2}{r^3}(\hat{\mathbf{r}}^\top \mathbf{v}) \mathbf{r} + \frac{\gamma\psi^2}{r^3} \mathbf{v} - \frac{945\gamma}{r^5}(\hat{\mathbf{r}}^\top \mathbf{v})^5 \hat{\mathbf{r}} \\
& + \frac{1050\gamma}{r^5}(\hat{\mathbf{r}}^\top \mathbf{v})^3 (\mathbf{v}^\top \mathbf{v}) \hat{\mathbf{r}} + \frac{1260\gamma\psi}{r^4}(\hat{\mathbf{r}}^\top \mathbf{v})^3 (\hat{\mathbf{r}}^\top \hat{\mathbf{r}}) \hat{\mathbf{r}} - \frac{225\gamma}{r^5}(\hat{\mathbf{r}}^\top \mathbf{v})(\mathbf{v}^\top \mathbf{v})^2 \hat{\mathbf{r}} \\
& - \frac{504\gamma\psi}{r^4}(\hat{\mathbf{r}}^\top \mathbf{v})(\mathbf{v}^\top \mathbf{v})(\hat{\mathbf{r}}^\top \hat{\mathbf{r}}) \hat{\mathbf{r}} - \frac{280\gamma\psi^2}{r^3}(\hat{\mathbf{r}}^\top \mathbf{v})(\hat{\mathbf{r}}^\top \hat{\mathbf{r}})^2 \hat{\mathbf{r}} \quad (\text{A.19})
\end{aligned}$$